

THE GASIFICATION OF CARBONACEOUS
MATERIALS IN MOLTEN
SODIUM PHOSPHATE

Thesis by
Mark A. Siddoway

In Partial Fulfillment of the Requirements
for the Degree of
Doctor of Philosophy

California Institute of Technology

Pasadena, California 91125

1982

(Submitted November 30, 1981)

ACKNOWLEDGEMENTS

I would like to express my appreciation to Professor George R. Gavalas. His suggestions as my academic advisor and encouragement as my research supervisor have helped to guide my efforts successfully. Dr. Gavalas' enthusiasm for experimental chemical reaction engineering has made my tenure as a graduate student both profitable and enjoyable.

The funding of this project by the Department of Energy is gratefully acknowledged. I would also like to thank Rockwell International, the National Science Foundation, and the California Institute of Technology for their financial assistance.

Charunya Phichitkul and Nick Kaffes have been both appreciated colleagues and personal friends. Nick Kaffes in particular laid the groundwork necessary for this project. I am indebted to many others in the Caltech community for many profitable discussions and close friendships including Dean Taylor, Chi-Ming Chan, and Ernest Chung. I am also grateful for the assistance and friendship of Dr. Basil Iatridis in the early stages of this project.

Special thanks are extended to George Griffith, Seichi Nakawatase, Ray Reed, Henry Smith, and John Yehle for their assistance throughout this project. George Griffith's suggestions were instrumental in helping to design and construct the experiments presented in this thesis.

Dow Chemical, DuPont, Texaco, Union Oil, Occidental Research, and Gulton Industries were very helpful in supplying samples and in answering questions. I am grateful to JPL (in particular Charunya Phichitkul and Dr. Miretta Stephanopolous) for the use of their analytical facilities. Harbison-Walker Corporation, WP Keith Company, and Emerson & Cummings were also cooperative in answering specific questions.

The figures for this thesis were drawn by Heather Marr and I am grateful to her for her skill as an artist.

My sincere gratitude and thanks also go to a special group of friends -- Elsie Amaya, Jack Moya, Wendy Graves, Maresa Windle, Brent and Esther Church, Charlyn Moser, and Toi, Miriam and Debbie Newberry for their moral support over these past few years.

My deepest gratitude and thanks go to my parents, Mildred and Denton Siddoway, for their patience, care, and encouragement throughout my tenure as a student. And a very special thanks to my wife, Gloria, not only for her love and encouragement, but also for typing this thesis and for putting up with innumerable delays. The author owes a great debt to all the members of his family and greatly appreciates all of them.

ABSTRACT

The gasification rates of petroleum coke, char, and residual oil were measured in molten sodium phosphate. Both oxygen and steam were used as oxidants, and a variety of reactor configurations were studied. Reactors consisted of fused ceramic parts sealed into a reactor configuration using castable refractory.

The reaction rate of carbon particles in a bubbling molten phosphate slurry was found to depend upon the rate of particle-bubble contacting. Upon contact, direct conversion of carbon particles with the gas phase occurs due to the large carbon-molten sodium phosphate contact angle (136°). The potential flow solution for flow around a bubble where particles are assumed to follow the streamlines gave a consistent picture of bubble-particle contacting. The reactivity of the carbon in the bulk liquid was found to be negligible due to the low solubility of oxygen in the melt.

Gas phase (no salt) results were generated to establish base cases and to examine treatment effects on the reactivity of green sponge and green needle cokes. The reactivities of both were favorably affected by toluene extraction and adversely affected by calcination to 1300 K. Extraction decreased the agglomerating nature of the sponge coke. Both extracts were largely aromatic with the needle coke extract being more so.

Molten sodium phosphate was found to catalyze the gasification of petroleum coke by steam and by oxygen. Such catalytic effects are limited due to the large carbon-salt contact angle and may be obscured in slurry reactors by the rate of particle-bubble contacting being slow. The steam reforming of residual oil revealed that the carbonized product in the molten salt phase closely resembled sponge petroleum coke (as produced by delayed coking).

Cold model experiments employing water and polymeric beads revealed that dilute slurries of small, non-wetting particles decreased the rise velocity of single bubbles and increased the rate of bubble coalescence in swarms. Dilute slurries of wetting particles had no effect in either case.

TABLE OF CONTENTS

	Page
Acknowledgement	ii
Abstract	iv
Table of Contents	vi
CHAPTER 1 - INTRODUCTION	1
1.1 General Introduction	2
1.2 Gasification of Carbon	3
1.3 Gasification in Molten Salts	7
1.4 Molten Salts in General	12
1.4.1 General Aspects of the Molten Ionic State	12
1.4.2 Past and Possible Future Applications of Molten Salts	16
1.4.3 Sodium Phosphate Salts	18
References	21
CHAPTER 2 - PARTICLE EFFECTS IN BUBBLE COLUMNS	25
2.1 Introduction	26
2.1.1 Bubble Characteristics	27
2.1.2 Gas Hold-Up	29
2.1.3 The Particle Effect on Bubble Coalescence and Break-Up	33
2.1.4 Particle-Bubble Encounter	37
2.2 Experimental	41

2.3	Particle Dispersion and Induced Countercurrent Flow	49
2.4	Particle-Bubble Interactions	61
2.4.1	Particle Location	62
2.4.2	Particle-Bubble Contacting	64
2.4.2.1	Single Bubbles Rising in Countercurrent Flow	65
2.4.2.2	Single Bubbles Rising in Stagnant Columns of Liquid	68
2.5	Gas Hold-Up	78
2.5.1	The General Features of Gas Hold-Up	80
2.5.2	The Particle Effect on Gas Hold-Up	86
2.6	Conclusions	92
	Notation	94
	References	99
CHAPTER 3 - THE REACTION MECHANISM OF CARBON PARTICLES IN MOLTEN SODIUM PHOSPHATE		103
3.1	Introduction	104
3.2	Solubilities of Gases in Molten Salts	112
3.3	Diffusion Correlations at High Temperatures	119
3.4	Experimental	126
3.4.1	Measurement of the Contact Angle	126
3.4.2	Measurement of the Reaction Rate in Molten Sodium Phosphate	128
3.5	Results and Discussion	132

3.6	Conclusions	137
	Notation	144
	References	149
CHAPTER 4 - THE GASIFICATION OF PETROLEUM COKE IN MOLTEN SODIUM PHOSPHATES		153
4.1	Introduction	154
4.2	Properties of Green Sponge Petroleum Coke	158
4.3	Experimental	167
4.4	Results and Discussion	177
4.4.1	Reactor I Results	179
4.4.2	The Particle Size Effect	187
4.4.3	Reactor II Results	197
4.4.4	Comparison of Results	201
4.5	Conclusions	205
	Notation	206
	References	209
CHAPTER 5 - PETROLEUM COKE IN THE PREGRAPHITIZATION REGIME		212
5.1	Introduction	213
5.2	Properties of the Carbons Studied	218
5.2.1	Treatment of the Green Cokes	218
5.2.2	Surface Area and porosity of the Carbons	220

5.3	Experimental	222
5.3.1	Devolatilization of the Green Coke	222
5.3.2	Agglomeration of the Green Coke	224
5.3.3	NMR Spectroscopy of the Toluene Extracts of the Green Cokes	229
5.3.4	Reaction Rate Experiments of the Carbons	234
5.4	Results and Discussion	235
5.5	Conclusions	247
	References	248
CHAPTER 6 - THE PARTICLE LOADING EFFECT IN MOLTEN PHOSPHATE SLURRIES		250
6.1	Introduction	251
6.1.1	Theory	251
6.2	Experimental	258
6.3	Results and Discussion	267
6.3.1	Fluid Mechanical Considerations	267
6.3.2	Reaction Rate Results for the Short Reactor	270
6.3.3	Reaction Rate Results for the Long Reactor	274
6.4	Conclusions	287
	Notation	288

CHAPTER 7 - THE GASIFICATION OF CHAR IN MOLTEN PHOSPHATE SLURRIES	291
7.1 Introduction	292
7.2 Experimental	293
7.3 Results and Discussion	293
7.3.1 The Reaction Rate of Char with No Salt	293
7.3.2 The Reaction Rate of Char in Molten Salt Slurries	301
References	307
CHAPTER 8 - THE GASIFICATION OF RESIDUAL OIL IN MOLTEN PHOSPHATE SLURRIES	308
8.1 Introduction	309
8.2 Experimental	309
8.3 Results and Discussion	318
8.4 Conclusions	326
CHAPTER 9 - THE DESIGN OF CERAMIC REACTORS FOR CONTAINING MOLTEN SODIUM PHOSPHATE	328
9.1 Introduction	329
9.2 Glazing	329
9.3 The Large System	333
9.3.1 The Annular Reactor	333
9.3.2 The Large Reactor System	337
9.4 The Small Reactor System	349
9.5 Failure Modes of Fused Ceramic Reactors	355
9.5.1 Thermal Shock Failure	355

9.5.2	Corrosion of the Ceramic Mullite Tubes	355
9.5.3	Corrosion of the Ceramic Crucibles	357
9.6	Conclusions	363
	References	363
CHAPTER 10 - CONCLUSIONS AND RECOMMENDATIONS		364
10.1	Introduction	365
10.2	General Conclusions	365
10.3	Recommendations for Further Research	367
10.4	Critique of the Molten Salt Gasification Process	369
APPENDICES		372
Appendix I	- Bubble Rise Velocities in Molten Sodium Phosphate	373
Appendix II	- The Effect of Mixing on the Observed Reaction Rate	377
Appendix III	- The Mixing Effects Caused by Laminar Flow	380
Appendix IV	- Thermal Pyrolysis and Steam Reforming Experiments	385
Appendix V	- The Materials Used for Reactor Construction	398

CHAPTER 1

INTRODUCTION

1.1 General Introduction

Oil and natural gas reserves have served as the staple of American energy consumption since the beginning of the twentieth century. With domestic reserves of these fuels declining and with the trade imbalance built by importing fossil fuels, a probable need of 150 Q annually¹ ($1Q=10^{15}$ BTU) by the year 2000 dictates the need for America to begin relying on alternative fuels.

The most obvious choice, due to its domestic abundance, is coal. And to offset conversion costs for changing existing gaseous or liquid combustion facilities to handle solids, it is desirable to convert the coal to either a synthetic liquid or gas. Such processes, liquefaction and gasification respectively, are being pursued along a variety of lines (2,3,4).

Here we will be concerned with gasification only. Such gasification need not be confined to coal. Heavy hydrocarbon mixtures such as residual oil and possibly the heavier products of coal liquefaction could also be gasified to produce a synthesis gas or a low BTU gas suitable for use near the point of its production such as in a combined power cycle. Littlewood (5) has reviewed many of these processes. They include both thermal and catalytic reforming of the mixture. Such processes generally combine a fuel rich mixture with steam and/or oxygen at high temperatures.

The main problems of gasification processes is their inability to handle a variety of feedstocks. With conventional fixed bed reforming of hydrocarbons, heavy hydrocarbons will plug the system with coke and high sulfur feeds can poison the catalyst. Fluidized or fixed bed gasification processes for the production of gas from solids such as coal cannot handle caking or agglomerating coals without pretreatment. And there is a general inability to interconvert liquid and solid gasification systems.

Herein shall be presented a study of a particular gasification process amenable to liquid and solid feedstocks -- gasification in molten salt. For now we will begin by discussing the general features of gasification. After this, the chemical engineering features and problems of the molten salt process will be presented. It is these features which will constitute the subsequent chapters of this study. This introductory chapter will then be concluded by discussing the general aspects and uses of molten salts.

1.2 Gasification of Carbon

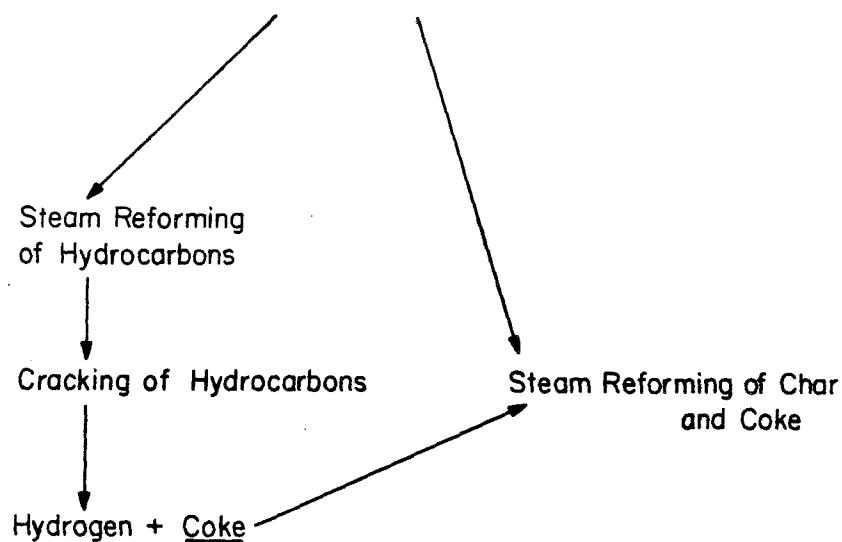
Gasification of carbon containing materials is simply the conversion of liquids or solids to gaseous products. Such conversion entails chemical interaction with a supplied reactant and thermal pyrolysis. The reactants we will be concerned with are steam and oxygen. Reforming with steam is a

relatively slow, endothermic process as contrasted to rapid, exothermic combustion with oxygen. The stoichiometry of the mixture as well as the residence time in the gasifier determines the utility of the offgas. The product gas could have zero heating value such as the effluent of a coal burning steam generator or a relatively high heating value when the offgas contains predominantly carbon monoxide, hydrogen, and light hydrocarbons. Here we are concerned with producing a gas with net heating value. That is, we are considering transferring the heating value extant in a liquid or solid to a gaseous product.

The chemical reactions involved in hydrocarbon and coal steam reforming are outlined in Figure 1. Combustion involves similar steps except for the reactant being oxygen. As is seen, thermal pyrolysis is the initial step in both types of reforming. It is also apparent that both processes entail the subsequent reaction of a solid product. The reaction of this carbonaceous solid is also the slowest step in the overall scheme and hence serves as the rate controlling step. Our principal concern in this study is this solid product, so we now turn our attention to the gasification of solid particles.

The oxidation of a carbon particle entails an intricate coupling of mass and heat transfer with chemical kinetics. The analysis of such systems must differentiate between the transport aspect and the chemical kinetics. Transport analysis

STEAM REFORMING OF RESIDUAL OIL
OR COAL/CHAR



A. HYDROCARBON STEAM REFORMING

- (1) Hydrocarbon Mixture \rightarrow Light Olefins, Light Paraffins, Coke
- (2) Light Olefins + $H_2O \rightarrow H_2 + CO + Coke$
- (3) Light Paraffins + $H_2O \rightarrow H_2 + CO + Coke$
- (4) $CO + H_2O \rightarrow CO_2 + H_2$
- (5) $Coke + H_2O \rightarrow CO + H_2$

B. COAL STEAM REFORMING

- (1) Coal \rightarrow Char. + Volatiles
- (2) Volatiles + $H_2O \rightarrow H_2 + CO + Coke$
- (3) $H_2O + Char \rightarrow CO + H_2 + Ash$
- (4) $H_2O + CO \rightarrow CO_2 + H_2$

Figure 1. The features of steam reforming of hydrocarbons and coal. The rate determining step is ultimately the carbon-water reaction.

of such systems starts by assuming a boundary layer or fluid film to surround the particle. At the outer boundary of this layer, there is a net influx of the oxidizing species requiring a net efflux of the oxidized species. In the boundary layer, the oxidizing species may be homogeneously reduced. If not, reduction is heterogeneous at the surface of the particle. Such heterogeneous reduction may take place only on or near the external surface of the particle if boundary layer transport is slow. But if transport through the boundary layer is suitably rapid, then we must consider the oxidant's penetration of the particle's pore structure. And finally, if the overall rate of mass transfer is found to be sufficiently rapid, the chemical kinetics may be analyzed as the observed reaction rate of the particle will yield the true activation energy of the chemical reaction, E_K .

This series coupling of resistances may be categorized into three temperature zones as by Walker et al (6). Defining the effectiveness factor, κ , in the usual manner as the ratio of the observed reaction rate to the reaction rate with infinitely fast mass transfer, we have:

<u>Zone</u>	<u>Rate Controlling Step</u>	<u>Effectiveness Factor (κ)</u>	<u>Activation Energy (E)</u>
I	Boundary Layer Mass Transfer	$\kappa \ll 1$	$E \sim 0$ (1)
II	Pore Penetration	$\kappa \leq \frac{1}{2}$	$E \sim \frac{E_K}{2}$
III	Chemical Kinetics	$\kappa = 1$	$E = E_K$

Several methods are available for modelling carbon particle gasification in a gaseous environment. Field et al (7) tabulated mass transfer and reactive resistances for the series rate process. Carem and Amundsen (8) have proposed a model for char gasification assuming a stagnant boundary layer. And Arri and Amundsen have modelled the gasification of a single char particle (9) and used the result to predict the performance of a countercurrent gasifier (10).

For gasification in Zone III, the reactivity of the carbon may be measured directly. In this zone, the catalytic effect of impurities may be measured by a decrease in the activation energy. However such catalytic effects have received the widest study by observing the lowering of the ignition temperature in the presence of impurities. Most substances (including both cations and anions) catalyze carbon gasification. Hence impure carbons such as coal have substantially greater reactivity than highly pure substances such as graphite. These effects have been reviewed by Walker et al (11).

1.3 Gasification in Molten Salts

Molten salt gasification was first studied on a significant basis by Cover et al (12) and more recently by Botts et al (13). These processes used molten sodium carbonate which is sensitive to hydrolysis by steam. This study employs

molten sodium phosphate which is more stable than the carbonate.

Gasification in molten salts entails a complex but sturdy coupling of transport phenomena and chemical kinetics. Reactant gas is bubbled through a slurry of molten salt and carbon particles. Hence the major transport aspect is transferring the gasifying agent to and gasified species from the carbon. The chemical kinetics entails gasifying carbon in the presence of the salt's cationic and anionic species.

The advantages of the molten salt process are detailed in Figure 2. All inherent advantages arise from the liquid nature of the reaction medium. Carbon deposition or sulfur deactivation cannot inhibit performance as the surface of the reactant gas bubble is continually renewed. The process also may be kept isothermal by agitation of the molten salt. And ash contaminants are removed by dissolution in the molten phase.

Several aspects of molten salt processes have been discussed by Glueck (14). Figure 3 represents a conceptual process whereby endothermic production of a product gas in one section receives heat by exothermic combustion in another section.

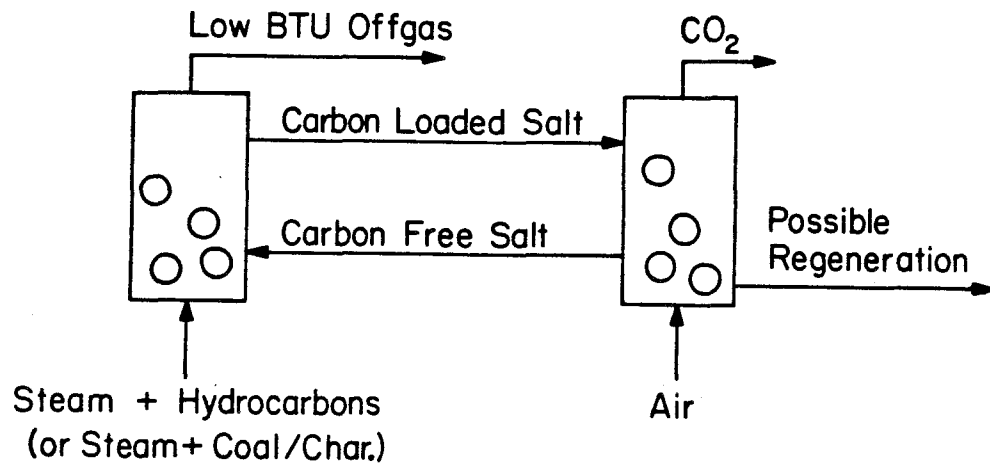
It is seen that the molten salt process is a bubble column slurry reactor entailing fluid mechanical and chemical kinetic considerations. This study will begin in Chapter 2 by presenting a review and experimental study of bubble columns.

ADVANTAGES OF MOLTEN SALT STEAM REFORMING

- (1) Renewable Surface Area
 - The salt phase is a liquid, and the surface exposed to the reactant is continually renewed.
- (2) Elimination of Sulfur Poisoning
 - The entire salt phase is an active homogenous catalyst thus preventing any non-renewable surface from becoming deactivated.
- (3) Excellent Heat Transfer Baths
 - The salt, being liquid, is kept isothermal by agitation and affords good heat transfer to the injected reactants due to its liquid nature.
- (4) Ash/Contaminant Removal
 - Ash and contaminants are retained in the salt phase, and this phase may be regenerated by withdrawing a stream of salt and dissolving the salt. This leaves insoluble matter to be discarded.

Figure 2. The advantages of the molten salt gasification process arise from the use of a liquid reaction medium.

MOLTEN SALT CONCEPTUAL PROCESS



CHARACTERISTICS and CONSIDERATIONS

- (1) Three Phase System
Gas - Liquid - Solid
- (2) Fluid Mechanical Considerations
Bubble - Particle Contacting
Gas - Liquid Interfacial Area
Gas Hold-Up in the Liquid Phase
- (3) Kinetic Considerations
Catalytic effect of the Salt
Catalytic effect of Impurities

Figure 3. The general features of a molten salt gasification process.

Principally in Chapter 2, we shall deal with the effects nonwetting particles have on the performance of such systems. That is, due to carbon and molten salt being chemically different, a nonzero contact angle between the salt and carbon is feasible. This assumption will be justified in Chapter 3. Chapters 4 through 7 will then deal with the rates of carbon particle gasification in molten salt. Chapter 8 will then present the case for liquid hydrocarbon gasification in molten salts.

In Chapter 9, the problems of designing molten salt reactors shall be discussed. Here we will deal with the main drawback of molten salts -- their corrosive nature. This study shall then be concluded with a critique of the process.

We are thus presenting a process with possibilities and distinct advantages. The emphasis here will be to illustrate the underlying features of the molten salt process. Admittedly, the most striking feature of molten salt gasification is the solvent properties of the salt -- particularly as applied to the dissolution of the reactor.

1.4 Molten Salts in General

Here we shall briefly review the general features of molten salts. Particular emphasis shall be given to their structure as influenced by their ionic state. Applications outside of carbon gasification of molten salts will then be discussed. Finally we will conclude with a discussion of sodium phosphate.

1.4.1 General Aspects of the Molten Ionic State

Molten salts are Newtonian fluids with thermal and electrical conductivities intermediate to those of water and liquid metals. Their transport properties follow the usual exponential temperature dependence and have been discussed by Bockris and Redding (15). Apparently the Stokes-Einstein relationship between viscosity and diffusion works well for predicting ionic self-diffusion in molten salts. However the Nernst-Einstein relation between diffusion and conduction is not followed. An interesting correlation is that the activation energies for viscosity and self diffusion seem to be about $3.7RT_m$ for many salts (16). Here R is the gas constant and T_m is the melting point temperature.

The state of molten ionic liquids has been the subject of extensive discussion over the years. Tempkin (17) first realized that there should be structure present in molten electrolytes as "cations should be surrounded by anions and vice versa." This led Tempkin to define the ideal solution

for molten salts. The entropy of a species (ie, an anion-cation pair) in a solution is postulated to consist of two parts -- the contribution from permutations of the cation among the cationic sites and from permutations of the anion among the anionic sites. Mutual permutations of cations and anions must be excluded due to the unfavorable Coulombic interaction in placing like ions in adjacent sites. In reality, extreme deviations apparently occur from this ideal model (18).

The gist of the Tempkin model though has been confirmed by X-ray and neutron diffraction of molten alkali halides (19). The radial distribution function (RDF) extracted from the diffraction spectra reveals the existence of two broad peaks corresponding to favorable placement of the nearest neighbors (unlike ions) and next nearest neighbors (like ions). This is surprising. While the solid structure of salts is a regular, crystalline array, the structure of the molten state should be quite random. While this reasoning holds true for long range order in molten salts, the above indicates that a degree of short range order is preserved. If the maxima of the peaks in the RDF are used, it is found that nearest neighbor distances actually decrease as compared to the solid state while next nearest neighbor distances increase slightly. The coordination number apparently decreases. Such short range ordering is also indicated by vibrational spectra (20).

Studies of the more complex anions (sulfates, nitrates, and carbonates) cannot yield data on average nearest neighbor distances due to the added number of centers. But it is found that the complex ions are preserved as entities on melting.

To reconcile these results, three types of liquid theories have been applied to the liquid state of salts. These structural theories have three common goals. As most salts are observed to experience about a 20% volume increase on melting, the model must inject volume into the molten state. It must also account for the apparent structure observed by the diffraction data. Finally, it should be useful in either correlating data into an equation of state or predicting the properties of the salts.

"Significant Structure Theory" has been applied by Eyring et al (21) to the molten alkali halides. For this model, voids are created in the solid upon melting, and the salt is partitioned between a solid-like phase and a gas phase in the voids. Semi-empirical partition functions so developed have had success in predicting thermodynamic properties. The model also enjoyed success in predicting some transport properties (22). Bockris (23) has applied the hole theory of Furth (24) to molten salts. Here liquid properties are described by molecular sized thermal fluctuations which yield spherical holes. While not empirical, the macromolecular surface tension is extended to molecular dimensions. Bockris was successful in using equations of state

developed from the hole theory to predict the compressibility and thermal expansion coefficient. The final model is the extension of the solid lattice to the liquid state as discussed by Stillinger (25). Here vacancies are created in the lattice to account for the increase in volume on melting. The emphasis of this model was to predict the microstructure which the model did qualitatively.

The law of corresponding states has been applied to molten salts by Reiss et al (26). Pairwise Coulombic interactions were summed assuming a rigid core for finite ion size. Thermodynamic properties of the alkali halide salts were well correlated, with lithium salts being peculiar exceptions.

Hence molten salts have been quite well characterized by the diligence of several researchers. While all structural theories of molten salts have their advantages, they have only been applied to the simpler salts, ie, the alkali or alkaline halides. For such salts, the hole theory (27) apparently gives an adequate representation at present. The active interest in molten salts has led to several scientific investigations of their properties over the past forty years. This in turn has led to the establishment of a Molten Salts Data Center at Rensselaer Polytechnic University in Troy, New York, under the direction of G. J. Janz and an extensive volume of molten salt properties (28).

1.4.2 Past and Possible Future Applications of Molten Salts

The uses of molten salts are conceptually varied but industrially confined to electrochemical processing. The Hall-Heroult process of 1886 is used to supply all of the world's aluminum by electrolytic reduction of alumina in molten cryolite (29). Other uses include the electrolytic production of magnesium and sodium from their respective molten chlorides. Future prospects of the use of high temperature electrolytes include electrodeposition (30) and the use of molten salt fuel cells (31).

An intriguing application of molten salts (specifically the molten fluorides) is for liquid fuels for nuclear reactors. Initially developed to fuel aircraft nuclear propulsion systems, apparent advantages led to the development of a molten salt reactor which first went critical in 1965 at Oak Ridge (32). The extension to breeder reactors is possible (33) due to the high solubility of fuels as well as fertile materials (^{232}Th) by the molten fluorides. The future use of molten salts as blanket fluids in controlled fusion reactors has been discussed by Grimes and Cantor (34).

Molten salts have also been employed as chemical reaction media. Such applications have been reviewed by Sundermeyer (35), Kenney (36), and Parshall (37). Chemical reactions which take place in molten salts may be divided into three areas (from Sundermeyer (35)):

1. Reactions involving participation of the melt and consumption of one or more of its components, with no simple means of regenerating the latter.
2. Reactions in which the melt simply acts as a solvent for the reactants, or in which the components of the melt are formed as by-products, or in which the by-products can be chemically or electrochemically reconverted into the starting compounds.
3. Reactions in which the melt acts as a catalyst.

Most chemical reactions studied supported the molten salt on an inert porous solid. The reactions studied include halogenation, oxidation, and nitration. Catalytic applications include zinc chloride and other Lewis acids for cracking highly aromatic feedstocks and vanadium pentoxide for the conversion of SO_2 to SO_3 .

Naturally the applicability of molten salts as liquid reaction media entails ultimate separation of the product from the salt. The easiest method is to have the product evolve as a gas. Other possible methods include decanting a separate product phase or electrodeposition. A number of extractive processes have been proposed for molten salt breeder reactors (33). The ultimate method would be to cool the salt and remove the product by dissolution or other means.

1.4.3 Sodium Phosphate Salts

Phosphorus is found to exist in several oxidation states including -3,+3,+4, and +5 (38). Here we will be concerned with the +5 oxidation state which includes phosphorus pentoxide (P_2O_5), metaphosphate (PO_3^{-1}), tripolyphosphate ($P_3O_{10}^{-5}$), pyrophosphate ($P_2O_7^{-4}$), and orthophosphate (PO_4^{-3}). In this oxidation state, phosphorus exhibits sp^3 -bonding and, as such, has fourfold coordination with oxygen atoms in tetrahedral symmetry. Sodium phosphates (as well as all phosphates with a monovalent cation) may be classified as $(Na_2O)_x(P_2O_5)_y$. Consequently to denote a particular phosphate, we will refer to its x/y ratio or λ .

The most important aspect of phosphate anions is their tendency to polymerize and form glasses (39). This tendency is maximized for lower values of λ . Increasing the concentration of the cation (ie, increasing λ) results in the scission of more P-O-P linkages with an attendant decrease in the degree of polymerization. Ultimately this process will lead to only orthophosphate ions being present. It is found for $\lambda \leq 1$, ring structures and branched chain anions are prevalent. For $\lambda > 1$, only straight chains are found. The effect of water on the glass is similar to the cation's in that it hydrolyzes the linkages and decreases the average chain length. Apparently at room temperature and neutral pH such hydrolysis is extremely slow. However for λ between 1.1 and 1.5, sodium phosphates are miscible with water.

Morey and Ingerson (40) have presented the phase diagram for sodium phosphates between $\lambda = 1$ and $\lambda = 2$. This has been extended to $\lambda = 3$ by Turkdogan and Maddocks (41). Crystalline compounds found to be in equilibrium with the liquid phase include metaphosphate, tripolyphosphate, pyrophosphate, and orthophosphate. The diagram reveals two eutectics corresponding to $\lambda = 1.28$ at 552°C and $\lambda = 2.33$ at 944°C .

The physical properties of molten sodium phosphates between $\lambda = 1$ and $\lambda = 2$ are given by Van Wazer (39). It is found that they are Newtonian fluids with very high surface tensions. Molten sodium phosphate is also a very good solvent, and platinum is the only known material which is not attacked.

The molten state is difficult to describe due to the polymerization of the anion. A recent study by Phalipou and Zarzycki (42) rapidly quenched molten sodium phosphate. The resulting average chain length of the anion was found to decrease from 5.25 phosphorous atoms for $\lambda = 1.38$ to 3.05 phosphorous atoms for $\lambda = 1.65$. For the lower λ , more than 30% by weight of the chains had eight or more phosphorus atoms. For the higher λ , all chains had less than eight phosphorus atoms. The monomeric anion (ie, the orthophosphate) concentration was negligibly small in both cases.

Addition of various elements to molten phosphates has been reviewed by Plambeck (43). Oxygen does not react. Metallic zinc and nickel apparently will reduce the phosphate to elemental

phosphorus. When added as cations, the normal oxidation states of Fe(+2,+3) and Ni(+2) are preserved. Octahedral coordination of transition metal ions is indicated with lithium phosphate (44). In this laboratory, the addition of Ni(+2) to sodium phosphate was found to substantially increase the viscosity of the melt. Due to the octahedral coordination, this increase is likely due to the increased size of the flow unit.

REFERENCES

1. Balzhiker, R. E., Chem. Eng., 84(No. 1), 73, (1977)
2. Perry, H., Chem. Eng., 81(No. 15), 88 (1974)
3. Berkowitz, N., Coal Gasification--A "State of the Art" Review, Information Series #64, Alberta Research, Edmonton, Alberta, April (1973)
4. Evaluation of Coal Conversion Processes to Provide Clean Fuels, EPRI 206-0-0, October (1974)
5. Littlewood, K., Prog. Energy Combustion Science, 3, 35 (1977)
6. Walker, P. L., Jr., Rusinko, F., Jr., and Austin, L. G., Advances in Catalysis, 11, 133 (1959)
7. Field, M. A., Gill, D. W., Morgan, B. B., and Hawksley, P. G. W., Combustion of Pulverized Coal, The British Coal Utilization Research Association, Leatherhead (1977)
8. Carem, H. S., and Amundsen, N. R., Ind. Eng. Fund., 16, 171 (1977)
9. Arri, L. E., and Amundsen, N. R., AIChE Journal, 24, 72 (1978)
10. Arri, L. E., and Amundsen, N. R., AIChE Journal, 24, 87 (1978)
11. Walker, P. L., Jr., Shelef, M., and Anderson, R. A., Chemistry and Physics of Carbon, 4, 287 (1968)
12. Cover, A. E., Schreiner, W. C., and Skaperdas, G. T., Chem. Eng. Prog., 69, 31 (1973)

13. Botts, W. V., Kohl, A. L., and Trilling, C. A., Proc. 11th Intersociety Energy Conversion Conference, Volume I, p. 280, September (1976)
14. Glueck, A. R., in Recent Advances in Air Pollution Control, (R. W. Coughlin, et al, eds.), p. 231, AIChE Symposium Series No. 137, Volume 70, (1974)
15. Bockris, J. O'M., and Redding, A. K. N., Modern Electrochemistry, Volume I, Plenum Press, New York (1970)
16. Eni, T., and Bockris, J. O'M., J. Phys. Chem., 74, 159 (1976)
17. Tempkin, M., Acta. Physicochem. U.R.S.S., 20, 411 (1945)
18. Blander, M., in Molten Salt Chemistry, (M. Blander, ed.), p. 127, Interscience Publishers, New York (1964)
19. Levy, H. A., and Danford, M. D., in Molten Salt Chemistry, (M. Blander, ed.), Interscience Publishers, New York (1964)
20. Smith, G. P., in Molten Salt Chemistry, (M. Blander, ed.), Interscience Publishers, New York (1964)
21. Carlson, C. M., Eyring, H., and Ree, T., Proc. Nat. Acad. Sci. (USA), 46, 333 (1960)
22. Lu, W. C., Ree, T., Gerrard, V. G., and Eyring, H., J. Chem. Phys., 49, 797 (1968)
23. Bockris, J. O'M., and Richards, N. E., Proc. Royal Soc. (London), A241, 44 (1957)
24. Furth, R., Proc. Cambridge Phil. Soc., 37, 252 (1941)

25. Stillinger, F. H., in Molten Salt Chemistry, (M. Blander, ed.) Interscience Publishers, New York (1964)
26. Reiss, H., Mayer, S. W., and Katz, J. L., *J. Chem. Phys.*, 35, 820 (1961)
27. Mackenzie, J. D., in Electrochemistry: The Past Thirty and Next Thirty Years, (H. Bloom and F. Gutman, eds.), Plenum Press, New York (1977)
28. Janz, G. J., Molten Salts Handbook, Academic Press, New York (1967)
29. Grjothem, K., Holm, J. L., Krohn, C., and Thonstad, J., in Selected Topics in High Temperature Chemistry (T. Forland et al, eds.), Universitetsforlaget, Oslo (1966)
30. Inman, D., and Williams, D. E., in Electrochemistry: The Past Thirty and the Next Thirty Years, (H. Bloom and F. Gutman, eds.), p. 273, Plenum Press, New York (1977)
31. Bockris, J. O'M., and Srinivasan, S., Fuel Cells: Their Electrochemistry, McGraw-Hill, New York (1969)
32. Rosenthal, M. W., Kasten, P. R., and Briggs, R. B., *Nucl. Appl. Tech.*, 8, 107 (1970)
33. Grimes, W. R., *Nucl. Appl. Tech.*, 8, 137 (1970)
34. Grimes, W. R. and Cantor, S., in The Chemistry of Fusion Technology, (D. M. Gruen, ed.), p. 161, Plenum Press, New York (1974)
35. Sundermeyer, W., *Angew. Chem. internat. edit.*, 4, 222 (1965)
36. Kenney, C. N., *Catal. Rev.*, 11, 197 (1975)

37. Parshall, G. W., J. Amer. Chem. Soc., 94, 8716 (1972)
38. Tomilou, A. P., and Chomutou, N. E., in Encyclopedia of Electrochemistry of the Elements, Volume III, p. 1 (A. J. Bard, ed.), Marcel Dekker, New York (1975)
39. Van Wazer, J. R., Phosphorus and its Compounds, Volume I, Interscience Publishers, Inc., New York (1958)
40. Morey, W., and Ingerson, E., Am. J. Sci., 242, 4 (1944)
41. Turkdogan, E. T., and Maddocks, W. R., J. Iron Steel Inst., 172, 6 (1952)
42. Phalipou, J. and Zarzycki, J., Ann. Chim. Fr., 3, 369 (1978)
43. Plambeck, J. A., in Encyclopedia of Electrochemistry of the Elements, Volume X, Fused Salt Systems, p. 373, Marcel Dekker, New York (1976)
44. Berretz, M., and Holt, S. L., J. Inorg. Nucl. Chem., 36, 49 (1974)

CHAPTER 2

PARTICLE EFFECTS IN
BUBBLE COLUMNS

2.1 Introduction

Gas-liquid-solid operations such as bubble column slurry reactors enjoy widespread use but are difficult to analyze fundamentally. This chapter will focus upon three aspects of bubble columns. First the component bubbles will be discussed. Secondly gas hold-up in such systems as influenced by swarms of bubbles will be discussed. Finally the effect of particles on bubble column characteristics and on individual bubbles will be dealt with. It is important to realize at the outset that laboratory results of such systems cannot be extended quantitatively to other systems. While liquid properties strongly influence behavior, geometrical constraints can have as strong an influence. Hence the emphasis here is a qualitative understanding of such systems and the elucidation of what the underlying mechanisms are which influence gross behavior.

2.1.1 Bubble Characteristics

The first most obvious aspect of bubbling columns is their component bubbles and the shapes of these bubbles. For single bubbles in water, there are three distinct shape regimes as given in Table 1 (1,2,3). This change in shape is due to surface tension forces (or capillary forces) becoming less important as compared to hydrodynamic forces as

TABLE 1. The bubble shape regimes.

Eotvos Number Range ^a (in water)	Weber Number Range ^a (in water)	Rise Velocity (u_B)	Shape	Surface Volume
$N_{E_0} < 0.003$	$N_{We} << 0.00008$	$\frac{gr_B^2}{3\nu}$	Spherical	$\frac{2}{r_B}$
$0.003 < N_{E_0} < 0.06$	$0.00008 < N_{We} < 0.2$	$\frac{gr_B^2}{9\nu}$	Spherical	$\frac{2}{r_B}$
$0.06 < N_{E_0} < 0.2$	$0.2 < N_{We} < 8$	$\frac{\sqrt{8gr_e/3C_D}}{b,c}$	Ellipsoidal	$\frac{2}{3b} + \frac{3b}{4a^2w} \ln\left(\frac{1+w}{1-w}\right)$ d,e
$N_{E_0} > 0.2$	$N_{We} > 8$	$\frac{f}{\sqrt{gR_c}}$	Spherical Cap	$\frac{5.1}{r_e} g$

a. The Eotvos and Weber numbers were calculated from literature values(1,2,3) of the Reynolds numbers ranges in water.

b. r_e = equivalent radius of spherical bubble of the same volume.

c. $C_D = \frac{48}{N_{Re}} \left(1 - \frac{2.21}{\sqrt{N_{Re}}} \right)$

d. a = one-half the major axis; b = one-half the minor axis.

e. $w = \frac{\sqrt{a^2 - b^2}}{a}$

f. R_c = the radius of curvature of the spherical cap.

g. The spherical cap is taken to have a 100° solid angle.

h. The density difference dependence (between the liquid and gas phases) is the same as the dependence on g , the acceleration of gravity. Hence the group $\frac{\rho_l - \rho_g}{\rho_l}$ may be assumed to

be included in g in the above expressions. For water this group has a value very close to unity.

the bubble size is increased. Harmathy (4) has demonstrated that shape is determined by two dimensionless groups:

$$\text{Shape} = f(N_{Eo}, N_{We}) \quad (1)$$

Here N_{Eo} is the Eotvos number:

$$N_{Eo} = \frac{g(\rho_l - \rho_g)d_B^2}{\gamma} = \frac{\text{Buoyancy Force}}{\text{Surface Tension Force}} \quad (2)$$

Here g is the acceleration of gravity, d_B is the bubble diameter, and γ is the surface tension. N_{We} is the Weber number:

$$N_{We} = \frac{\rho_l d_B u_B^2}{\gamma} = \frac{\text{Inertial Force}}{\text{Surface Tension Force}} \quad (3)$$

Here u_B is the bubble rise velocity. Also in the above expressions ρ_l is the bulk liquid density and ρ_g is the gas or bubble density. Hence as these dimensionless groups increase in value, distorting forces modify the bubble shape from its surface tension stabilized spherical shape.

As bubble size is further increased, the bubbles become unstable and fragment into smaller bubbles. Two destabilizing mechanisms are responsible. One as noted by Levich (1) is due to the internal dynamic pressure exceeding the capillary forces holding the bubble together. The other is due to buoyancy forces exceeding capillary forces. Fingers, known

as Taylor instabilities (5), are emitted from the bubble. These fingers then fragment into smaller bubbles. Thus the instabilities which break up the bubbles are extensions of what causes the distortion for the smaller bubbles.

Wall effects are very important. The rise velocities given in Table 1 are for the bubbles free from effects of a stagnant wall. The principal effect of a close wall is to increase the velocity gradient from the bubble to the wall. This results in increased momentum transfer from the bubble and a corresponding decrease in the bubble rise velocity. In turbulent columns of small diameter, this effect is amplified as bubbles may collide with the wall. The above two effects also distort the bubble from its free stream shape.

2.1.2 Gas Hold-Up

Consider now bubbling gas through a column of liquid. Upon introduction, gas flows into the column until a steady state is reached where the amount of gas entering and leaving the column is equal. The difference between the integral amount of gas that has left and gas that has entered is the gas hold-up or void fraction:

$$\epsilon = \frac{V_g}{V_l + V_g + V_{so}} \quad (4)$$

Here V_g is the volume of gas in the column with V_l and V_{so} as the liquid and solid volume respectively. Their sum is the total system volume. Here we will use the terms hold-up, gas hold-up, or void fraction exclusively for the volume fraction of gas in the column, ϵ . The term, porosity, shall refer exclusively to the volume fraction of liquid.

The general features of bubbling columns were first demonstrated by Verschoor (6). As the gas flow rate is increased from zero, the hold-up rises initially. Further increasing the flow rate results in rapid coalescence of the bubbles and the hold-up actually declines with increasing flow rate for some time. Ultimately, hold-up again increases at higher gas flow rates. It is however incorrect to assume that bubble coalescence alone determines the behavior of bubbling columns. Behavior is determined by a dynamic competition between bubble coalescence and bubble break up.

Hence in a bubble column, there is a distribution of bubble sizes and shapes. As they progress through the column, collisions between these bubbles result in coalescence with growth being limited by bubble break up. Several correlations have been developed to describe gas hold-up, and Butterworth (7) has demonstrated the similarity of many of them. The common fallacy of most correlations is that they predict a monotonic increase in gas hold-up with gas flow rate.

To examine this, we simply extend the method of Nicklin (8) (for monosized bubbles) to a distribution of bubble sizes. Here it is conceded that no two bubbles will have exactly the same size, consequently the entire size distribution of bubbles will be subdivided into p size ranges. Now let the average number of bubbles of a particular size, V_{B_i} , leaving the column per unit time be given by:

$$\left\langle \frac{\partial N_{B_i}}{\partial t} \right\rangle = A_c \langle u_{B_i} \rangle \langle n_{B_i} \rangle \quad (5)$$

Here $\langle n_{B_i} \rangle$ is the average number density of bubbles of this size with A_c being the cross-sectional area of the column. Hence the average volumetric flow of gas through the column by virtue of bubbles of this size is:

$$G_i = A_c \langle u_{B_i} \rangle \langle n_{B_i} \rangle V_{B_i} \quad (6)$$

But $\langle n_{B_i} \rangle V_{B_i}$ is the void fraction attributable to bubbles of size V_{B_i} . Summing the contributions, we then have for the total void fraction:

$$\epsilon = \sum_{i=1}^p \frac{\langle u_{gs,i} \rangle}{\langle u_{B_i} \rangle} \quad (7)$$

Here $\langle u_{gs_i} \rangle$ is the average superficial gas velocity accounted for by bubbles of volume, V_{B_i} .

Thus at a given total gas flow rate, the gas hold-up will decrease as the average bubble size increases. This arises as the above sum decreases as more gas flow is diverted into bubbles with larger rise velocities.

Extending this one step further, a growth (or decline) factor, χ_i , is allowed for bubbles of size V_{B_i} :

$$\epsilon = \sum_{i=1}^p \chi_i \frac{\langle u_{gs_i} \rangle}{\langle u_{B_i} \rangle} \quad (8)$$

Growth or decline of a particular sized bubble will be influenced by:

1. Average Bubble Size: If the average bubble size were very large, rapid growth would be expected for smaller bubbles due to break up. If the average bubble size were small, somewhat slower growth would be expected for larger bubbles due to coalescence.
2. Liquid properties and Liquid Purity: Liquid properties have a profound effect on bubble stability as has been discussed. It is also found that some liquids resist coalescence due to impurities present (9,10,11). Foams are examples. This is due to a difference between bulk and surface concentrations.

3. Bubble Introduction Method, Column Height, and Column Geometry: The gas introduction method and the column height are highly important for short columns. As the column height is increased, such factors decrease in importance as the competition between coalescence and break-up becomes dependent on liquid properties and column shape factors.

These diverse features illustrate the complexity of the problem of predicting the behavior of bubbling columns. Several correlations have been developed to describe the relative importance of the above effects (12-18). However the sheer volume of the number of variables as well as the lack of a governing analytic equation severely limit the extension of a given correlation to another system.

2.1.3 The Particle Effect on Bubble Coalescence and Break-up

The addition of a small amount of particles has been shown to have a significant effect on bubble coalescence (19,20,21). Much work has also been performed in three phase fluidization of the particle effect on bubble properties. In such systems, upward flow of liquid through denser than the liquid particles creates a fluidized bed. Bubbles are then injected into the bed and bubble properties are measured. Massimilla et al (22) injected bubbles of a constant volume into a fluidized bed of sand or glass particles. They found that bubble rise velocity

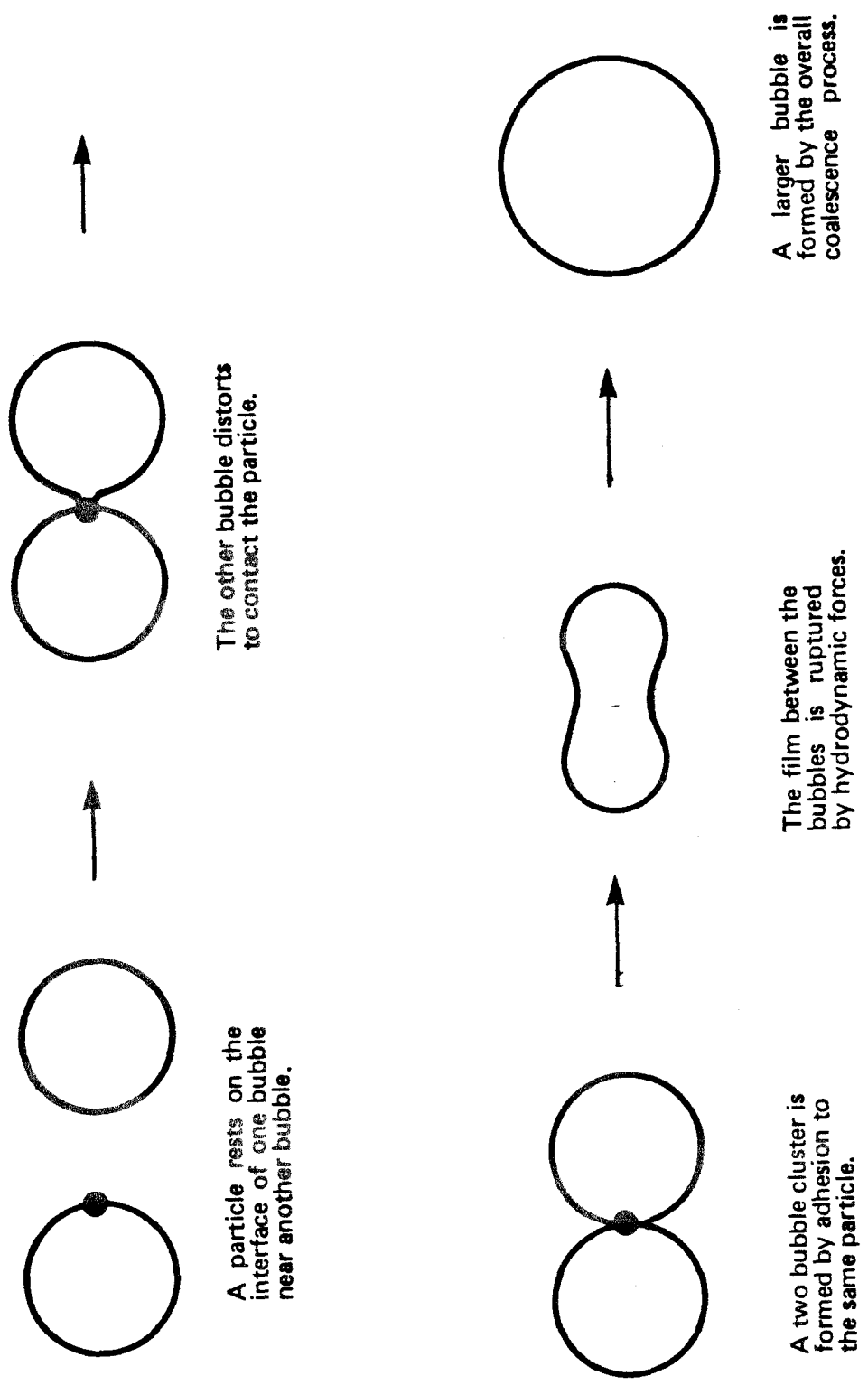
increased as bed porosity increased most likely due to the decreased viscosity of the expanded bed. They also found that coalescence decreased as bed porosity increased. Ostergaard (23) has observed that the rate of bubble coalescence is at a maximum at a bed porosity slightly above that at incipient fluidization. Rigby et al (24) found similar results in that bubble coalescence is dependent on bed expansion.

Hence it would appear that particles can influence bubble coalescence, and the results indicate that bubble coalescence increases as the particle concentration is increased. Particles may also cause bubble break-up if they are massive enough to penetrate the bubble and large enough to cause a disturbance to grow on the roof of the bubble (25).

The experiments reviewed above were for particles which were wetted by the liquid. Here we will use the term wetting particles for particles composed of a material which has a zero degree contact angle with the liquid. The term nonwetting particles will be used for particles composed of a material with a greater than zero degree contact angle, ie, a finite contact angle. Using wetting particles, an interesting aspect of such three phase fluidized beds is that they contract upon introduction of the gas (26,27). However by using teflon coated beads, Bhatia et al (28) have shown that bed expansion rises upon introduction of the gas. These results were compared with glass beads of the same density which did show contraction.

Contraction is caused by the bubble's wake being largely devoid of particles when the particles are wetted by the liquid. This effectively short circuits some of the liquid flow through the column. Less liquid flow is then available to suspend the particles resulting in the contraction. When the particles are not wetted, there is an adhesive force between the particle and the bubble due to the finite contact angle. This force acts on the particle toward the bubble's center and diverts the particle into the bubble's wake. Thus the particle-liquid contact angle can significantly affect three phase systems.

The effect of particle wetting properties on bubble coalescence has received very little study. If we consider a liquid-gas-solid system where the solid has a finite contact angle with the liquid, equilibrium dictates that the particle will be partly exposed to the gas and partly submerged in the liquid. Thus in a bubbling column with suspended nonwetting particles, it is presumed that bubbles will have particles located at their interfaces. Such phenomena are well utilized in industrial flotation processes. Bikerman (29) has postulated that these particles could serve as focal points for coalescence as shown schematically in Figure 1. Two bubbles may contact a common particle forming a cluster. Now the distortion required to produce this contact undoubtedly increases the total free energy of the bubble by creating more gas-liquid interfacial area. This is compensated for by the lowering of system free



The other bubble distorts to contact the particle.

A particle rests on the interface of one bubble near another bubble.

The film between the bubbles is ruptured by hydrodynamic forces.

A larger bubble is formed by the overall coalescence process.

A two bubble cluster is formed by adhesion to the same particle.

Figure 1. The effect of a nonwetting particle on bubble coalescence.

energy by the bubble attaining an equilibrium contact angle with the particle. After contact, the film existing between the bubbles may be broken by movement of the bubbles. The overall effect is that nonwetting particles provide a driving force for coalescence.

2.1.4 Particle-Bubble Encounter

Sutherland (30) has analyzed the rate of bubble-particle contacting in a suspension of nonwetting particles. By assuming a spherical bubble in potential flow, Sutherland showed that if the particles are assumed to follow the streamlines, the number of collisions per unit time is:

$$n_c = 3\pi r_B r_P u_B n_P \quad (9)$$

Here r_B and r_P are the bubble and particle radii respectively. The bubble rise velocity is u_B . The number density of particles is n_P . This is shown schematically in Figure 2.

Not all the collisions will result in adhesion of the particle as there must be a suitable induction period, τ_i , for the particles to adhere to the bubble. With this, Sutherland demonstrated that the number of fruitful collisions per unit time which will result in particle attachment is:

$$n_f = 3\pi r_B r_P u_B n_P \operatorname{sech}^2\left(\frac{3u_B \tau_i}{4r_B}\right) \quad (10)$$

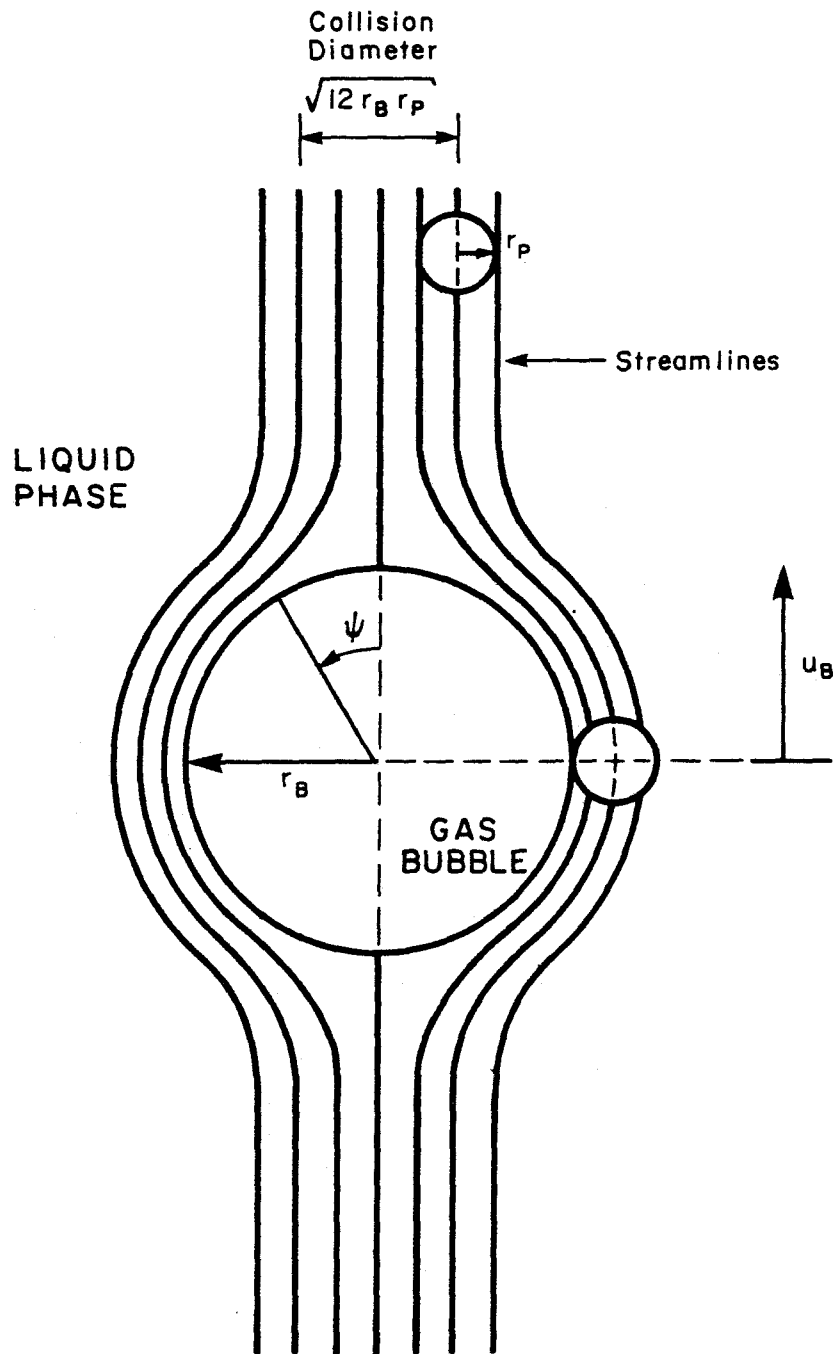


Figure 2. The Sutherland encounter model. The situation shown is for the particle just touching the bubble with zero induction time. ψ is the polar angle, and the effective collision area of the spherical bubble extends from $\psi = -\pi/2$ to $\psi = \pi/2$.

Assuming τ_i to be short (indicated by Sutherland to be from 0.005 to 0.1 seconds which is in agreement with the discussion of Scheludko et al (31)), the correction term should be of order unity. This is a very severe assumption as a very large τ_i makes n_f go to zero very rapidly. If we now apply a simple correction factor to the above, we then have:

$$n_f = 3\pi\eta r_B r_P u_B n_P \quad (11)$$

Here η will be assumed to take into account all nonideal effects including:

1. Correction due to finite induction time (above),
2. Nonspherical bubbles and high concentrations of bubbles,
3. Particles being stripped off the bubble by turbulence,
4. Saturation of the bubbles by the particles but see Chapter 6,
5. Hydrodynamic and electrical interaction between the bubble interface and the particle (below).

The fifth effect represents a departure from the noninteraction model of Sutherland. Electrical interaction is useful for the flotation of charged ions (as by collecting cationic species on the interface by the use of anionic surfactants (32)). The general problem for such attractive interaction has been discussed by Skrylev et al (33). Such electrical effects may be ignored in the present case as we shall deal with covalently bonded materials. Hydrodynamic interaction entails repulsion

between the particle and bubble interface. Such repulsion forces the particle to depart from the streamline it followed at infinite separation from the bubble (ie, the noninteraction streamline). Deryagin et al (34) have presented a hydrodynamic interaction model for flotation in potential flow using the results of Brenner (35) for the motion of a sphere normal to a free surface. On close approach to the interface, the particle's liquid film is assumed to thin until a critical thickness, h_c , is reached (36). Thereupon spontaneous rupture of the film occurs. The particle was found to follow the noninteraction streamlines until it approached to within one particle radius of the interface. Thereafter due to the hydrodynamic repulsion, the rate of particle contact with the interface was found to be less than that predicted by the noninteraction model. The form of the interaction model was the same as equation 9 with an additional dependence on h_c/r_p . However the departure of the interaction model from the noninteraction model was only weakly dependent on h_c/r_p . Hence these results do not dictate correction beyond the roughly constant factor, η , in equation 11.

All the above effects (except the electrical interaction which is not applicable) decrease the amount of particles collected by a given bubble. Hence η will be less than unity. If we now assume a residence time in the column, τ_c , the maximum number of particles on a bubble is given by:

$$N_{PM} = 3\pi r_B r_P u_B n_P \tau_c \quad (12)$$

The assumptions in arriving at the above equation are quite severe. This analysis can only claim quantitative prediction of the maximum number of collisions with a given bubble under ideal conditions. Hence the above gives the correct dependences on bubble and particle dimensions and on the particle number density but not a quantitative answer in general.

2.2 Experimental

The experimental system is shown in Figure 3. As indicated, air was filtered to remove any suspended oil in the line air by a glass wool packed filter and to remove particles larger than 0.22μ by a millipore membrane filter. After this filtering, the air was routed to the particular experiment being performed.

The U-Tube is separated into two sides. The bubbler side had a glass tube for the introduction of gas into the column while the sparger side utilized a coarse fritted glass disk for gas introduction. The annular system is also separated into two regions. Gas flow was directed into the inner tube region. The exterior region which is separated from the gas flow is called the annular region.

Flows were monitored by rotameter. The flow to the bubbler when it was emitting single bubbles was monitored by a finer flowmeter. This was a zero flow balanced thermistor bridge where flow was directed through one leg of the bridge.

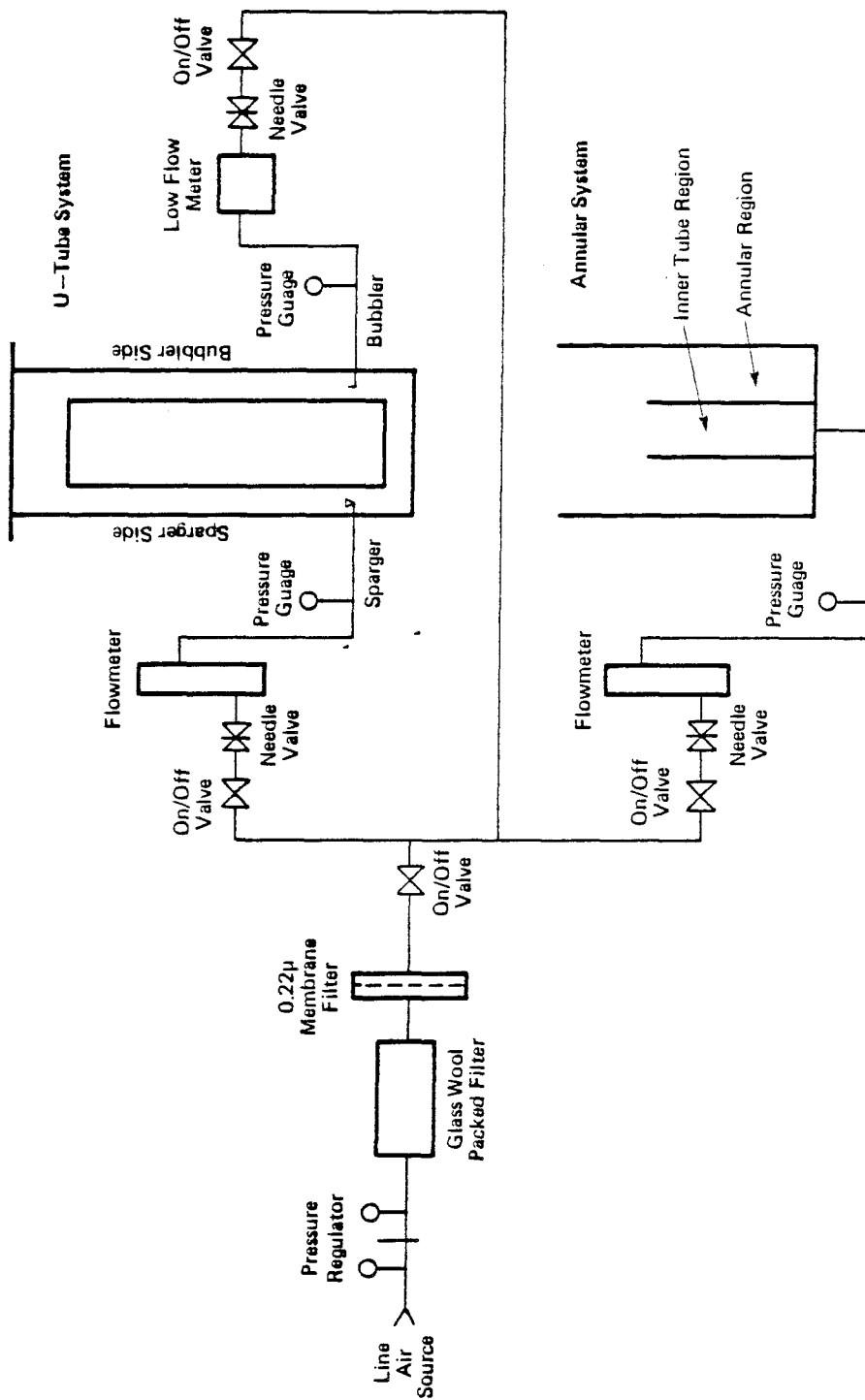


Figure 3. The experimental system for measuring the properties of bubble columns.

The cooling by the flow of the thermistor caused a voltage imbalance which was amplified, and flow was indicated on an analog voltmeter. This provided a method of insuring the flowrate to the bubbler was constant at low flow rates.

Figures 4 and 5 detail the dimensions of the U-tube and annular systems. All materials were lucite except the bubbler and sparger which were glass. The intake for liquid from the annular to the inner tube region of the annular system consisted of twenty-four 1/8" holes. The legs of the U-tube were connected by a two inch ID U-shaped plastic fitting at the bottom which fit smoothly with the legs. Seals where needed were accomplished with rubber O-rings.

Tables 2 and 3 list the properties of the particles used in these experiments. All particles, unless otherwise designated were subjected to a caustic (NaOH) rinse followed by extensive rinsing in distilled water. In all experiments, distilled water was the starting material for the fluid used. The U-tube and annular systems were also extensively rinsed in distilled water prior to an experiment. In some experiments to increase the liquid density, Baker Analyzed sodium chloride was added to the water. Thus while it is acknowledged that the water is only singly distilled and is not completely free of contaminants, extreme care was taken to insure that no contaminants beyond what exist in the distilled water were added by contact with the experimental system or the particles which were added.

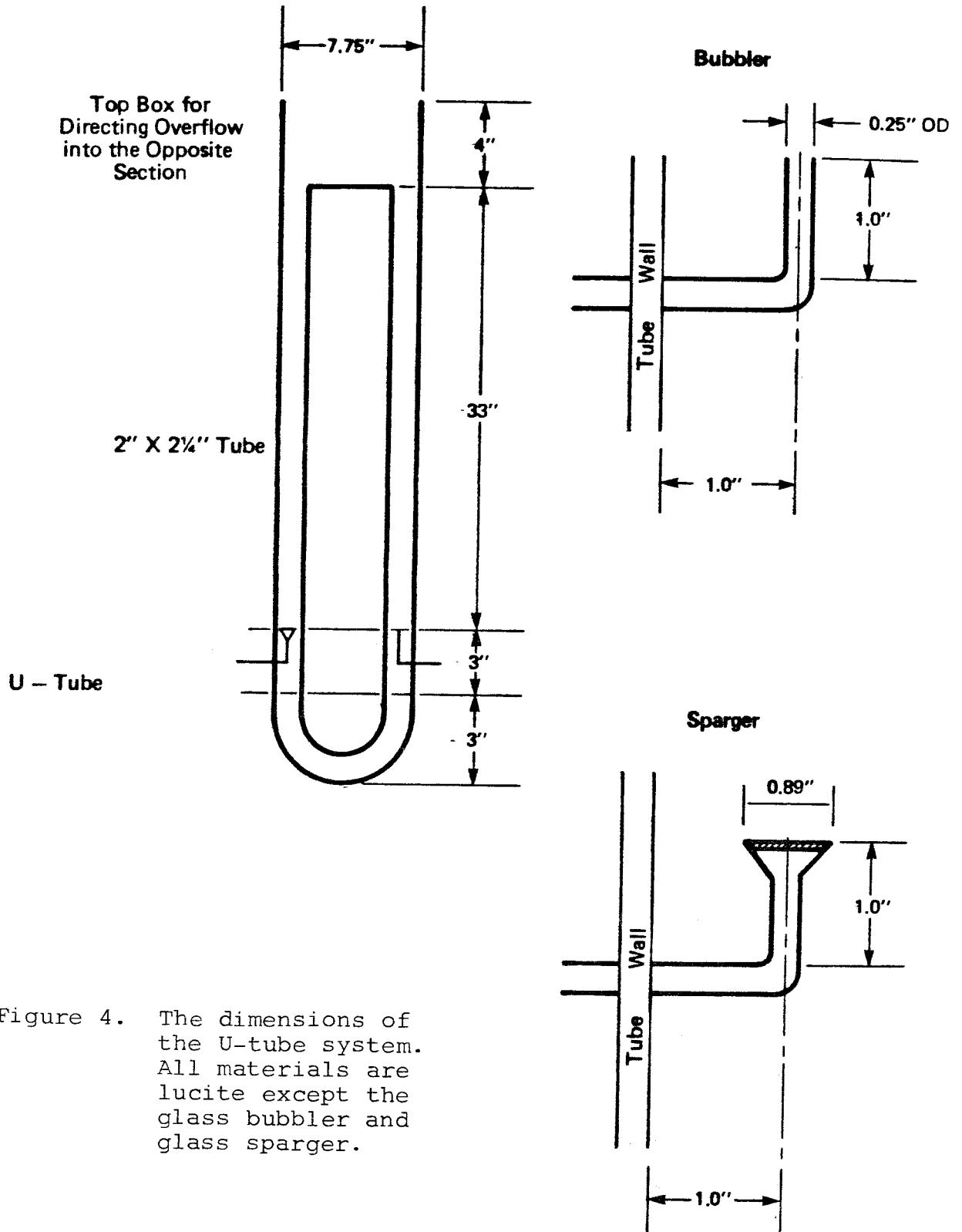


Figure 4. The dimensions of the U-tube system. All materials are lucite except the glass bubbler and glass sparger.

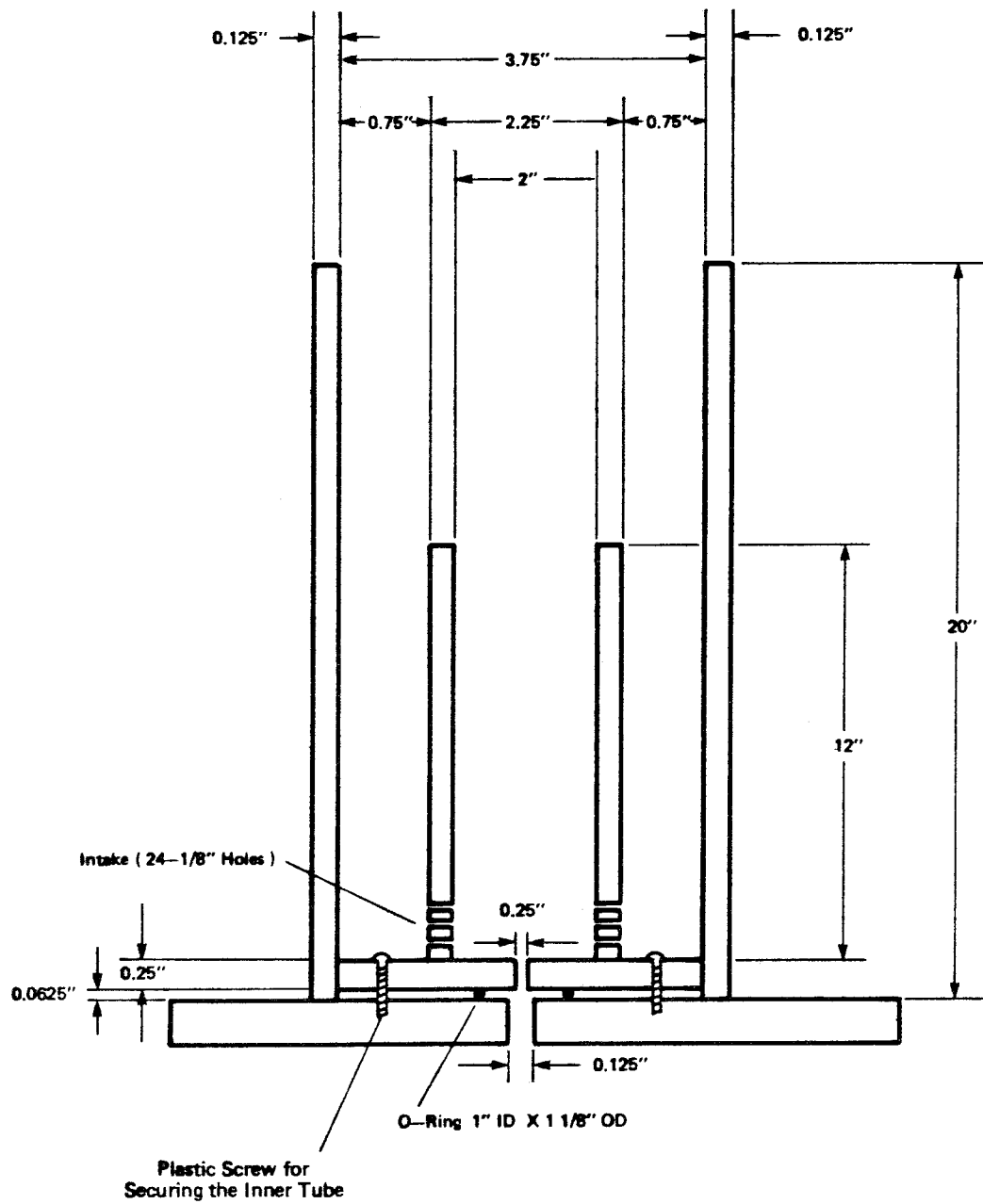


Figure 5. The dimensions of the annular system. All materials are lucite.

TABLE 2. Properties of the polymeric particles.

Dow Anion Exchange Resin Particles

Density (g/cm ³)	0.95
Average Particle Diameter (μ)	750
Mesh Range	-18 + 50

Dow Polystyrene/Divinylbenzene Cation Exchange Resin Particles

Density (g/cm ³)	1.05				
Average Particle Diameter (μ)	798	649	252	112	56
Mesh Range	-18+35	-18+50	-45+100	-100+200	-200+400

Monsanto Polystyrene Particles

Density (g/cm ³)	1.05	
Average Particle Diameter (μ)	630	
Size Distribution	Mesh Range	W+%
	-18+30	48.0
	-30+35	23.2
	-35+45	25.5
	-45+50	3.3

TABLE 3. Properties of the hollow spherical silica particles.

	Unclassified Eccospheres SI (Wetting)	Unclassified Eccospheres UT (Nonwetting)
Particle Density (g/cm ³)	0.254	0.272
Average Wall Thickness (μ) (Weight Basis)	1.5	1.7
Average Particle Diameter (μ) (Weight Basis)	80	80
Particle Size Distribution (μ) (Weight Basis)		
>175	0	0
149-175	14	14
125-149	10	15
100-125	12	16
62-100	40	43
44-62	15	7
<44	9	5

As particle effects were to be studied and contrasted to results without particles, the particle rinsing method was checked. PS/DVB particles were washed as described above. They were then added to the bubbler side when the U-tube was filled with water and allowed to settle. Single bubbles emitted from the bubbler were observed to have the same rise velocity before and after particle addition. Thus possible surfactants on the particles surface as well as soluble organics which can affect rise velocities were effectively removed by the described washing process.

The contact angle of polystyrene with water is 91° as reported by Zisman (37). The PS/DVB particles should have a contact angle close to this value as they are 95% polystyrene.

The hollow spheres of Table 3 were manufactured by Emerson and Cummings. Eccospheres VT are made from Eccospheres SI by bonding a Werner complex to the glass. An unsaturated organic in the complex then orients outward. This group is then combined with polyesters. Hence the complex acts as a coupling agent between the glass and the organic polymer. The end result is that the surface is coated by a strongly cross-linked polyester. With these, we then have two very similar particles-- one with zero degree contact angle with water (SI) and the other with a finite contact angle (VT). The contact angle between a VT surface and water has not been measured. A typical value for polyesters such as polyethylene terephthalate is given by Zisman as 80° (37).

A final clarification is added as several operational modes of the U-tube system were employed. In one mode, both columns were filled to above the top box (or slightly below) with liquid. Downward flow could then be supplied to the bubbler side by sufficiently strong gas flow to the sparger side. Several experiments were conducted in this manner with low gas flow through the bubbler side to create bubbles travelling upward through the column against the downward liquid flow. Such liquid flow was countercurrent to the bubble rise velocity and is so designated in the sections to follow. On the other hand, if the columns were not filled sufficiently with liquid, gas flow to either side of the U-tube did not supply countercurrent flow to the other side as the top edge of the bubbling column was kept below the top box of the U-tube system. While there are internal dynamics in such columns, as will be discussed, the flowrate of liquid through a given cross-section of one column leg in this case is zero. Such columns will be denoted as stagnant.

2.3 Particle Dispersion and Induced Countercurrent Flow

For adequate performance of bubble column slurry reactors, it is important to insure that the particles are evenly distributed throughout the column. Here we will deal with particle dispersion in systems where the particles are lighter than the liquid. Now in a bubbling column, liquid flow is observed

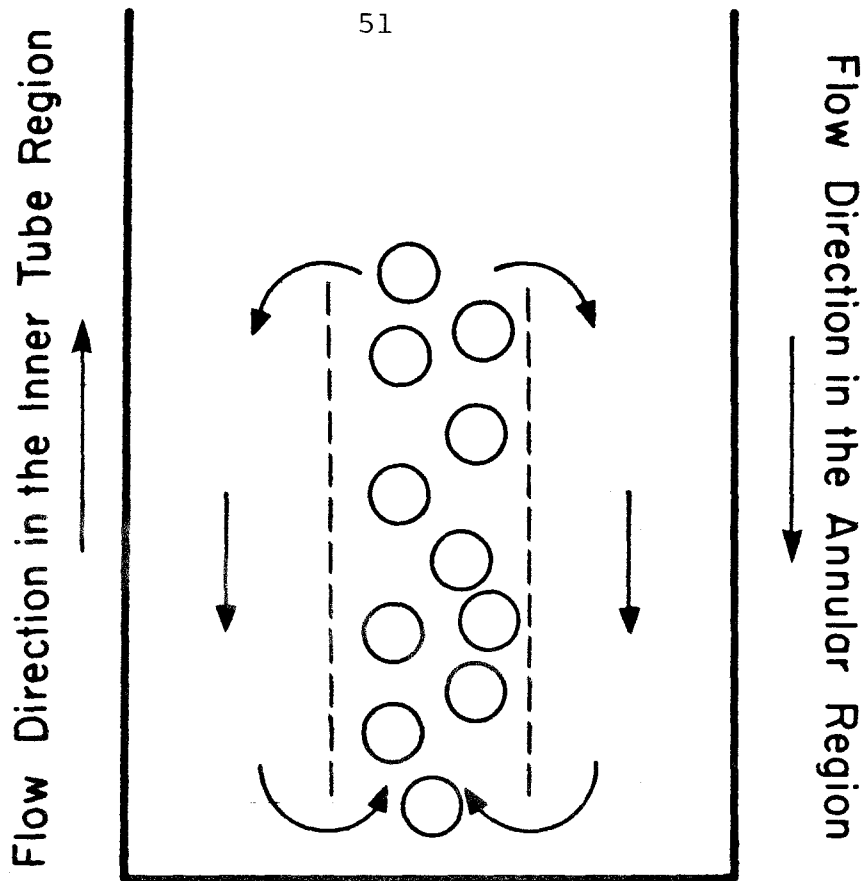
downward near the tube walls with the bubbles largely travelling through the column center. The top diagram in Figure 6 demonstrates such an annular model of a bubbling system as suggested by Bhavaraju et al (38). This induced countercurrent flow in such systems is quite important, and it is appropriate to review the general features of such flow. The flow is induced by two mechanisms--gas hold-up in the central region providing a static head and momentum transfer from the rising bubbles to the liquid. The former is given by:

$$\Delta P_h = gh(\rho_A - \rho_I) \quad (13)$$

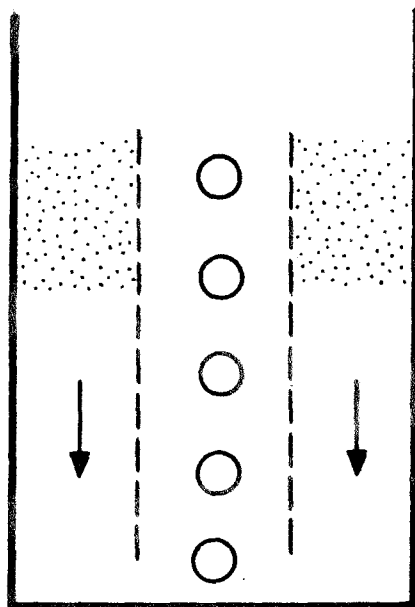
Here h is the column height. ρ_A is the fluid density in the annular region which should be roughly equal to the density of the liquid. ρ_I is the density in the inner region which is less than the liquid density due to the gas hold-up. Momentum transfer from the bubbles to the liquid is given by:

$$\Delta P_t = \sum_{i=1}^p \langle N_{Bi} \rangle S_{mi} \quad (14)$$

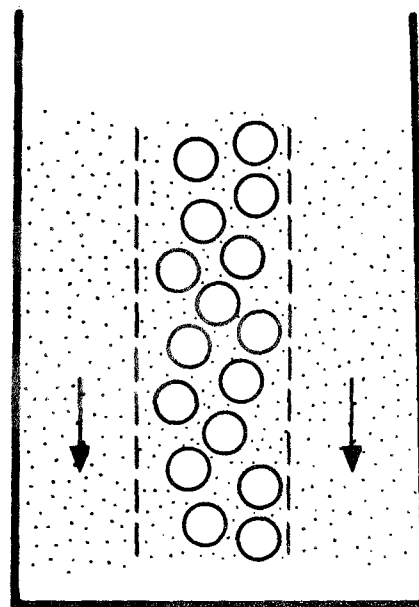
Here S_{mi} is the integral amount of momentum transport from the bubble to the liquid. S_{mi} is a strong function of the bubble concentration as more bubbles will alleviate velocity gradients and decrease the amount of momentum transfer that would take place as compared to a single bubble. This would be difficult to estimate in practice due to the turbulence in bubble columns.



Annular Model of a Bubble Column



Low Gas Flows
Fluidization in the
Annular Region



High Gas Flows
Dispersed Particles

Figure 6. The annular model of particle dispersion in bubble columns.

Momentum dissipation in such systems will include wall effects as well as homogenous dissipation due to turbulence. Hewitt and Boyce (39) have reviewed such dissipation effects in multiphase flow. For handling the homogenous dissipation, Beattie (40) has suggested neglecting gas phase dissipation and proposed in analogy with Prandtl's mixing length theory (41):

$$\tau_{\text{hom.}} = k\rho_1 (1-\epsilon) \left\langle \left(\frac{du_1}{dy} \right) y \left| \frac{du_1}{dy} \right| \right\rangle \quad (15)$$

Here k is a constant of order unity with u_1 being the liquid axial velocity and y being the distance from the tube wall.

Finally it is important to realize the effects particles will have on the flow. Rapid relative motion as in turbulence between the particle and the liquid will dissipate momentum. Particles will also serve as focal points in the cascaded momentum transfer process where momentum is continually transferred from large eddies to eddies small enough for viscous dissipation to ensue. The size of the eddies at the end of this process is increased due to the finite particle size.

Now in a bubbling column, moderately increasing the gas flow will result in increased gas hold-up in the inner region of the tube. Hence the fluid density difference between the annular and inner region rises as gas flow is increased providing more driving head for the countercurrent flow.

At very low gas flows, particles are first inversely fluidized in the annular region as shown in the bottom of Figure 6. This bed expands as the gas flow is increased until the particles become well dispersed throughout the column as the drag induced by the countercurrent liquid flow overcomes the particle buoyancy.

Two types of experiments were performed to illustrate these features. The annular system was used to conduct an inverse fluidization experiment. A complete dispersion experiment was conducted in the U-tube system. The conditions for these experiments are given in Table 4. Dow anion exchange beads were selected as the particles to be dispersed or fluidized as they are lighter than water and due to their size, they have relatively large terminal velocities. Their terminal velocities which are given in Table 4 represent the average of ten sets of experiments with two velocities being measured per experiment. Errors indicate reproducibility. Due to the wall effects being more extreme in the annular system, the average terminal velocity of the beads in the U-tube was found to be larger than the corresponding velocity in the annular system. In the U-tube, the beads were initially charged to the bubbler section. For the annular system, the beads were charged to the annular region.

These experiments entailed inducing downward liquid flow in one section of the system by suitable gas flow to a separate

TABLE 4. Experimental parameters for the fluidization and dispersion experiments.

FLUIDIZATION EXPERIMENT - ANNULAR SYSTEM		
	<u>Amount Added</u>	<u>Terminal Velocity</u>
Liquid:	7.2% by weight NaCl in distilled water solution	1980 ml. -
Particles:	-18+50 Mesh Dow Anion Exchange Beads	41.24 g. 2.67 ± 0.22 cm/s
	-18+35 Mesh Dow PS/DVB Beads	1.00 g. 0.00
Ambient(No Flow) Bed Dimensions:		
	Bed Length = 22.0 mm	
	Bed Porosity = 0.567	
Porosity Expressions:		
	$\epsilon_b = \text{Apparent Porosity} = \frac{\text{Length} - \text{Ambient Length}}{\text{Ambient Length}}$	
	$\epsilon_A = \text{Actual Porosity} = \frac{22\epsilon_b + 12.5}{22\epsilon_b + 22}$	
DISPERSION EXPERIMENT - U-TUBE SYSTEM		
	<u>Amount Added</u>	<u>Terminal Velocity</u>
Liquid:	Distilled Water	3720 ml. -
Particles:	-18+50 Mesh Dow Anion Exchange Beads	77.8 g. 2.99 ± 0.40 cm/s
	-18+35 Mesh Dow PS/DVB Beads	* 1.21 ± 0.15 cm/s
Ambient Bed Length: 87 mm		

*Added after dispersion experiment completed to obtain the countercurrent flow.

section of the system. The induced liquid flow was measured by observing the velocity of PS/DVB beads in the flow. For the U-tube, gas flow through the sparger provided the downward liquid flow in the bubbler section. For the annular system, gas flow through the inner tube region provided the downward liquid flow in the annular region. It was found that the induced liquid flow could be carefully controlled by suitable manipulation of the gas flow for both systems. Thus a turbulent, bubbling column can provide steady and consistent induced liquid flow.

The PS/DVB beads used to measure the liquid flow in the annular system were added before the fluidization experiment was performed. Hence the liquid flow rate could be measured during the experiment. For the dispersion experiment, the PS/DVB beads were added after the experiment, and at the same flow rates used in the experiment, the induced liquid velocity was measured by subtracting the terminal velocity of the beads from the observed velocity.

For the fluidization experiments, both actual bed porosity, ϵ_A , and apparent bed porosity, ϵ_b , were correlated with a similar type of expression. Here actual porosity is the porosity existing in the ambient bed plus that due to the expansion caused by the flow. At complete dispersion, ϵ_A , would be $1-\phi$, where ϕ is the volume fraction of solid particles. Apparent bed porosity is the expansion divided by the ambient length. The relationship between ϵ_A and ϵ_b is given in Table 4.

Figure 7 presents the data correlated to the actual bed porosity. The interstitial velocity, u_{is} , is the average liquid velocity as it is forced through the constrictions caused by finite particle volume in the fluidized bed. A least squares fit of the data gave:

$$\epsilon_A = \frac{0.585}{\left(1 - \frac{u_{is}}{u_t}\right)^{0.2375}} \quad (16)$$

Here u_t is the terminal velocity of the Dow anion exchange beads. This expression correctly tends to the ambient porosity as the liquid velocity goes to zero. It does not give agreement with the dispersed endpoints. The Richardson-Zaki correlation (42) gave poorer agreement with the data. This correlation agrees with the dispersed endpoints but does not correctly predict ambient porosity. The correlation presented here does give good results over the range that the particles are in a fluidized mode.

Figure 7 also presents the correlation which is more cogent to this dispersion study. The apparent bed porosity, ϵ_b , is correlated to a similar form to that of equation 16. A least squares fit of the data yielded:

$$\epsilon_b = \frac{0.140}{\left(1 - \frac{u_{is}}{u_t}\right)^{1.68}} \quad (17)$$

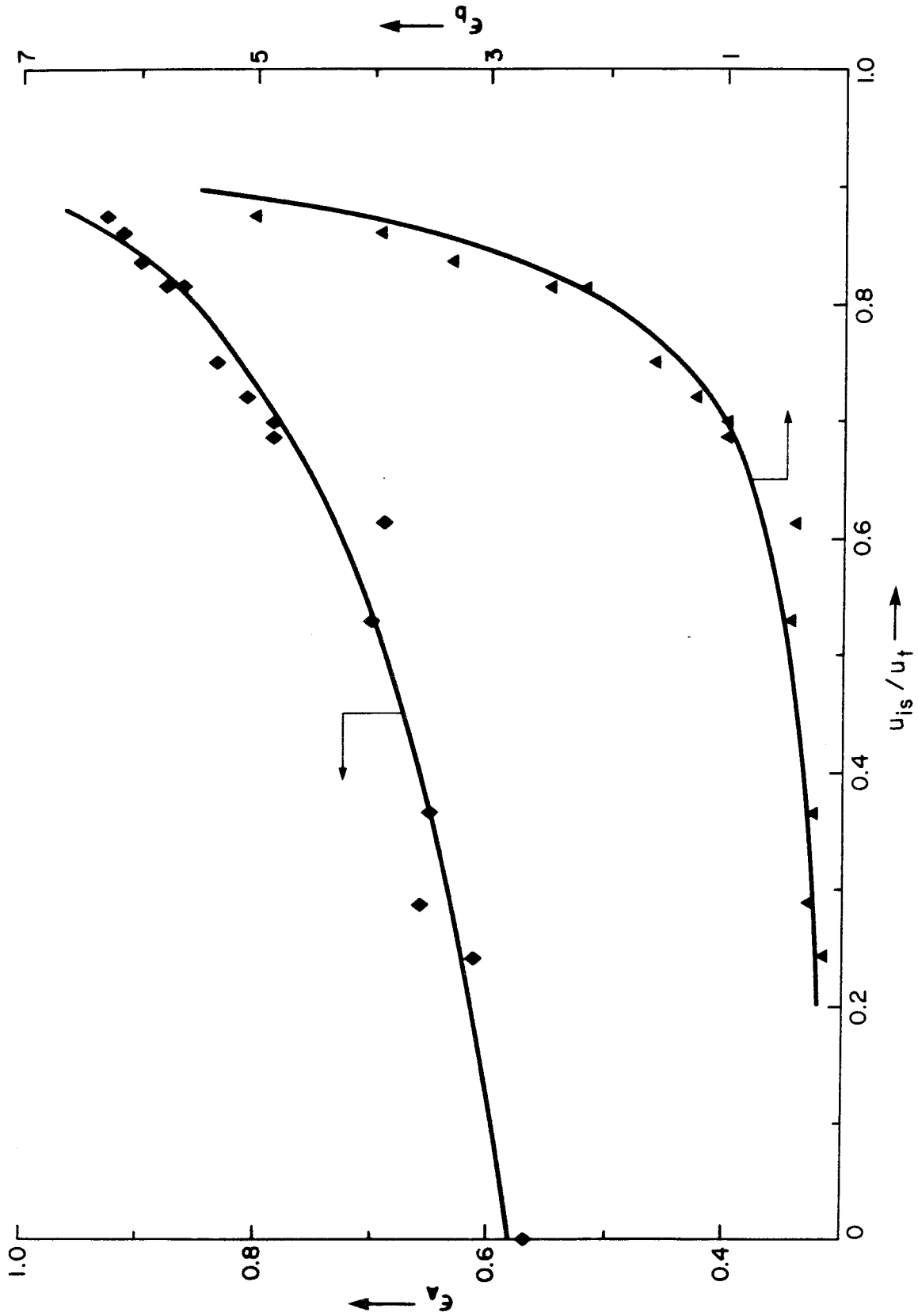


Figure 7. The variation of actual porosity, ϵ_A , and apparent porosity, ϵ_b , with interstitial velocity in the annular system. For ϵ_A , the solid line corresponds to equation 16. For ϵ_b , the solid line corresponds to equation 17.

This gives poor agreement with the ambient endpoint as it evidently does not tend to zero as the liquid velocity goes to zero. It does agree with the dispersed endpoints as it tends to infinity as u_{is} approaches u_t . From equation 19, the system is seen to approach complete dispersion as roughly the inverse square of the difference between the particle settling velocity and the liquid interstitial velocity.

Figure 8 presents the total picture for dispersion in the U-tube. Gas flow through the sparger in this case provided the downward liquid flow in the bubbler section. Dispersion is seen to increase rapidly after the ratio of the superficial velocity to particle terminal velocity reaches unity. Here the terminal velocity again corresponds to that of the anion exchange beads. The superficial velocity of the liquid, u_{1s} , is related to the interstitial velocity by:

$$u_{is} = \frac{u_{1s}}{\epsilon_A} \quad (18)$$

Thus, as ϵ_A goes to unity at complete dispersion, u_{is} tends to u_{1s} . As is seen for u_s beyond three or four times the particle terminal velocity, the particles are well dispersed and the profile flattens.

Two deviations to the idealized picture are noticed. The first is that dispersion is not complete when the

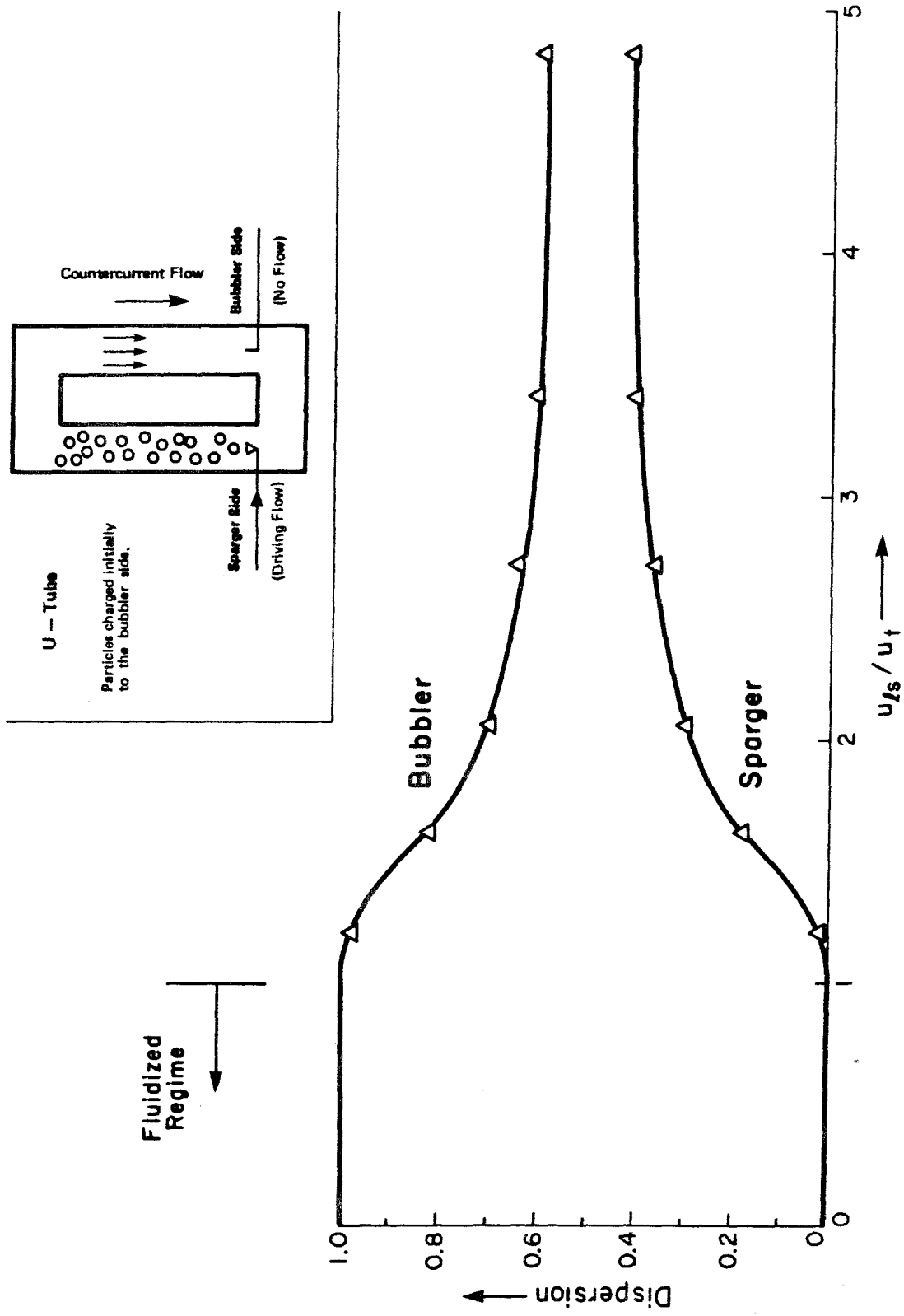


Figure 8. Particle dispersion in the U-tube system.

superficial velocity is equal to the particle terminal velocity. Geometry influences this feature. The particles had to traverse through the bend in the bottom of the U-tube to reach the sparger side where gas flow was provided. Particles rise to the top of this bend. The particles are slowed due to the wall effects and are prevented from circulating properly. In simple bubbling columns, dispersion will flatten more quickly as they are free from this constriction. Hence for systems without the simple geometry of a unstricted tube, complete particle dispersion will be hindered by the geometry.

The second deviation is that particle dispersion does not tend to 50% in each side. This is due to the gas hold-up in the sparger side. As the particle laden liquid enters the sparger, it is forced through more rapidly due to the constriction now caused by the gas hold-up. The liquid phase on the gas flow side is probably not less concentrated in particles but the total volume including the gas and liquid is. This feature will be affected by particle wetting characteristics and particle density. The anion exchange particles used here are not wetted by the water, and they have approximately the same density as the water. Hence bubble wakes are not significantly depleted in particles which results in the profiles shown. If the particles were wetted and were much more dense, bubble wakes could be

expected to be largely devoid of particles as discussed previously. This then creates a separate particle devoid liquid phase which moves rapidly through the bubbling side. The more slowly moving liquid-particle phase outside the wakes must then be more concentrated. This would result in a greater total volume fraction of particles in the gas flow side. The magnitude of this effect cannot be predicted, but intuitively it should result in the total number of particles in the two sections being more nearly equal. Hence the profiles presented in Figure 8 should flatten closer to 0.5. The case of denser particles is the inverse of the one presented here. For if the particles are more dense than the liquid, they are dragged against buoyancy through the bubbling section and fall with buoyancy through the nonbubbling sections. Such types of bubbling columns have been investigated recently by Kojima and Asano (43).

2.4 Particle-Bubble Interactions

Here the interactions between single bubbles and particles suspended in the liquid will be discussed. Three related features will be examined. First the particle location shall be examined. This will be followed by a study of the effect of countercurrent flow on rising bubbles in particle suspensions with wall effects. Finally the effect of particle properties on bubble rise velocities shall be discussed.

2.4.1 Particle Location

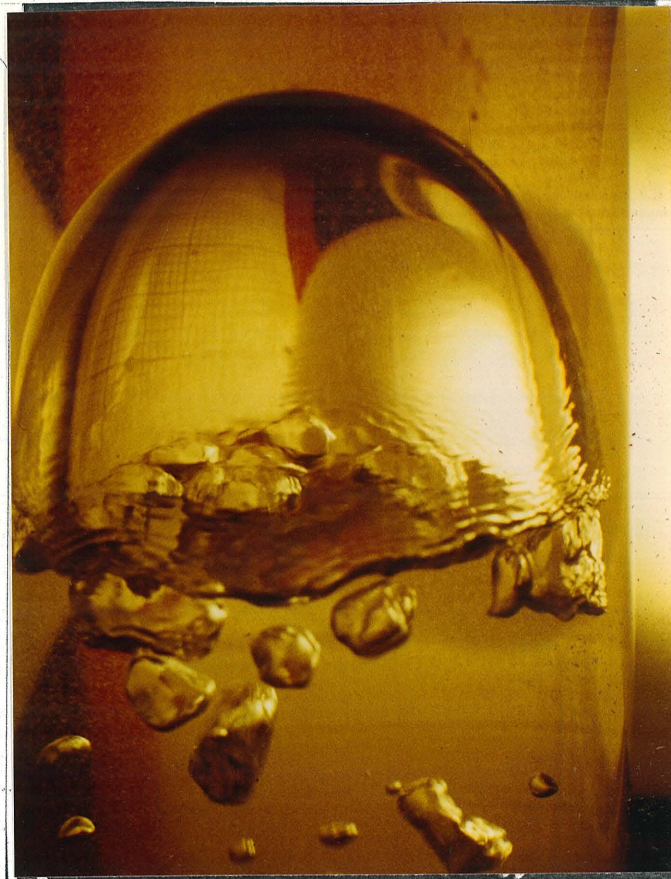
Particle-bubble contacting was first examined visually by suspending large bubbles in the bubbler side of the U-tube with sufficient countercurrent flow. These large bubbles rise much more rapidly through the liquid than smaller bubbles. Hence the relative velocity between these bubbles and the suspended particles is much greater than the smaller bubbles rising through a stagnant column of water. Thus impulsive forces of the particles onto the bubble interface are larger for the larger bubble system. As shown in Figure 9, the particles do not enter the bubble proper. Particles are so prevented by being stabilized on the interface by surface tension forces. Thus the force of adhesion which stabilizes the particle at the interface (44) apparently exceeds the impulsive force which tends to force the particle through the interface. As was mentioned previously, Ostergaard and Henriksen (25) have demonstrated that for a massive enough particle, the interface may be broken through. However for particles of approximately the same density as the liquid, they are excluded from the bubble proper in much the same manner as the surface tension forces that hold the bubble together exclude water.

An interesting aspect of such systems is that the particles concentrate around the interface as is seen most readily by referring to the darkened edges of the bubble suspended in the polystyrene particle system. Such crowding



Countercurrent Flow Direction ↓

BUBBLE IN A DILUTE SUSPENSION OF -18+50 MESH DOW ANION BEADS IN WATER



BUBBLE IN A DILUTE SUSPENSION OF UNCLASSIFIED ECCOSPHERES VT IN WATER

BUBBLE IN A CONCENTRATED SUSPENSION OF -18+50 MESH POLYSTYRENE BEADS IN A 7.2% BY WEIGHT SALT SOLUTION

Particles are noticeably concentrated around the frontal surface of the bubble

Countercurrent Flow Direction ↓

Figure 9.

Large bubbles suspended by induced countercurrent flow in the bubbler section of the U-tube. The suspended particles have densities less than or equal to that of the liquid. Particles in such flow are observed not to penetrate the bubble but to concentrate around the frontal surface of the bubble.

is in basic agreement with the model of Sutherland, but it does point out a notable exception. As streamlines approach the bubble, they come closer together. Due to the size of the particles, they can no longer follow the streamlines close to the surface of the bubble and in effect swarm around the interface. In such dense suspensions, the bubble surface would be expected to be saturated quickly and such swarming will cause deviation from the contacting model of Sutherland. For a detailed discussion of this saturation effect, see Chapter 6.

2.4.2 Particle-Bubble Contacting

Here we will be strictly dealing with single bubbles emitted from the bubbler. The volume of the bubble emitted at low gas flow rates in what is called the single bubble regime, is determined by balancing surface tension with buoyancy (45,46):

$$V_B = \frac{\pi D_o \gamma}{g (\rho_l - \rho_g)} \quad (19)$$

Here D_o is the orifice diameter taken as the internal diameter as the orifice material in the present case, glass, is wetted by the liquid. In general, the above requires correction if the liquid has a finite contact angle with the orifice material. For this study, bubbles were emitted from a 0.37 cm. ID glass

orifice and had a measured average volume of 0.066 cm^3 .

The above predicted this value to within 20%.

2.4.2.1 Single Bubbles Rising in Countercurrent Flow

Now if countercurrent flow is directed against the bubbler, bubble size should ideally increase as the countercurrent flow will act opposite to buoyancy:

$$V_B \sim \frac{\pi D_o \gamma}{g (\rho_l - \rho_g)} + \frac{\pi \rho_l u_{cc}^2 r_B^2}{g (\rho_l - \rho_g)} \quad (20)$$

Table 5 details the results for the change of bubble frequency with countercurrent flow. Ten sets of ten bubbles were measured with error indicating data reproducibility. Here u_{cc} is the average downward liquid velocity in the bubbler section. It is observed that countercurrent flow does not significantly change the bubble release frequency, and hence the bubble size remains relatively constant as these experiments maintained a constant flow to the bubbler. Calculations reveal that for a countercurrent flow of five cm/s, the second term is only about three percent of the first. If the average bubble size is taken to be indicative of the above results, it is apparently the case that the bubbles are dislodged prematurely rather than held on the orifice by the countercurrent flow.

TABLE 5. The countercurrent flow effect on the bubble release frequency. The flow rate to the bubbler is kept constant.

Sparger u_{gs} (cm/s)	u_{cc} (cm/s)	Release Frequency (s^{-1})
0.0	0.0	0.84 ± 0.07
0.5	0.96	0.85 ± 0.06
1.1	1.58	0.85 ± 0.06
1.7	1.78	0.94 ± 0.05
2.2	2.06	0.95 ± 0.07
3.0	2.73	0.99 ± 0.09
3.8	3.23	1.02 ± 0.12
4.4	3.91	1.05 ± 0.10
5.2	*	1.03 ± 0.10
7.7	*	0.93 ± 0.10
10.5	*	0.95 ± 0.11
Average:		0.95 ± 0.07

* Unavailable

The above bubbler, in the single bubble regime, emitted bubbles which had rise velocities of 25.4 cm/s. in distilled water. To the bubbler section of the U-tube, -18+35 mesh PS/DVB particles were added. As these particles fell through the column at a density of about ten beads per cubic centimeter, bubbles were allowed to rise through the now particle laden liquid. The rise velocity was unaffected by the presence of the particles. This was surprising as it was expected that the bubble would pick up a load of particles and slow down.

To further test this and increase the bubble residence time in the system, countercurrent flow was induced against bubbles rising in the bubbler section of the U-tube by gas flow in the sparger side. The system was filled with a 7.2% by weight salt solution with a density of 1.05 g/cm^3 . The bubble rise velocity in the stagnant column was again found to be 25.4 cm/s. Now at this point it is important to realize that bubble rise velocities in the present case are strongly influenced by wall effects (47). These bubbles were observed visually to be roughly spherical cap in shape and to rise in a zigzag fashion through the column. The effect of inducing a countercurrent flow against such bubbles provides increased residence time between the wall and the bubbles as well as between the bubbles and particles.

-18+50 mesh polystyrene beads were added to the system incrementally. For each addition, the bubble rise velocity was measured for several countercurrent velocities. The ambient (no countercurrent flow) bubble rise velocity is u_{BA} and is equal to 25.4 cm/s. The actual rise velocity with countercurrent flow is u_B . The results are given in Figure 10.

As is seen, the countercurrent flow provided only a simple transformation of reference frame. No significant change of this simple effect was noticed by the addition of up to 5% by volume of particles. Thus the particles do not provide any additional bubble-wall slip. Also the increased residence time does not apparently allow the bubble to pick up of any of these large particles. If this was the case, a noticeable deviation should occur at the higher countercurrent flows due to bubble slowdown caused by particle adhesion to the bubble's interface.

2.4.2.2 Single Bubbles Rising in Stagnant Columns of Liquid

Upon adding smaller particles, bubble rise velocity slowdown was observed as given in Table 6. These experiments were performed with PS/DVB particles in a neutrally buoyant salt solution. Rise velocities were measured corresponding to the time it took the bubbles to travel between ten and twenty inches above the bubbler in the U-tube with no countercurrent flow. Bubbles in these experiments were emitted such

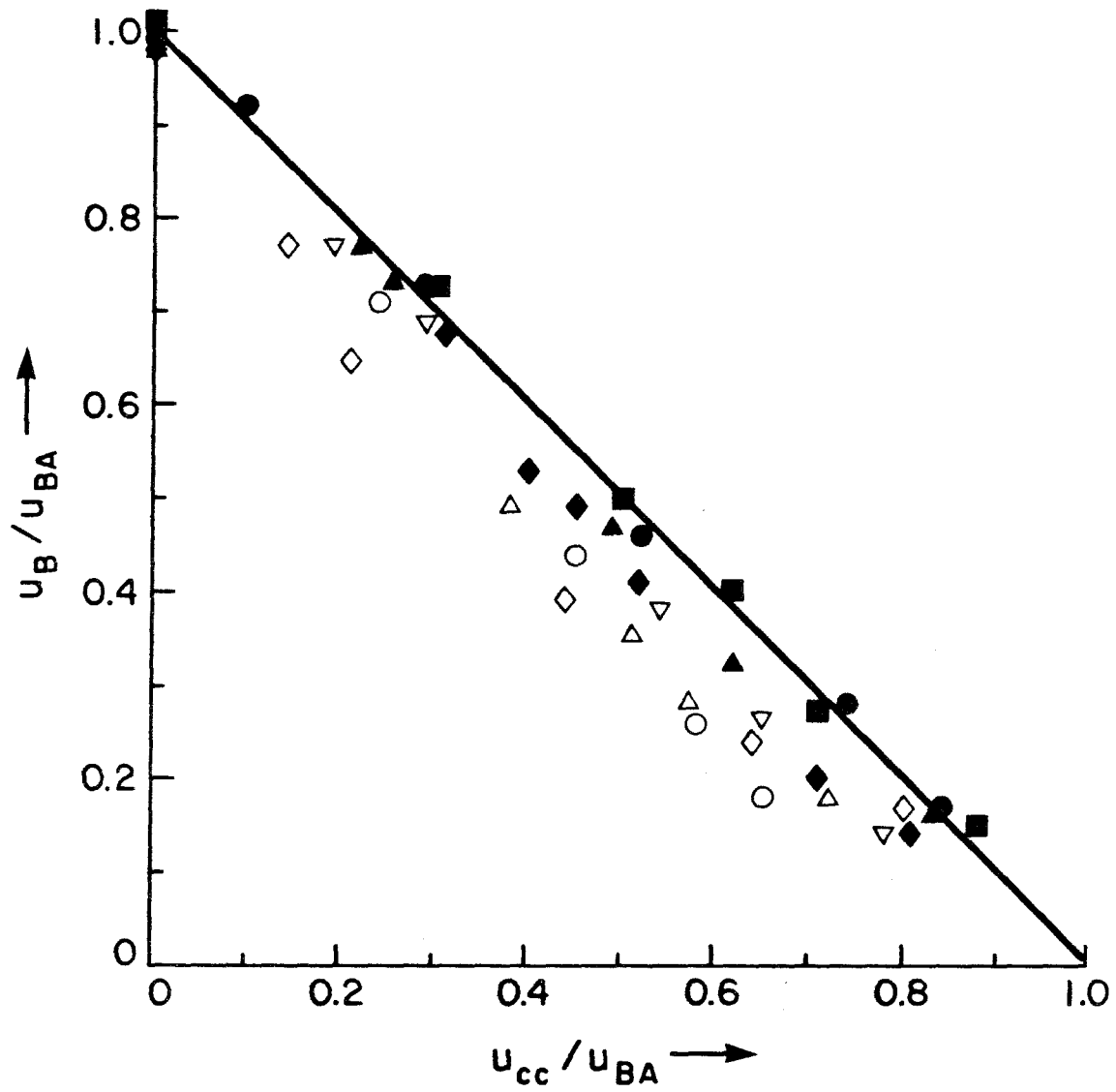


Figure 10. The change in bubble rise velocity with induced countercurrent flow in suspensions of -18+50 polystyrene beads in a neutrally buoyant salt solution. In volume percent of particles:
 \triangle , 0.1%; \circ , 0.2%; \diamond , 0.4%; ∇ , 0.6%;
 \blacktriangle , 1.0%; \bullet , 2.0%; \blacksquare , 3.0%; \blacklozenge , 4.0%.

TABLE 6. Bubble slowdown in a suspension of PS/DVB particles in a neutrally buoyant salt solution. Particles were added incrementally to the same suspension.

Particles Added Grams	Mean Diameter(μ)	Bubble Rise Velocity (cm/s)	Volume Fraction Added ($\phi \times 10^6$)	Total Volume Fraction Added ($\phi \times 10^6$)
0.00	-	25.4 ± 0.3	0	0
1.23	252	24.7 ± 0.5	301	301
1.15	112	23.9 ± 0.5	266	567
1.24	56	23.6 ± 0.8	308	875

that no more than one bubble was in the column at any time to insure no interbubble interactions. The indicated rise velocities correspond to the average of ten experiments with each experiment measuring ten rise velocities. Errors indicate data reproducibility.

A possible cause of the slowdown is the change in the rheology of the suspension of particles as compared with the pure liquid (48,49,50). Suspensions are found to be Newtonian for a volume fraction of particles, ϕ , less than 0.1, and the viscosity of the suspension, μ_s , increases with increasing ϕ . For dilute suspensions ($\phi < 0.01$) of noninteracting particles, the Einstein formula may be used:

$$\frac{\mu_s}{\mu_l} = 1 + \frac{5}{2} \phi \quad (21)$$

We find that for $\phi = 0.004$, the viscosity of the suspension is only 1% greater than the pure liquid viscosity, μ_l . Even if the bubbles had the strong viscosity dependence of the smallest bubbles in Table 1 (which our spherical cap bubbles do not have), the increase in viscosity could not account for the slowdown observed. Hence the mechanism for the observed slowdown must be due to direct contact between the bubbles and the particles.

Slowdown was not observed for the larger particles due to impulsive forces which tend to separate the particles from

the bubble exceeding the adhesion force of the particles to the bubble as detailed by Gaudin (51). Hence no slowdown is observed as there is no stable adhesion of the particle to the bubble.

Figure 11 details the results for a 7.2% by weight salt solution. Here u_{BA} is the bubble rise velocity with no particles present while u_B is the velocity in the presence of particles. Eccospheres VT were also used. These particles settle in water ($N_{Re} \sim 0.2$). Hence they were dispersed by large flows to the bubbler preceding an experiment. The flow was then reduced to the single bubble regime (about 0.3 bubbles per second); turbulence was allowed to diminish; and an experimental reading of ten rise velocities was taken. This procedure was repeated ten times for each data point presented. Error bars indicate data reproducibility.

It is seen that no significant difference was observed for slowdown for the PS/DVB and Eccospheres VT particles. And, as noted earlier, the larger particles did not cause bubble slowdown. The slowdown also appears to become saturated at very low particle concentrations as the curve descent flattens.

Similar experiments were conducted using distilled water without salt. The bubbler was changed for these experiments, and the ambient (no particle) rise velocity was 22.3 cm/s. Figure 12 shows the results. Eccospheres VT again caused slowdown. But it is apparent that Eccospheres SI did not cause

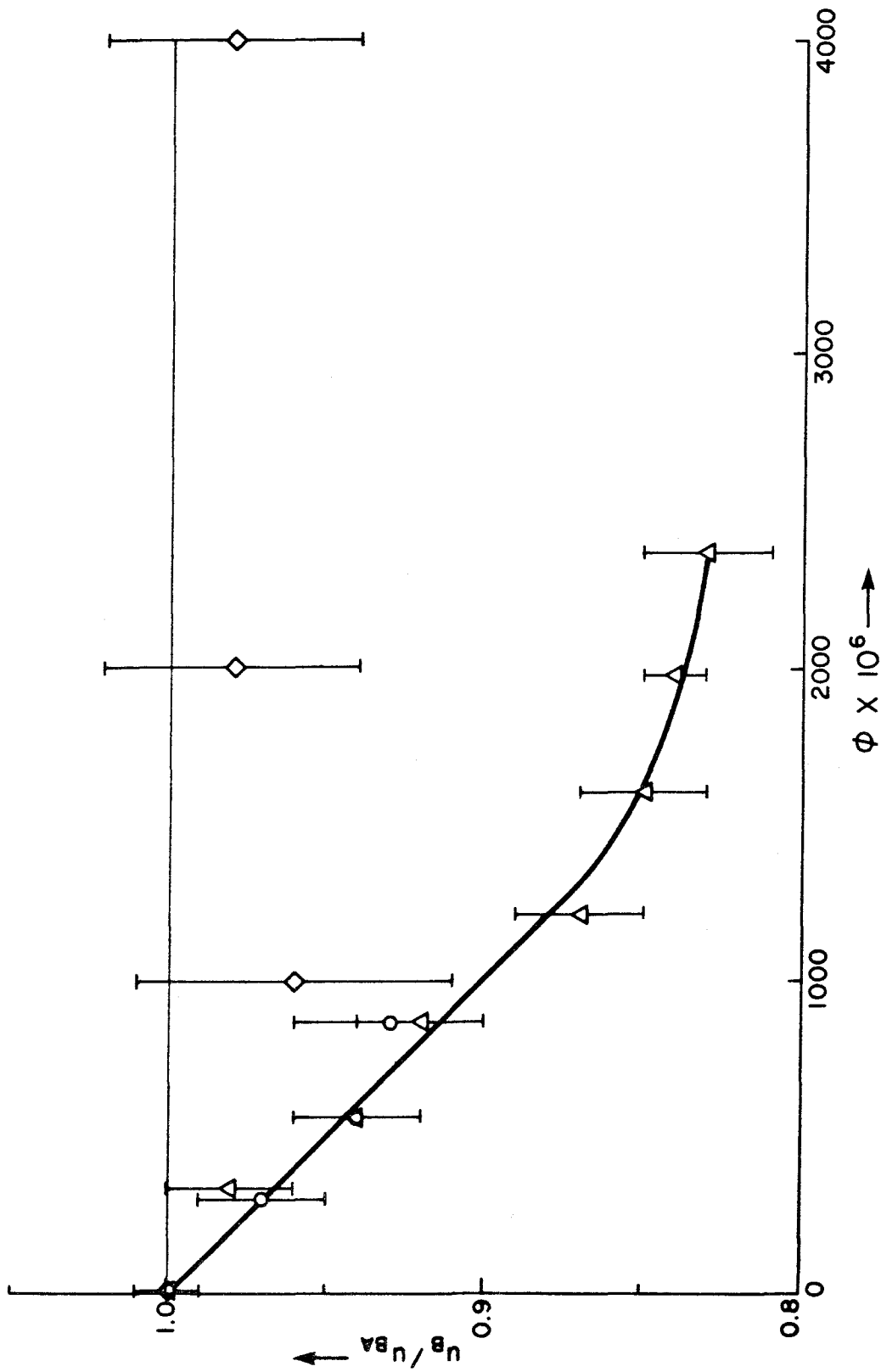


Figure 11. The effect of particle concentration on bubble rise velocities in a 7.2% by weight salt solution. \diamond , -18+50 mesh polystyrene beads; \circ , -45+400 PS/DVB beads; Δ , unclassified Eccospheres VT.

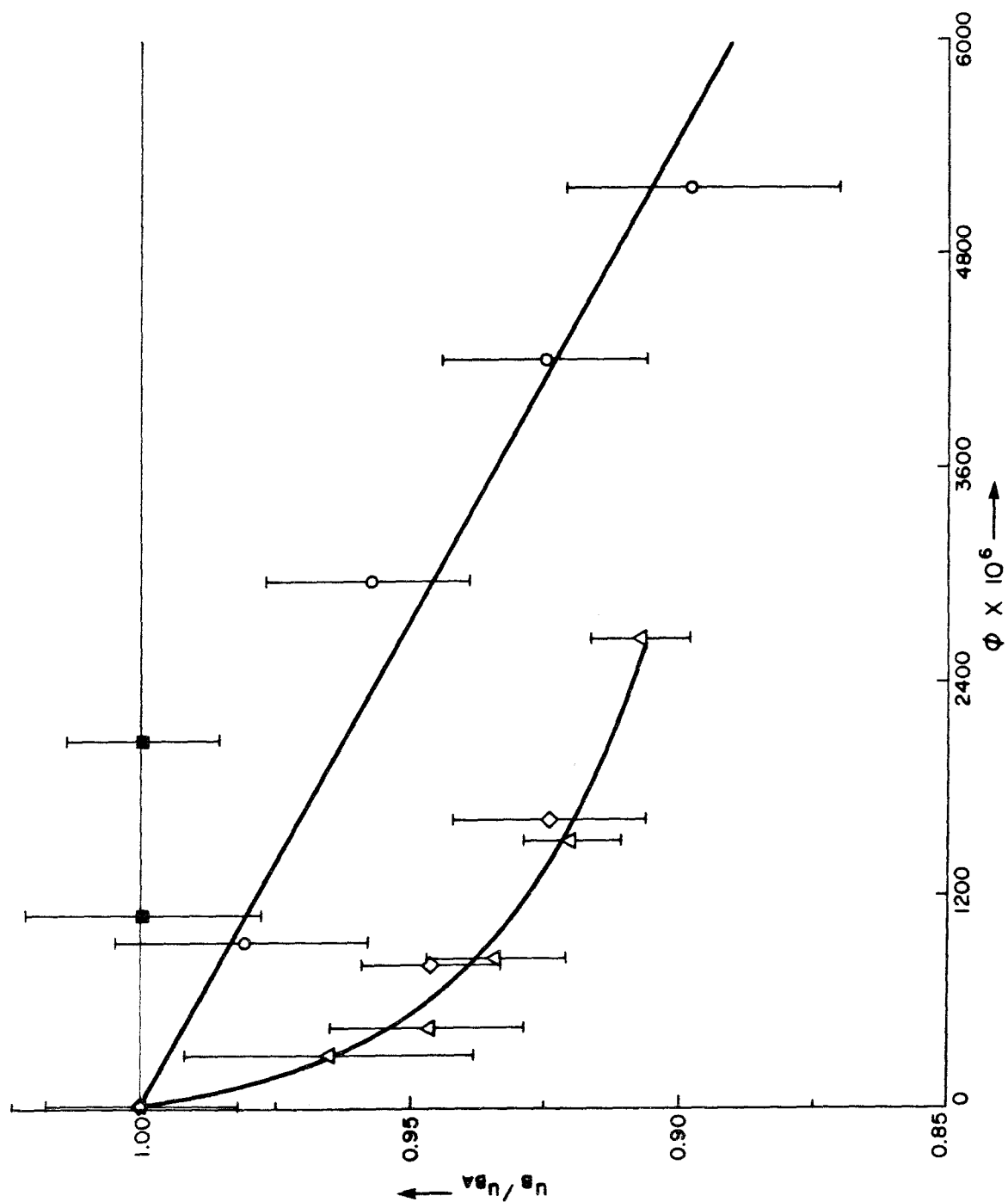


Figure 12. The effect of particle concentration on bubble rise velocities in water. O, -120+150 mesh Eccosphere VT; \diamond , unclassified Eccospheres VT; Δ , -200+400 PS/DVB beads; \blacksquare , unclassified Eccospheres SI.

such slowdown. The reason is of central importance as the contact angle between the SI particles and water is 0° indicating no particle adhesion to the bubble. The concern about surfactants compelled the author to more extensively rinse the Eccospheres VT and SI for the above experiments. Both were first rinsed in methanol. This was followed by an acid and then a caustic rinse. Finally the beads were extensively rinsed in distilled water. As indicated, slowdown was still observed leading the author to the firm conclusion that this is not caused by surfactants.

Figure 12 also indicates that the larger particles (-120+140 mesh Eccospheres VT) did not cause slowdown to commence as quickly with ϕ . From the Sutherland encounter model, the rate of collision is proportional to the particle radius multiplied by the particle number density. At a given ϕ , the rate of collision is then inversely proportional to the square of the particle radius. Hence slowdown is to be expected to be more gradual as the particle radius is increased as these experiments indicate.

The saturation effect is again observed for the smaller particles. For both Figures 11 and 12, these effects become apparent near a volume fraction of particles of 2500×10^{-6} . This slowdown is caused by two effects. First the effective density of the bubble is increased by the particles on the interface. Secondly the drag on the bubble is increased due

to the particles on its interface. To examine the relative importance of these two effects, two models will be assumed to calculate the number of particles on the bubble. One is the maximum collision model which will modify the results of Sutherland previously discussed to include a spherical cap bubble. The other assumes the bubble interface is completely covered with particles. The weight of the particles will then be used to calculate the effective bubble density, ρ_B' . The slowdown, noting the dependence on density given in Table 1, is then:

$$\frac{u_B}{u_{BA}} \equiv \left(\frac{\rho_l - \rho_B'}{\rho_l - \rho_g} \right)^{1/2} \quad (22)$$

Thus we may calculate the slowdown that can be accounted for by the increased weight of the bubble due its load of particles.

The bubble parameters are given in Table 7. In water free from wall effects, a spherical cap bubble rises as given in Table 1 and subtends a solid angle of 100° . If we neglect the wall effects in our system, the radius of curvature of the cap bubble may be calculated from its observed rise velocity and its surface area from its volume and the surface to volume ratio given in Table 1. For the distilled water experiments, the bubble had an ambient rise velocity of 22.3 cm/s, and we will assume the volume is close to that of the previous experiments in salt solutions where the bubble volume was

TABLE 7. The slowdown of bubble rise velocities due to the increased density of particle laden bubbles.

Bubble Characteristics: Shape = Spherical Cap
 Bubble Volume = 0.066 cm^3
 Radius of Curvature = 1.1 cm.
 Residence Time = 1.9 s
 Interfacial Area = 1.2 cm^2
 Ambient Rise Velocity = 22.3 cm/s

Particles	Model	$\phi \times 10^6$	Number of Particles on the Bubble	Bubble Density with Particles (g/cm^3)	$\frac{u_B}{u_{BA}}$
Unclassified Eccospheres UT	Maximum Collisions	2500	4700	0.0063	0.997
Unclassified Eccospheres UT	Saturated Area	-	23,000	0.0265	0.987
-200+400 PS/DVB	Maximum Collisions	2500	9600	0.0152	0.992
-200+400 PS/DVB	Saturated Area	-	47,000	0.0699	0.964

measured. The rise velocity in the suspension is taken to be that measured at $\phi = 2500 \times 10^{-6}$ (about 20 cm/s). The residence time is the time required for the bubble to travel 38 cm. which is the distance from the bubbler to the midway point of the observation section where bubble rise velocities were measured.

For the two models, the average particle diameter will be used as given in Table 2 or 3. The bubble interfacial area is calculated using the assumptions above, and the saturated area model used here will assign πr_p^2 as the area needed per particle. From this the number of particles the surface will accommodate is immediately calculated.

To estimate the maximum number of collisions with a cap bubble, the Sutherland model will be extended slightly. We will use a hypothetical bubble of radius R_c , the radius of curvature of the spherical cap. Then only the collisions which occur in the cap section are counted. This is readily done by allowing τ_i in equation 11 to correspond to the time it takes the particle to traverse along the hypothetical bubble section from a polar angle of fifty degrees to a polar angle of 90° , ie from the edge of the cap to the edge of the effective collision area of the sphere indicated in Figure 2. From Sutherland, this time is (if $r_p/R_c \ll 1$):

$$\tau_i = \frac{2 R_c}{u_B} \ln \cot \left(\frac{\psi}{2} \right) \quad (23)$$

ψ is the polar angle which is taken to be one half the solid angle subtended by the cap or 50° . Using this time in equation 11 for the "induction time", the maximum number of collisions is calculated assuming η is unity. This assumes, of course, that the actual contact time needed for stable adhesion is suitably short. The results for this maximum collision model are listed in Table 7 along with the aforementioned saturated area model. Both models give results of the same order of magnitude.

As is seen, the slowdowns calculated are much less than those observed for both models. Hence the density difference alone does not account for the slowdown. It is apparently the case that the observed slowdown in bubble rise velocities in slurries of nonwetting particles must be caused largely by the increased drag on the bubble by virtue of the particles on its interface.

2.5 Gas Hold-Up

Here two aspects of gas hold-up will be studied. The first deals with the effect of gas introduction method and column height on gas hold-up. The second effect will deal with the particle effect on gas hold-up at low particle concentrations.

2.5.1 The General Features of Gas Hold-Up

Hold-up was measured initially in the sparger side at various column heights in distilled water with no particles. Figure 13 shows the results. Here gas hold-up, ϵ , is presented as a function of the superficial gas velocity. This clearly indicates that this column has not reached equilibrium between coalescence and break-up. Hence as the column height is increased, the increased bubble residence time results in added bubble coalescence. Thus the result is a decreasing fraction of gas in the column as is evident in Figure 13.

Figure 14 contrasts the hold-up in the sparger and bubbler sides of the U-tube in a column of distilled water again with no particles. The ambient column height (with no gas flow) was 660 mm. Both are seen to give approximately the same gas hold-up, but the curve shapes are markedly different. Now for bubbles which do not coalesce and rise at approximately the same velocity as the bubble concentration is increased, equation 8 predicts a linear increase of hold-up with increasing gas flow rate. The downward curvature is due primarily to bubble coalescence, although admittedly some of this curvature is due to the increased rise velocity of bubbles in a swarm. The difference in the curves is due to the different processes occurring for the two systems.

The sparger emits a stream of fine bubbles as shown schematically in Figure 15. These fine bubbles then coalesce

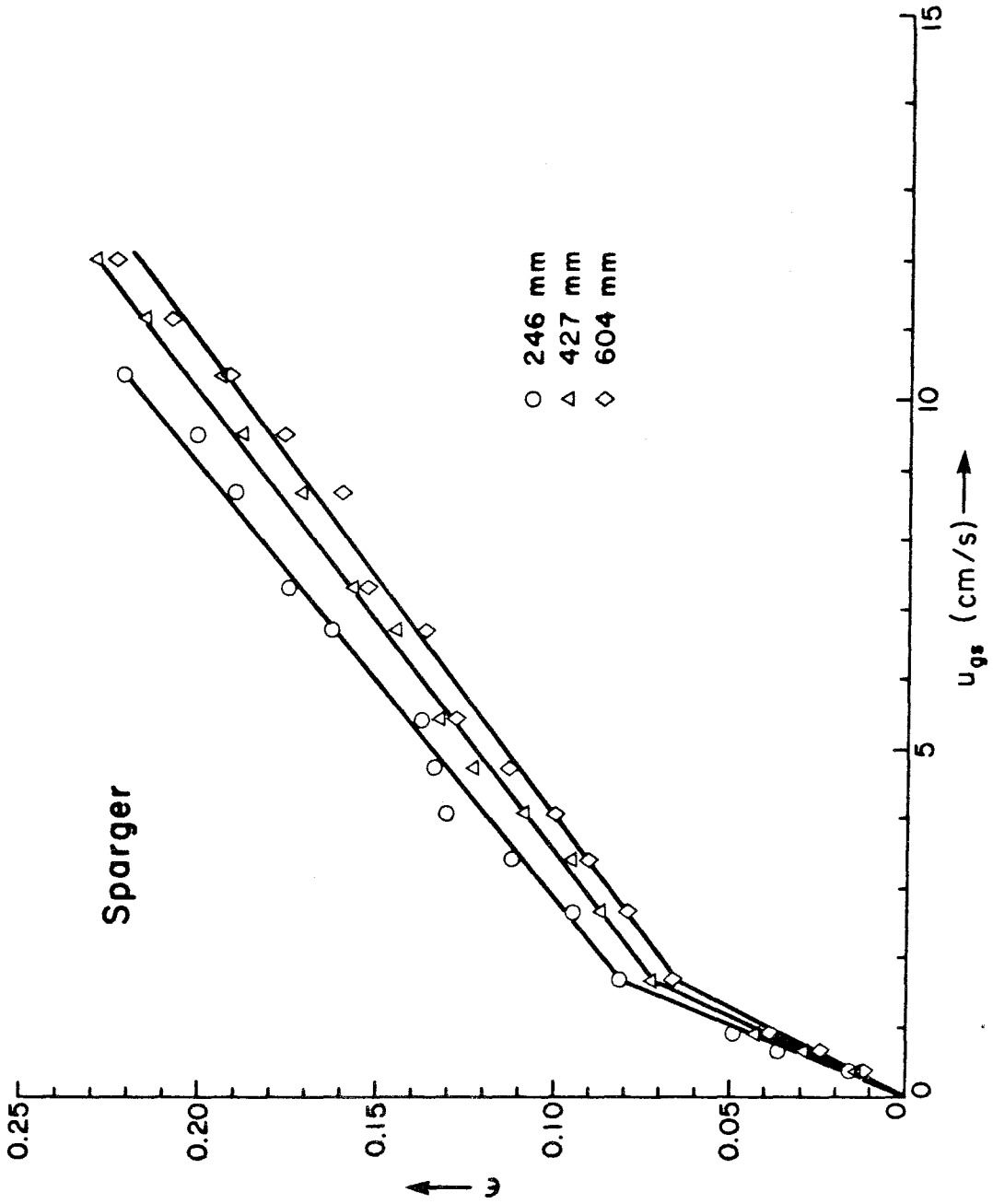


Figure 13. Gas hold-up, ϵ , in the sparger side of the U-tube system for various ambient (no flow) column heights.

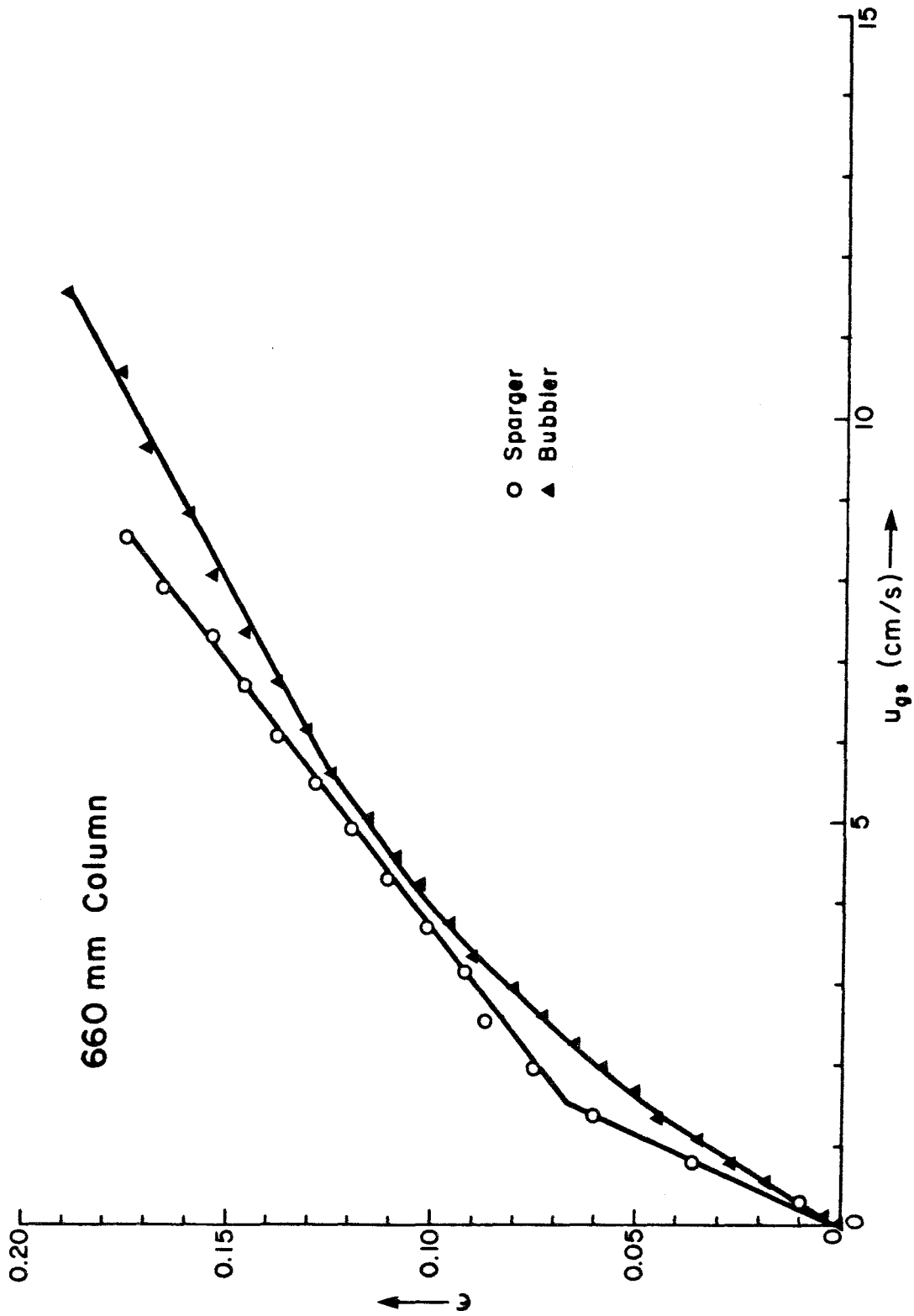
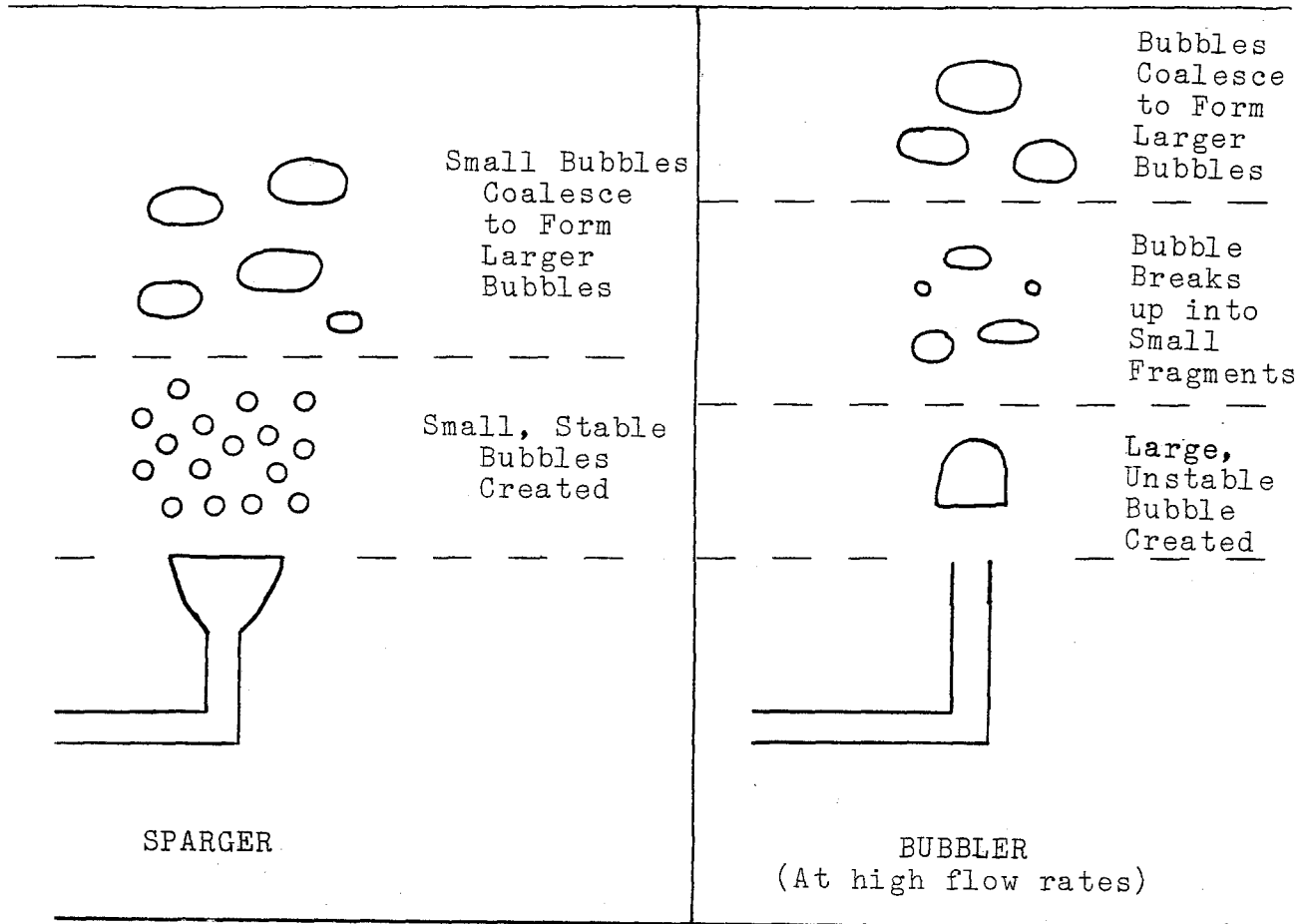


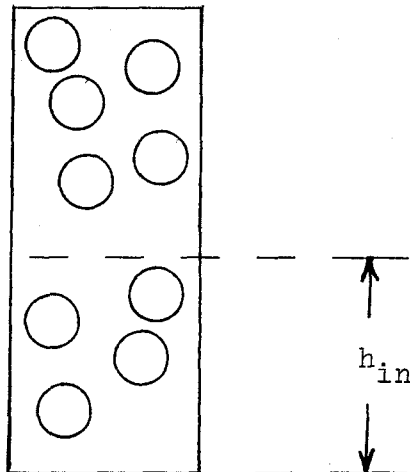
Figure 14. The difference in gas hold-up, ϵ , for the sparger and bubbler sections of the U-tube.

Figure 15. Schematic presentation of bubble coalescence and break-up phenomena in bubbling columns.



Equilibrium is reached between bubble coalescence and bubble break-up

Bubble size is determined by the characteristics of the gas flow introduction method



In a long bubbling column, bubble coalescence and bubble break-up come to equilibrium after an induction length, h_{in} . The average bubble size after the induction length becomes dependent only on liquid properties and column shape.

as they traverse up the column. The abrupt break in the curve is due to two separate effects. First as flow to the sparger is increased, larger bubbles are emitted due to coalescence of bubbles as they are formed on the sparger. Secondly, the bubbles reach a concentration where relatively large slugs are created in the column.

The bubbler emits small stable bubbles at low flowrates. On increasing the flow, the bubbler begins to emit large, unstable bubbles which break-up as shown schematically in Figure 15 and pictorially in Figure 16. After this break-up, the fragments then coalesce as they travel up the column. The gradual bending of the gas hold-up curve with increasing gas flow is due to this fragmentation process occurring initially in the bubbler section. Essentially the equilibrium between break-up and coalescence is more closely attained by this phenomenon.

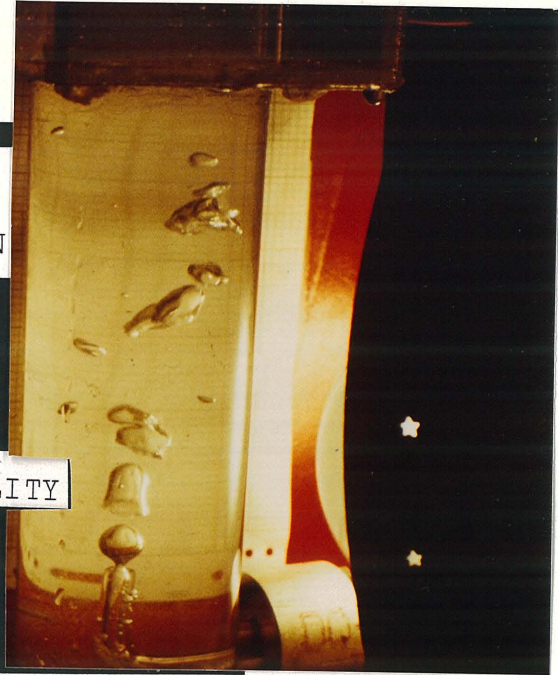
Figure 15 also presents the ultimate result. If the column is made long enough, average bubble size will be determined after a suitable induction length, h_{in} , by the equilibrium between coalescence and break-up. Total gas hold-up is given by:

$$\epsilon = \epsilon_{eq.} + \frac{h_{in}}{h} (\epsilon_{in} - \epsilon_{eq.}) \quad (24)$$

Here h is the total height of the column with ϵ_{in} being the average hold-up in the induction section and ϵ_{eq} being the

THE FRAGMENTS OF THE
UNSTABLE BUBBLES HAVE
A BROAD SIZE DISTRIBUTION

TAYLOR INSTABILITY



SMALL FRAGMENTS ARE NOTICED
AS THE REMNANTS OF LARGER
BUBBLES WHICH HAVE BROKEN
UP DUE TO INSTABILITIES

BUBBLE IS RELEASED
FROM THE ORIFICE

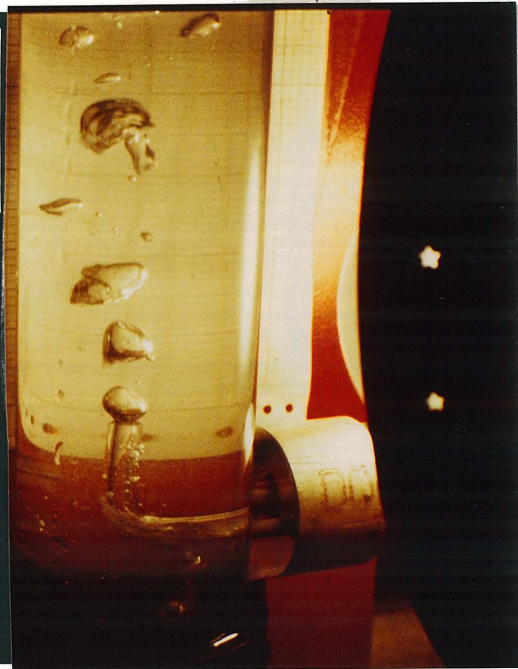


Figure 16. The bubbler emits small stable bubbles at low flow rates. At the higher flow rates shown here, large bubbles are emitted which fragment into smaller bubbles in a short distance above the bubbler.

average hold-up in the equilibrated section. Hence total gas hold-up is influenced by the method of introduction if h is not sufficiently greater than h_{in} . The deviation is lowered somewhat as ϵ_{in} should be approximately equal to ϵ_{eq} .

2.5.2 The Particle Effect on Gas Hold-Up

The effect of particle addition on gas hold-up was investigated for the sparger in Table 8 and for the bubbler in Table 9. Both were for ambient column heights of 660 mm of distilled water, and both employed Eccospheres VT particles. For the lower flow rates, complete particle dispersion was assured by first inducing high flow rates, then lowering the flow rate, allowing equilibrium, and taking a measurement. The results indicate a significant decline in gas hold-up for the addition of less than 0.5% by volume of the nonwetting particles. Errors in Table 9 represent the reproducibility of two experiments with no particles. The data for the particle experiments are the average of two experiments with reproducibility being the same as the no particle experiments. Experiments for Table 8 were not repeated.

Table 10 contrasts the results for wetting and non-wetting particles. No significant lowering of the gas hold-up was obtained for the wetting (SI) particles while a significant decline was observed for the nonwetting particle (VT). The results given here were for experiments performed in the same manner as those of Table 9.

TABLE 8. Particle effect on the gas hold-up, ϵ , in the sparger side of the U-tube.

660mm Column - Sparger				
-120 + 140 Mesh Eccospheres VT Particles				
$\phi \times 10^6$	0 (No Particles)	623	1613	4340
Flow rate u_{gs} (cm/s)	ϵ	ϵ	ϵ	ϵ
0.00	0.000	0.000	0.000	0.000
0.38	0.016	0.015	0.012	0.012
0.66	0.028	0.025	0.024	0.024
0.92	0.041	0.039	0.037	0.036
1.34	0.057	0.052	0.057	0.050
1.68	0.068	0.068	0.062	0.062
2.34	0.079	0.073	0.072	0.070
2.67	0.084	0.080	0.084	0.077
3.10	0.091	0.087	0.084	0.083
3.43	0.096	0.094	0.093	0.089
3.69	0.100	0.097	0.096	0.093
4.07	0.106	0.101	0.096	0.093
4.73	0.116	0.108	0.109	0.108
5.43	0.127	0.127	0.121	0.120
6.70	0.147	0.137	0.137	0.134
7.31	0.156	0.150	0.146	0.146
8.66	0.177	0.169	0.165	0.158
9.50	0.190	0.179	0.178	0.171
10.35	0.203	0.194	0.194	0.191

TABLE 9. Particle effect on the gas hold-up, ϵ , in the bubbler side of the U-tube.

660mm Column - Bubbler

-120 + 140 Mesh Eccospheres VT Particles

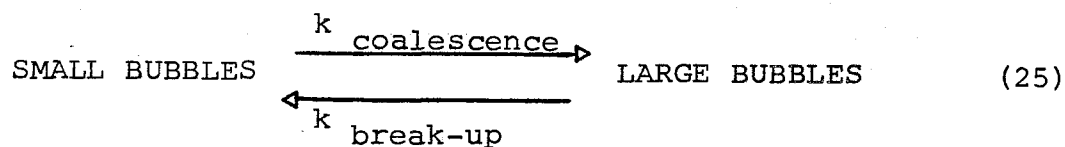
$\phi \times 10^6$	0 (No Particles)		947	2970
Flow rate u_{gs} (cm/s)	ϵ	Error	ϵ	ϵ
0.00	0.000		0.000	0.000
0.29	0.009	0.002	0.008	0.007
0.53	0.017	0.000	0.016	0.017
0.84	0.026	0.001	0.026	0.024
1.49	0.045	0.002	0.040	0.038
1.84	0.054	0.001	0.054	0.050
2.70	0.074	0.003	0.072	0.070
3.87	0.098	0.001	0.092	0.086
5.35	0.120	0.000	0.115	0.107
7.36	0.144	0.001	0.140	0.132

TABLE 10. The effect of wetting and nonwetting particles on gas hold-up, ϵ , in a 660mm column in the sparger side of the U-tube.

$\phi \times 10^6$	(No Particles)		Eccospheres VT (Nonwetting) 3180 8910		Eccospheres SI (Wetting) 4910 10,700	
	ϵ	Error	ϵ	ϵ	ϵ	ϵ
Flow rate u_{gs} (cm/s)						
0.0	0.000	0.000	0.000	0.000	0.000	0.000
0.32	0.010	0.001	0.009	0.008	0.010	0.010
0.84	0.036	0.002	0.031	0.032	0.036	0.034
1.42	0.060	0.003	0.055	0.054	0.058	0.057
1.99	0.075	0.003	0.071	0.070	0.074	0.074
2.58	0.087	0.004	0.079	0.077	0.084	0.085
3.17	0.092	0.004	0.087	0.086	0.090	0.090
3.75	0.101	0.004	0.097	0.094	0.097	0.098
4.34	0.111	0.003	0.105	0.100	0.108	0.108
4.93	0.119	0.003	0.113	0.110	0.116	0.118
5.52	0.128	0.002	0.119	0.122	0.125	0.126
6.11	0.138	0.005	0.131	0.130	0.135	0.134
6.74	0.146	0.002	0.137	0.139	0.146	0.146
7.34	0.154	0.001	0.145	0.146	0.153	0.155
7.93	0.166	0.002	0.153	0.154	0.164	0.162
8.55	0.175	0.002	0.164	0.162	0.174	0.175

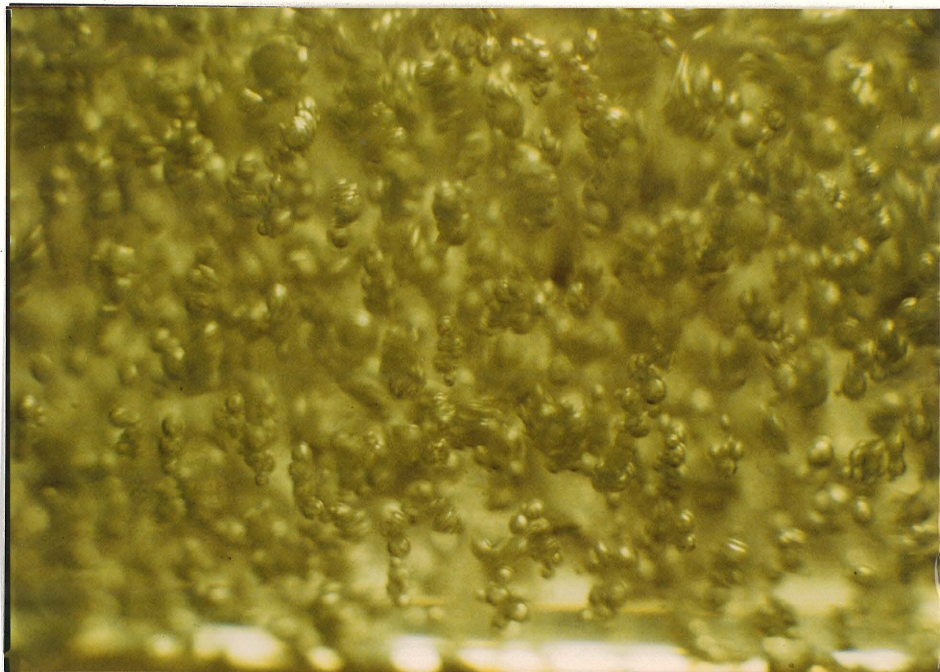
Thus it is seen that the wetting properties of the particles do indeed affect bubble coalescence as is manifested by decreased gas hold-up. This is quite likely due to the Bikerman mechanism of Figure 1. Such a mechanism requires the formation of bubble clusters. Figure 17 shows the bubble clusters formed in a suspension of nonwetting particles (-200+400 PS/DVB) in distilled water. These clusters were produced by sufficient gas flow through the sparger to produce countercurrent flow in the bubbler section. Significant clustering was not observed for distilled water or suspensions of wetting (SI) particles.

Nonwetting particles are seen to increase coalescence. As stated, the columns here were principally in the coalescing mode, ie, as column height was increased, coalescence was increased. With sufficient column height such that equilibrium exists between break-up and coalescence, we have:



Adding small, light, nonwetting particles increases $k_{\text{coalescence}}$. The equilibrium will then shift toward larger bubbles with an attendant decrease in gas hold-up. Hence this effect will manifest itself in long columns so long as the particles added do not correspondingly increase the rate of bubble break-up.

Countercurrent Flow Direction
↓



A CONCENTRATED SUSPENSION OF SMALL BUBBLE CLUSTERS IN COUNTERCURRENT FLOW IN THE U-TUBE



A LARGE CLUSTER OF BUBBLES

Figure 17. Bubble clusters formed in suspensions of -200+400 PS/DVB particles in distilled water.

2.6 Conclusions

1. Dispersion of particles lighter than the liquid in bubbling columns first passes through an inversely fluidized regime at low gas flowrates. Induced downward liquid flow is responsible. The tendency to complete dispersion will be hindered by complex geometry and affected by the contact angle of the particle with the liquid and the particle's relative density to that of the liquid.

2. The Sutherland encounter model where particles are assumed to follow the streamlines around a bubble gives a consistent picture of bubble-particle contacting in a slurry of nonwetting particles.

3. Bubble rise velocity slowdown is significant in dilute slurries of small non-wetting particles. This is caused by stable adhesion of the particle to the interface. Such slowdown is principally caused by the increased drag on a particle-laden bubble.

4. Large nonwetting particles of approximately the same density as the liquid do not adhere to the bubbles and do not cause slowdown. Such particles also do not penetrate the bubble proper. They are diverted around the bubble by the same surface tension forces which hold the bubble together.

5. Coalescence is enhanced in bubbling columns by the presence of small concentrations of non-wetting particles. Such coalescence was undetectable for similar particles which were wetted by the liquid.

6. For short bubbling columns, gas hold-up is strongly influenced by the gas introduction method. The curve shape is much sharper for sparger gas flow than for flow through a large circular orifice due to the instability of bubbles emitted from the orifice at the higher gas flowrates.

7. Strong countercurrent flow directed against bubbles rising with significant wall effects provides only a simple transformation of reference frame. Large, nonwetting particles do not significantly affect the bubble-wall slip.

8. Liquid flow induced in one region by gas flow in a separate region of a connected system such as a U-tube or annulus may be carefully controlled by varying the gas flowrate. Such pumping could be used successfully for transporting a corrosive or high temperature liquid through various sections of an enclosed system.

NOTATION

- a = One-half the major axis of an ellipsoid (cm)
 A_c = The cross-sectional area of the column (cm^2)
 b = One-half the minor axis of an ellipsoid (cm)
 C_D = The drag coefficient on an ellipsoidal bubble
 d_B = The bubble diameter (cm)
 D_o = The orifice diameter of a bubbler (cm)
 g = The acceleration of gravity (981 cm/s^2)
 G = The volumetric gas flow (cm^3/s)
 h = The column height (cm)
 h_c = The critical thickness of a liquid film on a unit particle near a gas-liquid interface at which spontaneous rupture of the film occurs.
 h_{in} = The height of the induction section of the column (cm)
 k = A constant of order unity relating average radial velocity to $y|\partial u_1/\partial y|$ in turbulent flow (usually ~ 0.4)
 n_B = The number density of the bubbles (cm^{-3})
 N_B = the total number of bubbles in the column
 n_c = The number of bubble-particle collisions per unit time (s^{-1})
 N_{EO} = The Eotvos number
 n_f = The number of fruitful bubble-particle collisions per unit time (s^{-1})

- n_p = The number density of particles (cm^{-3})
 N_{PM} = The maximum number of particles on a bubble after a residence time in the column of τ_c
 N_{Re} = The Reynolds number
 N_{We} = The Weber number
 p = The number of size ranges the bubbles are divided into
 ΔP_h = The hydrostatic head (dynes/cm^2)
 ΔP_t = The amount of momentum transfer from the bubble to the liquid (dynes/cm^2)
 r_B = The bubble radius (cm)
 R_c = The radius of curvature of a spherical cap bubble (cm)
 r_e = The equivalent bubble radius (cm) = $\left(\frac{3 V_B}{4 \pi}\right)^{1/3}$
 r_p = The particle radius (cm)
 S_m = The integral amount of momentum transport from the bubble to the liquid (dynes/cm^2)
 t = The time (s)
 u_B = The bubble rise velocity (cm/s)
 u_{BA} = The ambient bubble rise velocity (cm/s)
 u_{cc} = The induced countercurrent flow of liquid (cm/s)
 u_{gs} = The gas superficial velocity (cm/s)
 u_{is} = The interstitial liquid velocity (cm/s)
 u_l = The liquid velocity (cm/s)

- u_{ls} = The liquid superficial velocity (cm/s)
- u_t = The particle terminal velocity (cm/s)
- V_B = The bubble volume (cm³)
- V_g = The volume of gas in the column (cm³)
- V_l = The volume of liquid in the column (cm³)
- V_{so} = The volume of solids in the column (cm³)
- y = The distance from the tube wall (cm)

Greek Letters

- ϵ = The gas hold-up in the column
 ϵ_A = The actual porosity of a fluidized bed
 ϵ_b = The apparent porosity of a fluidized bed
 ϵ_{eq} = The gas hold-up in the equilibrated section of a column
 ϵ_{in} = The gas hold-up in the induction section of a column
 ϕ = The volume fraction of particles
 γ = The surface tension (dynes/cm)
 η = The correction factor for the amount of bubble-particle contact due to non-ideal effects
 ρ_A = The fluid density in the annular region of an annular system (g/cm^3)
 ρ_g = The gas density (g/cm^3)
 ρ_I = The fluid density in the inner region of an annular system (g/cm^3)
 ρ_l = The liquid density (g/cm^3)
 τ_c = The contacting time between a bubble and the suspended particles (s)
 τ_{hom} = The homogenous shear stress (dynes/cm^3)
 τ_i' = The induction time for a particle to adhere to a bubble (s)
 τ_i = The time it takes a particle to travel from a polar angle of 50° to a polar angle of 90° (s)

- μ_l = The viscosity of the liquid with no particles (cp)
- μ_s = The viscosity of the liquid with suspended particles (cp)
- ν = The kinematic viscosity of the liquid (cm^2/s)
- χ_i = The growth factor for bubbles of a particular size
- ψ = The polar angle (degrees)

REFERENCES

1. Levich, V. G., Physiochemical Hydrodynamics, Prentice-Hall, Englewood Cliffs, New Jersey (1962)
2. Moore, D. W., J. Fluid Mech., 23, 749, (1965)
3. Mendelson, H. D., AIChE Journal, 13, 250, (1967)
4. Harmathy, T. Z., AIChE Journal, 6, 281, (1960)
5. Taylor, G. I., Proc. Royal Society, (London), A201, 192, (1950)
6. Verschoor, H., Trans. Inst. Chem. Eng., (London), 28, 52, (1950)
7. Butterworth, D., Int. J. Multiphase Flow, 1, 845, (1975)
8. Nicklin, D. J., Chem. Eng. Sci., 77, 693, (1962)
9. Soo, S. L., Fluid Dynamics of Multiphase Systems, Blaisdel Publishing Company, Waltham, Massachusetts, (1967)
10. Marucci, G., Chem. Eng. Sci., 4, 975, (1969)
11. Marucci, G., Nicodeno, L., and Acierno, D., in Cocurrent Gas-Liquid Flow, Proc. of an International Symposium on Research in Cocurrent Gas-Liquid Flow, U. of Waterloo, 1968, (E. Rhodes and D. S. Scott, Eds.), p. 95, Plenum Press, New York. (1969)
12. Akita, K., and Yoshida, F., Ind. Eng. Proc. Des. Dev., 12, 76 (1973)
13. Akita, K., and Yoshida, T., Ind. Eng. Proc. Des. Dev., 13, 84, (1974)
14. Vermeer, D. J., and Krishna, R., Ind. Eng. Proc. Des. Dev., 20, 475 (1981)

15. Hills, J. H., Chem. Eng. J., 12, 86 (1976)
16. Yamashita, F., Mori, Y., and Fujita, S., J. Chem. Eng. Japan, 12, 5 (1979)
17. Einsele, A., and Finn, R. K., Ind. Eng. Proc. Des. Dev., 19, 600 (1980)
18. Nakanoh, M., and Yoshida, F., Ind. Eng. Proc. Des. Dev., 19, 190 (1980)
19. Bhaga, D., and Weber, M. E., Can. J. Chem. Eng., 50, 323 (1972)
20. Imafku, K., Wang, T.Y., Koide, K. and Kubota, H. J., J. Chem. Eng. Japan, 1, 153 (1968)
21. Afschar, A. S., and Schugel, K., Chem. Eng. Sci., 23, 267 (1968)
22. Massimilla, L., Solimando, A., and Squillou, E., Brit. Chem. Eng., 6, 632 (1961)
23. Ostergaard, K., in Fluidization, (J.F. Davidson and D. Harrison, Eds.), p. 751, Academic Press, London, (1957)
24. Rigby, G.K., Van Blockland, C. P., Park, W.H., and Capes, C. E., Chem. Eng. Sci., 25, 1729 (1970)
25. Henriksen, K., and Ostergaard, K., Chem. Eng. Sci., 29, 626 (1974)
26. Ostergaard, K., Chem. Eng. Sci., 20, 165 (1965)
27. Rigby, G. R., and Capes, C. E., Can. J. Chem. Eng., 48, 343 (1970)
28. Bhatia, V. K., Evans, K. A., and Epstein, N., Can. J. Chem. Eng., 48, 343 (1970)

29. Bikerman, J. S., Foams: Theory and Industrial Application, Reinhold, New York (1953)
30. Sutherland, K. L., J. Phys. Coll. Chem., 52, 394 (1948)
31. Scheludko, A., Tschaljowska, S. L., and Fabrikant, A., in Thin Liquid Films and Boundary Layers, p. 112, Special Discussions of the Faraday Society, Nov. 1, 1970, Academic Press, New York (1971)
32. Manohar, C., Kelkar, V. K., and Yakhmi, J. V., J. Coll. Int. Sci., 78, 565 (1980)
33. Skrylev, L. D., Lengenchenko, I. A., Sazonova, V. F., and Kerner, S. M., Colloid J. USSR, 41, 424 (1979)
34. Deryagin, B. U., Dukhin, S. S., and Rulev, N. N., Colloid J. USSR, 38, 227 (1976)
35. Brenner, H., Chem. Eng. Sci., 16, 242 (1961)
36. Scheludko, A., Kolloid. Z., 191, 52 (1963)
37. Zisman, W. A., Ind. Eng. Chem., 55, 19 (1963)
38. Bhavaraju, S. M., Russell, T. W. F., and Blanch, H. W., AIChE Journal, 24, 454 (1978)
39. Hewitt, G. S., and Bource, J. A., Int. J. Multiphase Flow, 1, 139 (1975)
40. Beattie, D. R. H., Nucl. Eng. Des., 21, 46 (1972)
41. Lander, B. E., and Spalding, D. B., Mathematical Models of Turbulence, Academic Press, London (1972)
42. Richardson, J. F., and Zaki, W. N., Trans. Inst. Chem. Eng. (London), 32, 35 (1954)

43. Kojima, H., and Asano, K., *Int. Chem. Eng.*, 21, 473
(1981)
44. Nutt, C. W., *Chem. Eng. Sci.*, 12, 133 (1960)
45. Datta, R. L., Napier, D. H., Newitt, D. M., *Trans. Inst. Chem. Eng. (London)*, 28, 14, (1950)
46. Kumar, R., and Kuloor, N. R., *Adv. Chem. Eng.*, 8, 255
(1970)
47. Uno, S., and Kintner, R. C., *AIChE Journal*, 2, 420 (1956)
48. Jeffreys, D. J., and Acrivos, A., *AIChE Journal*, 22, 417,
(1976)
49. Jinescu, V. V., *Int. Chem. Eng.*, 14, 397 (1974)
50. Clarke, B., *Trans. Inst. Chem. Eng. (London)*, 45, 251
(1967)
51. Gaudin, A. M., Flotation, McGraw-Hill, New York (1932)

CHAPTER 3

THE REACTION MECHANISM OF CARBON
PARTICLES IN MOLTEN SODIUM PHOSPHATE

3.1 Introduction

To discuss the molten salt, carbon particle, and oxidant bubble system, one first notes that the system is nothing more than a high temperature version of the relatively common bubble column slurry reactor. Such reactors are in use throughout the petroleum industry. Normally this entails a catalytic particle in the liquid phase and mass transfer across the gas-liquid interface. Such processes include catalytic hydrogenation and desulfurization of petroleum fractions as well as the Fischer-Tropsch process. Other processes which entail the chemical conversion of the particles are coal liquefaction and molten salt gasification schemes such as Rockwell International's (1).

In such processes, it should be noted that the exclusive mechanism of gaseous transfer need not be across the gas-liquid interface and to the particle in the bulk liquid as is quite clear when the particle is not wetted by the liquid. For in this case there is a thermodynamic driving force for the particle to penetrate the bubble, expel its liquid shrouding, and come into direct contact with the gas in the bubble. Such phenomena are well utilized in flotation (2).

The purpose of this chapter is to investigate each of the two particle reaction mechanisms in a process. This is shown schematically in Figure 1. Naturally the indirect mechanism (across the gas-liquid interface) would predominate for a system of particles with 0° contact angle with the liquid phase.

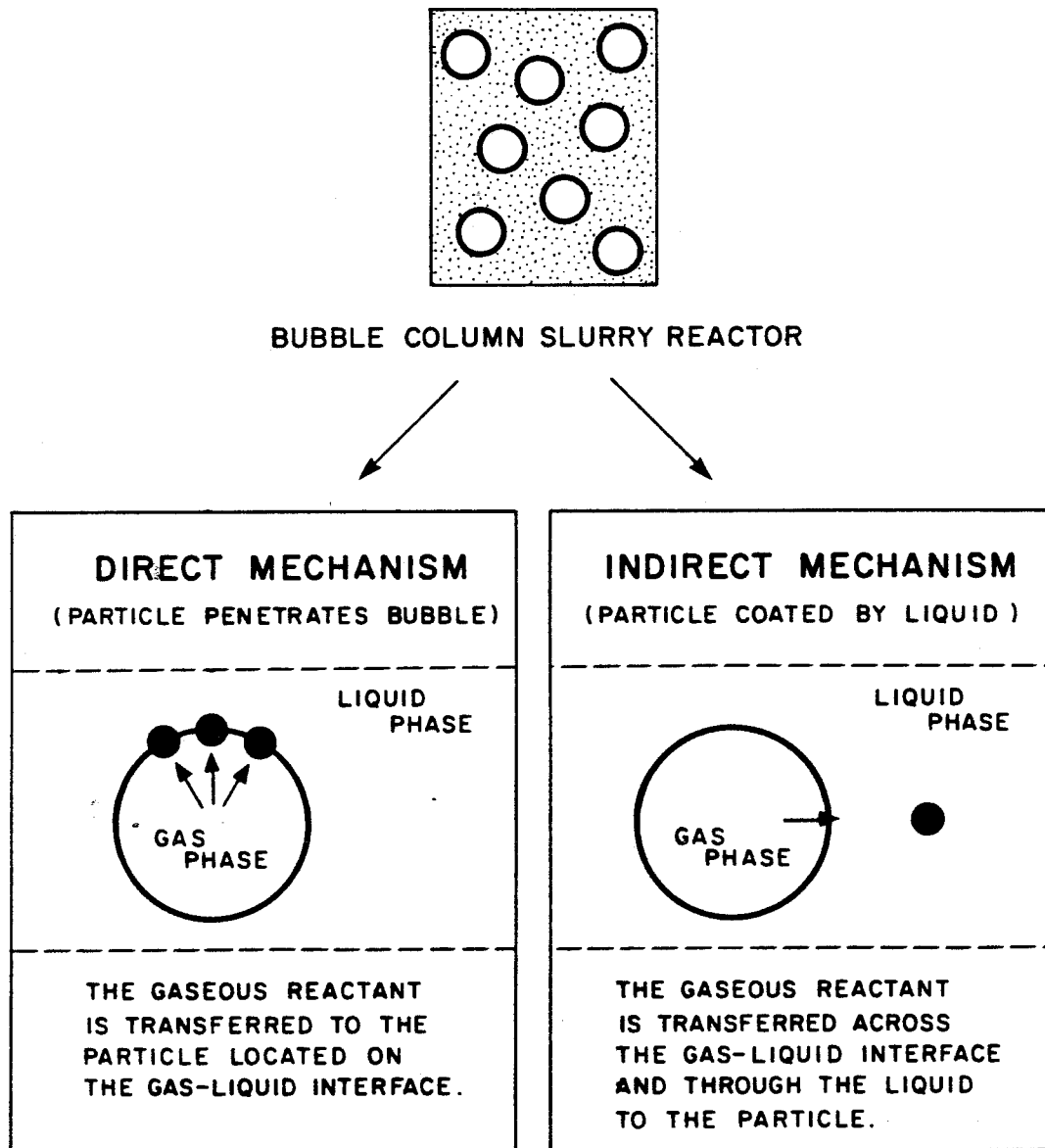
POSSIBLE PARTICLE REACTION MECHANISM

Figure 1. The two particle reaction mechanisms possible in a bubble column slurry reactor.

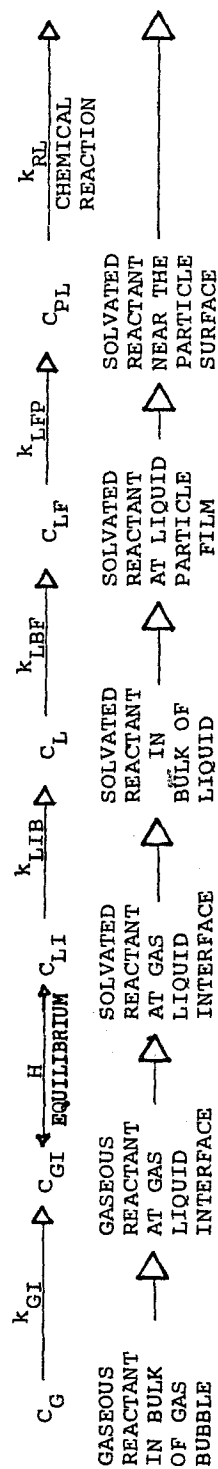
But as the contact angle is increased, a growing degree of influence would be expected of the direct particle-gas contacting mechanism. The relative importance of either mechanism would be dependent upon the contact angle, gas solubility in the liquid phase, mass transport in the various phases, and possible surfactant adsorption onto the particle surface.

It is very important to note that the overall reaction rate for the two cases is governed by two completely different mechanisms. For the indirect mechanism, the gaseous reactant is transferred to the particle, while for the direct mechanism, the particle is transferred to the bubble. The former is much discussed as by Goto and Smith (3). The latter is a matter of particle-bubble contacting the kinetics of which have been discussed by Sutherland (4).

For demonstrative purposes, two simple models shall be presented for the direct and indirect mechanisms. The particle shall be assumed impermeable and to react with a simple first order rate expression.

Figure 2 includes the analysis of the indirect mechanism. The rate expression assuming appropriate mass transfer coefficients at the various points of resistance is:

$$R_{\text{dir}} = \frac{C_G H}{\frac{1}{N_B A_B} \left(k_{GI} \frac{H}{k_{LIB}} + \frac{1}{k_{LIB}} \right) + \frac{1}{N_P A_P} \left(k_{LBF} \frac{1}{k_{LFP}} + \frac{1}{k_{LFP}} + \frac{1}{k_{RL}} \right)} \quad (1)$$



$$N_{GI} = k_{GI} N_{B^A} (C_G - C_{GI})$$

$$C_{LI} = HC_{GI}$$

$$N_{LIB} = k_{LIB} N_{B^A} (C_{LI} - C_L)$$

$$N_{LBF} = k_{LBF} N_{P^A} (C_L - C_{LF})$$

$$N_{LFP} = k_{LFP} N_{P^A} (C_{LF} - C_{PL})$$

$$R_{RL} = k_{RL} N_{P^A} C_{PL}$$

STEADY STATE: $N_{GI} = N_{GLI} = N_{LIB} = N_{LBF} = N_{LFP} = R_R$

$$R_{ind} = \frac{HC_G}{\left(\frac{H}{N_{B^A} k_{GI}} + \frac{1}{N_{B^A} k_{LIB}} + \frac{1}{N_{P^A} k_{LBF}} + \frac{1}{N_{P^A} k_{LFP}} + \frac{1}{N_{P^A} k_{RL}} \right)}$$

Figure 2. The model for the indirect gaseous transfer mechanism. The gaseous reactant is transferred across the gas liquid interface of the bubble and to the liquid coated particle.

As is seen, the first two resistances involve total bubble surface area while the final three involve total particle surface area and liquid phase mass transfer. The overall rate also has a direct proportionality to the gas solubility assumed to be given by the Henry's law constant, H . It should be noted that C_{PL} is the concentration near the particle surface with k_{RL} entailing all adsorption/desorption phenomena relative to the chemical reaction rate.

The analysis of Sutherland (4) is utilized for examining the direct mechanism. Consider a spherical bubble of radius, r_B , rising at velocity, u_B , in a frictionless fluid. Extrapolating the streamlines which come within one particle radius, r_P , of the bubble to the forward of the bubble's trajectory, a collision cross section is obtained. With this Sutherland obtained for the rate of particle-bubble contacting in a slurry of particle concentration, n_P :

$$R_c = 3\pi \eta u_B r_B r_P N_B n_P \quad (2)$$

Here η is a shape correction factor accounting for nonspherical bubbles and other effects discussed previously (5). N_B is the total number of bubbles. Taking an average contacting time, τ_c , for the bubbles, the average number of particles in contact with the bubbles in the column is:

$$N_{PI} = R_c \tau_c \quad (3)$$

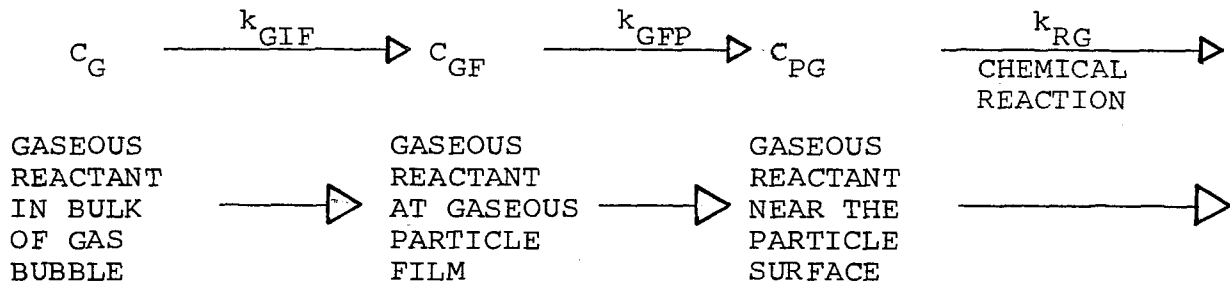
This analysis is incorporated in Figure 3 which also assumes a correction to the particle area, ξ , which should be approximately $\frac{1}{2}$ if the particle has a 90° contact angle with the liquid phase. In general this area correction will be influenced by the difference in particle and liquid densities and hydrodynamic forces on the particle in addition to the contact angle. The location of the particle is assumed to be on the bubble surface and to be held there by the work of adhesion:

$$W_{ad} = \gamma (1 - \cos\theta) S \quad (4)$$

Here θ is the contact angle with γ being the surface tension of the liquid exposed to the gaseous reactant. S is the solid gas interfacial area created which for the above expression is assumed equal to the solid-liquid and liquid-gas interfacial area destroyed. Hence from Figure 3, the overall rate of reaction for the direct mechanism is:

$$R_{dir} = \frac{3\pi \eta u_B \tau_c r_B r_P n_P \xi A_{PN} C_G}{\frac{1}{k_{GIF}} + \frac{1}{k_{GFP}} + \frac{1}{k_{RG}}} \quad (5)$$

The striking difference between R_{ind} and R_{dir} is that the indirect mechanism entails gas and liquid phase mass transfer. And generally as is pointed out by Ranade and Ulbrecht (6), the gas side mass transfer resistance is negligible. This would seemingly make the direct mechanism much faster than



$$N_{GIF} = k_{GIF} N_{PI} A_{PI} (C_G - C_{GF})$$

$$N_{GFP} = k_{GFP} N_{PI} A_{PI} (C_{GF} - C_{PG})$$

$$R_R = k_{RG} N_{PI} A_{PI} C_{PG}$$

STEADY STATE: $N_{GIF} = N_{GFP} = R_R$

NOTING: $N_{PI} = 3\pi\eta u_B r_B r_P \tau_c n_P N_B$

$$A_{PI} = \xi A_P$$

OVERALL STEADY STATE REACTION RATE:

$$R_{dir} = \frac{3\pi\eta u_B \tau_c r_B r_P n_P \xi A_P N_B C_G}{\left(\frac{1}{k_{GIF}} + \frac{1}{k_{GFP}} + \frac{1}{k_{RG}} \right)}$$

Figure 3. The model for the direct gaseous transfer mechanism. The particle is transferred to the gaseous reactant in the bubble.

the indirect mechanism. This increase is offset by the relative rate of bubble particle contacting being slow.

Considering special cases of the above expressions, take first the case of chemical reaction control on the overall rate. For this, the ratio of the rates is:

$$\frac{R_{dir}}{R_{ind}} = \frac{3\pi\eta u_B \tau_c r_B r_P n_P N_B \xi}{H N_P} \quad (6)$$

and for the case of film diffusion controlling the rate is:

$$\frac{R_{dir}}{R_{ind}} = \frac{3\pi\eta u_B \tau_c r_B r_P n_P \xi N_B (k_{GFP})}{H N_P (k_{LFP})} \quad (7)$$

Substantial dependence differences are to be noted in addition to gas vs. liquid phase mass transfer. First solubility dependence is noted only for the indirect mechanism. Secondly the direct mechanism is proportional to the particle density while the indirect mechanism is proportional to the total surface area of the particles, ie, their total number. Thirdly, the direct mechanism in both cases is proportional to the total number of bubbles while the indirect mechanism is not when particle film diffusion or the chemical reaction rate is slow.

From this simplified analysis, it would be expected that the correct mechanism or combination is very important in correlating data. The two yield completely different scaling factors.

Here these two mechanisms will be discussed in conjunction with the reaction of carbon particles in a slurry of molten sodium phosphate and oxygen containing bubbles. As the temperatures are high, conventional surfactants will be destroyed. Thus to proceed we need to measure the carbon-molten phosphate contact angle and the reaction rate. This will be done in the experimental section. But before proceeding directly to these results, solubility and mass diffusivities in molten salts will be discussed as these are very important parameters for the indirect mechanism.

3.2 Solubilities of Gases in Molten Salts

As no method existed in this laboratory to measure the solubility of gases in molten phosphates, the results of earlier workers will be employed to find a convenient correlating expression. Following the method of Prausnitz and Shair (7), the gas is first compressed to a hypothetical liquid with the same molar volume it will have in the melt. The associated free energy change for a mole of molecules, N_A , is:

$$\Delta G_1 = N_A k T \ln \left(\frac{f_L}{f_G} \right) \quad (8)$$

Here f_L is the fugacity of the hypothetical liquid with f_G being the gas phase fugacity. k is the Boltzmann constant.

We then create holes for the gas molecules in the liquid with free energy change:

$$\Delta G_2 = N_A A_H \gamma \quad (9)$$

Here A_H is the area of the hole necessary for the gas molecule with γ being the surface tension of the molten salt. Here naively, we have assumed surface tension to be valid for molecular dimensions. The hypothetical liquid is then mixed with the molten salt with associated free energy change:

$$\Delta G_3 = N_A kT \ln(\gamma_G X_G) \quad (10)$$

Here X_G is the mole fraction of the gas in the liquid phase and γ_G is the activity coefficient.

As we shall deal with low pressures and high temperatures, the ideal gas law will be assumed for the gas. Thus with our previous assumption of highly dilute solutions, we have for the solubility at one atmosphere as $\Delta G_1 + \Delta G_2 + \Delta G_3 = 0$:

$$\ln\left(\frac{C_L}{C_G}\right) = \ln\left(\frac{\rho_L RT}{M_L f_L \gamma_G}\right) - \frac{A_H \gamma}{kT} \quad (11)$$

Here C_L is the molar concentration of the dissolved species and C_G is the molar concentration of the gaseous species. M_L is the molecular weight of the salt with ρ_L being its mass density. This has the same general form as the model of Grimes et al (8) who employed a simple Eulig model which

ignored the first term on the right hand side of equation 11. From this equation, it would be expected that larger gas molecules with associated larger A_H would be less soluble as is generally observed. This would be offset somewhat by the larger molecules being relatively easier to compress to the liquid state by virtue of the f_L term.

We proceed to correlate data by assuming the first term on the right hand side of equation 11 to be approximately constant for nonpolar gases at high temperatures in similar solvents and employ the data of Grimes et al (8,9,10) and Malinauskas and Richardson (11) who studied the solubilities of the noble gases and hydrogen and deuterium in three molten fluoride mixtures from 773 to 1073 K. The data were found to be reasonably correlated by equation 12.

$$\ln \left(\frac{C_L}{C_G} \right) = -2 - \frac{2k \gamma \sigma^2}{kT} \quad (12)$$

Here σ is the gas molecular diameter in \AA and γ is in dynes/cm. It is noted that the molecular area has been set equal to a factor multiplied by the square of the hard sphere gas constants of the various gases. Using the factor of $2k$ the slope of the surface tension term for the individual gases yielded hard sphere diameters that compared very favorably with the hard sphere diameters obtained from viscosity correlations using the Lennard-Jones potential as Table 1 indicates.

Table 1. Molecular size parameters from viscosity data and from correlated molten fluoride solubilities of inert nonpolar gases.

GAS	(Å)	(Å)
	Hard Sphere Diameter (12) From Correlating Viscosity Data of Gas Using the Lennard-Jones 6-12 Potential	Diameter from Correlating Molten Fluoride Solubilities (Equation 12)
He	2.58	2.56
Ne	2.86	2.83
Ar	3.46	3.49
Xe	4.06	4.01
H ₂	2.97	3.01
D ₂	2.95	2.83

Malinauskas and Richardson (11) as well as Grimes et al (8) have discussed the choice of diameters. There are several choices as may be seen by referring to Huheey (13). Due to the above fit, it would seem appropriate to proceed with the viscosity diameters. Figure 4 presents the solubility data for the fluorides correlated with equation 12 using the hard sphere diameters from viscosity data.

From this simple model, the area seems to be $0.88 \pi \sigma^2$ for use in computing the hole size. It is important to point out the unrealistic nature of the above model as it assumes a molecular surface tension which is, of course, nonsense. The model simply says colligatively for several gas molecules, the surface tension seems to be a convenient correlating parameter.

A substantial amount of work has also been conducted for noble gas and nitrogen solubilities in molten nitrates. The measured solubilities are compared in Table 2 which extrapolated data to a common temperature using the heat of solution when available. As experimental agreement was poor, no attempt was made to correlate the results. Equation 12 did yield good agreement with the lower valued solubilities, particularly so in the case of helium.

For purposes of this paper, an approximate solubility expression was needed for oxygen in molten phosphates. Shenke et al (22) have measured the solubility of oxygen in two sets

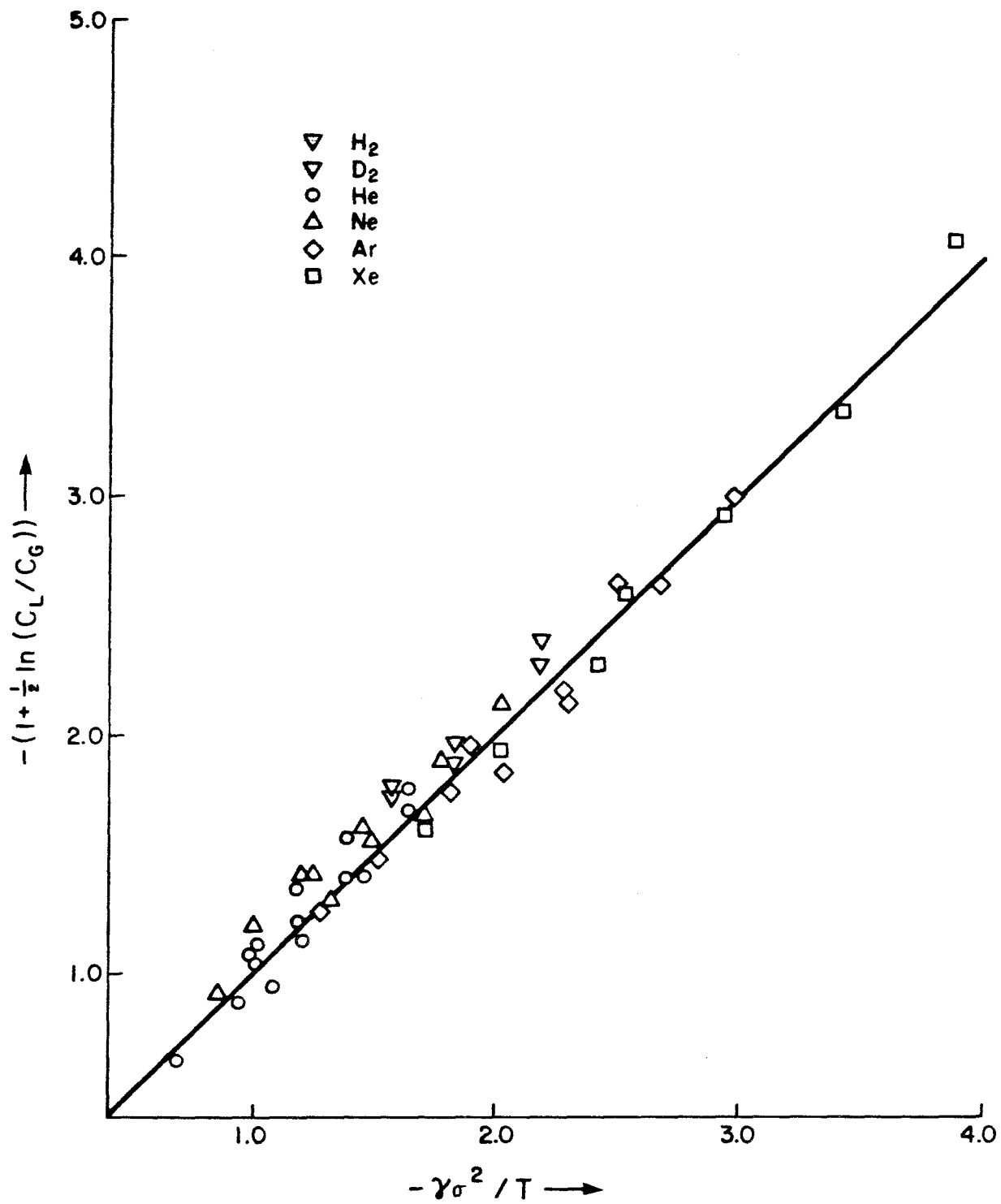


Figure 4. Gas solubilities in molten fluorides. The solid line is for the ordinate equal to the coordinates.

Table 2. Inert, nonpolar gas solubilities in molten nitrates.
From the Henry's Law constants at 1 atmosphere.

Solvent	Gas	T(K)	C_L (10^{-6} gmoles/cm ³)	ΔH (kcal/gmole)	Ref.
NaNO ₃	He	642	2.27		(18)
NaNO ₃	He	642	0.11	3.2	(20)
NaNO ₃	He	642	0.21	3.2	(14)
NaNO ₃	Ar	642	1.72		(17)
NaNO ₃	Ar	642	0.07	3.5	(18)
NaNO ₃	Ar	642	0.06	3.8	(14)
NaNO ₃	N ₂	642	1.97	-2.7	(15)
NaNO ₃	N ₂	642	0.23	3.5	(20)
NaNO ₃	N ₂	642	0.06	3.8	(14)
AgNO ₃	Ar	523	3.35		(16)
AgNO ₃	Ar	507	0.02		(14)
LiNO ₃	Ar	578	0.17	8.0	(19)
LiNO ₃	Ar	578	0.11	3.3	(14)
LiNO ₃	N ₂	550	0.18	1.8	(19)
LiNO ₃	N ₂	550	0.07		(14)
(Na,K)NO ₃ *	O ₂	511	0.9	4.2	(21)
(Na,K)NO ₃ *	O ₂	603	1.6	4.2	(21)

*Eutectic Mixture

of molten carbonates at the approximate temperature range of interest in these experiments (900-1200K). Correlating these results using the data of Ward and Janz (23) for surface tension and density prediction, a least squares fit of the data yielded:

$$\ln \left(\frac{C_L}{C_G} \right) = -2 - \frac{2k \gamma_o^2}{kT} \quad (13)$$

This equation was compared with the results of Desimoni et al (21) for oxygen solubilities in molten nitrates at somewhat lower temperatures and predicted results to within 30% of the experimental solubility. Consequently, with some reservation, this expression will be used to predict the solubility of oxygen in the molten phosphates.

3.3 Diffusion Correlations at High Temperatures

Before proceeding directly to diffusion, we will demonstrate how some old, simple, easily available correlations can be used to predict the properties of the molten salts. These are particularly useful in helping to predict missing properties, for consistency checks, and for helping to estimate a molecular weight for molten phosphates which have a tendency to have rather high molecular weights due to polymerization.

The first method is utilizing MacLeod's equation to arrive at the parachor which is then set equal to the sum

of the atomic parachors. The data for this are from Janz (24) and Van Wazer (25), and Table 3 indicates the results.

$$\frac{M_L \gamma^{1/4}}{\rho_L} = P = \sum p_i, \text{ atomic} \quad (14)$$

Data for the Snugden parachors are from Adam (26) with sodium being estimated from the molten salt data as 68.5. These parachors are for univalent coordination with no ring structures. As the gas density has been neglected, the correlation was applied as near to the melting point of the salt as data temperature ranges permitted. As is seen the correlation is quite good, and we have that surface tension data may be well estimated from density data. Unfortunately this method did not yield the degree of polymerization, Σ . Hence this method was extended to the Eotvos correlation:

$$K_E (T_c - T - 6) = \gamma \left(\frac{M_L}{\rho_L} \right)^{2/3} \quad (15)$$

Here the critical temperature, T_c , is related to the surface tension and molar volume. By differentiating this expression, we obtain:

$$\frac{K_E}{M_L^{2/3}} = \frac{-\frac{\partial \gamma}{\partial T}}{\rho_L^{2/3}} + \frac{\left(\frac{2\gamma}{3}\right) \left(\frac{\partial \rho_L}{\partial T}\right)}{\rho_L^{5/3}} \quad (16)$$

Table 3 Molten Salt Correlation using the Snugden Parachor. Atomic parachors are from Adam (26) except for sodium which was found to be 68.5 for molten sodium salts.

SUBSTANCE	T (K)	γ (dynes/cm)	ρ_L (g/cm ³)	M_L (g/mole)	P (cm ³ /mole) (dynes/cm) ^{1/2}	$\frac{M_L^{1/4}}{P\rho_L}$
NaF	1270	186.	1.94	41.99	94.2	0.85
NaCl	1076	116.	1.56	58.44	122.8	1.00
NaBr	1030	98.9	2.33	102.9	136.5	1.02
NaI	943	87.1	2.73	149.9	159.5	1.05
Na ₂ CO ₃	1150	211.	1.96	106.0	201.8	1.02
NaNO ₃	590	116.	1.90	84.99	141.0	1.04
Na ₂ SO ₄	1173	192.	2.06	142.0	265.2	0.97
Σ (Na _{2.56} P ₂ O _{6.28})	973	211.	2.25	Σ (221.3)	Σ (376.4)	1.00

In general the above equation would not be expected to give as good results as the original due to the dependence on the temperature coefficients of density and surface tension.

Table 4 compares the results of equation 16 with equation 15 using critical data for the molten halides (24). These critical data for the salts were generated by either the method of rectangular diameters (27) or the use of partition function developed for the alkali halides (28) which predicted other measurable thermodynamic properties well. Both methods give similar critical temperatures. The average of the predictions using the differentiated Eotvos equation yielded a factor which compared favorably with that using the critical data. Consequently this factor was compared with the results for eutectic sodium phosphate yielding a molecular weight of approximately 440 corresponding to roughly two of the pseudomonomers given in Table 3. Hence, the average molecular weight will be taken as 442.6 corresponding to the composition, $\text{Na}_{5.12}\text{P}_4\text{O}_{12.56}$.

We now have sufficient data to estimate the diffusion coefficients in molten salts using two correlations. Both are based on the Nernst-Einstein equation and generally have only been applied in practice to low temperatures. The first is taken from Chang (29) where:

$$\left(\frac{kT}{D_c \mu}\right) \left(\frac{N_A}{V_s}\right)^{1/3} = K_C \quad (17)$$

Table 4. Molten Salt Correlation Using the Eotvos Correlation.

SALT	K_E (Equation 16)	Error	Temperature Range (K)	K_E (Equation 15)
NaF	0.37	0.01	1273-1373	0.48
NaCl	0.76	0.02	1074-1174	0.56
NaBr	0.49	0.01	1073-1173	0.58
NaI	1.04	0.03	973-1073	0.55
Na ₂ CO ₃	0.28	0.003	1173-1273	
Na ₂ MoO ₄	0.83	0.01	1073-1173	
NaNO ₃	0.13		600	
Na ₂ SO ₄	0.55	0.01	1173-1273	
Na ₂ WO ₄	0.76	0.05	1073-1873	
Average	0.58	\pm 0.29		

MOLTEN EUTECTIC SODIUM PHOSPHATE (Na _{2.56} P ₂ O _{6.28}) _Σ			
T(K)	γ (dynes/cm)	ρ_1 (g/cm ³)	$\frac{K_E}{\frac{2}{M^3}}$ (ergs/K)
973	211.	2.25	0.0098
1073	207.	2.22	0.0099
1173	203.	2.18	0.0100
1273	199.	2.15	0.0102
Average			0.0100
Error			0.0002

Here μ is the viscosity in poise with D_C being the diffusion coefficient. V_S is the solute molar volume which will be taken from liquid density data at the temperature of interest or as the hard sphere volume using viscosity diameters if the solute is a gas. K_C is a parameter which will be varied to account for the high temperatures. Wilke (30) proposed an alternate correlation where:

$$\frac{10^{10} V_S^{0.6} D_W \mu}{7.4 M_L^{1/2} T} = K_W \quad (18)$$

All parameters are as described above with D_W being the diffusion coefficient. K_W is again a parameter which will be varied to account for the high temperatures and was given as the square root of an association parameter by Wilke.

Table 5 gives the values of K_C and K_W using these equations with high temperature diffusion coefficients. Even though in some cases, the diffusing component is undoubtedly ionic, the order of magnitude of the diffusion coefficient may be generally predicted if K_C is set equal to π and K_W is set equal to 1.6 which is what Wilke proposed for water.

Table 5. Diffusion coefficient prediction using hydrodynamic theory and the Wilke correlation for molten salts and liquid metals.

T(K)	Solvent	Solute	V_s (cm^3/gmol)	μ (cp)	D_L (cm^2/s) ($\times 10^5$)	$\left(\frac{kT}{D_L \mu}\right) \left(\frac{N}{V}\right)^{\frac{1}{3}}$ (Chang)	$\frac{10^{10} M_L^{-\frac{1}{2}} D_L \mu}{7.4 V_s^{-0.6} T}$ (Wilke)	Ref.
1053	KBr	AgBr	36	1.1	4.9	7.1	0.5	(24)
1053	KI	AgI	44	1.3	5.1	5.4	0.6	(24)
633	KNO ₃	AgNO ₃	45	2.6	4.6	1.8	2.5	(24)
623	KNO ₃	K	52	2.7	1.5	4.7	1.0	(24)
633	KNO ₃	KBr	57	2.6	3.0	2.5	1.9	(24)
633	KNO ₃	KI	69	2.6	3.0	2.3	2.1	(24)
653	KNO ₃	TlNO ₃	58	2.3	3.4	2.5	1.9	(24)
1111	NaCl	Na	32	1.3	9.6	3.4	1.5	(24)
943	NaI	Na	30	1.5	7.4	3.2	1.0	(24)
623	NaNO ₃	Na	28	2.4	2.3	4.3	1.0	(24)
633	NaNO ₃	AgNO ₃	45	2.3	5.1	1.8	2.0	(24)
623	NaNO ₃	CsNO ₃	67	2.4	1.2	6.2	0.8	(24)
633	NaNO ₃	TlNO ₃	57	2.3	4.3	2.0	0.9	(24)
1168	Na ₂ CO ₃	Na	32	3.1	3.0	4.5	0.9	(24)
623	AgNO ₃	Ag	12	2.2	0.4	37.2	0.1	(24)
623	LiNO ₃	Li	14	3.5	2.9	3.0	1.3	(24)
863	CdCl ₂	Cd	15	2.4	2.6	6.7	0.4	(24)
943	CsCl	Cs	90	1.4	3.5	4.9	0.8	(24)
783	PbCl ₂	Pb	20	4.3	1.0	7.9	0.3	(24)
1273	Ag	O ₂	14	3.7	9.6	1.7	1.8	(31)
1473	Ag	O ₂	14	2.8	15.4	1.7	1.8	(31)
1500	Cu	Cu(64)	8	3.5	5.6	4.5	0.8	(32)
800	Zn	Zn(65)	10	2.8	3.5	4.4	0.8	(32)

3.4 Experimental

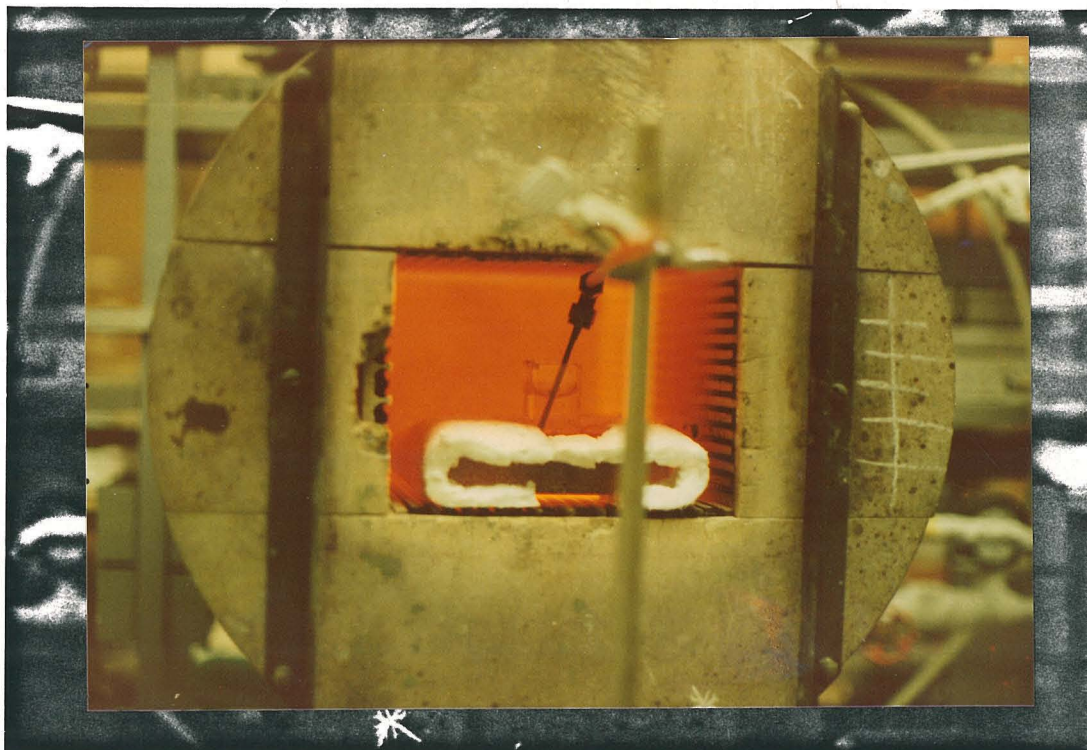
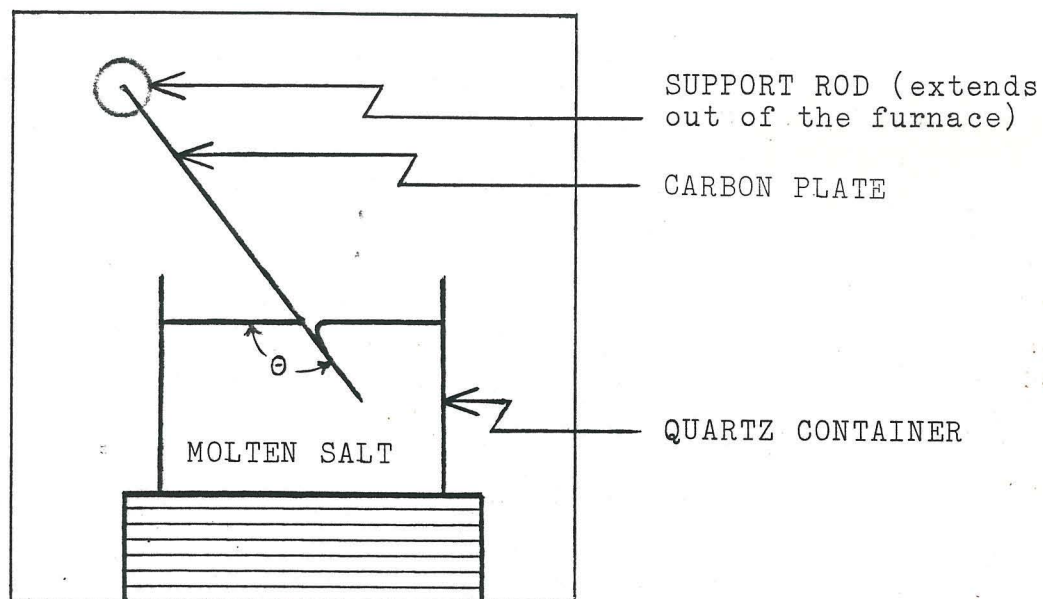
3.4.1 Measurement of the Contact Angle

The equilibrium contact angle between carbon, molten salt, and air was measured. The experiment consisted of melting sodium phosphate in a quartz container in an electric furnace. The tilting plate method of Adam and Jessop (26) was then used to determine the contact angle as outlined in Figure 5.

For the plate, spectroscopic carbon electrodes from Union Carbide were used. These $\frac{1}{4}$ " cylindrical electrodes were filed smooth to form plates and dipped in the molten salt vessels. Once so placed, the plate was rotated until the surface remained horizontal upon contacting the salt. The contact angle was measured visually and photographed. Molten salt samples were also cooled with the plate intact. From these observations, the most likely contact angle was found to be $136^{\circ} \pm 5^{\circ}$. The temperature was in the range of 1000 to 1200 K. The sodium phosphate used corresponded to the eutectic composition ($\text{Na}_2\text{O}:\text{P}_2\text{O}_5 = 1.28:1.00$) (25).

This procedure was repeated at higher temperatures for sodium carbonate. The experiments were less conclusive due to the high melting point of the carbonate. However the contact angle was large and seemingly greater than 90° .

Figure 5. Adam and Jessop experiment for measuring the static contact angle, θ . The contact angle is measured when the surface remains horizontal upon contacting the plate. The picture is indicative of the situation where the plate is not tilted far enough counterclockwise.



3.4.2 Measurement of the Reaction Rate in Molten Sodium Phosphate

The reaction rate of the spectroscopic electrodes was measured for two cases. In one case, the rods were submerged in oxygenated salt while in the other case, the rods were exposed directly to the gaseous oxygen. The experimental system shown in Figure 6 consisted of two separate sources for filtered air and pre-purified nitrogen. The flow from each was summed and then injected into the reactor. The offgas was monitored for CO_X by infrared adsorption with the temperature being measured by thermocouple. The temperature was varied from 967 to 1219 K.

The reactor shown in Figure 7 was used to measure the reaction rate of the submerged or segregated electrodes. This consisted of anchoring the electrodes in the annular region and oxygenating the salt in the central region thus insuring no direct carbon-gaseous oxygen contact. In essence, the liquid phase is oxidized in the central region and reduced in the annular region. Fluid flow in such cases has been discussed by Nevers (33). Such flow is driven by the phase in the central region being lighter by virtue of gas hold-up. Substantial flows are easily obtained so long as the expanded liquid height is above the inner tube. As Table 6 demonstrates such levels are well attained at all temperatures for the ambient case, ie, with no bubbling.

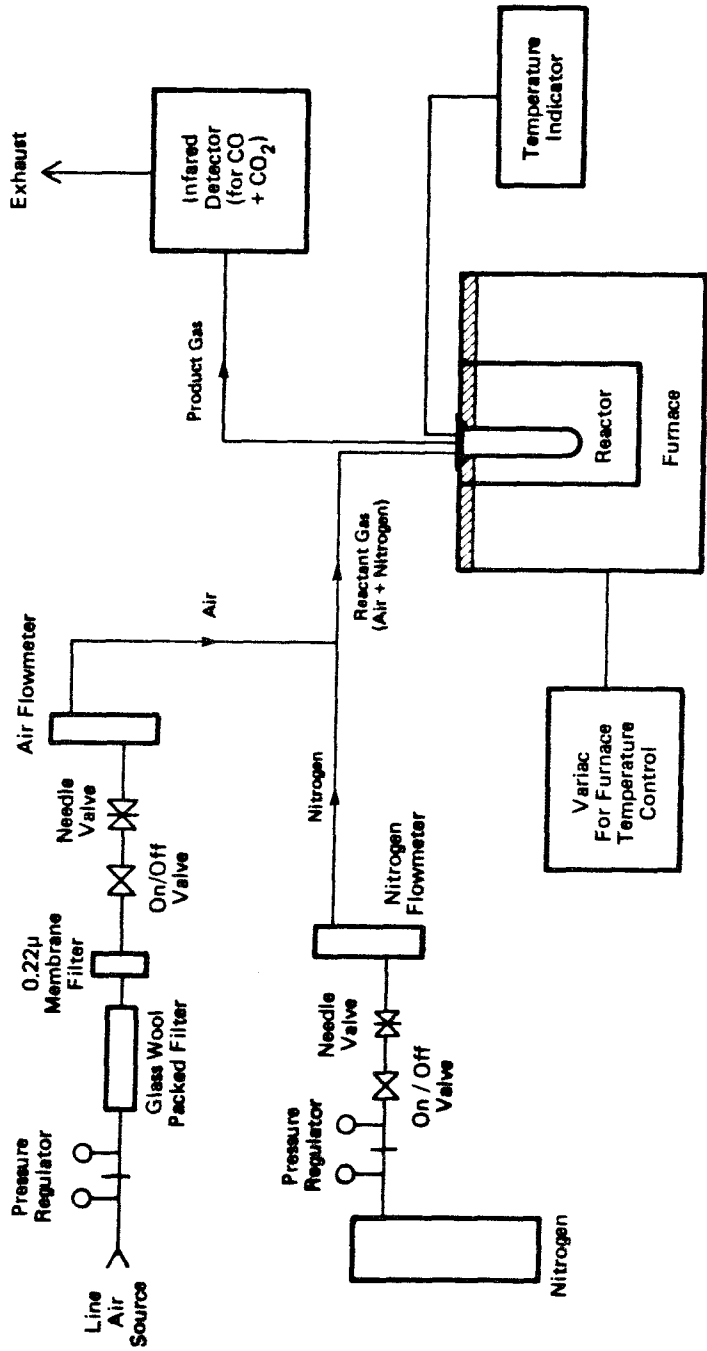


Figure 6. The experimental system for measuring the reaction rate of spectroscopic carbon electrodes.

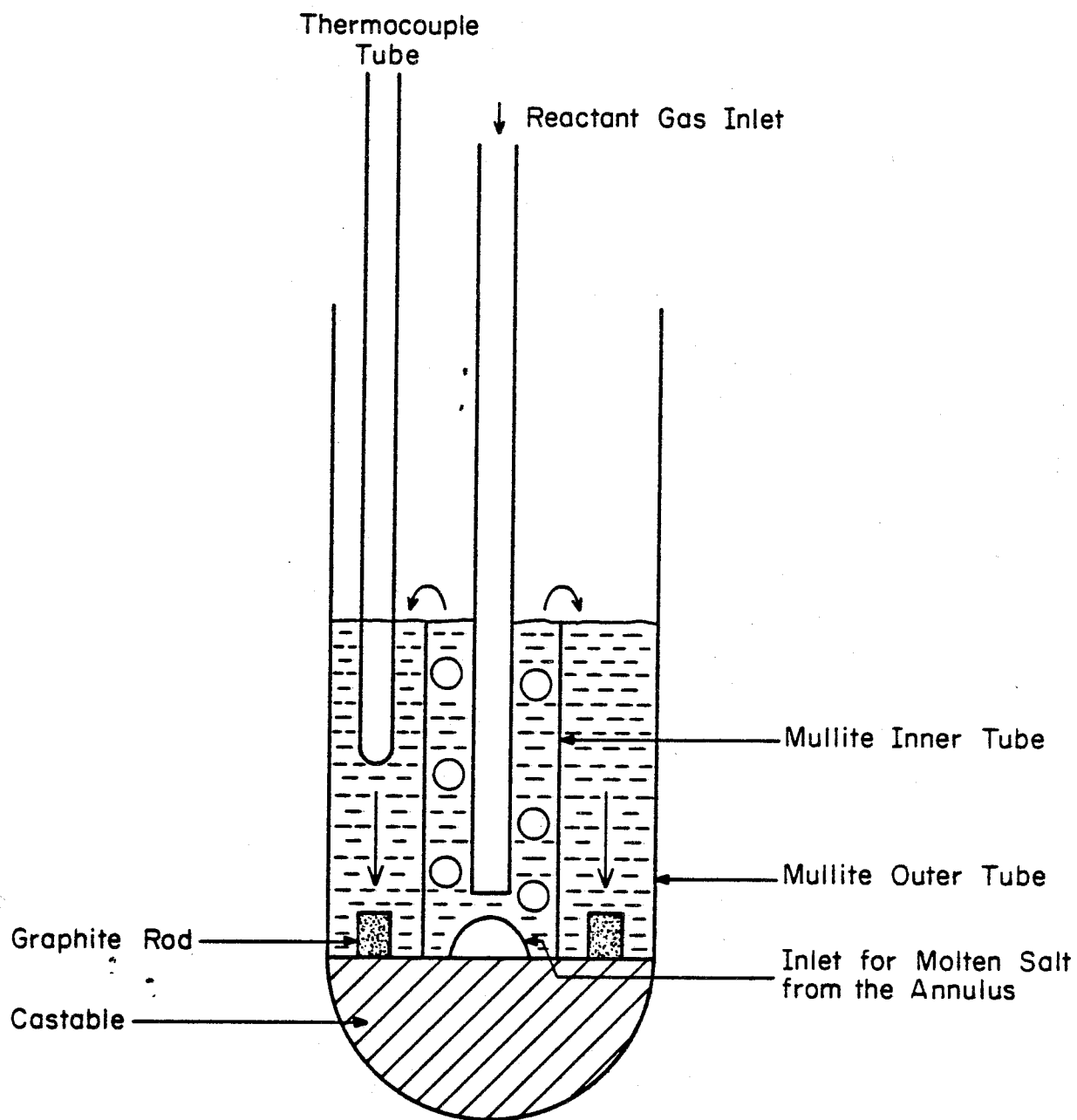


Figure 7. The reactor employed for measuring the reaction rate of the electrodes when prevented from direct contact with the gaseous reactant.

Table 6. Ambient Salt Height Levels in the Segregated Reactor

T(K)	AMBIENT SALT HEIGHT (cm) (Above Castolast Base)	AMBIENT SALT HEIGHT (cm) (Above Mullite Inner Tube)
973	10.6	3.0
1073	10.8	3.2
1173	10.9	3.3
1273	11.1	3.5

Reactor preparation employed an outer mullite tube for ultimate containment of the molten salt. Castolast G of Harbison-Walker Corporation was then used to anchor the electrodes and inner mullite tube. After curing, salt was added, the system was heated, and the experiments were conducted. The gas injection point in the central region was one inch above the castolast base.

The dimensions of the materials used and various reaction parameters are listed in Table 7. Here again the phosphate salt employed was the eutectic composition.

Upon cooling, system examination insured all features remained intact. This was necessary due to the extremely corrosive nature of molten sodium phosphate.

A similar reactor was used to measure the reaction rate of electrodes exposed directly to the gaseous oxidant. In this case the reactor consisted of carbon electrodes in a clean mullite crucible. The flowrate and oxygen partial pressure were the same as for the segregated reactor. Here the total exposed electrode surface area was 29.4 cm^2 . The reactor was heated to the various temperatures in pre-purified nitrogen. Oxygen was then introduced and the readings were taken.

3.5 Results and Discussion

Tables 8 and 9 contain the generated data for the two cases. It is noted that the scatter is considerable for the

Table 7. Dimensions of materials used in constructing the reactor and various dimensions of the constructed reactor. All dimensions of mullite materials are in inches.

I. DIMENSIONS OF MATERIALS	ID	x	OD	LENGTH
MULLITE OUTER TUBE	2"	x	2 1/4" x	9"
MULLITE INNER TUBE	13/16"	x	1" x	3 3/4"
MULLITE INJECTION TUBE	1/16"	x	1/4" x	18"
SPECTROSCOPIC CARBON RODS	1/4"	x	1/4" x	2"

II. REACTION PARAMETERS

EXPOSED CARBON SURFACE AREA	27.4 cm ²
EUTECTIC SODIUM PHOSPHATE SALT	484. grams
FLOWRATE	350 scc/min
OXIDANT	0.10 atm. O ₂
TOTAL PRESSURE	1.0 atm.

Table 8. Data for the segregated reaction.

T(K)	Rate (gc/cm ² /hr x 10 ⁶)
1030	42.0
1044	49.4
1057	86.3
1066	123.
1076	67.9
1093	142.
1110	77.1
1118	179.
1125	105.
1137	105.
1160	123.
1162	160.
1169	216.
1170	271.
1190	225.
1219	412.

Table 9. Data for the exposed reaction.

T(K)	Uncorrected Rate (gc/cm ² /hr)	Corrected Rate (gc/cm ² /hr)	Error (gc/cm ² hr)
967	0.0103	0.0119	0.0002
1023	0.0190	0.0253	0.007
1055	0.0240	0.0351	0.0012

segregated reaction due to the low conversions of the carbon. The predominant product for both cases was carbon dioxide with carbon monoxide accounting for less than 0.01% of the offgas.

For the segregated experiments, the flowrate was varied and this did not seem to influence the reaction rate beyond experimental error. This essentially varies the flow in the annular region by varying the gas hold-up in the central region hence changing the driving head for the flow.

For the exposed electrode experiments, conversions of oxygen were quite high. These were corrected assuming an order with respect to oxygen of unity (34) to the rate at zero conversion. The errors in Table 9 represent the estimated standard deviation of ten readings. The corrected data will be used in the analysis to follow. These reaction rates correspond to very low total carbon conversions. Total conversion of electrode carbon was kept well below 2% in all cases studied.

The results for the exposed and segregated cases are compared graphically in Figure 8. As is seen, the rate for the exposed case is three orders of magnitude above the segregated case. A least squares fit to an Arrhenius expression yielded for the segregated case:

$$R_{SU} = 6.5 \exp(-24000/RT) \text{ gC/cm}^2/\text{hr} \quad (19)$$

Similarly for the exposed case:

$$R_E = 5700 \exp(-25000/RT) \text{ gC/cm}^2/\text{hr} \quad (20)$$

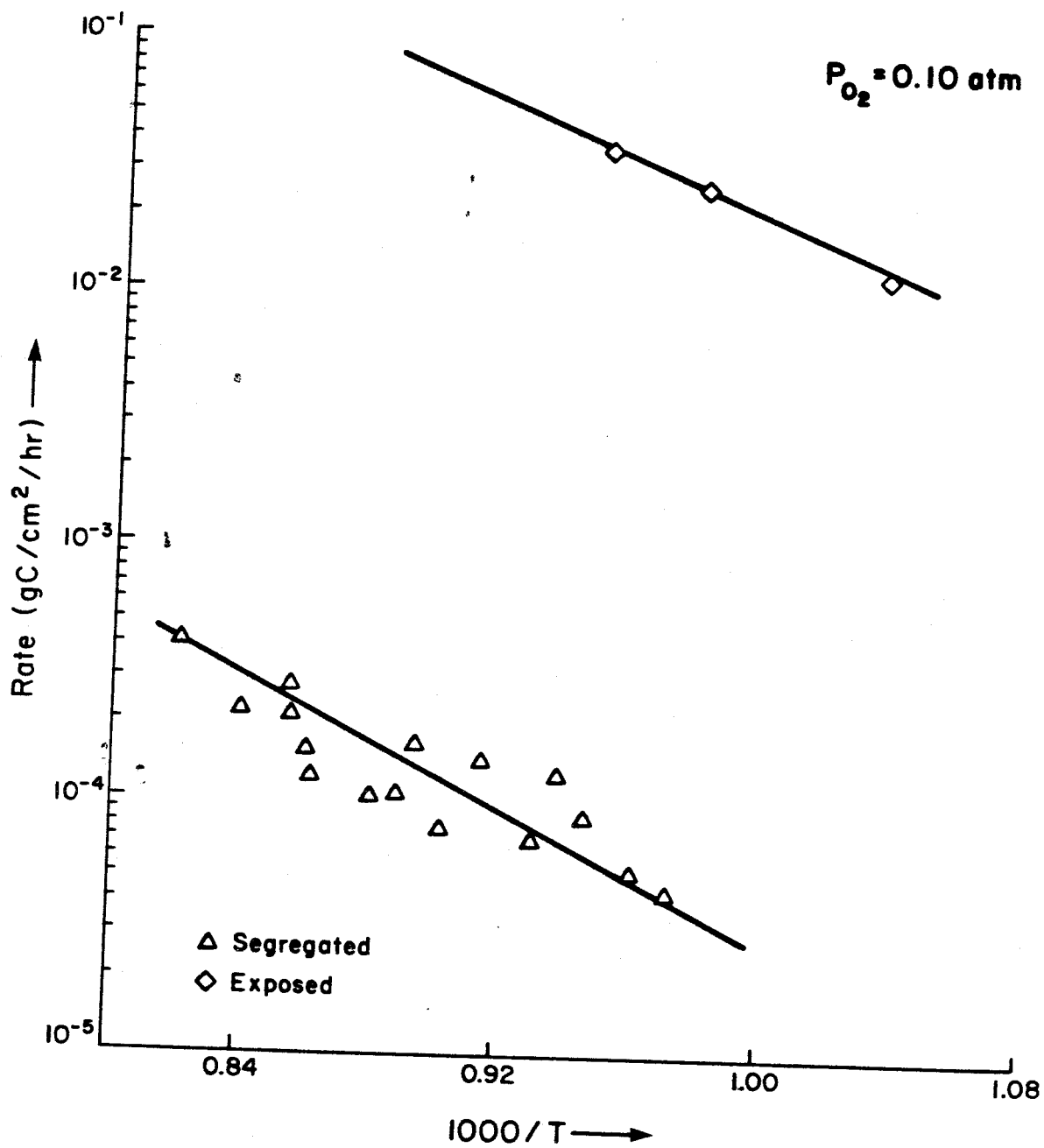


Figure 8. The Arrhenius plot for the reaction rate for the segregated and exposed cases.

The true activation energy for the pure carbon-oxygen reaction is closer to 60 kcal/gmole (35,36). As these activation energies are approximately $\frac{1}{2}$ the true activation energy, a transport limitation is the most likely cause.

Several other researchers have investigated the oxidation of spectroscopic carbon electrodes. The activation energy at low temperatures, generally less than 800 K, has been variously reported as from 30 to 60 kcal/gmole (37,38,39). At higher temperatures, the activation energy has been found to be lower. Kuchta et al (40) found activation energies from 20 to 25 kcal/gmole from 1273 to 1573 K. And Baetke (from Wicke) (38) found an activation energy of 28 kcal/gmole from 1173 to 1373 K. From this, it is quite reasonable to expect an activation energy of 25 kcal/gmole as is observed in the high temperature experiments presented here.

It is surprising that the rate expressions for the exposed and segregated cases yielded similar activation energies. The difference lies in the pre-exponential factor which contains concentration dependence and perhaps transport variables. If we assume dissolved oxygen to be responsible for the reaction in the segregated case and film diffusion control in both the segregated and exposed cases, we may postulate the rates to be of the form:

$$\text{Gas Film:} \quad R_E = k_{GFP} C_G \quad (21)$$

$$\text{Liquid Film:} \quad R_{SU} = k_{LFP}^{HC} C_G = k_{LFP} C_L \quad (22)$$

Experimentally it is found generally that the mass transfer coefficient is proportional to the square of the diffusivity. Assuming all other factors approximately the same, the ratio of the rates is:

$$\frac{R_E}{R_{SU}} = \frac{k_{GFP} C_G}{k_{LFP} C_L} \sim \left(\frac{D_G}{D_L}\right)^{\frac{1}{2}} \left(\frac{C_G}{C_L}\right) \quad (23)$$

C_L may be predicted by equation 13 with C_G from the ideal gas law. D_G is predicted as recommended by Perry and Chilton (41) with D_L given by equation 17 or 18 using viscosity data from Van Wazer (25). Table 10 presents the results, and as is seen, the ratio is roughly 1000 which is the observed ratio of the rates.

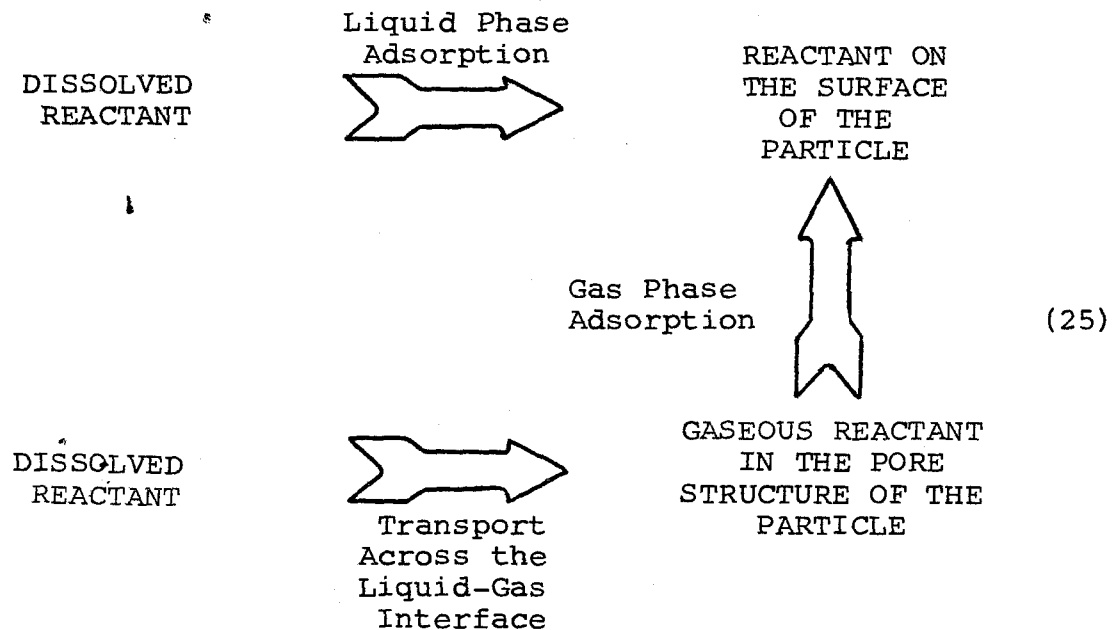
While numerically consistent, these results do not agree with the activation energies observed. The activation energy for film diffusion would likely be lower than that observed. It is more likely that the transport limitation is into the bulk of the carbon solid. Such effects may be readily shown (as for the case of a long, cylindrical pore) to give $\frac{1}{2}$ the true activation energy. This would then be consistent with the results presented here. The ratio of the rates in this case would be (if k_{RG} and k_{RL} are extended to include pore penetration):

$$\frac{R_E}{R_{SU}} = \left(\frac{C_G}{C_L}\right) \left(\frac{k_{RG}}{k_{RL}}\right) \sim 0(10) \times \left(\frac{k_{RG}}{k_{RL}}\right) \quad (24)$$

T(K)	C_L (10^{-6} moles/cm ³)	C_G (10^{-6} moles/cm ³)	D_G (cm ² /s)	D_C (10^{-5} cm ² /s)	D_W	$\frac{D_G}{D_C} \frac{1}{2} \frac{C_G}{C_L}$	$\frac{D_G}{D_W} \frac{1}{2} \frac{C_G}{C_L}$
973	0.4	12.5	0.06	0.06	0.2	10000	50000
1073	0.7	11.4	0.07	0.01	0.4	4000	2000
1173	1.0	10.4	0.08	0.2	0.7	2000	1000
1273	1.4	9.6	0.10	0.3	1.1	1000	1000

Table 10. Prediction of the ratio of the reaction rates for the exposed and segregated cases assuming film diffusion to be the rate controlling step. Oxygen solubility and diffusion coefficients are predicted using correlations developed or discussed in the text.

The relation, k_{RG}/k_{RL} , is difficult to obtain. Even if the salt had no catalytic effect, the rate of oxygen adsorption onto the carbon surface as well as the rate of oxygen absorption into the pore structure for the liquid case poses analytical problems. That is, here we will have two parallel mechanisms as the liquid cannot penetrate the pore structure of the carbon due to the large contact angle:



k_{RG} poses some problems. The rate of penetration by the reactant of the carbon's pore structure requires a detailed pore size distribution. Adsorption onto the surface of the

carbon may be computed by assuming a sticking factor multiplied by the collision rate of the molecules with the surface. For gases, kinetic theory may be used. For liquids, kinetic theory is less developed and accurate predictions are very difficult. However due to the mean free path being less in the liquid phase and pore penetration being slower in the liquid case due to the added resistance across the liquid-gas interface, we would expect k_{RL} to be less than k_{RG} . And while the magnitude of the difference cannot be predicted, we would expect these results to be in order with what was observed experimentally. Hence this result is seemingly better than the film diffusion model.

These order of magnitude calculations indicate that the cause of the reaction in the segregated case for molten phosphates may be roughly accounted for by dissolved oxygen. This is important as it would be expected that the rate of the indirect reaction in molten salts would necessarily have to be quite low due to the low solubility of nonpolar gases in the salt. Solubilities of polar molecules such as water have also been investigated as by Frame et al (42). Due to the dipole, a higher solubility is obtained as compared to the nonpolar molecules. However such strong interactions make the solubility process exothermic (as opposed to endothermic for the nonpolars) and solubility decreases with increasing temperature (43). Hence for a high temperature molten salt

gasification scheme with carbon reacting with steam or oxygen, it would apparently seem that the bulk of the reaction would have to proceed via the direct mechanism if the rate of reaction of the suspended particles was of the same order of magnitude as the reaction of the particles exposed directly to the gas. Such has been the case for the reaction of petroleum coke with steam in this laboratory (44).

3.6 Conclusions

1. The contact angle for the system molten phosphate-air-carbon is about 136° . With this large contact angle, it is probable that a significant amount of direct gas-particle contacting takes place in bubbling molten salt slurries.

2. The indirect mechanism is very slow in molten phosphates as compared to the reaction rate where the carbon is exposed directly to the gas.

3. Dissolved oxygen may be responsible for the indirect mechanism. As oxygen and nonpolar molecules have low solubilities in molten salts, the indirect mechanism in general should be much slower than the exposed reaction rate. With the conclusions above, we are then led to conclude that the direct mechanism may be dominant in the gasification of carbonaceous material in bubbling molten salt slurries.

NOTATION

- A_B = The single bubble surface area (cm^2)
 A_H = The hole area needed for one gas molecule (cm^2)
 A_P = The single particle surface area (cm^2)
 A_{PI} = The single particle surface area on the gas-liquid interface (cm^2)
 C_G = The gaseous reactant concentration in the bulk of the gas bubble (moles/cm^3)
 C_{GF} = The gaseous reactant concentration at the edge of the gas film around the particle (moles/cm^3)
 C_{GI} = The gaseous reactant concentration at the gas-liquid interface (moles/cm^3)
 C_L = The solvated reactant concentration in the bulk liquid (mole/cm^3)
 C_{LF} = The solvated reactant concentration at the edge of the particle liquid film (moles/cm^3)
 C_{LI} = The solvated reactant concentration at the gas-liquid interface (moles/cm^3)
 C_{PL} = The solvated reactant concentration near the particle's surface (moles/cm^3)
 C_{PG} = The gaseous reactant concentration near the particle's surface (moles/cm^3)
 D_C = The liquid phase diffusion coefficient from the Chang correlation (cm^2/s)
 D_G = The gas phase diffusion coefficient (cm^2/s)

- D_L = The liquid phase diffusion coefficient (cm^2/s)
 D_W = The liquid phase diffusion coefficient from the Wilke correlation (cm^2/s)
 f_G = The gas phase fugacity of the reactant (atm)
 f_L = The fugacity of the hypothetical liquid phase (atm)
 ΔG_1 = The free energy change for a process (kcal/gmole)
 H = The Henry's Law constant ($\text{moles}/\text{cm}^3 \text{ atm}$)
 ΔH = The heat of solution (kcal/gmole)
 k = The Boltzmann constant (ergs/K)
 K_C = The constant for the Chang correlation
 K_E = The Eotvos constant
 k_{GFP} = The mass transfer coefficient across the particle film to the particle surface (cm/hr)
 k_{GI} = The mass transfer coefficient from the bulk gas in the bubble to the gas-liquid interface (cm/hr)
 k_{GIF} = The mass transfer coefficient from the bulk gas in the bubble to the gaseous particle film (cm/hr)
 k_{LBF} = The mass transfer coefficient from the bulk liquid to the particle film (cm/hr)
 k_{LFP} = The mass transfer coefficient across the particle film to near the particle surface (cm/hr)
 k_{LIB} = The mass transfer coefficient from the gas-liquid interface to the liquid bulk (cm/hr)
 k_{RG} = The reaction rate at the particle surface in the gas phase (cm/hr)

- k_{RL} = The reaction rate at the particle's surface in the liquid phase (cm/hr)
- K_W = The constant for the Wilke correlation
- M_L = The molecular weight of the molten salt (g/gmole)
- N_A = The Avogadro's Number
- N_B = The number of bubbles
- N_{GFP} = The rate of mass transfer across the gaseous film of the particle (mole/hr)
- N_{GI} = The rate of mass transfer from the bulk gas of the bubble to the gas liquid interface (moles/hr)
- N_{GIF} = The rate of mass transfer from the bulk gas of the bubble to the gaseous particle film on the gas-liquid interface (moles/hr)
- N_{LBF} = The rate of mass transfer from the liquid bulk to the liquid film of the particle (moles/hr)
- N_{LFP} = The rate of mass transfer across the particle's liquid film (moles/hr)
- N_{LIB} = The rate of mass transfer from the gas liquid interface to the liquid bulk (moles/hr)
- n_p = The number density of particles ($\#/cm^3$)
- N_p = The total number of particles
- N_{PI} = The number of particles on the gas liquid interface
- P = The molecular parachor
- P_i = The atomic parachor
- r_B = The bubble radius (cm)

- r_p = The particle radius (cm)
 R = The gas constant (cal/mole K)
 R_c = The rate of particle bubble contacting (hr^{-1})
 R_{dir} = The rate of the direct reaction (moles/hr)
 R_E = Rate of reaction for the exposed case ($\text{moles/cm}^2 \text{ hr}$)
 R_{ind} = The rate of the indirect reaction (moles/hr)
 R_{RG} = The rate of chemical reaction on the particle's surface
in the gas phase (moles/hr)
 R_{RL} = The rate of chemical reaction on the particle's
surface in the liquid phase (moles/hr)
 R_{SU} = The rate of the segregated reaction ($\text{moles/cm}^2 \text{ hr}$)
 S = The solid-gas interfacial area created when a particle
penetrates a bubble (cm^2)
 T = The absolute temperature (K)
 T_c = The critical temperature (K)
 u_B = The bubble rise velocity (cm/hr)
 x_G = The mole fraction of the gas in the liquid phase
(moles/mole)
 V_s = The molar volume of the solute (cm^3/mole)
 W_{ad} = The work of adhesion (ergs)

Greek Letters

- ξ = The area correction factor = A_{PI}/A_P
 η = The correction factor for nonideal bubble-particle contacting
 γ = The surface tension of the liquid (dynes/cm)
 γ'_G = The activity coefficient of the solvated gas
 μ = The liquid viscosity (poise)
 ρ_L = The mass density of the salt (g/cm^3)
 σ = The hard sphere diameter (\AA)
 Σ = The degree of polymerization of the pseudo-monomer for the sodium phosphates
 τ_c = The average bubble residence time (hr)
 θ = The liquid phase contact angle with the solid

REFERENCES

1. Botts, W. V., Kohl, A. L., and Trilling, C. A., Proceedings of the 11th Intersociety Energy Conversion Conference, Vol. I, p. 280 (1976)
2. Gaudin, A. M., Flotation, McGraw-Hill, New York (1957)
3. Goto, S., and Smith, J. M., AIChE Journal, 24, 286 (1978)
4. Sutherland, K. L., J. Phys. Coll. Chem., 52, 394 (1948)
5. Chapter 2
6. Ranade, V. R., and Ulbrecht, J. J., AIChE Journal, 24, 796 (1978)
7. Prausnitz, J. M., and Shair, F. H., AIChE Journal, 7, 682 (1961)
8. Grimes, W. R., Smith, N. V., and Watson, G. M., J. Phys. Chem., 62, 862 (1958)
9. Watson, G. M., Evans, R. B., Grimes, W. R., and Smith, N. V., J. Chem. Eng. Data, 7, 285 (1962)
10. Blander, M., Grimes, W. R., Smith, N. V., and Watson, G.M., J. Phys. Chem., 63, 1164 (1959)
11. Malinauskas, A. P., and Richardson, D. M., Ind. Eng. Fund., 13, 242 (1974)
12. Hirschfelder, J. V., Curtiss, C. F., and Bird, R. B., Molecular Theory of Gases and Liquids, John Wiley and Sons, Inc., New York (1954)
13. Huheey, J. E., J. Chem. Educ., 45, 791 (1968)
14. Cleaver, B., and Mather, D. E., Trans. Far. Soc., 66, 2469 (1970)

15. Copeland, J. L., and Seibles, L., J. Phys. Chem., 70, 1871 (1966)
16. Copeland, J. L., and Radak, S., J. Phys. Chem., 71, 4360 (1967)
17. Copeland, J. L., and Zybko, W. C., J. Phys. Chem., 69, 3631 (1965)
18. Copeland, J. L., and Zybko, W. C., J. Phys. Chem., 70, 181 (1966)
19. Green, W. J., and Field, P. E., J. Phys. Chem., 84, 3111 (1980)
20. Field, P. E., and Green, W. J., J. Phys. Chem., 75, 821 (1971)
21. Desimoni, E., Paniccia, F., and Zamboni, P. G., Electro. Anal. Chem., 38, 373 (1972)
22. Shenke, M., Broers, G. H. J., and Ketelaar, J. A. A., J. Electrochem. Soc., 113, 404 (1966)
23. Ward, A. T., and Janz, G. J., Electrochim. Acta., 10, 849 (1965)
24. Janz, G. J., Molten Salts Handbook, Academic Press, New York (1967)
25. Van Wazer, J. R., Phosphorus and Its Compounds, Volume I, Interscience Publishers, Inc., New York (1958)
26. Adam, N. K., The Physics and Chemistry of Surfaces, Dover Publications, New York (1968)
27. Kirshenbaum, A. D., Cahill, J. A., McGonigal, P. J., and Grosse, A. V., J. Inorg. Nucl. Chem., 24, 1287 (1962)

28. Carlson, C. M., Eyring, H., and Ree, T., Proc. Nat. Sci. (USA), 46, 333 (1960)
29. Li, J. C. M., and Chang, P., J. Chem. Phys., 23, 518 (1955)
30. Wilke, C. R., and Chang, P., AIChE Journal, 1, 264 (1955)
31. Sano, N., Honma, S., and Matsushita, Y., Met. Trans., 1, 301 (1970)
32. Metals Reference Book, (C.J. Smithells, Ed.), 5th Edition, Butterworths, London (1976)
33. Nevers, N. D., AIChE Journal, 14, 222 (1968)
34. Walker, P. L., Shelef, M., and Anderson, R. A., Chemistry and Physics of Carbon, 4, 287 (1968)
35. Thomas, J. M., Chemistry and Physics of Carbon, 1, 121, (1966)
36. Rakszawski, J. F., and Parker, W. E., Carbon, 2, 53 (1964)
37. Gulbranson, E. A., and Andrew, K. F., Ind. Eng. Chem., 44, 1034 (1952)
38. Wicke, E., 5th Symposium on Combustion, p. 245, Reinhold, New York (1955)
39. Rossberg, M., Z. Electrochem., 60, 952 (1956)
40. Kuchta, J. M., Kant, A., and Damon, G. H., Ind. Eng. Chem., 44, 1559 (1952)
41. Chemical Engineers Handbook, 5th Edition, (R. H. Perry and C. H. Chilton, Eds.), McGraw-Hill, New York (1973)

42. Frame, J. P., Rhodes, E., and Ubbelohde, A. R., *Trans. Far. Soc.*, 57, 1075 (1961)
43. Field, P. E., and Shaffer, J. H., *J. Phys. Chem.*, 71, 3218 (1967)
44. Chapter 4

CHAPTER 4

THE GASIFICATION OF PETROLEUM COKE
IN MOLTEN SODIUM PHOSPHATES

4.1 Introduction

Molten salts can prove to be an attractive medium for the cracking and gasification of heavy oils. The advantage of a liquid reaction medium is apparent as this would disallow plugging by coke which is a grave problem for fixed, entrained, and fluidized bed gasification. In general such a gasification process would entail hydrocarbons either directly gasifying or degrading to coke. Hence it is very proper to investigate the reaction of petroleum coke in such systems.

Petroleum coke is a loosely structured carbon. Commercially two processes are used to produce coke--delayed and fluid coking. Delayed coking fills a barrel with accumulated coke at approximately 800 K and is semi-continuous whereas fluid coking entails the continuous circulation of seed coke particles (1). Upon heating to less than 2000 K, the coke may be envisaged as in a pregraphitization regime (2). Here as the temperature is increased, devolatilization occurs and cleaning up of the disordered structure ensues. If at the same time, the particle is being gasified, there is a competition between these two rate processes. It is this competition which would dictate what would occur in a real system.

Walker et al (3) have reviewed the effect of heat treatment to high temperatures of petroleum coke on the reactivity to oxygen. Reported here was that delayed coke heated to 2900 K was less reactive to oxidation than the same coke treated to

1400 K (4). Thus reorganization in this case decreased reactivity. The general case reveals that heat treatment of carbons may increase or decrease reactivity dependent upon the crystalline orientation of any graphitic basal planes present and of course upon total crystallinity. Orientation is important as the rate of oxidation parallel to the basal plane has been shown to be faster than perpendicular to these planes (5,6). Consequently the reactivity to gases of cokes is dependent upon the orientation of existing basal planes to exposed surfaces. The tendency of delayed cokes to orient basal planes parallel and perpendicular to exposed faces has been investigated by Walker et al (7).

Petroleum coke produced during a molten salt gasification process would be expected to be strictly pregraphitic due to the relatively low temperatures employed (<1300 K). Coke will most likely be formed on the surface of reactant gas bubbles and from thence be transferred to the bulk of the liquid. At this point we then have a bubble column slurry reactor where petroleum coke particles are gasified by the direct mechanism (where the particle penetrates the bubble and comes into direct contact with the gas in the bubble) or the indirect mechanism (where the particle reacts in the bulk liquid with the dissolved reactant). Due to the large carbon-molten sodium phosphate contact angle of 136° and the low solubilities of gases in the melt (8), it is reasonable to

assume that the rate of the direct mechanism should be significant. Hence this work is directed to measuring the rate of the direct mechanism in molten sodium phosphate.

The reaction rate of pure carbon with steam has been shown rather conclusively to be (9,10,11):

$$R_{pc} = \frac{k_1 C_{H_2O}}{1 + k_2 C_{H_2O} + k_3 C_{H_2}} \quad (1)$$

C_i is the gas phase molar concentration of species i . k_1 is proportional to the rate of water adsorption onto the carbon with k_2 and k_3 being related constants. This type of rate expression is clearly indicative of a competition between hydrogen and water adsorption onto the active sites of the carbon surface. The activation energy of this reaction is about 80 kcal/gmole (3).

Impurities generally aid in the gasification of carbon. Metallics have been shown to lower the ignition temperature substantially in many cases (12,13,14,15). These catalysts have been shown to be mobile during the course of the reaction and to channel in the basal plane of the carbon (16,17,18). Salts have also been widely studied as to their effect upon gasification reactions. The most actively studied have been the carbonates which are active for the catalytic reduction of CO_2 , H_2O , and O_2 (19,20,21) over carbon. Phosphates have been shown not to be active catalysts in lowering ignition

temperatures of carbons in oxygen (22,23,24). In fact in many cases phosphorus compounds have been shown to inhibit gasification (25,26) or to poison the catalytic effect of active compounds (27). McKee (28) has studied the effect of POCl_3 on graphite oxidation and found it to be strongly adsorbed onto dislocations and on the edges of etch pits in the basal plane. It was also found to strongly inhibit etch pit formation.

These results do not rule out catalytic activity of phosphates as the type of carbon, the phosphate compound, the reactant gas, and the reaction temperature can yield different results. Indeed for a cellulose char, ferric phosphate has been shown to lower the ignition temperature slightly (29). And in molten phosphates, Dugan and Higgins (30) reported a catalytic effect of the salt on carbon gasification. Hedden and Wicke (31) have also shown POCl_3 in low concentrations to catalyze CO_2 gasification of spectroscopic carbon while inhibiting gasification at higher concentrations as contrasted to inhibition for all concentrations for a pure natural graphite.

For carbon gasification in molten sodium phosphate, a contact angle of 136° precludes liquid penetration into the particle pore structure at conventional pressures. Consequently any catalytic effect of the molten salt must take place on the external surface of the particle. This effect is further limited to the area where the particle is in contact with the

molten media. Hence the catalytic effect in such cases as that investigated here is expected to be quite limited.

Here we will proceed to give the properties of the petroleum coke selected for study. Measurements of the reactivity of this coke with steam will then be reported for a variety of reaction configurations. The reactivity will be reported in the absence of salt and in a slurry reactor. The reaction rate in a configuration which imitates the direct mechanism will also be reported.

4.2 Properties of Green Sponge Petroleum Coke

The petroleum coke selected for study was a green sponge coke from Union Oil Corporation. These amorphous cokes are produced by delayed coking of heavy oils or bottoms with low aromaticity. The composition as well as the size distribution of the unclassified sample are given in Table 1. The external surface area was calculated from a coarse and fine size distribution assuming spherical particles. From the two distributions, this external surface area may be estimated to be no more than $0.1 \text{ m}^2/\text{g}$ for this unclassified sample. A -200 mesh sample was also investigated. The external surface area of these smaller particles is similarly calculated to be about 25% greater than for the unclassified sample or approximately $0.13 \text{ m}^2/\text{g}$.

Table 1. The composition and particle size distribution of the unclassified petroleum coke sample. Total external surface areas are based on one gram of the sample.

ELEMENTAL COMPOSITION		COARSE SIZE DISTRIBUTION		
Component	Weight %	$\bar{d}_p (\mu)$	Weight %	Area (cm ²)
Carbon	91.5	>589	0.9	0.4
Hydrogen	4.2	357	12.2	9.1
Nitrogen	2.7	100	17.5	46.7
Sulfur	0.7	37	69.4	500.2
Oxygen or Ash	0.9			
TOTAL	100.0 %	TOTAL	100.0 %	556.4 cm ²
Volatile Matter	13.9 %			
FINE SIZE DISTRIBUTION				
$\bar{d}_p (\mu)$	Weight %	Area (cm ²)	Σ Area (cm ²)	
>589	0.9	0.4	0.4	
472	1.7	1.0	1.4	
302	2.0	1.8	3.2	
215	3.7	4.6	7.8	
152	4.8	8.4	16.2	
114	4.5	10.5	26.7	
97	4.5	12.4	39.1	
82	8.5	27.6	66.7	
68	2.6	10.2	76.9	
53	24.4	122.8	199.7	
22	42.4	526.0	725.7	

To further characterize the sample, the specific nitrogen BET surface area and specific porosity were measured and are given in Table 2 for the two samples. Porosity here corresponds to the volume of liquid nitrogen adsorbed by the sample at a relative nitrogen pressure of 0.963 at 77 K. This would correspond to an equivalent pore radius of 271 Å. In all calculations presented here the pores are assumed to be cylindrical with the equilibrium pressure of the condensed liquid nitrogen in the pores being given by the Kelvin equation (32).

As is seen, the specific BET area of the -200 mesh sample is 24% greater than the unclassified sample. This increase cannot be accounted for by the increase in external surface area. Thus the smaller particles must have a greater amount of specific internal pore surface area. Also by comparing the results of the size distributions given in Table 1, the external surface area is seen to constitute at most approximately six percent of the total BET surface area for the unclassified coke. If it is now assumed that all BET surface area corresponds to pore surface area, the average pore diameter may be calculated from the ratio of porosity to surface area. These calculations are given in Table 2 where it is seen that the average pore diameter is smaller for the -200 mesh sample.

It is very important to acknowledge two shortcomings in the above calculations. First of all, the external surface area calculations assumed spherical particles. Surface

Table 2. Nitrogen BET surface area and total porosity for the petroleum coke. Porosity is for pore radii less than 271 Å. The average pore diameter is calculated by assuming cylindrical pores.

Sample	Surface Area (m ² /g)	Porosity (10 ⁻³ cm ³ /g)	Average Pore Diameter (Å)
Unclassified	1.30 ± 0.02	3.09 ± 0.03	97
-200 Mesh	1.61 ± 0.01	3.28 ± 0.04	82

roughness as well as odd particle shapes would increase the external surface area somewhat. Secondly it is realized that a great deal of macropore volume ($>271\text{\AA}$) exists in petroleum cokes as reported by Walker et al (7) using mercury porosometry. However such large pores would be expected to contribute little to total surface area due to their relatively low surface/volume ratios. Hence the average pore diameter reported here is to be taken as nothing more than a relationship between microporosity and total surface area. It will be taken to be indicative of average pore size, although this indication could be obscured or obviated by the two effects described above or by the assumption of cylindrical pores.

Adsorption and desorption isotherms for the unclassified petroleum coke sample are given in Figure 1. Here desorption was from a relative pressure of 0.963 corresponding to an equivalent pore radius of 271\AA . As is seen a severe hysteresis effect was noted down to very low relative pressures. If this is assumed to be governed by the inkbottle hypothesis of McBain (33,34), it is in order for petroleum coke to exhibit such a severe hysteresis effect. Petroleum coke is formed by the condensation of hydrocarbons into a carbonaceous solid. Some devolatilization takes place leaving voids in the initial solid. These volatiles may recondense plugging the pore's exit. Petroleum vapor may also penetrate these voids or pores. But due to transport limitations into the pore structure,

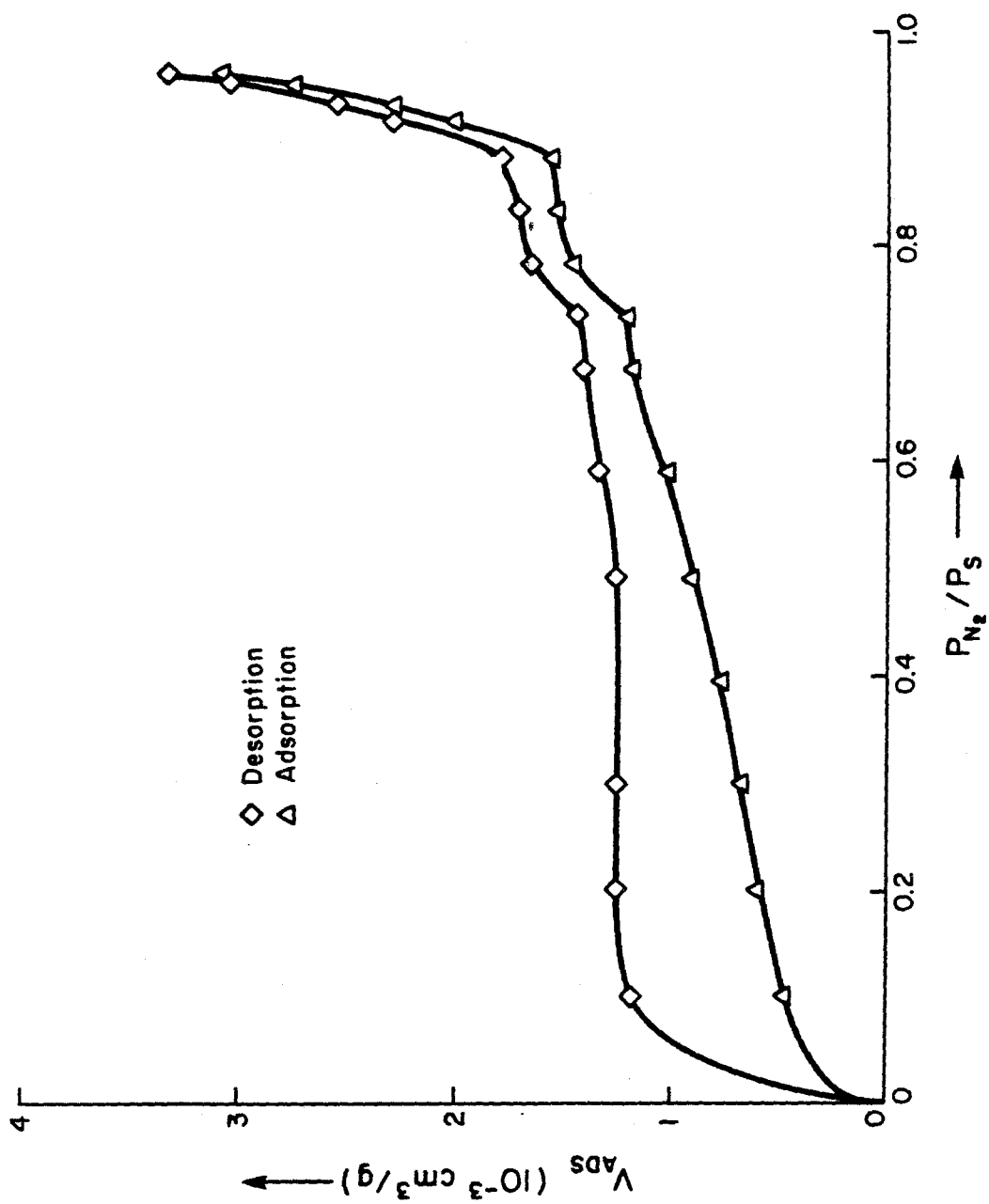


Figure 1. The adsorption and desorption isotherms for the unclassified petroleum coke sample. Desorption is from a relative nitrogen pressure of 0.963.

relatively more hydrocarbon condensation would take place near the external surface of the particle. These plugging effects on the pores would leave relatively wider voids on the interior connected to the exterior of the particle by narrower voids. Hence the petroleum coke pore structure would be expected to resemble in some respects a series of inkbottle pores.

Figure 2 presents the pore volume distributions obtained from the adsorption and desorption isotherms. Both are presented due to the extreme hysteresis effect. Both isotherms yielded peaks at 44 and 106 Å. The adsorption isotherm seemed to indicate an additional peak at 18 Å. This additional peak is however quite close to the limit of applicability of the Kelvin equation. Table 3 presents the estimate of the pore surface areas for the two cases. As is seen the adsorption isotherm distribution more closely matches the total surface area as attained by BET measurements. This is due to the additional peak for the adsorption case.

Hence the petroleum coke selected for study is shown to be a high volatile content material with low porosity and quite low surface area. The coke's makeup is largely carbon with hydrogen, nitrogen, and sulfur impurities.

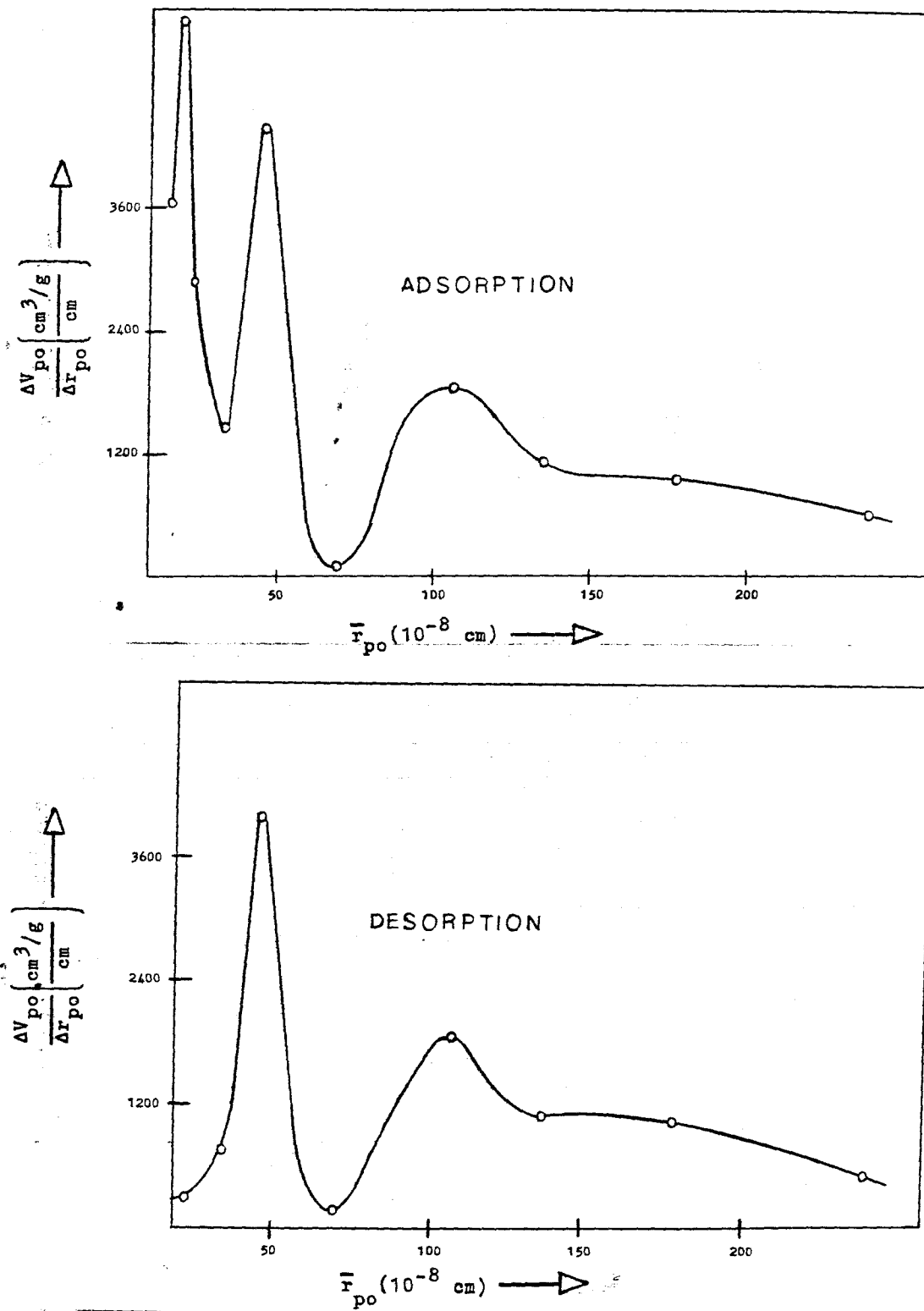


Figure 2. The pore volume distributions from the adsorption and desorption isotherms for the unclassified sample.

Table 3. Pore surface areas for the adsorption and desorption isotherms assuming cylindrical pores.

	ADSORPTION ISOTHERM		DESORPTION ISOTHERM	
$\bar{r}_{po} (\text{\AA})$	$\frac{\Delta V_{po}}{\Delta r_{po}} (\text{cm}^2/\text{g})$	Area (m^2/g)	$\frac{\Delta V_{po}}{\Delta r_{po}} (\text{cm}^2/\text{g})$	Area (m^2/g)
239	597	0.03	509	0.03
177	944	0.06	1040	0.07
135	1110	0.04	1090	0.04
106	1840	0.12	1850	0.12
68.9	112	0.01	179	0.02
44.4	4400	0.18	3980	0.16
32.7	1440	0.13	760	0.07
22.8	2880	0.13		
20.9			294	0.03
18.3	5420	0.22		
14.9	3640	0.14		
TOTAL		1.06 m^2/g		0.54 m^2/g

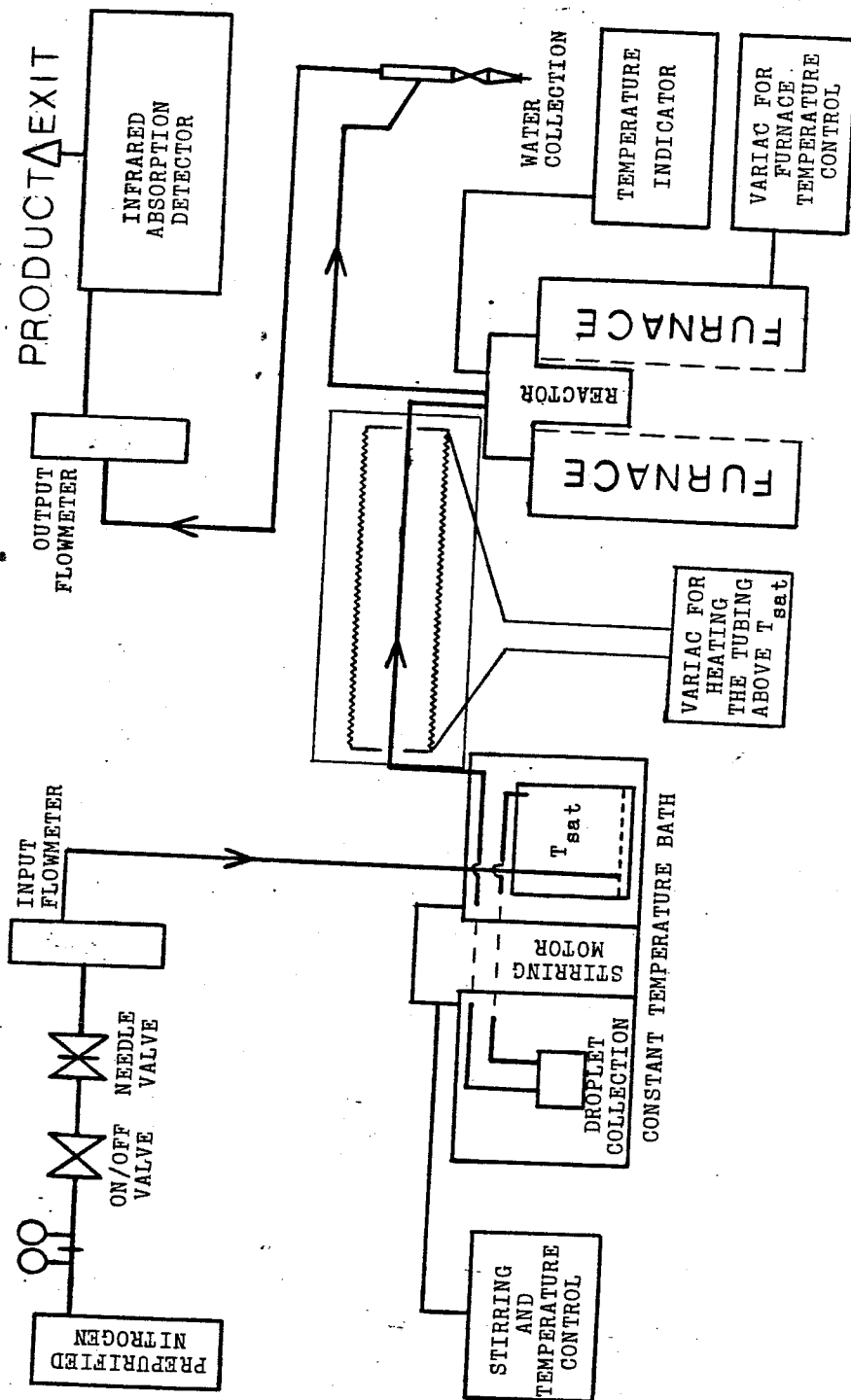
4.3 Experimental

Experiments consisted of exposing petroleum coke particles to various concentrations of water vapor in nitrogen. The experimental system is outlined in Figure 3. Prepurified nitrogen was saturated with water corresponding to the temperature of the constant temperature bath. This gas was then passed through the reactor, excess water was condensed by air cooling and collected, and the offgas was monitored by infrared adsorption for CO and CO₂.

To saturate the nitrogen, the gas was passed through a fritted glass filter with the resulting bubbles passing through an isothermal column of distilled water. Saturation was assured as the characteristic time for diffusion using the bubble radii was short compared to bubble residence time. As convection of the gas inside the bubble assists this saturation process, it may be safely assumed that complete saturation took place. Monitoring collected water also indicated complete saturation.

The gas passing out of the constant temperature bath was then heated to above 150°C assuring no condensation in the tubing leading to the reactor. Flow control through the system was provided by pressure regulation of the nitrogen source and a needle valve located prior to input flow monitoring.

Figure 3. The experimental apparatus for measuring the reaction rate of petroleum coke with steam.



Two types of reactors were constructed to conform to the objectives outlined in Figure 4. Reactor I is the nonbubbling reactor and is depicted in Figure 5. This reactor is used in two cases. For the no salt case, the reacting particles rested on the mullite. This corresponds to the measuring of the base reaction rate, ie, with no possible salt effect. The situation shown in Figure 5 corresponds to the situation after salt has been added to the reactor. Particles rest on the surface of the salt and react with gas passed over this surface. This is directly analogous to a particle lying on the gas-liquid interface of a bubble. Convection currents in the bubble are set up by induced drag on the gas at the interface. Such currents effectively pass the reactant gas over the restive particle. Hence this situation corresponds to the particles reacting by the direct mechanism.

Reactor II is the bubbling reactor and is depicted in Figure 6. This is the more conventional case where reactant gas bubbles are passed through a carbon particle-molten salt slurry.

The dimensions of materials used in these reactors are given in Table 4. These materials were anchored and the reactor was sealed using Castolast G of Harbison-Walker Corporation. It is noted that the salt did not come into direct contact at any time with the castable. Contact with the liquid salt was limited to the fused mullite parts of the respective reactors.

Figure 4. The experimental objectives of Reactors I and II.

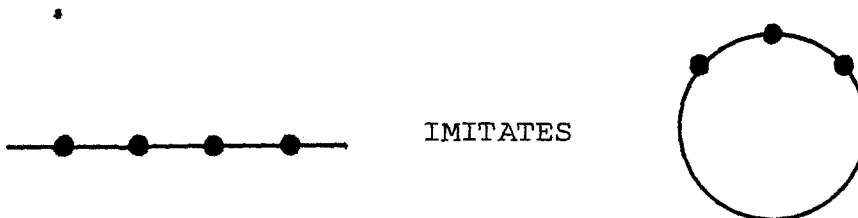
REACTOR I: NO SALT CASE

-TO MEASURE THE REACTION RATE OF COKE PARTICLES IN THE ABSENCE OF SALT. A BASE CASE IS THUS ESTABLISHED TO WHICH THE SALT EFFECT MAY BE COMPARED.

SALT CASE

-TO MEASURE THE REACTION RATE OF COKE PARTICLES ON THE REACTANT GAS-MOLTEN SALT INTERFACE.

-THIS IMITATES THE DIRECT REACTION MECHANISM.



REACTOR II: MOLTEN SALT SLURRY REACTOR

-TO MEASURE THE REACTION RATE OF COKE PARTICLES IN A SLURRY REACTOR.

-THE DIRECT AND INDIRECT MECHANISMS ARE BOTH POSSIBLE.

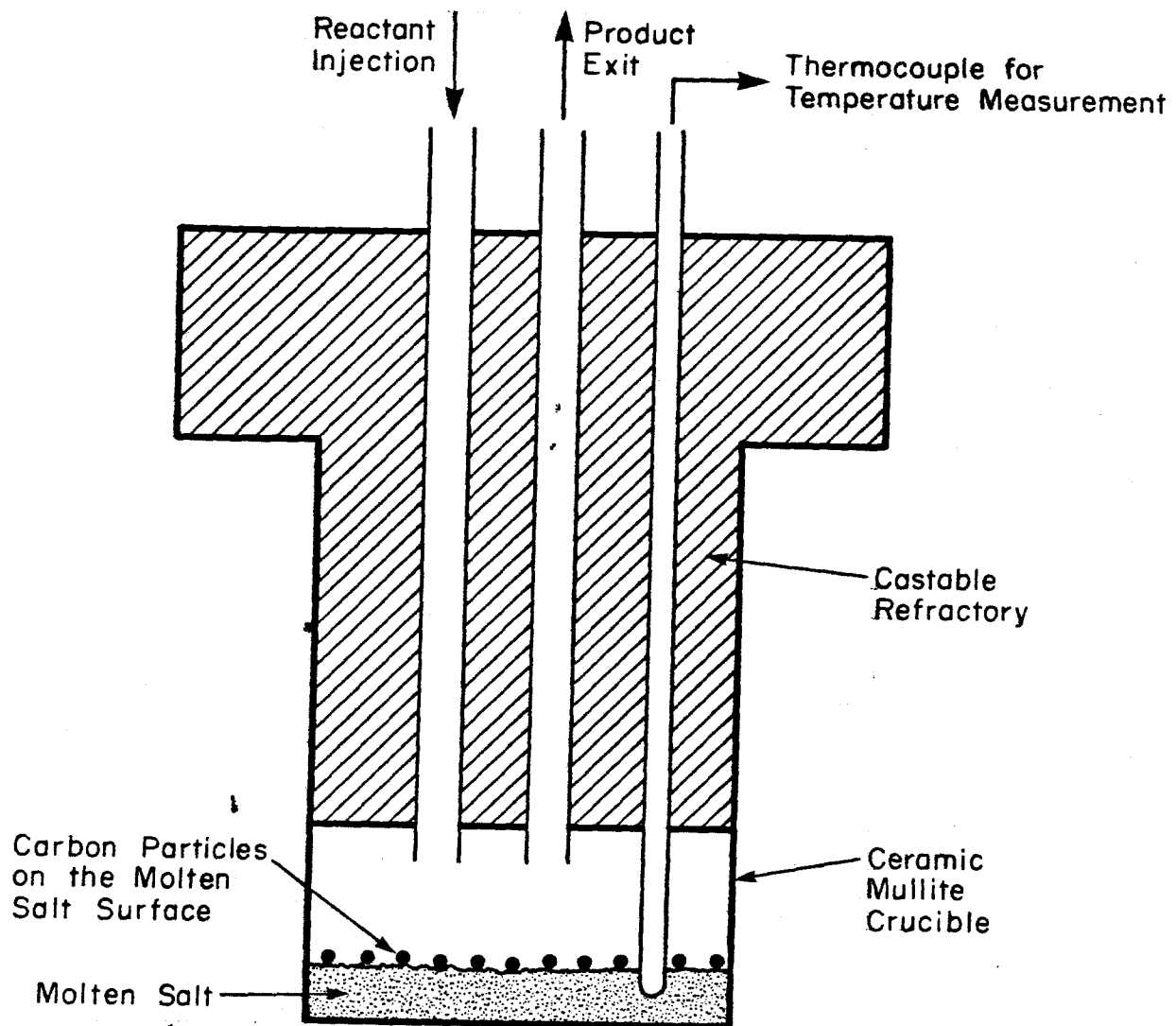
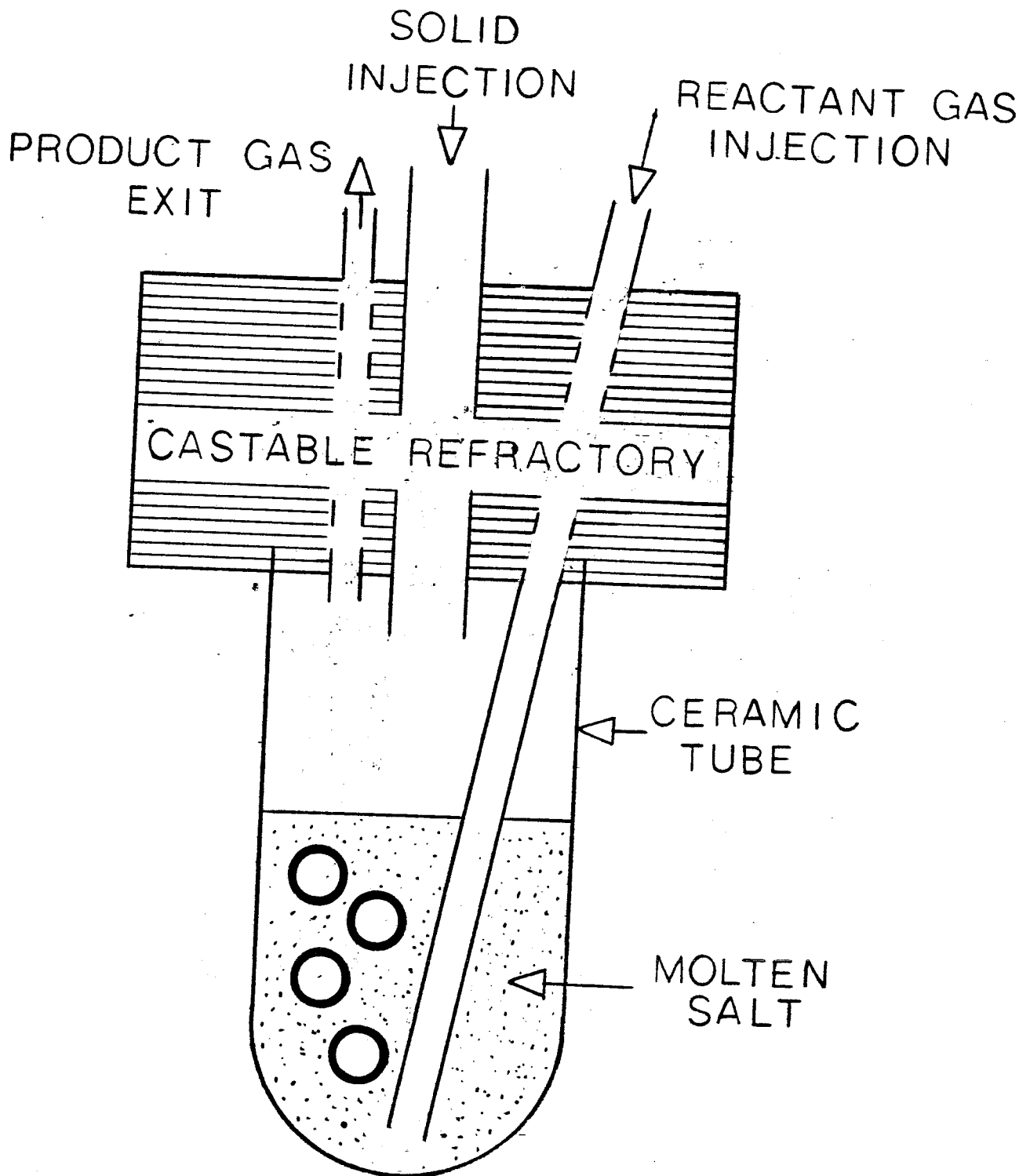


Figure 5. Reactor I. This reactor was used in two modes. In one case there was no salt in the vessel. In the second case which is pictured there was salt in the bottom of the vessel. For clarity the solid injection tube is not shown.



BUBBLING REACTOR

Figure 6. Reactor II. For clarity, the thermocouple tube is not shown.

Table 4. Dimensions of materials used in constructing the reactors and various dimensions of the constructed reactors. All dimensions of mullite materials are in inches.

	ID	x	OD	x	LENGTH
REACTOR I: THERMOCOUPLE TUBE	3/16"	x	1/4"	x	18"
REACTANT INJECTION TUBE	3/16"	x	1/2"	x	18"
PRODUCT EXIT TUBE	3/16"	x	1/2"	x	18"
CERAMIC MULLITE CRUCIBLE	2"	x	2 1/4"	x	9"
SOLID INJECTION TUBE	7/8"	x	1"	x	12"
REACTOR FREE VOLUME	75 cm ³				
	ID	x	OD	x	LENGTH
REACTOR II: THERMOCOUPLE TUBE	3/16"	x	1/4"	x	18"
REACTANT INJECTION TUBE	3/16"	x	1/2"	x	18"
PRODUCT EXIT TUBE	1/4"	x	3/8"	x	18"
CERAMIC MULLITE CRUCIBLE	2"	x	2 1/4"	x	9"
SOLID INJECTION TUBE	7/8"	x	1"	x	10"
REACTANT TUBE BUBBLE INJECTION POINT (ABOVE THE INSIDE BASE OF THE CERAMIC MULLITE CRUCIBLE)	3/8"				
REACTANT TUBE INCLINATION (FROM VERTICAL)	4.2°				
REACTOR FREE VOLUME	320 cm ³				

An experiment consisted of opening either reactor for solid particle injection, reducing reactant gas flow to less than one-sixth of operational flow, and adding the particles. Upon sealing, total reactant gas flow was resumed. The response time of the infrared detector was recorded and constituted time zero for the reaction. Subsequent readings were taken at equally spaced time intervals. Simpson's discrete rule was used to integrate the total amount of carbon passing out of the system in the form of CO_x . With the room temperature and flowrate, these readings were converted to grams of carbon using the ideal gas law. Carbon balances on comparing the Simpson's rule total carbon with the measured initial charge ranged from 70 to 90%. The balance of the carbon evolved as hydrocarbons or was caught on the relatively cold walls of the solid injection tube. At the flowrate selected, fines entrainment was not noted as the water collected from the offgas was clear. This situation was in direct contrast to high flowrates where substantial carbon particle content was noted in the condensed water for the no salt case for Reactor I.

The reaction rate was then divided by the Simpson's rule integrated carbon mass, and a specific rate was obtained. This method eliminates any dependence on the flowrate and it should also limit absolute errors in the infrared adsorption cell sensitivity. This does not however account for total carbon in the rate. It does account for total reacted carbon.

Chargings of petroleum coke were kept below 5 mg. per experiment. The petroleum coke used has a tendency to agglomerate, and chargings of greater than 5 mg. produced a marked degradation of the rate due to this agglomeration. Due to the small amount charged, a degree of error was introduced as these low weights were close to the detection limit of the balance used (± 0.1 mg.). Hence this is another possible explanation for the carbon balance fluctuation indicated above.

Table 5 includes the relevant reactor parameters. The flowrate was selected as the maximum where fines entrainment was not noted. Reducing the flowrate by a factor of two from this did not influence the reaction rate beyond experimental error. Ambient molten salt heights are calculated from the density data of Van Wazer (35).

Temperature control for the reactor was provided by the variac for the furnace. A voltage setting was selected, and experiments were conducted after temperature readings became steady with time. Temperatures were measured by a 1/16" diameter inconel sheathed thermocouple housed in the mullite thermocouple tube indicated in Table 4. This mullite tube prevented the salt from attacking the inconel sheath. The temperature was monitored at the exact location where the reaction was taking place for Reactor I. Hence there is no trouble with temperature gradients in this case. For

Table 5. Reaction parameters for Reactors I and II.

<u>REACTOR I:</u>	NITROGEN FLOWRATE	180 scc/min
	SODIUM PHOSPHATE SALT	10 grams (Dry Basis)*
	SALT COMPOSITION	$\text{Na}_2\text{O}/\text{P}_2\text{O}_5 = 1.31$
<u>REACTOR II:</u>	NITROGEN FLOWRATE	180 scc/min
	SODIUM PHOSPHATE SALT	220 grams (Dry Basis)*
	-SALT COMPOSITION	$\text{Na}_2\text{O}/\text{P}_2\text{O}_5 = 1.31$
	-SALT COMPOSITION	$\text{Na}_2\text{O}/\text{P}_2\text{O}_5 = 1.60$

THE AMBIENT SALT HEIGHT ABOVE THE INSIDE BASE OF THE MULLITE CRUCIBLE AND *THE AMBIENT SALT HEIGHT ABOVE THE POINT OF BUBBLE INJECTION. (THE CASE WITH NO GAS FLOW THROUGH THE REACTOR)

T(K)	$\text{Na}_2\text{O}/\text{P}_2\text{O}_5 = 1.31$		$\text{Na}_2\text{O}/\text{P}_2\text{O}_5 = 1.60$	
	MOLTEN SALT HEIGHT ABOVE BASE (cm)	HEIGHT ABOVE BUBBLE INJECTION (cm)	MOLTEN SALT HEIGHT ABOVE BASE (cm)	HEIGHT ABOVE BUBBLE INJECTION (cm)
1100	5.93	4.98	5.89	4.94
1200	6.03	5.08	5.96	5.01
1300	6.10	5.15	6.03	5.08

*The salt weight is for the dehydrated salt.

Reactor II, the temperature of the molten salt bath was measured and assumed to be isothermal by agitation.

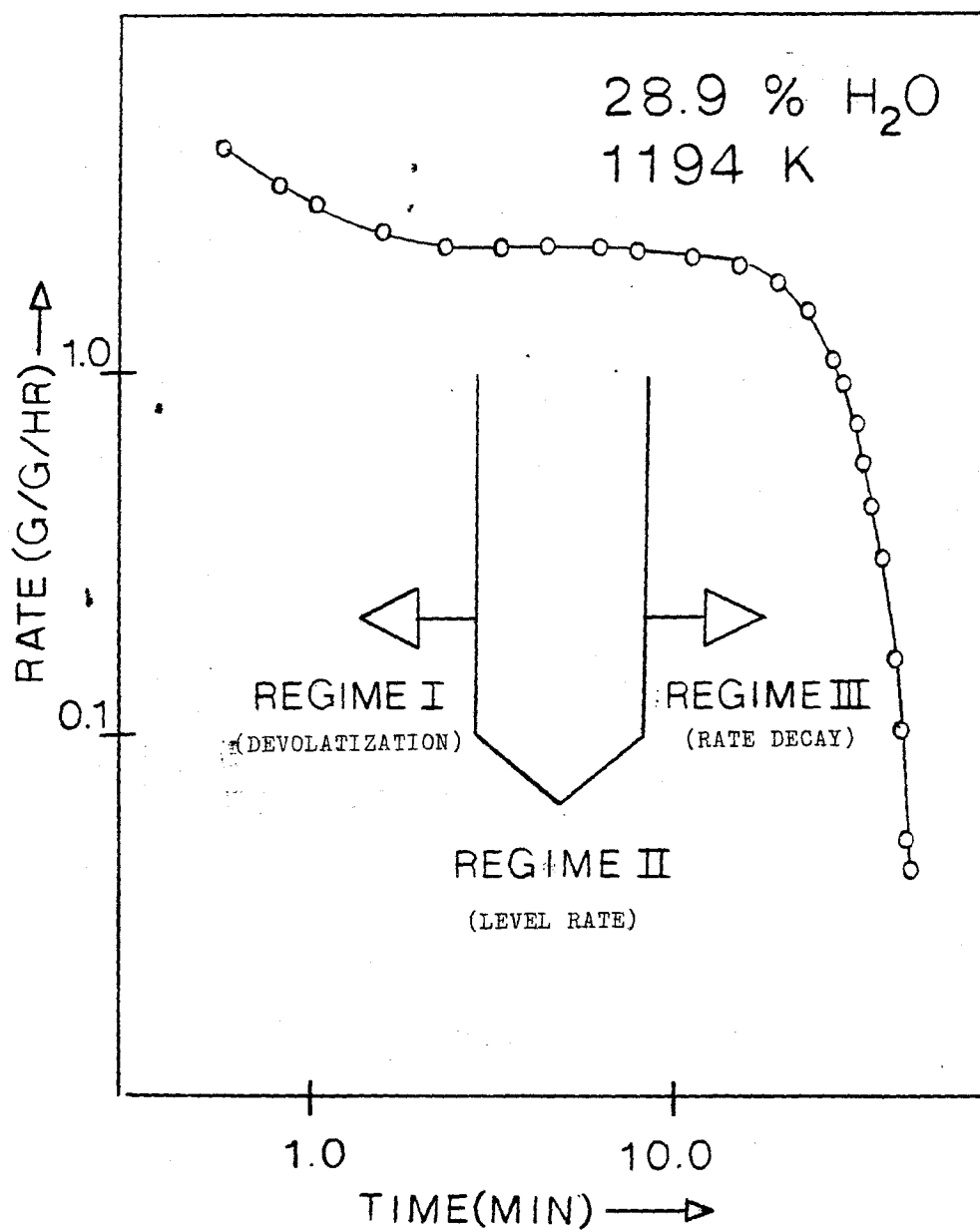
A final note is appropriate on the carbon balances and solid injection. Some carbon is assumed to be collected on the injection tube during the carbon charging and hence is not accounted for in the integrated carbon mass total as noted earlier. This was thought initially to have an effect on the tail end of the carbon conversion curve as it would essentially place carbon in a region where it was less reactive. Thus experiments were conducted with a removable injection tube to monitor this effect. No difference was detectable between these removable injection tube experiments and the experiments with a fixed solid injection tube on the tail end conversion of the carbon. Consequently any carbon which collects on the sides of the solid injection tube may be assumed nonreactive.

4.4 Results and Discussion

The bulk of this study deals with the reactivity of the unclassified petroleum coke sample with size distribution as given in Table 1. The particle size effect will be dealt with later in this section.

A typical reaction rate vs. time curve is shown in Figure 7 for the unclassified coke. This reaction rate curve may be divided into three regimes. The first regime constitutes devolatilization of the sample. It is here that the bulk of

Figure 7. The reaction rate time curve for the unclassified petroleum coke sample. The no salt case for Reactor I is shown.



the volatile hydrocarbons escape. From time zero, the CO_x concentration climbs very rapidly and then begins to die down gradually. Regime II follows this, and here the rate is level with time. It is this rate which is selected to be characteristic of the petroleum coke, and it will be used as the rate of reaction in all cases to follow. Regime III constitutes the ultimate decay of the reaction rate to complete carbon conversion. The reaction rate was monitored to approximately 99% conversion, with the remainder being extrapolated. The particular reaction rate time curve of Figure 7 was for the no salt case for Reactor I. This type of behavior was typical for all reactor configurations using the unclassified petroleum coke sample.

4.4.1 Reactor I Results

Reaction rate vs. % conversion is given as a function of temperature for Reactor I for the no salt case in Figure 8 and for the salt case in Figure 9. For clarity, the volatile release regime has been deleted, and the reaction rate shown is after the level rate regime has been attained. It is seen that both exhibit similar behavior. The most striking feature of these curves is that the level rate regime narrows as the reaction rate is increased. In reference to Figure 7, the level rate regime decreases from 40% conversion at 1194 K to less than 25% conversion at 1286 K. Competition between oxidation and

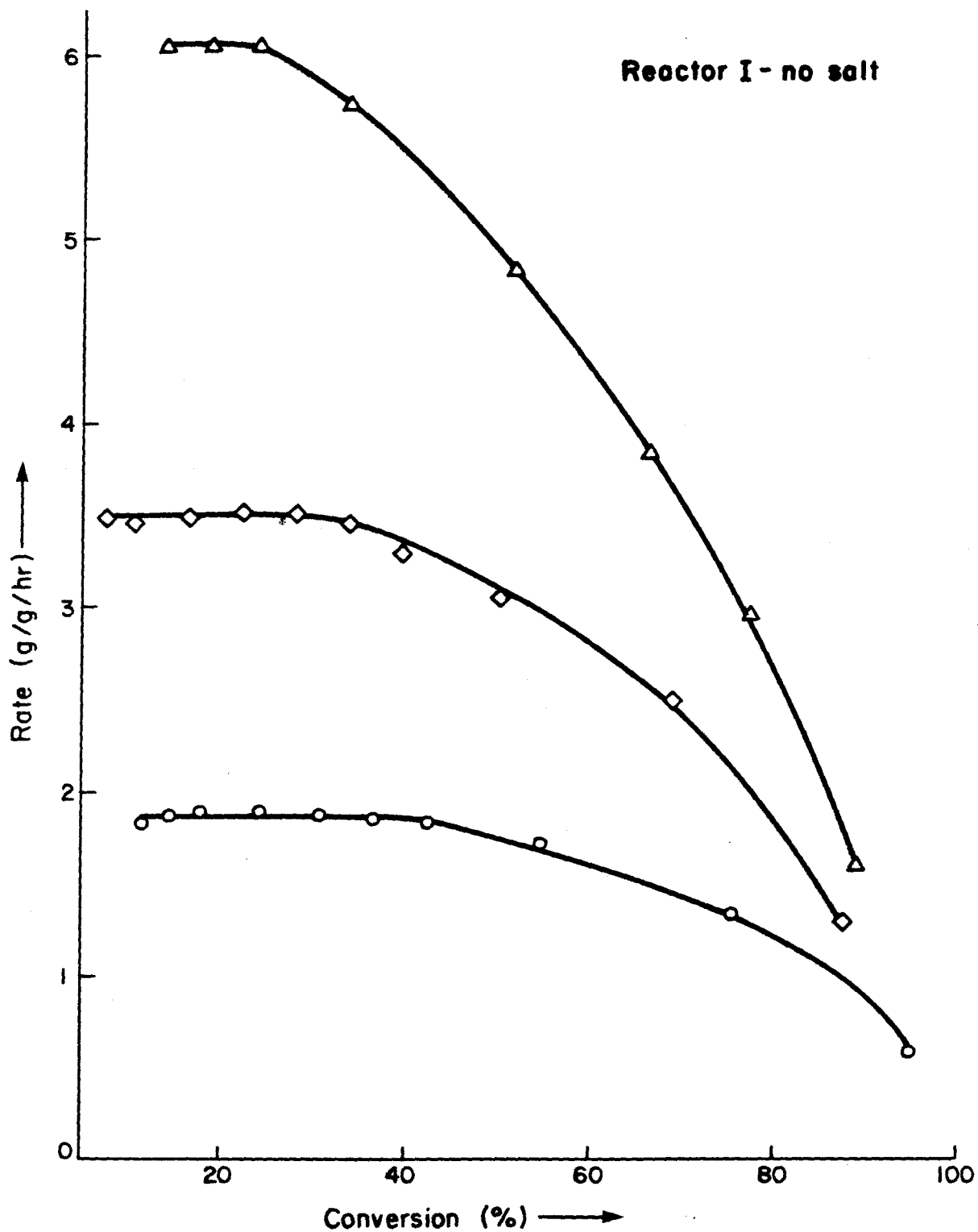


Figure 8. The temperature effect on the reaction rate vs conversion curve for the no salt case for Reactor I. O, 1194 K and 19.9% H₂O; ◇, 1235 K and 19.8% H₂O; △, 1286 K and 21.0% H₂O.

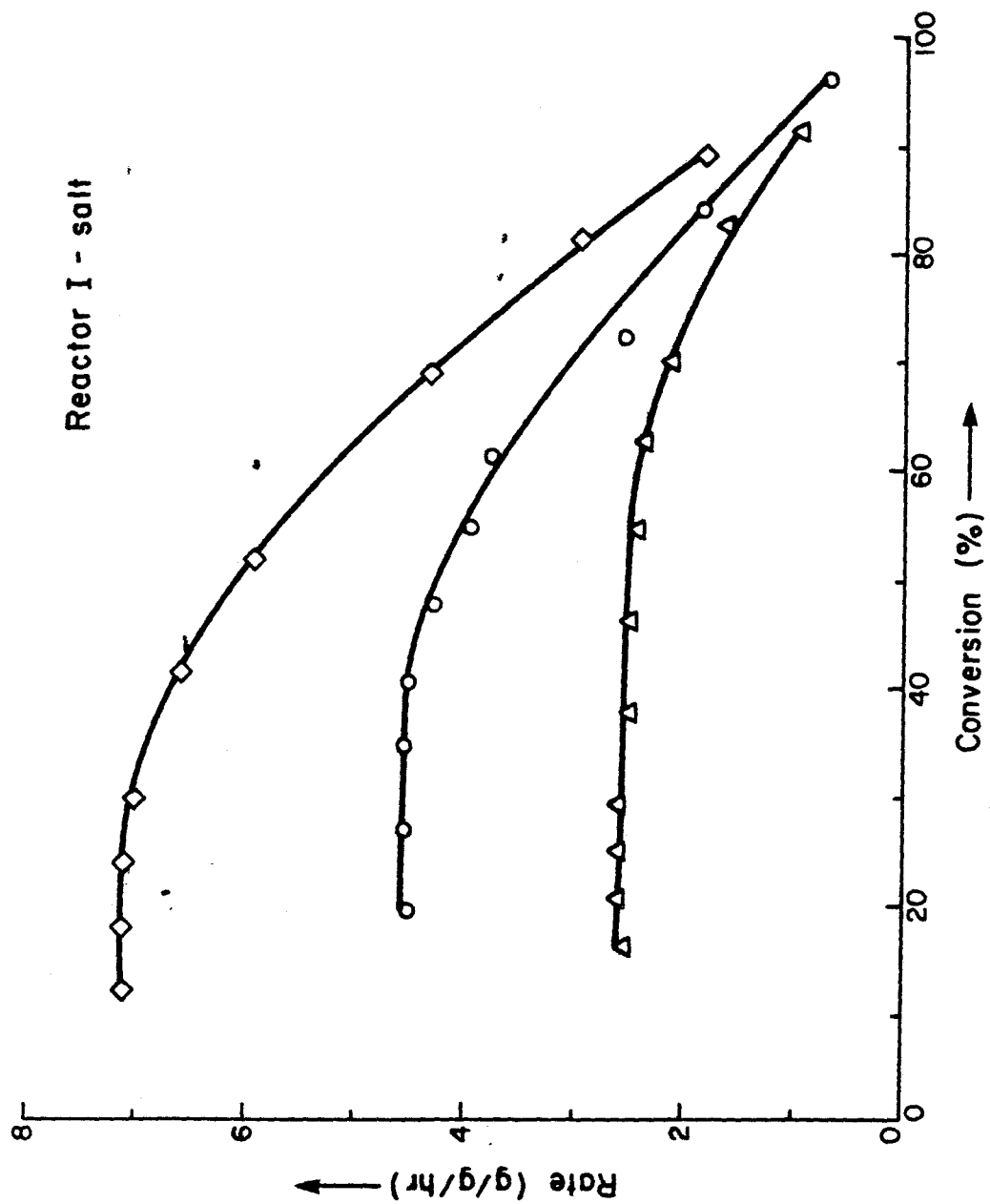


Figure 9. The temperature effect on the reaction rate vs conversion curve to the salt case for Reactor I. Δ , 1196 K and 21.0% H_2O ; \circ , 1237 K and 21.0% H_2O ; \diamond , 1272 K and 21.0% H_2O .

structural ordering of the carbon is a likely cause of this behavior. These two rate processes increase with temperature. If the ordering is assumed to demote the reactivity of the carbon, then such demotion apparently has a greater temperature response (ie, a higher activation energy) than the rate of oxidation. The result is that less carbon is available at the level rate at higher temperatures. This will be dealt with in more detail in the following chapter.

Figure 10 details the effect of water concentration on the reaction rate for the salt and no salt cases for Reactor I. The effect appears linear from the data. A least squares fit of the logarithmic rate vs. the logarithmic water concentration yielded a slope of 0.829 for the no salt case and 0.837 for the salt case. It is noted that data shown in Figure 10 indicate reproducibility of two experiments for the no salt case and three experiments per data point for the salt case. From this we deduce that the water order may be taken as 0.83 ± 0.01 and as equivalent for both cases. This is reasonable as is noted by referring to equation 1. Dependent upon the importance of k_2 , the order should be between zero and unity. Hydrogen concentrations were purposely kept low as water conversion was kept below 5%.

Table 6 contains the data for the temperature effect on the rate for the salt and no salt cases. Errors indicated represent the estimates of the standard deviation of three to

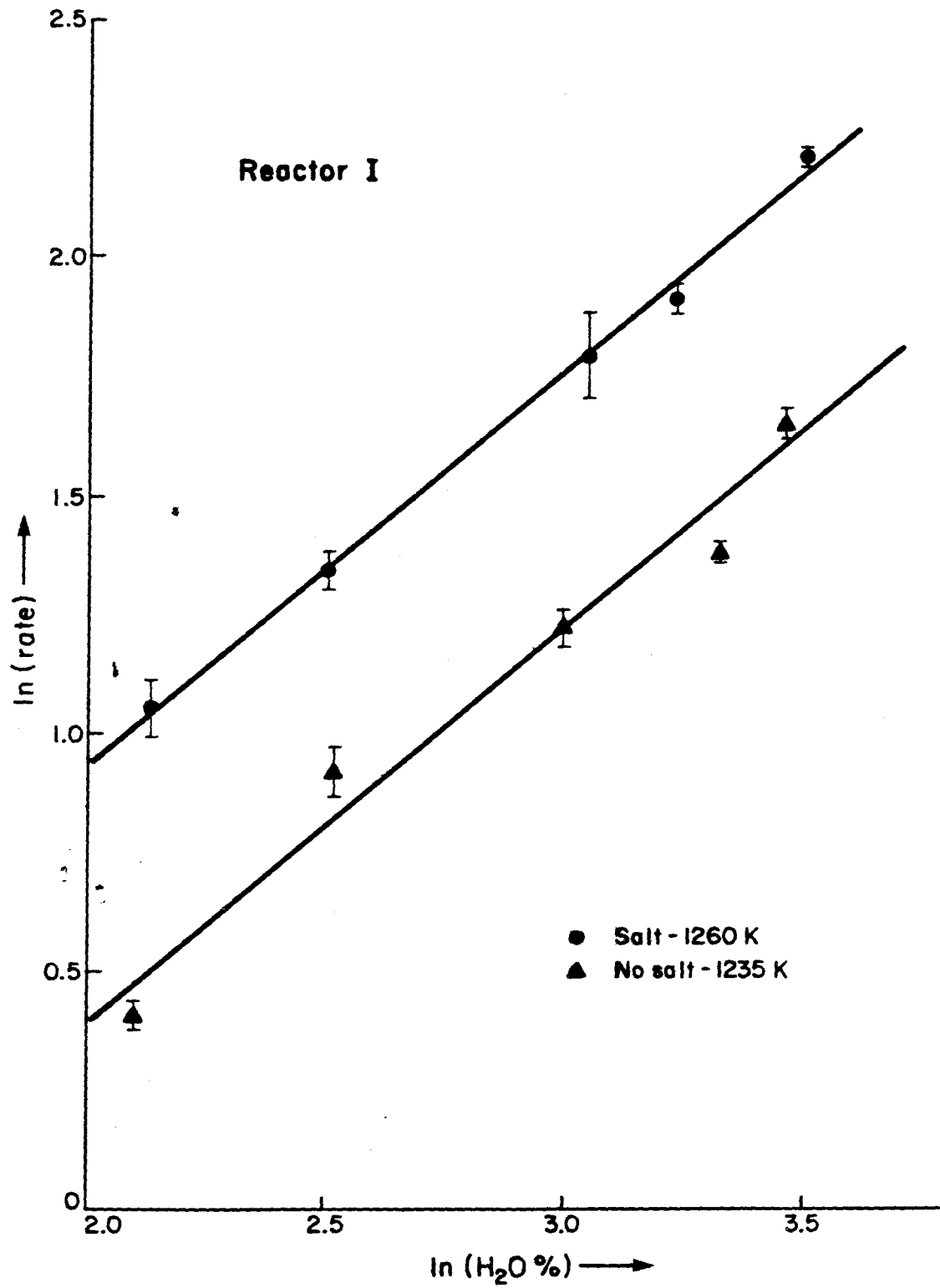


Figure 10. The effect of the water concentration on the reaction rate for the salt and no salt cases for Reactor I. The order is 0.83 for both cases.

Table 6. Data for the temperature effect for the reaction rates with and without salt using Reactor I.

REACTION RATE WITHOUT SALT		
T(K)	Rate @ 21% H ₂ O (g/g/hr)	Error (g/g/hr)
1082	0.40	-
1164	1.42	0.16
1180	1.80	0.24
1194	2.03	0.29
1235	3.53	0.29
1286	6.11	0.20
REACTION RATE WITH SALT		
T(K)	Rate @ 21% H ₂ O (g/g/hr)	Error (g/g/hr)
1171	1.79	0.19
1196	2.56	0.05
1237	4.43	0.27
1260	6.01	0.56
1272	7.25	0.61
1286	8.29	1.19

five experiments. The rate in these cases has been extrapolated to the rate at 21% H₂O using the order of 0.83 for experiments not conducted at this water concentration. An Arrhenius plot of this data follows in Figure 11.

As is seen in reference to Figure 11, the salt reaction rate was slightly higher than the no salt case indicative of a catalytic effect of the salt. For the two reactions, a least squares fit of the data yielded for the no salt case:

$$R_{NS} = 2.32 \times 10^7 \exp\left(\frac{-35400}{RT}\right) X_{H_2O}^{0.83} \text{ g/g/hr.} \quad (2)$$

and for the salt case:

$$R_S = 2.14 \times 10^8 \exp\left(\frac{-40300}{RT}\right) X_{H_2O}^{0.83} \text{ g/g/hr.} \quad (3)$$

It is seen that the coke has an activation energy of approximately one-half of the activation energy of the pure carbon-steam reaction. This decrease may be due to the impurities present which lower the activation energy (36) or to a pore penetration effect (37). It is most likely that the reaction rate of petroleum coke exposed to the oxidant gas is affected by both of these factors. It is peculiar that the catalytic effect in this case raised the activation energy for the reaction. This is quite in contrast to the general case where catalysis proceeds by lowering the activation energy. This may be explained by a parallel reaction mechanism which is discussed

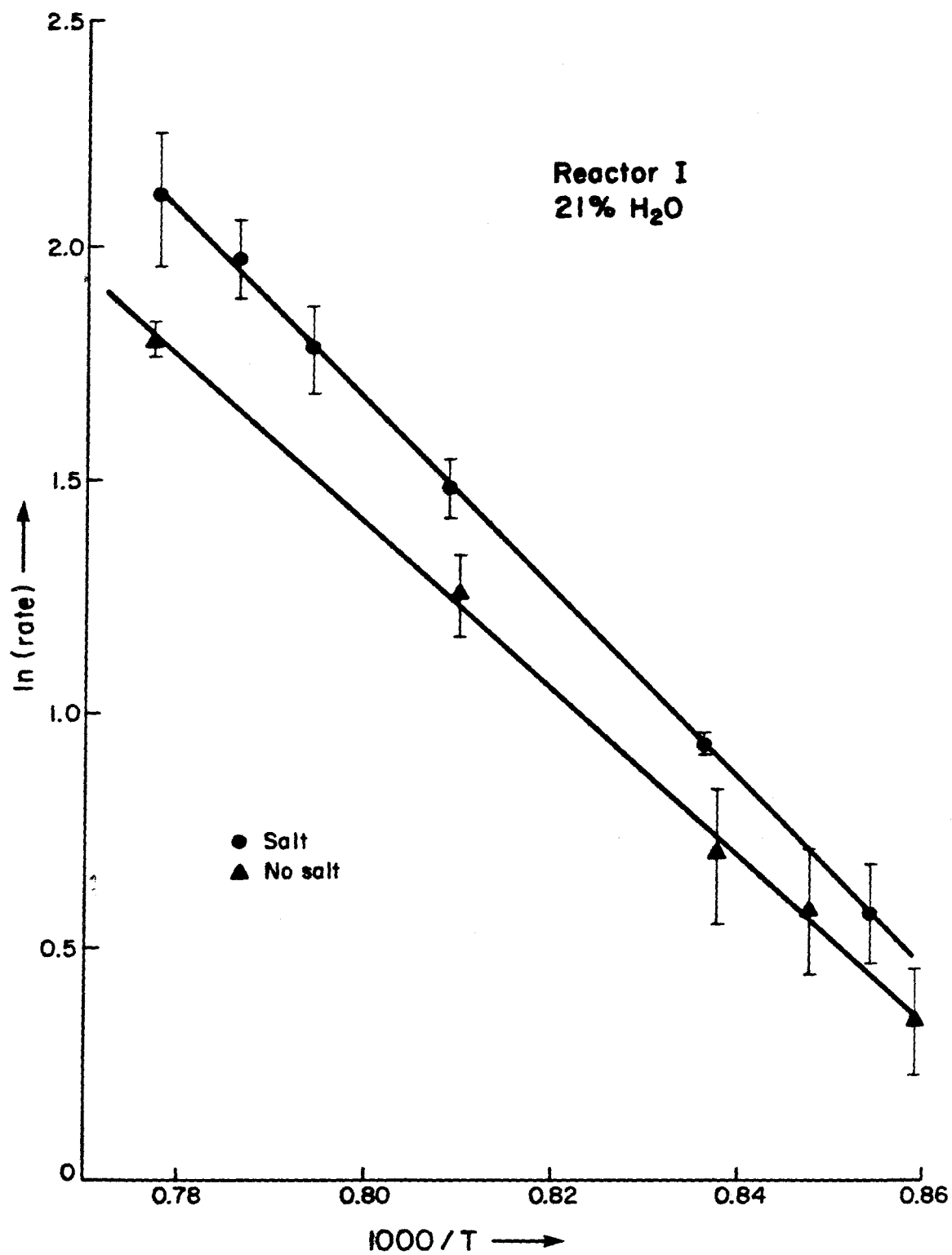


Figure 11. The Arrhenius plot for the change in reaction rate with temperature for the salt and no salt cases for Reactor I.

later in this section. An additional effect may be the viscosity or mobility of the salt. Molten sodium phosphates are quite viscous with a viscosity of 1.14 poise at 1100 K with this decreasing to half its value at 1271 K (35). Hence increasing the temperature decreases the viscosity substantially and this additional mobility may aid the catalytic effect. To test this hypothesis and measure any additional catalytic effect, nickel oxide was added to the salt in Reactor I. Nickel oxide has been shown to be an active catalyst in carbon gasification (38), and in this laboratory, it has been observed that higher concentrations of nickel oxide greatly increase the viscosity of the resulting molten phosphate mixture. Hence while nickel oxide could possibly increase the catalytic activity of the salt phase, it assuredly will lower the salt's mobility. The reaction rate of the petroleum coke was observed to be unaffected (as compared to the salt case) for 0.1% NiO in the molten phosphate. Increasing this to 1.0% lowered the rate to approximately the no salt case. Hence no catalytic effect for the addition of nickel oxide in the configuration of Reactor I was noted. Indeed it lowered the rate presumably by making the salt less mobile.

4.4.2 The Particle Size Effect

Figure 12 indicates the reaction rate of three different particle size ranges for the no salt case for Reactor I. As

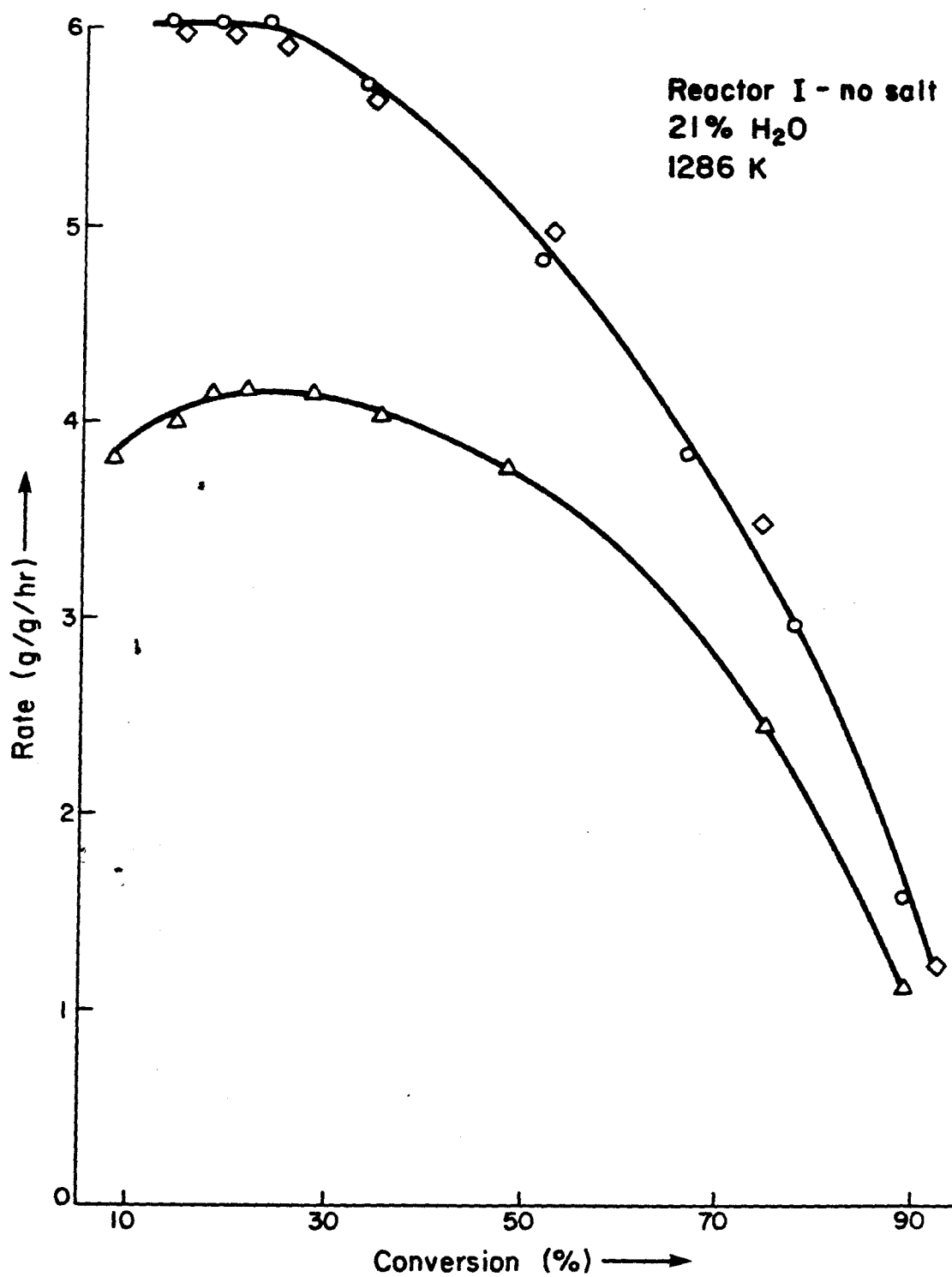


Figure 12. The particle size effect on the reaction rate of petroleum coke for the no salt case for Reactor I. O, Unclassified; ◇, -200 Mesh; △, -120+140 Mesh.

is seen the unclassified coke reacts equivalently to the -200 mesh coke. Thus the 24% greater BET surface area of the -200 mesh coke has no noticeable effect. By referring to Figure 2 and Table 3, this additional surface area may in large part be due to very fine pores which may not participate in the reaction due to transport limitations. The -200 mesh fraction was observed to conform to the reaction rate time curve of Figure 7. The -120+140 mesh petroleum coke depicted in Figure 11 did not conform to this type of curve. The reaction rate in this case slowly increased to a maximum rate where it remained relatively constant and then decayed to zero. Hence in this case while a roughly constant rate was attained, there was no apparent devolatilization regime as noted for the other samples. Such behavior was noted for all +200 mesh fractions reacted separately from the unclassified sample.

Figure 13 details the particle size effect for the salt and no salt cases for Reactor I. By comparing the catalytic effect for the -120+140 and -200 mesh particles, it is apparent that the catalytic effect increases with decreasing particle size. This effect is detailed in Table 7 for all particle size ranges studied. While there is apparent scatter, the effect of decreasing the size is to enhance the relative catalytic effect. Presumably this is due to a larger relative area being catalyzed for the smaller particle sizes.

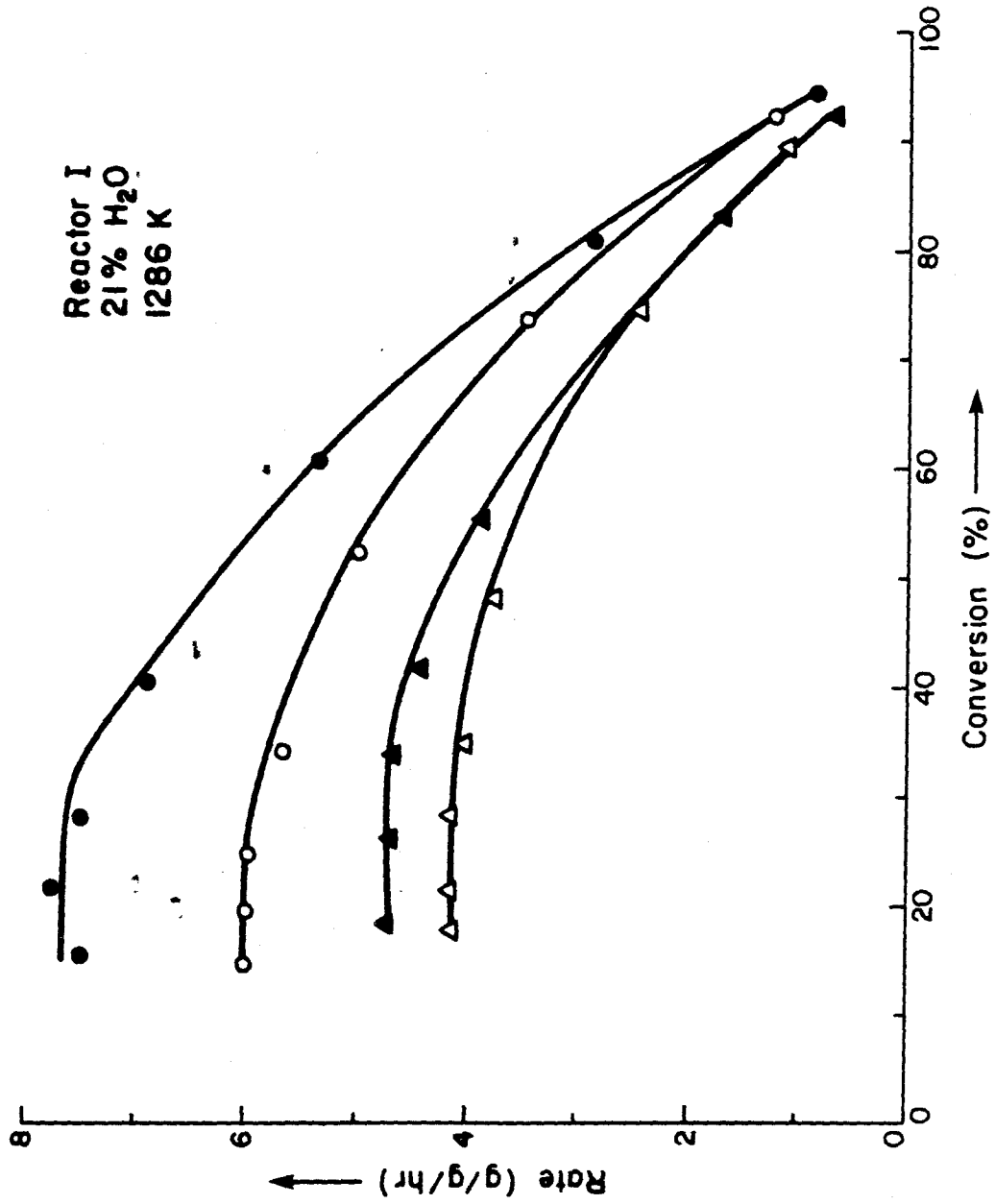


Figure 13. The particle size effect on the relative amount of catalysis of the steam-carbon reaction by molten salt. Δ , -120+140 Mesh with no salt; \blacktriangle , 120+140 Mesh with salt; \circ , -200 Mesh with no salt; \bullet , -200 Mesh with salt.

Table 7. The particle size effect on the catalysis by molten salt for carbon particle gasification.

PARTICLES (MESH RANGE)	R_{NS} (g/g/hr) (NO SALT CASE) (1286 K-21% H ₂ O)	R_S (g/g/hr) (SALT CASE) (1286 K-21% H ₂ O)	$\frac{R_S}{R_{NS}}$
+120	4.02	4.65	1.16
-120+140	4.13	4.70	1.14
-140+200	4.02	4.94	1.23
-200	5.97	7.61	1.27
Unclassified	6.11	8.29	1.36

To examine this, assume the reaction rate for the no salt case to be:

$$R_{NS} = k_{ex} \kappa V_P S_V \quad (4)$$

Here k_{ex} is the reaction rate per unit surface area incorporating the reactant gas concentration dependence. V_P is the particle volume. κ is the effectiveness factor corresponding to not all pore surface area being used due to transport limitations. S_V is the surface area to volume ratio for the particle. The particle volume, of course, will contract in a shrinking particle manner, and S_V will not remain constant throughout the course of the reaction. But as we are considering only the level rate regime, we will allow these dimensions to remain constant. Hence our model assumes a pseudo-steady state for the reacting particle.

For the salt case, a portion of the particle's external surface area is covered by the molten salt wherein lies the catalytic effect. The catalysis will be accounted for by a parallel rate mechanism. Allowing A_C to be the catalyzed area and k_C to be the catalytic rate per unit area, we then have:

$$R_S = k_{ex} \kappa' V_P S_V + k_C A_C \quad (5)$$

κ' is used as the effectiveness factor will be adversely affected by not all of the particle's external surface area being exposed to the gas.

If a spherical particle has the same density as the salt and rests with static contact angle, θ , on the salt surface, we have the situation of Figure 14. The density assumption is appropriate as the petroleum coke due to its low porosity and high carbon content should have a density close to that of graphite which has approximately the same density as the molten salt. Soft carbons such as petroleum coke have been shown (38) to have 60 to 90% the density of graphite for highest temperature treatments ranging from 800 to 1500 K. If the area catalyzed is further assumed to be contained in a thin slice, δ , centered on the line of particle-gas-liquid contact^a, the reaction rate of the particle resting on the salt surface is:

$$R_S = \frac{k_{ex} \kappa' \pi d_P^3 S_V}{6} + k_c \pi d_P \delta \sin \theta \quad (6)$$

Hence the ratio of the reaction rate for the salt and no salt cases is:

$$\frac{R_S}{R_{NS}} = \frac{\kappa'}{\kappa} + \frac{6 k_c \delta \sin \theta}{k_{ex} \kappa d_P^2 S_V} \quad (7)$$

^a Using the measured overall rate and diffusion coefficients from Chapter 3, the Einstein equation predicts δ to be about 0.01 to 0.1 cm. This estimate is dubious as the catalyzed rate may be much larger than the overall rate.

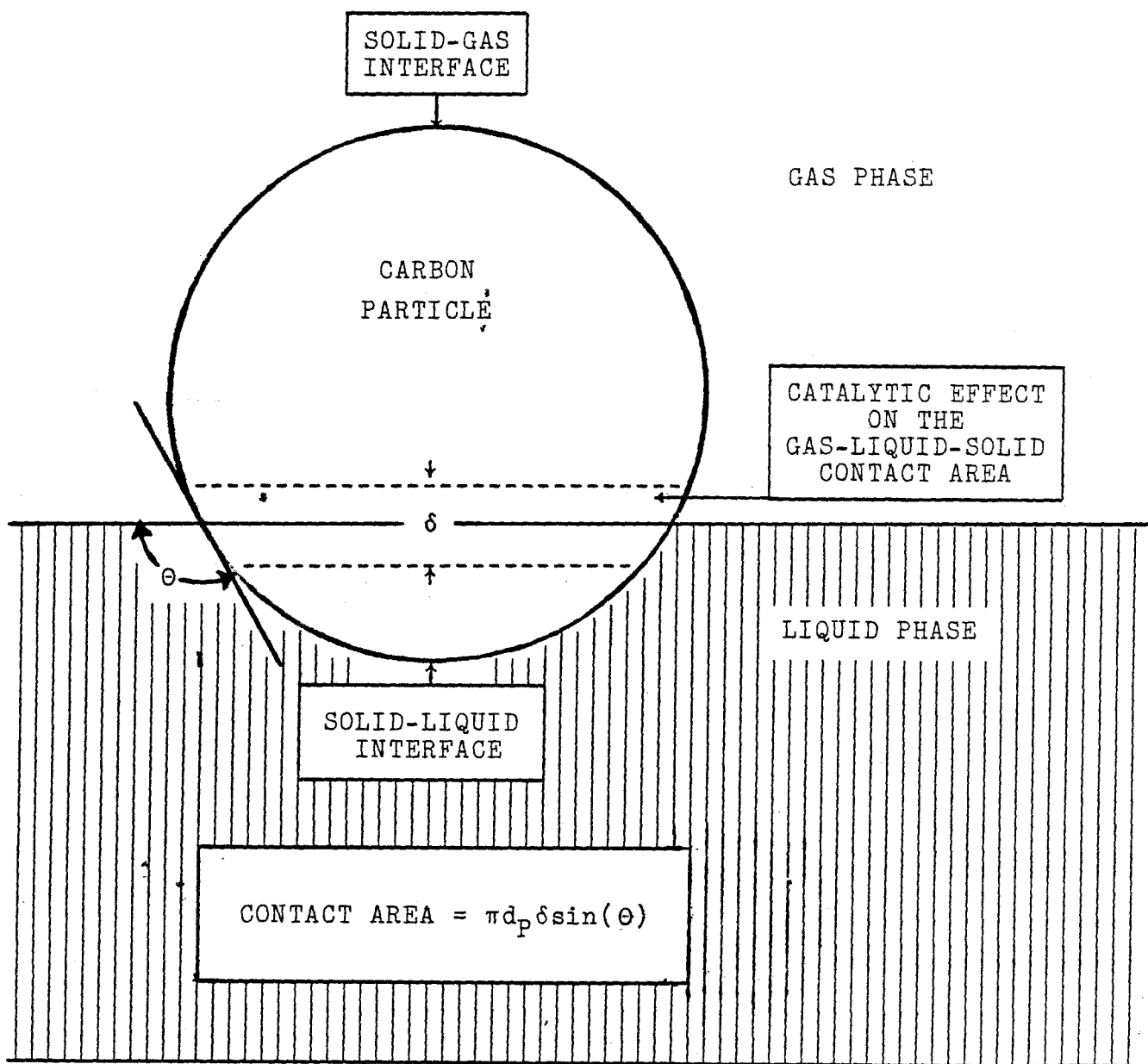


Figure 14. The area catalyzed for the carbon particle gasification reaction in molten sodium phosphates.

Thus we have the situation of Table 7 with the ratio increasing with decreasing particle size. If the entire submerged portion was catalyzed, the ratio would be:

$$\frac{R_S}{R_{NS}} = \frac{\kappa'}{\kappa} + \frac{6 k_c (1+\cos\theta)}{\kappa_{ex} \kappa d_p S_v} \quad (8)$$

This would lessen the dependence of the relative rates on the particle size, d_p .

It is appropriate to examine the dependence of the other variables in equations 7 and 8 on the particle size. Now κ and S_v are intrinsically coupled such that:

$$\kappa S_v = \frac{A_{active}}{V_p} \quad (9)$$

Here A_{active} is the effective surface area that is actively participating in the reaction. Naturally as we are dealing with a nonzero order reaction, the utilized surface area would incorporate a sparser density of total active surface sites as the gas concentration is diminished toward the interior of the particle. A_{active} is then that amount of surface area which would encompass the total amount of surface sites that are participating in the reaction. With severe transport limitations into the pores, A_{active} would only incorporate the external surface area of the particle; and κS_v would be inversely proportional to d_p . As A_{active} incorporates a larger amount of pore surface area as transport limitations become

less severe, the dependence of κS_v on d_p would tend to zero order. Hence the dependence of κS_v on the particle size could obviate the dependence of equation 8 on d_p but could not completely void the dependence in equation 7. Also the ratio of the effectiveness factors may be estimated if we consider only pores connected to the external surface of the particle and disallow pore interconnections. With this assumption, we will have a linear dependence of the effectiveness factor on the amount of exposed area. For the situation of Figure 14, this becomes:

$$\frac{\kappa'}{\kappa} = \frac{(1-\cos \theta)}{2} \quad (10)$$

If interior pore connections are allowed--particularly macropore interconnections for which transport is relatively rapid, then this ratio will tend to unity.

As indicated earlier, the salt case had a higher activation energy than the no salt case. This requires the parallel mechanism, ie $k_c A_c$, to have a higher activation energy than the no salt or exposed mechanism. The difference between the reaction rates for the salt and no salt cases reveals the activation energy of the catalytic mechanism to be about 60 kcal/gmole.

4.4.3 Reactor II Results

The reaction rate for the bubbling reactor was measured for two cases corresponding to different $\text{Na}_2\text{O}/\text{P}_2\text{O}_5$ (λ) ratios. The data are given in Table 8 for the two cases with the Arrhenius plot following in Figure 15. Again the unclassified coke was employed. All rates were measured at a water concentration of 21.0%. The errors indicate data reproducibility. Unfortunately reactor failure due to the corrosiveness of the salt precluded repeating data points in most cases for the lower molar ratio of sodium oxide to phosphorus pentoxide (λ). The Arrhenius expressions for the two cases follow as obtained by a least squares fit of the data:

$$R_{1.3} = 1.09 \times 10^9 \exp \left(\frac{-48200}{RT} \right) \text{ g/g/hr} \quad (11)$$

$$R_{1.6} = 1.26 \times 10^7 \exp \left(\frac{-37700}{RT} \right) \text{ g/g/hr} \quad (12)$$

Here $R_{1.3}$ corresponds to $\lambda = 1.31$ with $R_{1.6}$ being the rate for $\lambda = 1.60$.

The flowrate effect was also investigated to insure that complete mixing took place. It should be noted that these experiments are for extremely dilute slurries of no more than 5 mg. of coke in 220 g. of molten salt. Table 9 details the rates obtained by varying the flowrate showing no apparent effect. Interestingly, no particle entrainment was observed

Table 8. Rate data for Reactor II.

REACTION RATE FOR $\text{Na}_2\text{O}/\text{P}_2\text{O}_5 = 1.31$		
T(K)	RATE @ 21% H_2O (g/g/hr)	ERROR
1144	0.67	-
1194	1.58	-
1237	3.26	0.66
1291	7.52	-
REACTION RATE FOR $\text{Na}_2\text{O}/\text{P}_2\text{O}_5 = 1.60$		
T(K)	RATE @ 21% H_2O (g/g/hr)	ERROR
1185	1.41	0.01
1197	1.55	-
1246	3.04	0.27
1265	3.75	0.12
1303	5.86	0.12

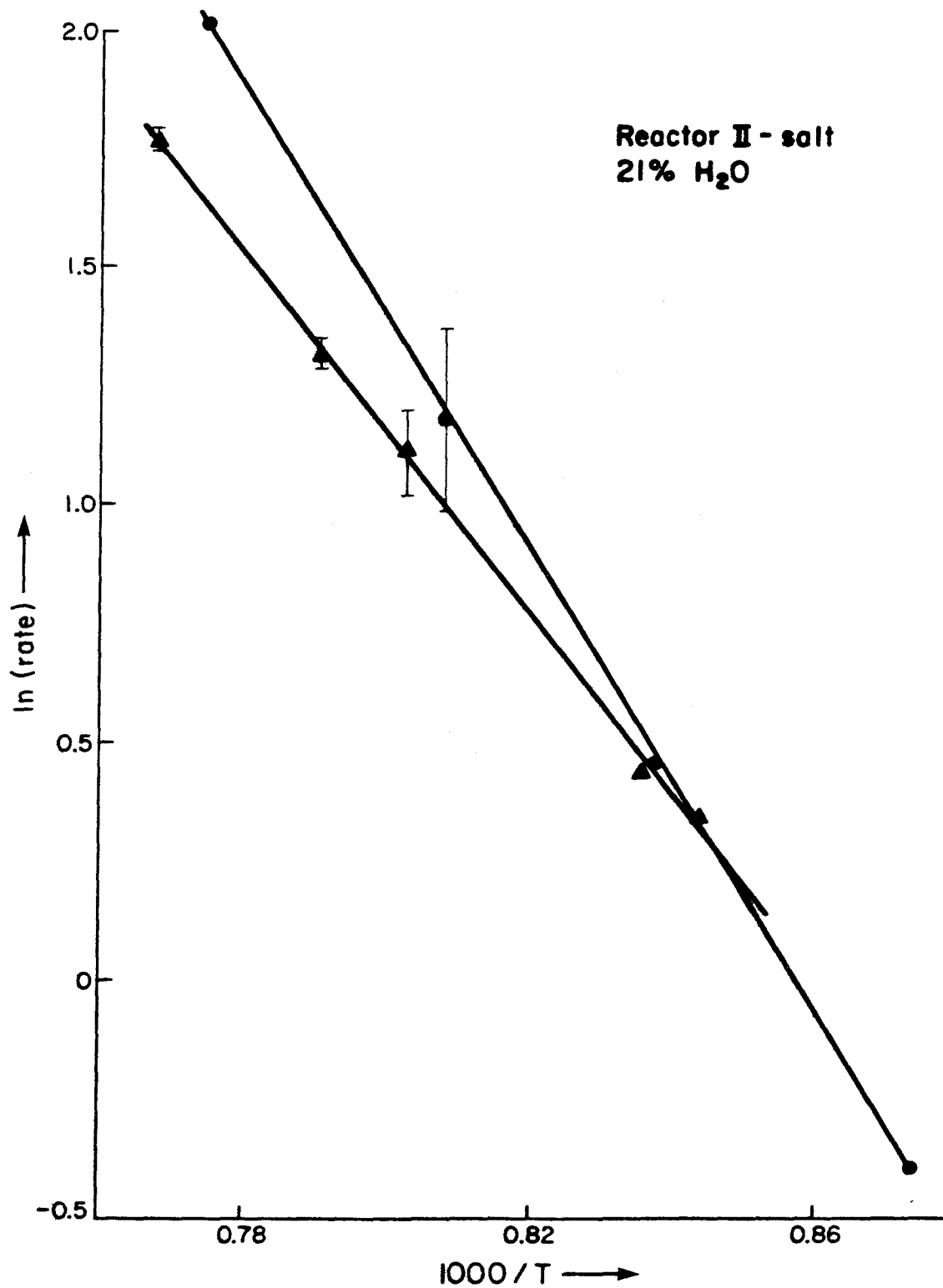


Figure 15. The change in the reaction rate with temperature for the bubbling reactor (Reactor II).
●, $\text{Na}_2\text{O}/\text{P}_2\text{O}_5 = 1.31$; ▲, $\text{Na}_2\text{O}/\text{P}_2\text{O}_5 = 1.60$.

Table 9. The flowrate effect for Reactor II. The dry nitrogen flow at room temperature is given as well as the superficial velocity at the reaction temperature including the water vapor concentration.

ROOM TEMPERATURE NITROGEN FLOWRATE (scc/min)	REACTOR TEMPERATURE SUPERFICIAL VELOCITY (cm/s)	RATE(g/g/hr) (1220 K - 21% H ₂ O) (Na ₂ O/P ₂ O ₅ = 1.60)
62.4	0.25	2.09
89.2	0.36	2.30
150	0.61	2.28
269	1.09	2.08
339	1.37	2.23
410	1.66	2.27

by monitoring the condensed water for even the high flowrates used in this case. This was corroborated by the carbon balance being unaffected by the flowrate. This contrasted to the results using Reactor I in the no salt configuration where at the higher flowrates indicated in Table 9 significant carbon particle content was noted in the condensed water. The difference is attributable to the particles adhering to the molten salt by the work of adhesion (8,31).

4.4.4 Comparison of Results

Figure 16 compares the three configurations. As is seen, the bubbling reactor had a lower rate as compared to Reactor I results at the lower temperatures. At the higher temperatures, it is above the no salt case but still lags the salt case. It is seen that all rates are of the same order of magnitude.

Previously, the rate of the indirect mechanism has been measured (8). While these results were for oxygen, they did indicate that the indirect mechanism was three orders of magnitude below the exposed case (no salt case). The results presented here indicate that the reaction rate in a bubbling slurry is of the same order of magnitude as the no salt case. Thus it is reasonable to presume that the direct mechanism is dominant for carbon particle gasification by steam in a molten phosphate slurry.

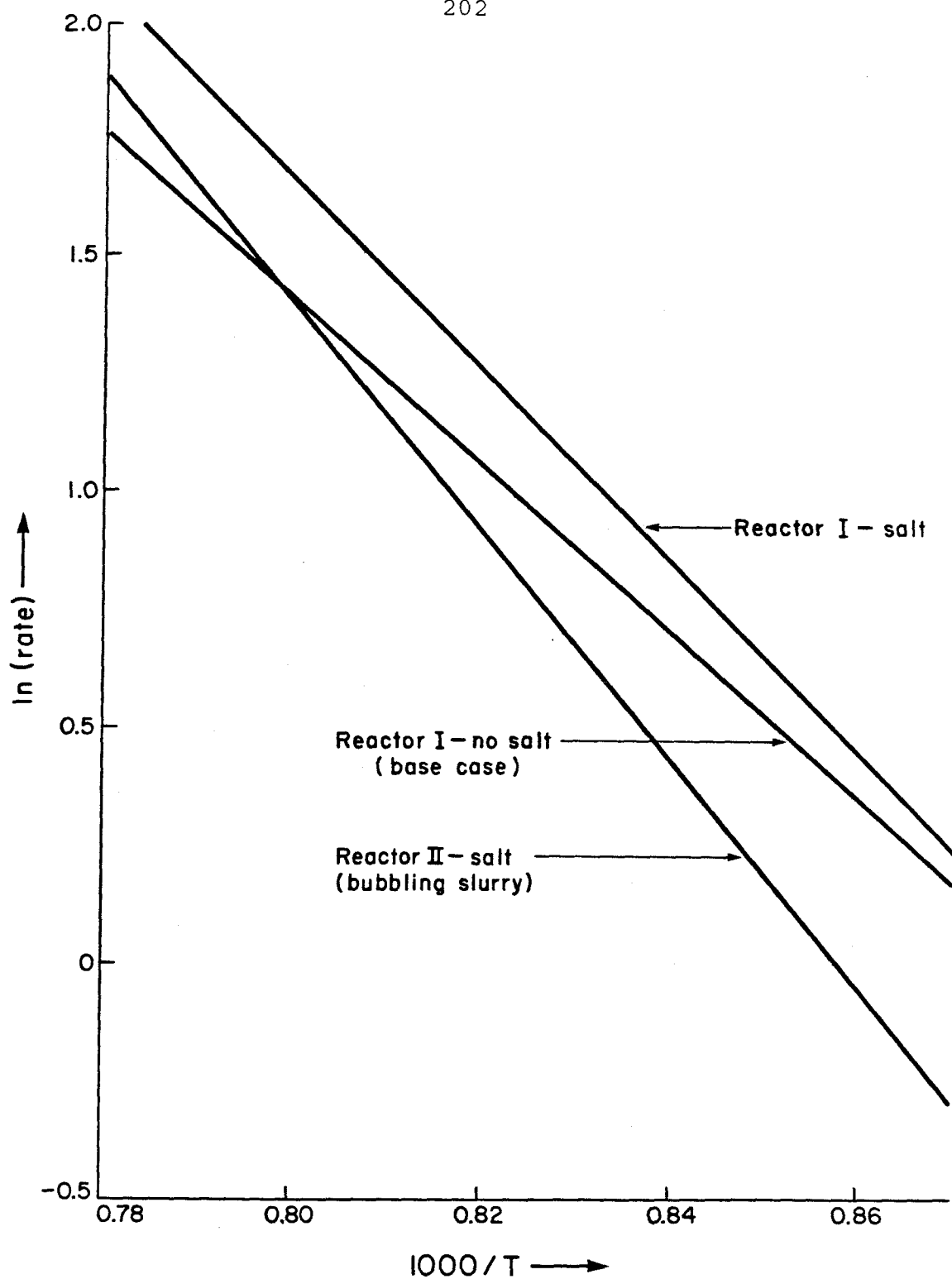


Figure 16. A comparison the reaction rate at 21% H_2O in the various configurations for $\text{Na}_2\text{O}/\text{P}_2\text{O}_5 = 1.31$.

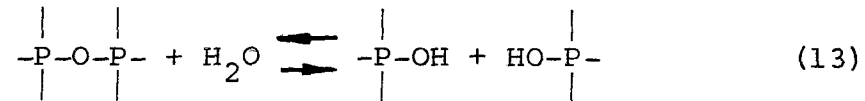
The rate of bubble-particle contacting is not investigated here as this requires measuring the bubble size as well as the bubble density, ie, the gas hold-up. These will be dealt with in a later chapter. It is noted here that the rate of the direct mechanism may be obscured by principally two effects.

The first effect is that the carbon particles may have their own individual supply of air while in the bulk liquid. This effect is best demonstrated by placing hydrophobic particles in water. Most of the particles even if heavier than water rest on the surface. Close examination reveals the attachment of air bubbles to the particles. Upon mixing this slurry, the particles are suspended in the water with many having attached air bubbles. This is directly analogous to carbon particles in molten salt. When the particles are on a gas-liquid interface of the salt slurry, the large contact angle prevents complete wetting of the particle leaving attached air. Upon entering the bulk liquid, the gas should remain attached. Hence the rate of the direct mechanism will be enhanced by this mechanism.

The second effect is the substantially better particle-molten salt contacting in the molten slurry. As the liquid shrouding of the particle bursts upon contacting a gas-liquid interface, the roughness of the particle will preclude a perfect scission. Hence molten salt droplets will be left

on the surface. This would enhance the catalytic activity above that which the salt case for Reactor I measured.

A final note is appropriate on the mechanism of the catalytic effect on the salt. There are two distinct possibilities. The first is an electronic effect whereby the molten media in contact with the particle weakens the carbon-carbon linkages hence making it more vulnerable to reaction (3). The second is an oxygen transfer mechanism by the molten salt (40). One possibility here is the cleaving of phosphorus linkages by water:



These end groups may then interact with the carbon producing the carbon oxide. Hence the mechanism here is a cyclical oxidation reduction where a species, S, is alternatively oxidized and reduced.



This in essence lowers the system resistance to carbon gasification by providing a parallel route to the direct gasification scheme.

4.5 Conclusions

1. Green sponge petroleum coke reacts with a water order of 0.83 and an activation energy of about 1/2 that of the pure carbon-steam reaction. After an induction period corresponding to sample devolatilization, the reaction rate remains level for some time before ultimate decay sets in.

2. Molten sodium phosphate has been shown to have a slight catalytic effect on the gasification of petroleum coke by steam. The magnitude of this effect is dependent upon particle-salt contacting which is poor as the salt cannot penetrate the pore structure of the particle.

3. The reaction rate in a bubbling slurry of petroleum coke particles in molten salt is within an order of magnitude of the reaction rate of the particles exposed directly to the oxidant gas. As the rate of the indirect mechanism has been shown previously to be very slow compared to the exposed rate, this indicates that the direct mechanism is dominant in such molten phosphate slurries.

NOTATION

- A_{active} = The effective surface area participating in the reaction (cm^2)
- A_c = The surface area of the particle catalyzed by the molten salt (cm^2)
- C_{H_2} = The hydrogen concentration in the reactant gas (mole/cm^3)
- $C_{\text{H}_2}^0$ = The water molar concentration in the reactant gas (mole/cm^3)
- d_p = The diameter of the particle (cm). Particles are assumed to be spherical and to have an equivalent diameter corresponding to the middle of the mesh range.
- k_1 = The rate constant in the reaction rate expression for the water-carbon reaction ($\text{cm}^3/\text{mole hr}$)
- k_2 = A constant in the reaction rate expression for the water carbon reaction (cm^3/mole)
- k_3 = A constant in the reaction rate expression for the water carbon reaction (cm^3/mole)
- k_c = The reaction rate per unit area for the catalyzed carbon reaction ($\text{g}/\text{g cm}^2 \text{ hr}$)
- k_{ex} = The reaction rate per unit area for the uncatalyzed carbon-water reaction ($\text{g}/\text{g cm}^2 \text{ hr}$)
- P_{N_2} = The partial pressure of nitrogen the particle is exposed to in the adsorption/desorption experiments (atm)

- P_S = The saturation pressure of liquid nitrogen at its boiling point (atm)
- R = The gas constant (cal/mole K)
- $R_{1.3}$ = The reaction rate for $\lambda = 1.31$ for Reactor II (g/g/hr)
- $R_{1.6}$ = The reaction rate for $\lambda = 1.60$ for Reactor II (g/g/hr)
- R_{NS} = The reaction rate for the no salt case for Reactor I (g/g/hr)
- R_{pc} = The reaction rate of the pure carbon-water reaction (hr^{-1})
- r_{po} = The equivalent radius of the pores calculated using the Kelvin equation (cm or \AA)
- R_S = The reaction rate for the salt case for Reactor I (g/g/hr)
- S_V = The ratio of surface area to volume for the particle (cm^{-1})
- T = The absolute temperature (k)
- V_{ads} = The total specific volume of liquid nitrogen adsorbed by the particles (cm^3/g)
- V_P = The particle volume (cm^3)
- ΔV_{po} = The specific volume of liquid nitrogen adsorbed into pores of a specific size range (cm^3/g)
- x_{H_2O} = The molar fraction of water in the gas phase

Greek Letters

- δ = The contact section thickness for the catalytic effect of molten salt on the particle (cm)
- κ = The effectiveness factor
- λ = The molar ratio of sodium oxide to phosphorus pentoxide
- θ = The static contact angle (degrees)

REFERENCES

1. Chemical and Process Technology Encyclopedia, (D. M. Considine, ed.), McGraw-Hill, New York (1974)
2. Fishbach, D. B., *Chem. Phys. Carbon*, 7, 1 (1971)
3. Walker, P. L. Jr., Rusinko, F. Jr., and Austin, L. G., *Advances in Catalysis*, 11, 133 (1959)
4. Walker, P. L. Jr., and Nichols, J. R., in Industrial Carbon and Graphite, p. 334, Society of Chemical Industry, London (1957)
5. Grisdale, R. O., *J. Appl. Phys.*, 24, 1288 (1953)
6. Smith, W. R., and Polley, M. H., *J. Phys. Chem.*, 60, 689 (1956)
7. Walker, P. L. Jr., Rusinko, F. Jr., Rakzawski, J. F., and Liggett, L. M., *Proceedings of the Third Conference on Carbon*, p. 643, University of Buffalo, 1957, Pergamon Press, New York (1959)
8. Chapter 3
9. Long, F. J., and Sikes, K. W., *Proc. Royal Society*, (London), A193, 377 (1948)
10. Gadsby, J., Hinshelwood, C. N., and Sikes, K. W., *Proc. Royal Society* (London), A187, 129 (1946)
11. Johnstone, H. F., Chen, C. Y., and Scott, D. S., *Ind. Eng. Chem.*, 44, 1564 (1952)
12. Marsh, H., and Adair, R. R., *Carbon*, 13, 327 (1975)

13. Walker, P. L. Jr., Shelef, M., and Anderson, R. A.,
Chemistry and Physics of Carbon, 4, 287 (1968)
14. McKee, D. W., Chemistry and Physics of Carbon, 16, 1,
(1981)
15. L'Homme, G. A., and Boudart, M., 11th Symposium on Combustion,
p. 197, Combustion Institute, Pittsburgh, Pennsylvania
(1967)
16. McKee, D. W., Carbon, 12, 453 (1974)
17. Gallagher, J. T., and Harker, H., Carbon, 2, 163 (1964)
18. Baker, R. T. K., and Harris, P. S., Carbon, 11, 25
(1973)
19. Yokoyama, S., Miyahara, K., Tanaka, K., Takakuwa, I.,
and Tashiro, J., Fuel, 58, 510 (1979)
20. Harker, H., Proceedings of the Fourth Conference on
Carbon, p. 125, University of Buffalo, 1959, Pergamon
Press, New York (1960)
21. Kayembe, N., and Pulsifier, A. H., Fuel, 55, 211 (1976)
22. Nebel, G. J., and Cramer, P. L., Ind. Eng. Chem., 47,
2393 (1955)
23. Burk, F. C., Test, J. L., and Jackson, H. R., Proc. Am.
Pet. Inst., 34, 270 (1954)
24. Jeffrey, R. E., Griffith, L. W., Dunning, E., and Baldwin,
B. S., Petroleum Refiner, 33, 92 (1954)
25. Arthur, J. R., and Bowring, J. R., Ind. Eng. Chem., 43,
528 (1951)

26. Rakzawski, J. F., and Parker, W. E., *Carbon*, 2, 53 (1964)
27. Watts, H., *Trans. Far. Soc.*, 54, 93 (1958)
28. McKee, D. W., *Carbon*, 10, 491 (1972)
29. Gallagher, J. T. and Harker, H., *Carbon*, 2, 163 (1964)
30. Dugan, J. J., and Higgins, J. P., U.S. Patent 3, 852,188 (1974)
31. Hedden, K., and Wicke, E., *Proceedings of the Third Conference on Carbon*, p. 249, University of Buffalo, 1959, Permagon Press, New York (1960)
32. Adamson, A. W., *Physical Chemistry of Surfaces*, 2nd Edition, Interscience Publishers, New York (1960)
33. McBain, J. W., *J. Chem. Soc.*, 57, 697 (1935)
34. Biorci, C., and Pescetti, D., *Proceedings of the Fifth Conference on Carbon*, Volume I, p. 88, Pennsylvania State University, 1961, Permagon Press, New York (1962)
35. Van Wazer, J. R., *Phosphorus and Its Compounds*, Volume I, Interscience Publishers, New York (1958)
36. Long, F. J., and Sykes, K. W., *J. Chim. Phys.*, 47, 576 (1950)
37. Acharya, T. R., and Olander, P. R., *Carbon*, 11, 7 (1973)
38. McKee, D. W., *Carbon*, 8, 623 (1970)
39. Delhaes, P., and Carmona, F., *Chemistry and Physics of Carbon*, 17, 89 (1981)
40. McKee, D. W., *Carbon*, 8, 623 (1970)

CHAPTER 5

PETROLEUM COKE IN THE
PREGRAPHITIZATION REGIME

5.1 Introduction

Petroleum coke is a carbonaceous material made principally by delayed coking of residues of crude oil distillation. Its manufacture is justified on zero net value for the coke as the principal products are the hydrocarbons that escape during the coking process. Hence little attention is paid to the final coke product.

Although produced as a side product, the uses for petroleum coke are many. Known as a soft carbon as the raw materials stay liquid during the early stages of heat treatment, it is the preferred starting material for the manufacture of graphite. Other uses range from low ash fuel to structural applications (1).

Petroleum coke is broadly classified into two types dependent on the feedstock to the delayed coker. Sponge or amorphous coke is made largely from virgin bottoms. Needle coke is manufactured from refined tars of high aromaticity. The high aromaticity of the feedstock is the key for making needle coke the best material for graphitic electrodes.

Delayed coking is basically a pyrolysis process. Thus it is appropriate to review the general features of hydrocarbon pyrolysis. Three major steps are involved (2). Initially long chain hydrocarbons crack to smaller molecules. Secondly the chains form cyclic compounds which become aromatic. The final step is the condensation of the aromatic rings into polycyclic systems. Hence the initial degradation step is

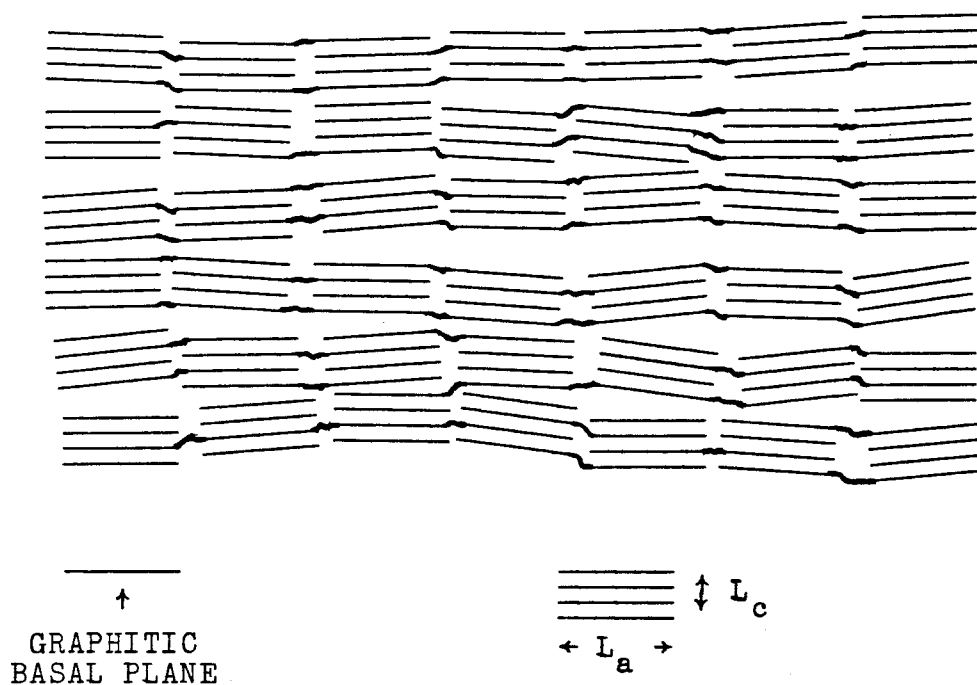
followed by subsequent synthesis reactions.

The residue left is then a carbon with a largely aromatic structure. Further heat treatment to less than 2000 K results in more devolatilization and more synthesis reactions and an ordering of the polycyclic ring system in what is known as the pregraphitization regime. Here the polycyclics begin to resemble graphitic basal planes. Cokes and other disorganized carbons treated to these relatively low temperatures have a degree of crystalline order as is evidenced by the appearance of (001) and (hk0) peaks in their respective XRD patterns. The (hk0) peaks indicate regular structure in the graphitic type basal planes while the (001) peaks arise from stacks of parallel planes. (hkl) peaks are notably absent indicating no correlation between adjacent layers. Another notable feature of such disorganized carbons is that the average interlayer spacing remains quite large ($\geq 3.44 \text{ \AA}$).

By noting these general features, Warren et al (3,4,5) have proposed and developed a turbostratic model with near perfect graphitic basal planes arranged in parallel stacks with little or no correlation between adjacent layers and adjacent stack normals. The large interlayer spacing as opposed to graphite (3.354 \AA) is postulated to be due to rotational and translational defects of the normals to the respective adjacent basal plane layers. The parallel stacks or crystallites are described by two dimensions -- L_a , the

stack diameter parallel to the basal plane, and L_c , the stack height normal to the basal plane. As graphitization proceeds with increasing temperature-time treatment, these stack dimensions grow and three dimensional order sets in as evidenced by the appearance of diffuse (hkl) peaks. Franklin (6) has characterized carbons as graphitic or nongraphitic dependent on the appearance of (hkl) peaks and further classified carbons as graphitizing or nongraphitizing if (hkl) lines appear or not after heat treatment to approximately 3000 K. Within the confines of this model, growth apparently occurs by the movement of whole layers rather than individual atoms, and the graphitizing carbons would apparently consist of somewhat aligned plane layer segments as shown in Figure 1.

The main shortcoming of the turbostratic model is the assumption of near perfect graphitic type basal planes. Noting this Maire and Mering (7,8,9,10) postulated a model for disorganized carbons based on average interlayer spacing. The degree of graphitization (taken as the linear distance between disorganized layer spacing $\{\sim 3.44 \text{ \AA}\}$ and graphitic layer spacing $\{3.354 \text{ \AA}\}$) is postulated to depend on interstitial defects disappearing. Hence graphitization in the confines of this model proceeds by the removal of imperfections in a grand graphitic-type lattice. This has been extended by Ruland (11) who relied on average crystalline dimensions as



The structure of a non-graphitic carbon which will graphitize upon treatment to high temperatures. The linkage between neighboring crystallites is weak and conversion to crystalline graphite requires only a slight bending of the layer segments.

LAYER GROWTH OF A PETROLEUM COKE IN THE PREGRAPHITIZATION REGIME.

Heat Treatment T(K)	Layers per Parallel Group ($\approx L_c$)	Layer Diameter L_a (Å)
1273	4.1	22
1493	9.9	35
1753	13.0	40
1993	31	66

Figure 1. The structure and procession toward graphitic carbon of petroleum coke in the pregraphitization regime. The data and schematic representation are from Franklin (6).

well as the deviations and allowed for more types of crystalline imperfections than Maire and Mering.

Most likely a combination of these two extremes is in order as Fishbach (12) has noted. However it may be concluded that all carbons and in particular petroleum coke have varying degrees of basal plane structures present with imperfections in and surrounding these structures. Graphitic transitions, such as measured by the degree of graphitization, for many carbons show quite sharp temperature transitions (ie, graphitization proceeds with a high activation energy) almost resembling a phase change (13). These are known as hard carbons. Softer carbons such as petroleum coke have transitions which are less sharp in general and measurable changes occur with relatively mild heat treatment. The kinetics of these processes as well as many environmental effects other than temperature have been discussed by Fishbach (12) and Pacault (14).

This study is concerned with the reactivity of petroleum coke in the pregraphitization regime. Total crystallinity should be low. However reactivity should be dependent upon heat treatment in this low temperature regime as the softness of the petroleum coke allows a suitable degree of graphitic alignment to take place. Previous studies including that of Walker et al (15) have concentrated on the reactivity of cokes treated to high enough temperatures for significant graphitization. These studies have shown a rough correlation between the decrease

in reactivity and the increase in crystallinity as evidenced by the increasing intensity of the (002) peaks.

5.2 Properties of the Carbons Studied

The materials selected for study were green sponge and green needle coke from Union Oil Corporation as sponge and needle coke would be expected to exhibit the widest range of behavior for petroleum cokes. A calcined sponge coke was also supplied. The compositions of these materials are listed in Table 1. As expected hydrogen content is markedly decreased for the calcined sponge coke sample as compared to the other two samples.

5.2.1 Treatment of the Green Cokes

Two types of treatment were applied to the green cokes -- toluene extraction and calcination. Extraction provided a method of removing material at lower temperatures while calcination both removes matter and orders the carbon by the temperature treatment.

For toluene extraction, dry -14+30 mesh particles of the two cokes held in #1 Whitman filter paper were placed in toluene reflux for 24 hours. The material was then dried for 72 hours under vacuum in a drying tube in water reflux. Hence the maximum temperature treatment corresponded to the boiling point of toluene which is substantially below the process

Table 1. Elemental composition of the carbons.

Carbon Type	Weight %					
	C	H	S	N	O or Ash (by diff.)	VCM
Green Sponge Coke I	91.5	4.2	0.7	2.7	0.9	13.9
Green Needle Coke	95.0	3.6	1.1	0.3	<0.05	6.15
Calcined Sponge Coke II	96.4	0.3	1.0	1.3	1.0	<0.5

temperature of delayed coking.

Calcination was performed by placing dry +14 particles in a clean crucible in a cool furnace. Pre-purified nitrogen flushed the vessel of air. To insure absolutely no oxidation of the coke, the nitrogen was first passed through a bed of highly reactive char ($135 \text{ m}^2/\text{g}$ nitrogen BET surface area) held at the temperature of the crucible. The temperature monitored by thermocouple was slowly raised to 1300 K, held there for $\frac{1}{2}$ hour, and then lowered.

Weight losses (based on dry starting and ending samples) follow in Table 2 for the various treatments. Calcination of the supplied calcined sample (calcined sponge coke II) was performed by Union Oil by slowly lowering a sealed crucible into a preheated furnace. Again it was kept in a nitrogen (oxygen free) environment but calcination was to 1670 K.

5.2.2 Surface Area and Porosity of the Carbons

The nitrogen BET surface area and total porosity (for pores less than 271 \AA in radius) was also measured for all cokes and a spectroscopic carbon ground from electrodes from Union Carbide Corporation. These are given in Table 3. It is important to note that macropore volume and closed pore volume which Walker et al (15,16) have shown to be considerable for petroleum cokes was not measured. Microporosity should be the main contributor to surface area due to the high surface

Table 2. The various treatment of the coke particles. Weight losses are for a dry basis.

CARBON TYPE	Mesh Ranges	Treatment	Maximum Treatment Temperature (K)	Weight Loss (%)
Green Sponge Coke I	-14+30	Toluene Refluxed	384	4.3
Green Sponge Coke I	+14	Calcined to 1300 K	1300	10.4
Green Needle Coke	-14+30	Toluene Refluxed	384	1.1
Green Needle Coke	+14	Calcined to 1300 K	1300	*
Green Sponge Coke II	*	Calcined to 1670 K	1670	*

*Unavailable

Table 3. Nitrogen BET Surface Areas and Porosity for the various carbons. Porosity corresponds to pores of radii less than 271 Å.

CARBON TYPE	Treatment	Porosity (10^{-3} cm ³ /g)	Surface Area (m ² /g)	\bar{d}_{po} (10^{-8} cm)
Needle Coke	Green	0.76	0.32	95
Needle Coke	Toluene Refluxed	1.42	0.77	74
Needle Coke	Calcined to 1300 K	2.27	1.23	74
Sponge Coke I	Green	1.24	0.54	91
Sponge Coke I	Toluene Refluxed	2.00	0.75	107
Sponge Coke I	Calcined to 1300 K	2.46	1.42	69
Sponge Coke II	Calcined to 1670 K	1.87	0.48	150
Spectroscopic Carbon		2.73	1.24	88

to volume ratio for the very fine pores. As indicated previously (17) the large part of the surface area may be accounted for by these micropores.

From Table 3, it is seen that toluene refluxing and calcination increase porosity and surface area substantially for both samples. The greatest effect is noted for calcination as more material is removed. The average pore diameter indicated as obtained by assuming cylindrical pores provides a useful relative ratio between microporosity and total surface area. Calcination lowers this ratio for both cokes and hence appears to operate on the smaller pores, perhaps even opening some small pores. Toluene refluxing increased this ratio for the sponge coke on removing a substantial amount of material and decreased it for the needle coke on removing less material. The spectroscopic carbon revealed a similar ratio to the two cokes while the supplied calcined coke was anomalous in that it contained quite large pores. All materials measured consisted of -120+140 mesh particles ground from the respective starting materials.

5.3 Experimental

5.3.1 Devolatilization of the Green Coke

Pretreatment and flushing of reactant particles with inert gases such as nitrogen and helium are normally employed

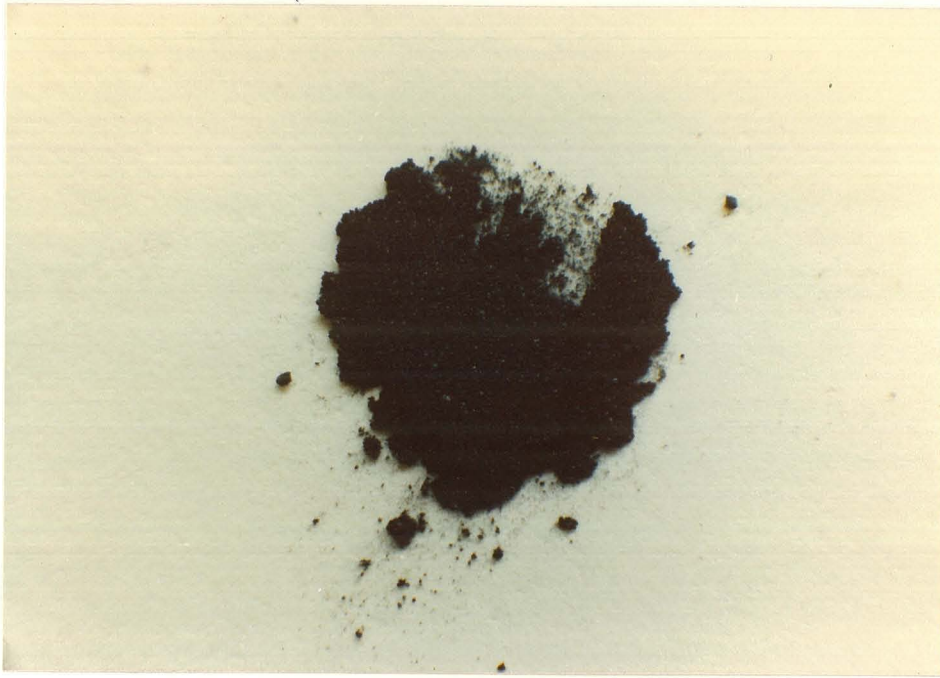
in most experimental situations with reaction rates measured upon exposure to the oxidizing gases. Due to the nature of particle addition for these experiments, this was not possible with the apparatus used. As discussed previously, these particles had very low specific surface area. Calculations assuming a monolayer of oxidizing species adsorbed which is far and above the worst case insured a completely negligible carbon conversion. Nevertheless devolatilization experiments were conducted by heating fine unclassified green sponge coke I samples described previously (17) in a quartz vessel from room temperature to 1000 ± 30 K at a heating rate from 300 to 400 K/Min. Samples were then held at 1000 K for three minutes. The sponge coke sample after being flushed with nitrogen for 48 hours and kept in nitrogen during the pyrolysis yielded a 14% weight loss. This compared to a 15% weight loss for heating in air. Reproducibility was $\pm 1\%$ for these experiments indicating no difference in initial weight loss for the two methods. Hence it would appear that any oxidizing agent present in the sample when charged reacts only with volatile fragments.

5.3.2 Agglomeration of the Green Coke

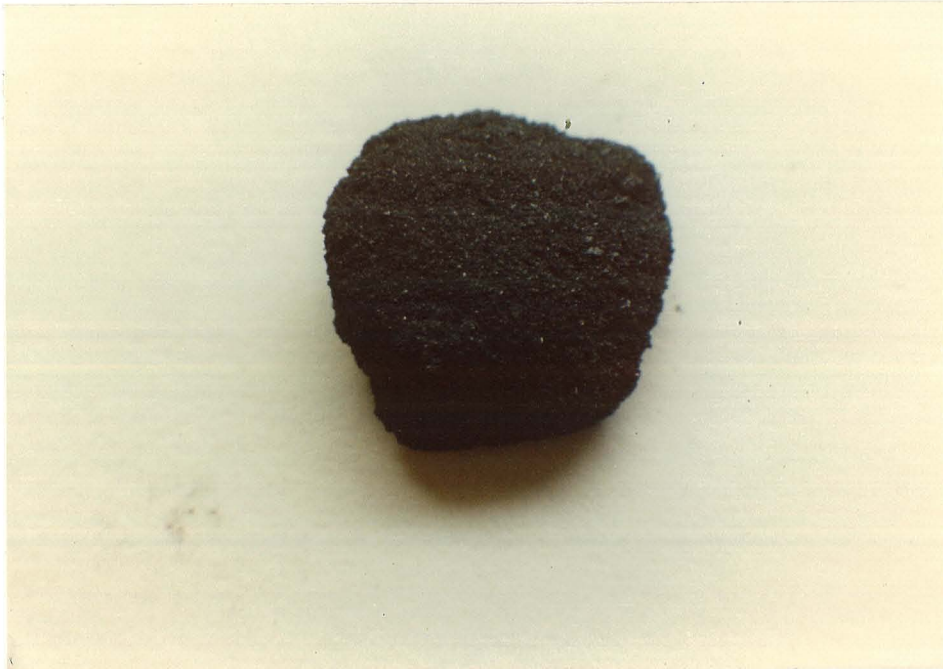
Agglomeration of the green sponge petroleum coke has been a problem in this laboratory as large chargings into reactors mass together and react much slower than the smaller chargings.

This agglomeration is illustrated for particles calcined by dropping an amount of the sample into a cylindrical metal block held at 1250 K. Particles were allowed one minute in the block and then discharged. Severe agglomeration for the unclassified and coarse green sponge coke I particles was observed while only very slight agglomeration was noted for needle coke particles. The green sponge coke I particles as seen in Figures 2 and 3 converged into a solid mass. Crushing the fine coke particle mass lightly with a spatula and comparing the nitrogen surface area before and after charging revealed the surface area to have increased slightly even though the light crushing by no means returned the fine coke particles to their previous small size (before heating).

Toluene refluxing the green sponge coke I particles removed the agglomerating character as shown in Figure 4. Presumably this is due to the extraction removing heavy oils which exit the particle as a liquid and subsequently condense to a carbonaceous solid which acts as a bridge between particles. Such behaviour has been observed visually by heating large green sponge coke I particles in a bunsen flame and seeing that liquid streams exiting from two particles in close proximity may converge providing the bridge.

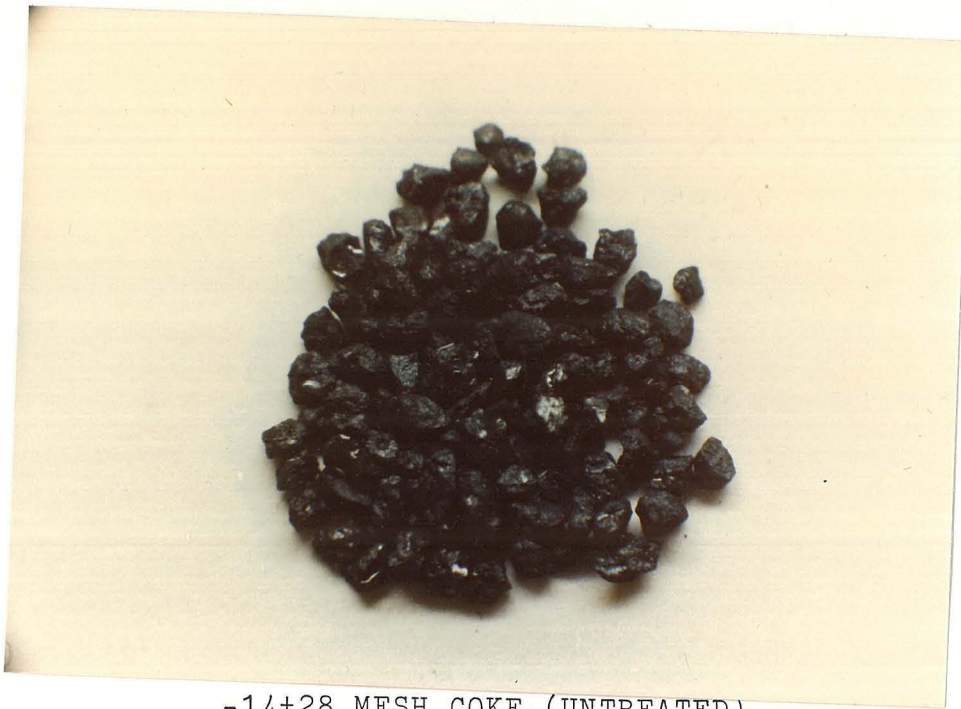


UNCLASSIFIED COKE (UNTREATED)



UNCLASSIFIED COKE (CALCINED)

Figure 2. Agglomeration of unclassified green sponge coke I particles by heat treatment to 1250 K.

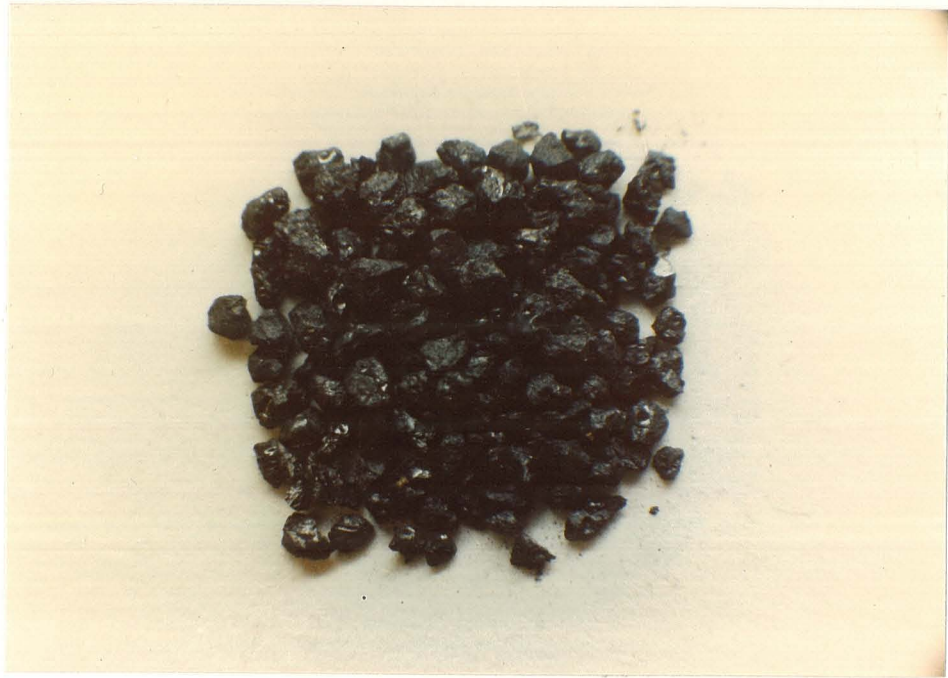


-14+28 MESH COKE (UNTREATED)



-14+28 MESH COKE (CALCINED)

Figure 3. Agglomeration of coarse green sponge coke I particles by heat treatment to 1250 K.



-14+28 COKE (TOLUENE REFLUXED ONLY)



-14+28 COKE (TOLUENE REFLUXED AND CALCINED)

Figure 4. Agglomeration prevention by toluene refluxing of coarse green sponge coke I particles. Heat treatment was to 1250 K.

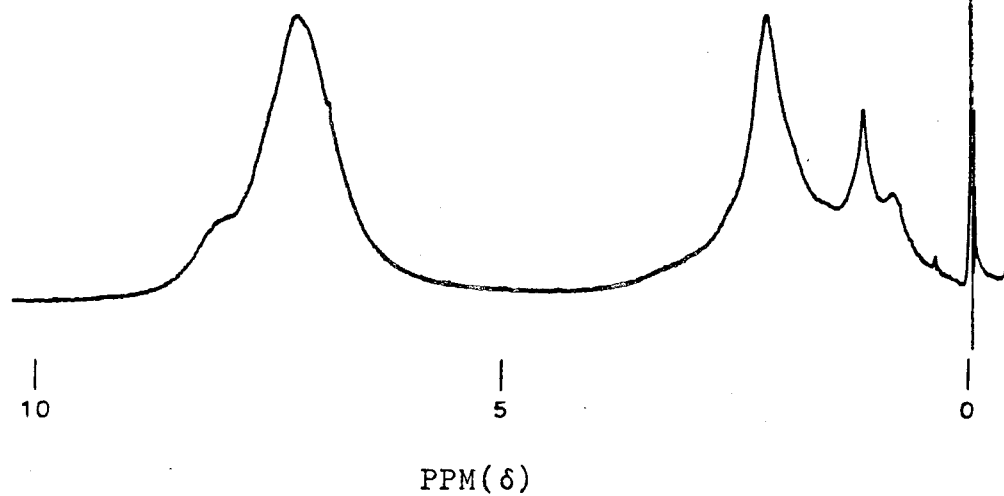
5.3.3 NMR Spectroscopy of the Toluene Extracts of the Green Cokes

The toluene extracts of the needle and sponge cokes were also investigated by NMR spectroscopy. Toluene solutions of the extracts were first filtered through #1 Whitman filter paper, and the toluene was evaporated from the sample in a tube under water reflux until only solid extract remained. Thereafter the coke extract was placed under vacuum and drying continued again under water reflux for a minimum of 72 hours assuring no residual toluene. The solid extract remaining was found to be soluble in chloroform. Hence deuterated chloroform was used as the solvent for NMR spectroscopy.

Figure 5 shows the ^1H NMR spectroscopy on a 90 MHz machine using TMS as a reference peak at 0 ppm. As seen the needle coke extract has a much sharper spectrum particularly so in the aliphatic region (<4.5ppm) than the sponge coke extract. This is to be expected due to the more highly aromatic feed-stock being used for the needle coke. For this coke the synthesis reactions in pyrolysis are not as necessary to clean up aliphatic disorder.

Table 4 indicates the hydrogen concentrations in the various ranges of the spectra by peak integrations on the 90 MHz spectrometer. These values represent the average of several runs with reproducibility being $\pm 1\%$ in the various ranges. Assignments of hydrogen types were made by reference to Bartle and Jones (18) for coal extract assignments which

SPONGE COKE EXTRACT



NEEDLE COKE EXTRACT

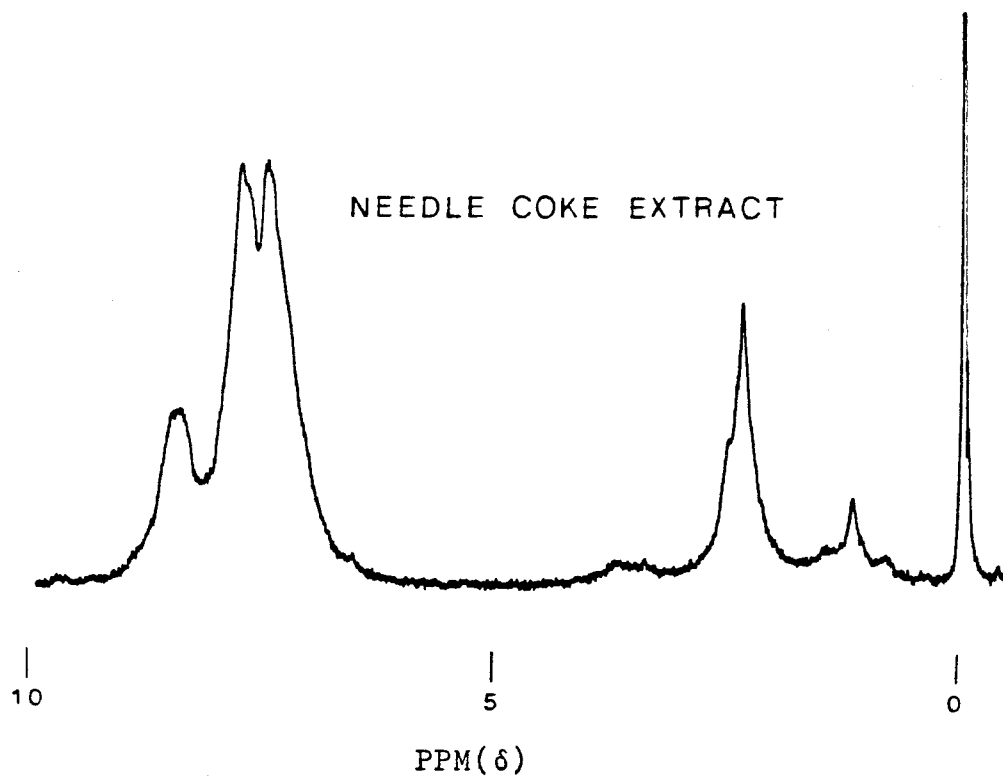


Figure 5. ^1H NMR spectra of the toluene extracts of the green sponge and green needle cokes.

Range-PPM (from TMS)	Designation	NEEDLE COKE EXTRACT			SPONGE COKE EXTRACT		
		Percentage (of total H)	Position (PPM)	Structure Type	Percentage (of total H)	Position (PPM)	Structure Type
5.5-9.0	Aromatic & Phenolic	71	8.5 7.8 7.6	Shoulder Peak Peak	49	8.1 7.3	Shoulder Peak
4.7-5.5	Olefinic	1					
2.0-4.5	Alpha to Aromatic	19	2.4	Peak	25	2.3	Peak
0.5-2.0	Beta to Aromatic & Further	9	1.2 0.9	Peak Shoulder	24	1.2 0.9	Peak Shoulder

Table 4. The hydrogen concentrations in the various ranges of the NMR spectra.

were similar to those for bitumen extracts (19). Hydrogens for both samples are concentrated in aromatic positions with the needle coke particularly concentrated in aromatics. The aromaticity of the carbon is higher than the hydrogen's due to the lower H/C ratio for aromatics as compared to aliphatics. Brown and Ladner (20) have proposed a method for calculating aromaticity from the C/H atomic ratio and the concentrations of alpha and beta hydrogens. By further assuming the C/H atomic ratio in these aliphatic linkages to be one-half and the overall C/H ratio to be that of the parent coke, the aromaticity of carbons in the sponge coke is approximately 87% as compared to 94% for the needle coke.

Structural similarities were observed particularly so in the aliphatic region. Both spectra revealed strong peaks at 2.3 to 2.4 ppm for alpha hydrogen. Beta and further removed hydrogen yielded peaks at 1.2 ppm and shoulders at 0.9 ppm for the two samples.

Figure 6 gives the higher resolution ^1H spectra on a 500 MHz NMR spectrometer for the needle coke. A great deal of fine structure is observed particularly in the aromatic region.

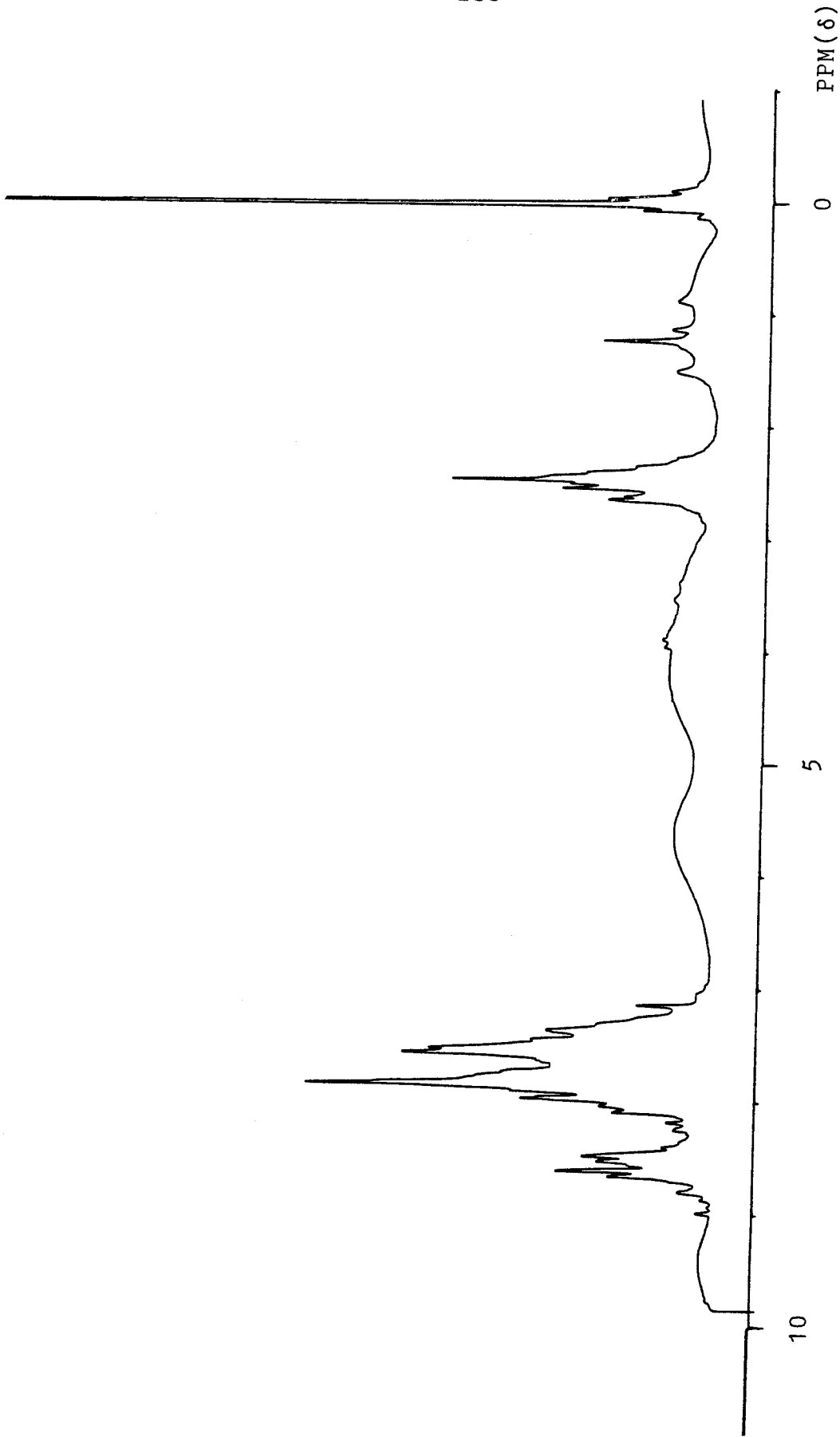


Figure 6. ^1H NMR spectra for the needle coke extract on a 500 MHz spectrometer.

5.3.4 Reaction Rate Experiments of the Carbons

The reaction rates with oxygen of the various cokes were measured in an apparatus described previously (17). Samples were reacted under a total flow of 145 scc/min in the bottom of a two inch crucible. -120+140 mesh particles were used, and the oxidant gas impinged after exiting a 3/16" ID mullite tube on the samples set one inch below. Reactor temperature was measured by thermocouple placed at the point where the reaction was taking place.

The oxidizing gas consisted of 0.10 atm. oxygen with a water vapor concentration of 3.1%. The balance of the gas consisted of nitrogen with total pressure being 1.0 atm. The water vapor has negligible effect on the reaction rate of the carbon due to the rate of the steam-carbon reaction being several orders of magnitude below the steam-oxygen reaction (21).

Offgases were monitored for CO_x by infrared absorption. The total carbon was then integrated by Simpson's rule from these readings which were taken at equally spaced time intervals. Hence carbon which escapes as non CO_x volatiles is not accounted for in the total carbon. Individual readings were then divided by the total integrated carbon revealing a specific rate. Carbon balances obtained by comparing the amount charged with the integrated carbon were substantially better than 90% for all samples. The amount of carbon charged to the reactor for an experiment was purposely kept small due to the

aforementioned agglomerating effects of the green cokes. No decline in the reaction rate was observed for these -120+140 mesh particles if chargings were kept below 10 mg.

5.4 Results and Discussion

The reaction rate of the parent green sponge and needle cokes and their derivatives were measured at 900 K. In all cases, the reaction rate vs. conversion curves initially rose to a maximum and then declined as conversion proceeded. Presumably this is due to a situation such as that portrayed by Gavalas (22) whereby the available surface area increases due to the widening of interior pores. Another similar but different explanation is the opening of closed pore volume in the cokes by the oxidation process. In any case, the explanation is due to the oxidation process opening greater surface area and revealing more surface reaction sites for the oxidant.

Figures 7 and 8 show the reaction rate curves for the sponge and petroleum coke samples respectively. That even the calcined cokes indicate a maximum reactivity substantiates the fact that the observed maxima are due to accessible surface area increasing by the two phenomena described above. It is also at once apparent that calcination substantially demotes the reactivity. Demotion occurs for both cokes due to the ordering of fixed carbon by the temperature treatment.

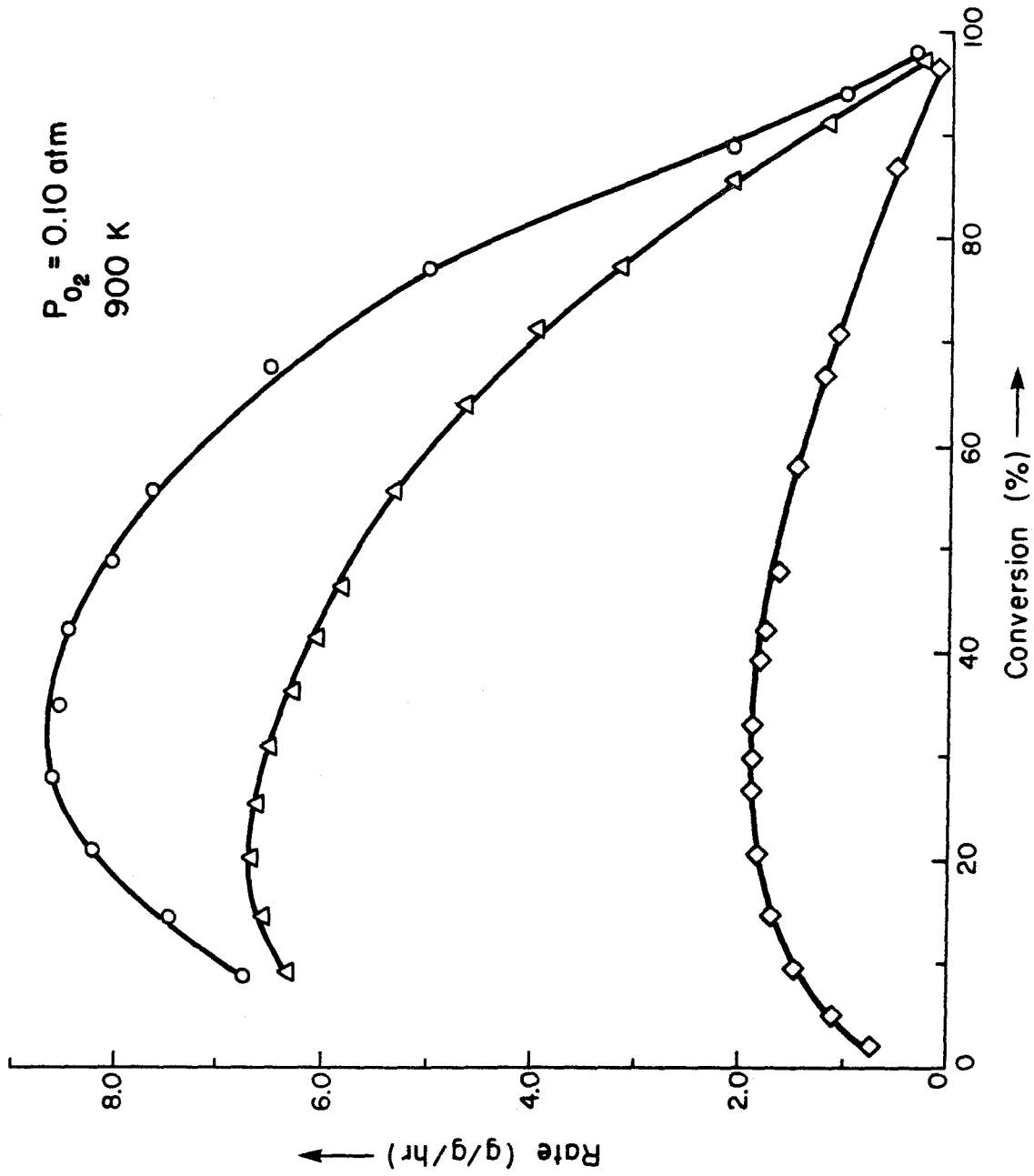


Figure 7. The reaction rate of -120+140 mesh sponge coke I. Δ , green sponge coke I; \circ , toluene refluxed sponge coke I; \diamond , calcined sponge coke I.

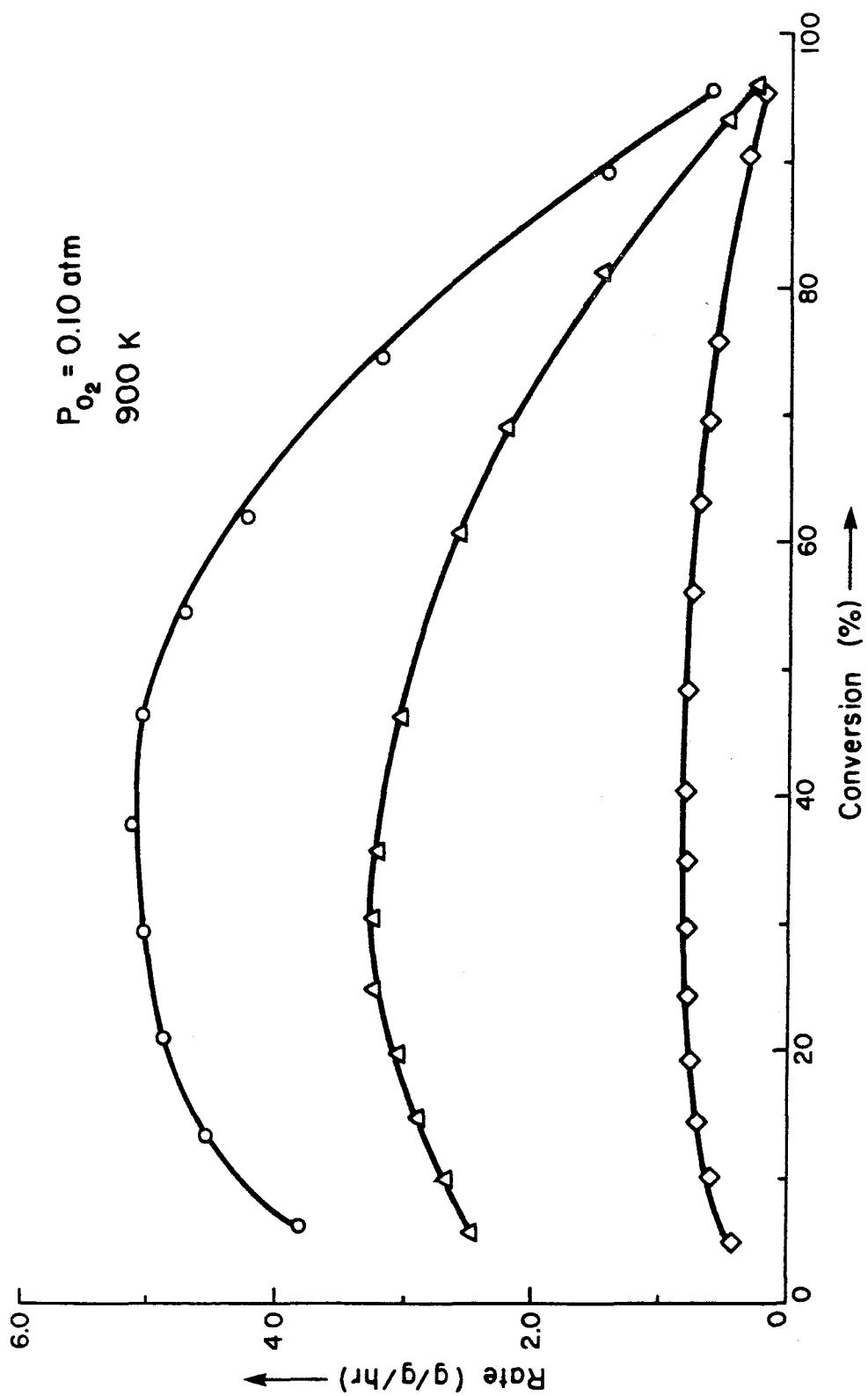


Figure 8. The reaction rate of -120+140 mesh needle coke. Δ , green needle coke; O, toluene refluxed needle coke; \diamond , calcined needle coke.

It is also seen that toluene refluxing substantially increases the reactivity in both cases. As this process removes material which is liquid at reaction temperatures and which would intuitively be more reactive than fixed carbon, it would seem that the increase in surface area is the reason for the increased reactivity.

Another notable feature as may be observed on Figures 7 and 8 or by referring to Table 5 is the shifting of the maxima to greater conversion when material is removed from the samples by either calcination or toluene refluxing. These effects shift the maxima for the needle and sponge cokes by roughly 10% in both cases as compared to the green samples. This shift is peculiar as it is apparently unrelated to temperature treatment or total reactivity.

Table 5 indicates the maximum rates for the two samples. If the maximum rates may be taken as characteristic, it is seen that the sponge coke and its toluene refluxed residue react roughly according to BET surface area. The needle coke which shows a greater relative increase in BET area also shows a greater relative increase in reactivity for the toluene refluxed sample. That it does not show as much increased relative reactivity may be due to the lowering of average pore diameter as shown in Table 3. This would effectively limit the increase due to transport limitations into the smaller pores. The sponge coke on the other hand showed an increase in average pore diameter and more closely matched the BET area increase.

-120+140 Mesh Sponge Coke						
Treatment	Maximum Rate (g/g/hr)	Maximum Rate Position (% Conversion)	Rate Green Rate (%)	Surface Area Green Surface Area (%)		
Green	6.66	19	100	100		
Toluene Refluxed	8.58	28	129	139		
Calcined to 1300 K	1.89	30	28	263		

-120+140 Mesh Needle Coke						
Treatment	Maximum Rate (g/g/hr)	Maximum Rate Position (% Conversion)	Rate Green Rate (%)	Surface Area Green Surface Area (%)		
Green	3.27	28	100	100		
Toluene Refluxed	5.14	38	157	241		
Calcined to 1300 K	0.81	36	25	384		

Table 5. The maximum rates for the needle and sponge petroleum coke samples at 900 K. The oxidant is 0.10 atm. oxygen.

Both sample reactivities lagged the relative increases in areas due most likely to some transport limitations in accessing all increased area.

Another notable effect which requires discussion is the heating effect on pore volume and surface area when the sample is charged. As shown here slow calcination increases the pore volume and area substantially. Okada et al (23) have studied the effect of rapid heating to 3100 K on cokes pretreated to greater than 1300 K. These results revealed a substantial effect of heat treatment on total closed pore and open pore volume. Thus rapid heating by charging the cold green coke into the furnace is expected to increase surface area and pore volume although it is apparent that such increases are proportional to starting BET area as discussed above.

Another feature is the change in specific reactivity divided by surface area or S . For green needle compared to green sponge the S ratio is 0.8 due to the greater aromaticity of the needle coke. Calcining to 1300 K decreased the S ratio to 0.5 indicative of the needle coke cleaning up its structure and aligning more readily than the green sponge sample. Apparently some of this effect is due to less aliphatic disorder for the needle specimen as shown in Figure 5. Thus while BET surface area is a rough indicator of the reactivity of green coke samples, higher temperature treatment decreases

the ratio and more greatly reflects the precursor to the coke sample (ie, the material feedstock for the delayed coking operation).

It is important to refer to previous results (17) at this point. The BET areas of different particle sizes were roughly indicative of reactivity. At 1286 K, -120+140 mesh green sponge coke I particles as compared to unclassified sponge coke I particles had a BET surface area ratio of 0.4 and the ratio of their reactivities was 0.7. -200 mesh coke particles had 1.2 times the surface area of the unclassified coke and had 1.0 times the reactivity.

The temperature effect was investigated for the calcined sponge coke II and the spectroscopic carbon. As is seen and expected by comparing Figure 9 for calcined sponge coke II and Figure 10 for the spectroscopic carbon, the spectroscopic carbon is much less reactive due to its higher temperature treatment. Comparing the very similar curves at 912 K for the coke and 1085 K for the spectroscopic carbon reveal that the relative sharpness of the maxima is strictly dependent on the reactivity of the sample.

Table 6 indicates the maximum rates and their positions as percent conversion. The temperature effect is to shift the maximum positions to lower conversions. The 1151 K curves for the spectroscopic carbon represent the worst case for reproducibility as the reaction rate here was the highest

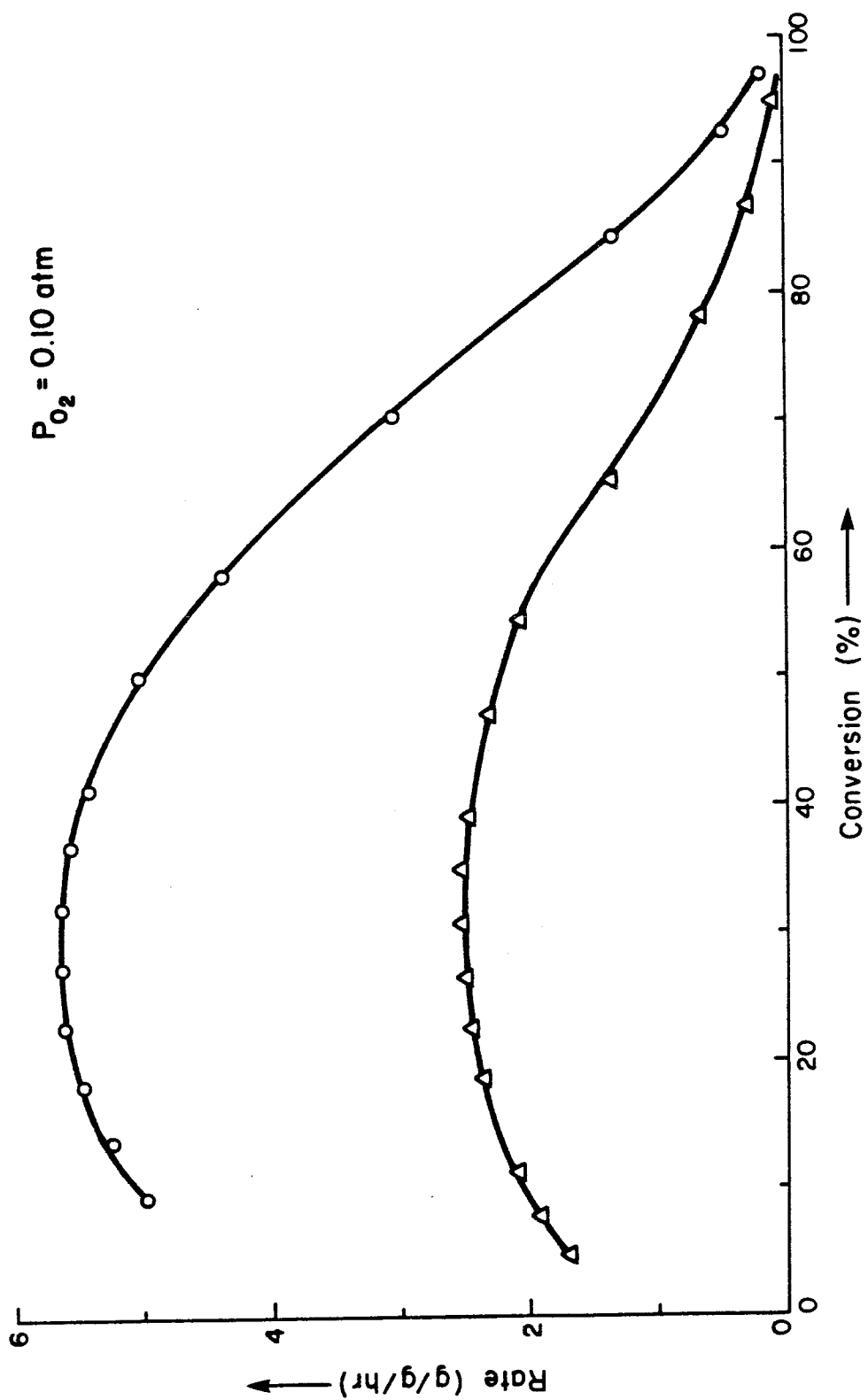


Figure 9. The reaction rate of -120+140 mesh calcined sponge coke II. Δ, 912 K and 0.10 atm O_2 ; O, 964 K and 0.10 atm O_2 .

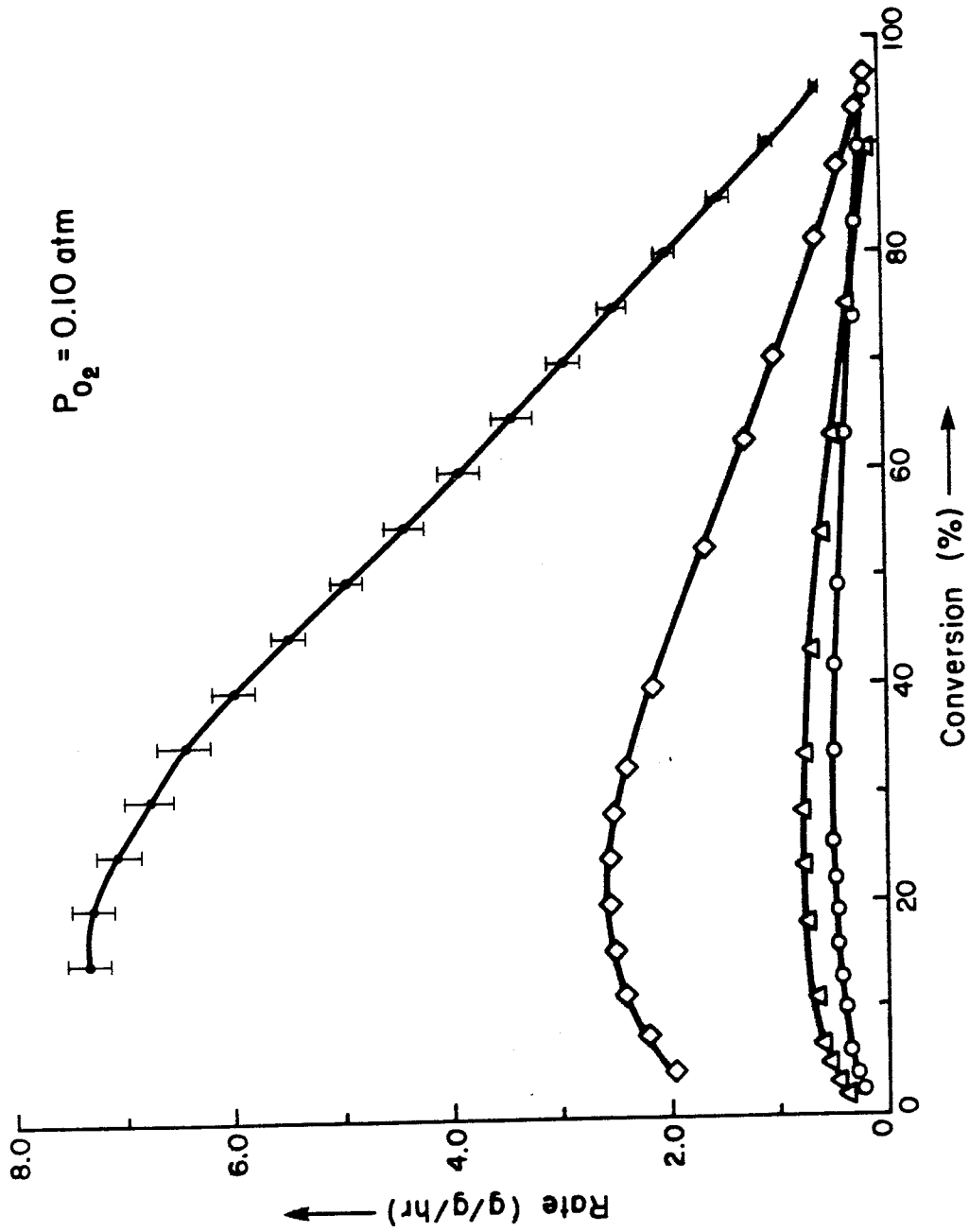


Figure 10. The reaction rate of -120+140 mesh spectroscopic carbon. O, 964 K; Δ, 1010 K; ◇, 1085 K; ■, 1151 K.

Table 6. The change of the maximum rates with temperature for the calcined sponge coke II and the spectroscopic carbon.

-120+140 Mesh Calcined Sponge Coke II		
T(K)	Maximum Rate (g/g/hr)	Maximum Rate Position (% Conversion)
912	2.52	33
964	5.64	28
-120+140 Mesh Spectroscopic Carbon		
T(K)	Maximum Rate (g/g/hr)	Maximum Rate Position (% Conversion)
964	0.49	27
1010	0.77	27
1085	2.57	22
1151	7.19	16
1151	7.46	17

resulting in fewer total data points in arriving at the curves. Reproducibility was found to be no worse than $\pm 4\%$ of the specific rate throughout the conversion curve.

Figure 11 is an Arrhenius plot of the maximum rates. Notable curvature is apparent for the spectroscopic carbon which was investigated over the widest temperature range. Thus the maximum rate would not be expected to follow a strictly linear pattern for all samples. However as curvature is slight, the maximum rates may be linearly extrapolated between the ranges and somewhat outside the ranges without great error.

It is also noted that the supplied calcined sponge coke II has a similar reactivity to the calcined sponge coke I. However S is much higher for calcined sponge coke II thus further indicating different precursors have substantially different reactivities after increasing calcination.

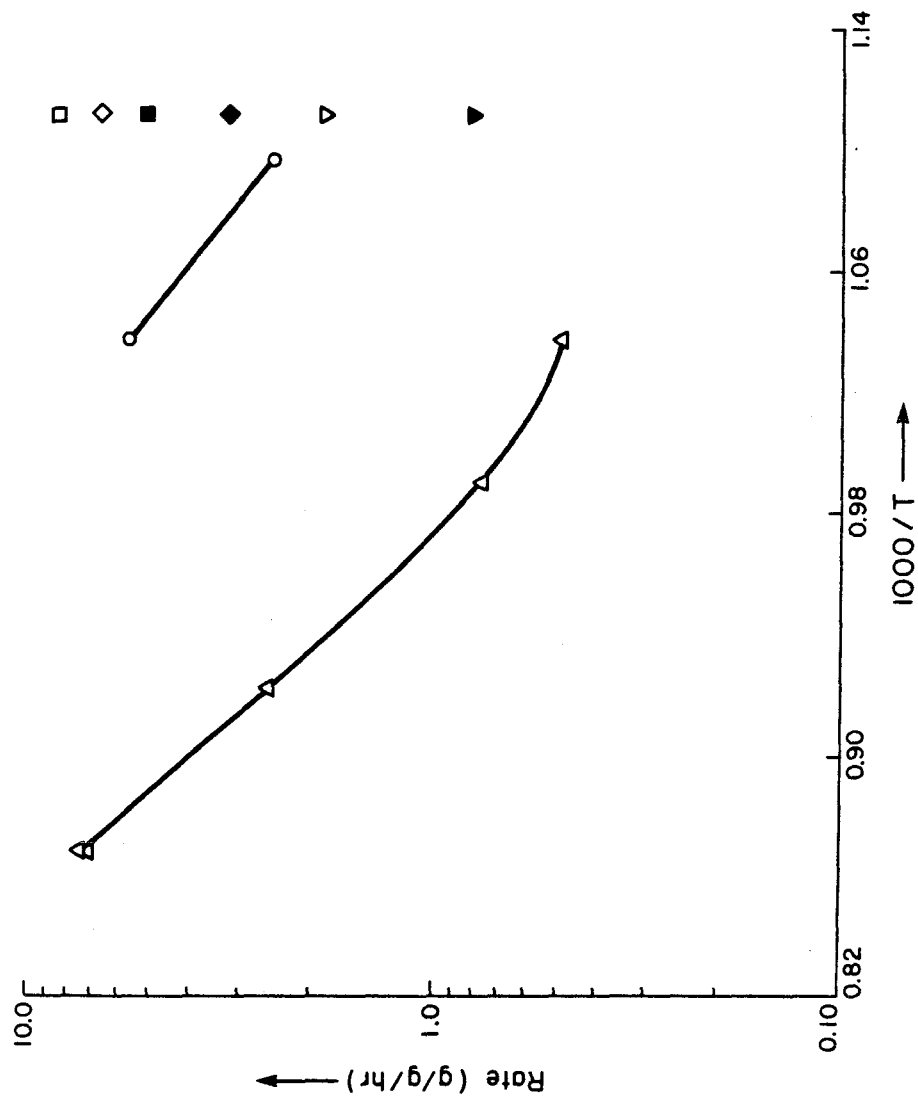


Figure 11. The Arrhenius plot of the maximum rates for the samples for 0.10 atm oxygen. △, Spectroscopic Carbon; ○, Calcined Sponge Coke II; ◇, Green Sponge Coke I; □, Toluene Refluxed Sponge Coke I; ▽, Calcined Sponge Coke I; ◆, Green Needle Coke; ■, Toluene Refluxed Needle Coke; ▼, Calcined Needle Coke.

5.5 Conclusions

1. Calcination and toluene refluxing substantially increase nitrogen BET surface area and microporosity for petroleum coke in the pregraphitization regime.

2. Large petroleum coke particles (-120+140 Mesh) have a reaction rate-conversion curve which passes through a maximum. The position of the maximum rate is dependent upon the pretreatment to which the coke is subjected.

3. Sponge coke has substantially more disorder than needle coke in its aliphatic linkages. This disorder apparently results in increased reactivity of calcined sponge coke samples as compared to calcined needle coke.

4. The nitrogen BET surface area of green samples is a relatively good indicator of reactivity for cokes which are not subjected to previous heat treatment. Heat treatment makes the reactivity of the coke less dependent on surface area and more dependent on the precursor feedstock.

5. Toluene refluxing prevents agglomeration of green sponge coke by removing substantial amounts of low melting materials. The apparent increase in reactivity by toluene refluxing is due to increased surface area by a process which does not order the carbon in the coke.

REFERENCES

1. Mantell, C. L., in Petroleum Derived Carbons, ACS Symposium Series 21, p. 18, American Chemical Society, Washington, D. C. (1976)
2. Fitzer, E., Mueller, K., and Shaefer, W., Chemistry and Physics of Carbon, 7, 237, (1971)
3. Warren, B. E., and Biscoe, J., J. Appl. Phys., 13, 364 (1942)
4. Warren, B. E., Phys. Rev., 59, 693 (1941)
5. Warren, B. E., and Bodenstein, P., Acta. Crystal., 20, 602 (1966)
6. Franklin, R. E., Proc. Royal Soc., (London), A209, 196 (1951)
7. Mering, J., and Maire, J., J. Chim. Phys., 57, 803 (1960)
8. Schiller, C., Mering, J., Cornuault, P., and Duchaffaut, F., Carbon, 5, 385 (1967)
9. Schiller, C., Mering, J., Cornuault, P., and Duchaffaut, F., Carbon, 5, 507 (1967)
10. Maire, J., and Mering, J., Proceedings of the Fourth Conference on Carbon, p. 345, University of Buffalo, 1959, Permagon Press, New York (1960)
11. Ruland, W., Acta. Crystal., 18, 992 (1965)
12. Fishbach, D. B., Chem. Phys. Carbon, 7, 1 (1971)
13. Akamatu, H., and Kuroda, H., Proceedings of the Fourth Conference on Carbon, p. 355, University of Buffalo, 1959, Permagon Press, New York (1960)

14. Pacault, A., Chemistry and Physics of Carbon, 7, 107 (1971)
15. Walker, P. L. Jr., Rusinko, F., Rakszawski, J. F., and Liggett, L. M., Proceedings of the Third Conference on Carbon, p. 643, University of Buffalo, 1957, Permagon Press, New York (1959)
16. Kotlensky, W. V., and Walker, P. L. Jr., Proceedings of the Fourth Conference on Carbon, p. 423, University of Buffalo, 1959, Permagon Press, New York (1960)
17. Chapter 4
18. Bartle, K. D., and Jones, D. W., Adv. Org. Chem., 8, 317 (1972)
19. Speight, J. G., Fuel, 49, 76 (1970)
20. Brown, J. K., and Ladner, W. R., Fuel, 39, 87 (1960)
21. Walker, P. L. Jr., Rusinko, F. Jr., and Austin, L. G., Advances in Catalysis, 11, 133 (1959)
22. Gavalas, G. R. AIChE Journal, 26, 577 (1980)
23. Okada, J., Sekiguchi, A., and Ishii, T., Proceedings of the Fifth Conference on Carbon, Volume I, p. 497, Pennsylvania State University, 1961, Permagon Press, New York (1962)

CHAPTER 6

THE PARTICLE LOADING EFFECT IN
MOLTEN PHOSPHATE SLURRIES

6.1 Introduction

To extend the results presented in Chapter 4, it is necessary to include the effect of particle loading on the reaction rate in a bubbling molten salt reactor. Referring to the results of Chapter 3, the low solubility of oxygen in the melt apparently makes the direct mechanism dominant as compared to the indirect mechanism. And with reference to Chapter 2, we may expect a complex fluid mechanical effect due to the nature of bubble-particle contacting.

Here we shall begin by analyzing specific cases of the direct reaction mechanism. The overall scheme it is recalled consists of two series rate processes -- bubble particle contacting and chemical conversion of the particles. Specifically, we shall determine what types of overall reaction rates are observed as a function of particle loading. Trends so predicted will then be compared to the measured reaction rate of petroleum coke particles in bubbling molten salt reactors.

6.1.1 Theory

To examine the direct mechanism, it is necessary to refer to the results of Chapter 2 and 3. Here we will consider a bubble of constant radius rising through a bubble column of total height, h . The rise velocity is only weakly affected by particle loading as was demonstrated

in Chapter 2, so we shall assume the rise velocity, u_B , to be constant. For a particular particle radius, r_B , then the group f is a constant:

$$f = 3 \pi \eta r_B r_P \quad (1)$$

From Chapter 3, the rate of the direct mechanism is:

$$R_{dir} = k_{RG} N_{PI} A_{PI} C_G \quad (2)$$

Here k_{RG} is the reaction velocity which is constant for isothermal conditions. We shall assume a constant gas concentration, C_G . This, of course, assumes the particle reaction rate is relatively slow. A given particle's surface area at the interface, A_{PI} , is constant for similar particles. Hence we have:

$$R_{dir} = k' N_{PI} \quad (3)$$

Here k' incorporates the above constants. But we note that the number of particles on the interface, N_{PI} , is the integral of the bubble-particle collision rate over time:

$$N_{PI} = \int R_c dt \quad (4)$$

Now for the case of the bubble linearly picking up particles all the time it traverses up the column, we may assume as in Chapter 3 that:

$$N_{PI} = f u_B \frac{N_P}{V} \tau \quad (5)$$

Here N_p is the total number of particles in the column with V being the column's total liquid volume. τ is the average residence time in the column or $(h/2 u_B)$. The specific rate, R_I is R_{dir} divided by a constant, m , multiplied by the total number of particles, N_p .

$$R_I = \frac{k' f h}{2 m V} \quad (6)$$

Hence the reaction rate for this case is independent of the total number of particles, N_p .

Now we know that a given bubble can only hold a maximum number of particles. For concentrated particle slurries, saturation of the bubble may occur as the bubble is created or very close to the bottom of the reactor. In this case the specific rate is given by:

$$R_{III} = \frac{(k' N_s)}{m} \left(\frac{1}{N_p} \right) \quad (7)$$

Here N_s is the maximum number of particles that may be accommodated by a given bubble. For this case, R_{III} is inversely proportional to the number of particles. That is, the addition of more particles to our reactor will not result in an increased reaction rate as our bubbles are saturated with particles. N_{pI} from equation 4 is now the constant value, N_s .

Consider now the intermediate case. Here the bubble saturates part way up the column as shown in Figure 1.

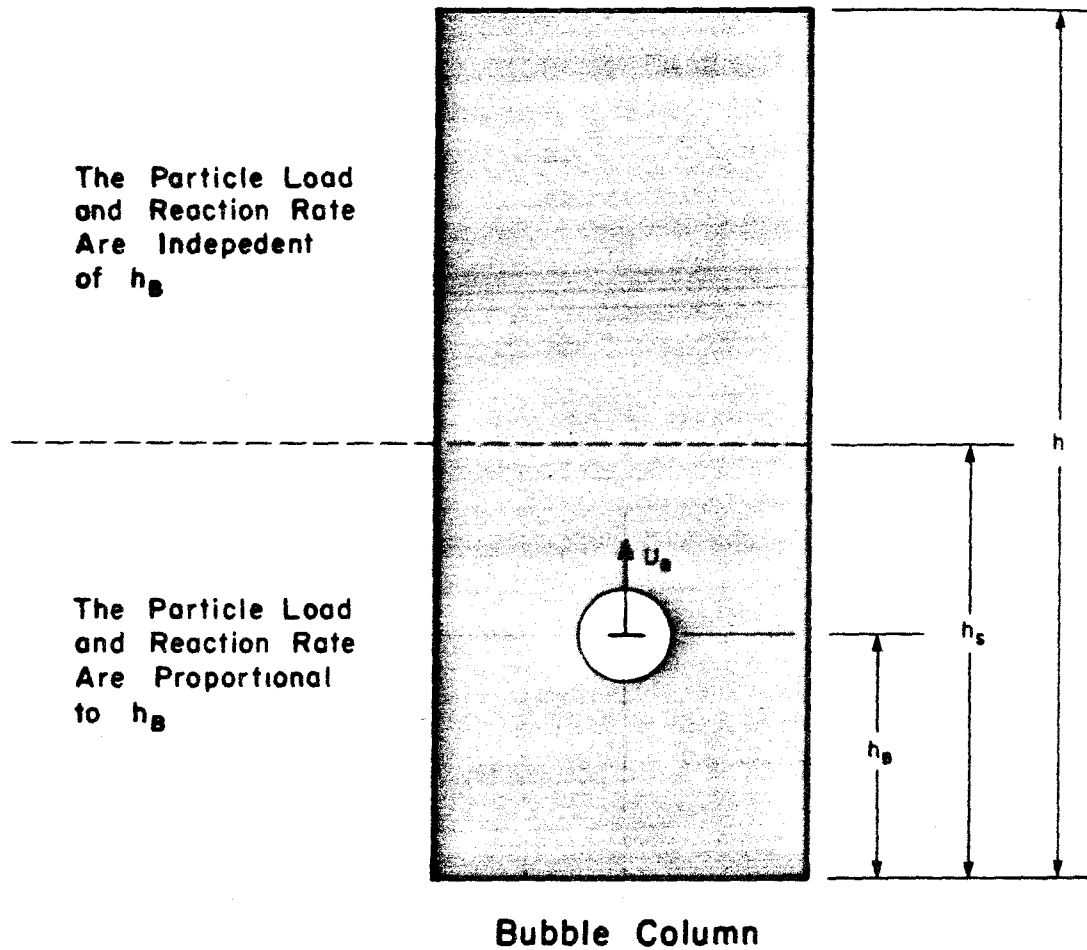


Figure 1. For intermediate particle loadings, the bubble may become saturated during its ascent through the column.

We must now divide the residence time into two parts. The first part corresponds to the bubble going from no particles to complete saturation at h_s . Assuming saturation is approached in a linear manner:

$$h_s = \frac{N_s V}{f N_p} \quad (8)$$

Now the average specific reaction rate, $R_{II,b}$, in the bottom section is given by:

$$R_{II,b} = \frac{k' N_s}{2 m N_p} \quad (9)$$

For the top section, the specific reaction rate is constant and exactly twice $R_{II,b}$. Multiplying these two reaction rates by their respective residence times and summing gives the total conversion of carbon by a given bubble. The rate of conversion is then just this sum divided by the total residence time of the bubble in the column:

$$R_{II} = \frac{u_B}{h} \left[\frac{k' N_s}{2m N_p} \left(\frac{h_s}{u_B} \right) + \frac{k' N_s}{m N_p} \left(\frac{h-h_s}{u_B} \right) \right] \quad (10)$$

For convenience we employ the constants:

$$\alpha = \frac{k' N_s}{m} \quad (11)$$

$$\beta = \frac{N_s V}{2 f h} \quad (12)$$

With these, we then have:

$$R_{II} = \frac{\alpha}{N_P} - \alpha\beta/N_P^2 \quad (13)$$

R_{II} is equal to R_I when:

$$N_P = \frac{N_S V}{f h} \quad (14)$$

Thus the rate will continuously pass through the three regimes given in Table 1. Dilute particle loadings were investigated in Chapter 4. We will proceed here to examine the intermediate and concentrated cases experimentally.

Before proceeding, one final clarification is required. In all instances, the reaction rate is proportional to the total number of bubbles in the column. However at very dilute particle loadings and for large bubbles, we may jeopardize the assumption of a constant particle number density, N_P/V . In this case, then the dependence of the reaction rate on the number of bubbles will lessen. This may explain why no flowrate effect was observed in Chapter 4 for dilute concentrations. Such effects are in order if bubbles sweep out a significant fraction of the column cross-section.

No Saturation	Intermediate Saturation	Complete Saturation
<p data-bbox="393 1540 419 1668"><u>Case I</u></p> <p data-bbox="488 1455 546 1747">Dilute Particle Slurry</p> $R_I = \frac{\alpha}{4\beta}$	<p data-bbox="393 991 419 1119"><u>Case II</u></p> $R_{II} = \frac{\alpha}{N_P} - \frac{\alpha\beta}{N_P^2}$	<p data-bbox="393 336 419 485"><u>Case III</u></p> <p data-bbox="488 272 546 563">Concentrated Particle Slurry</p> $R_{III} = \frac{\alpha}{N_P}$

Table 1. The three possible cases for the direct reaction mechanism.

6.2 Experimental

For these experiments, calcined sponge coke II particles were selected. These particles are not agglomerating nor are they temperature sensitive as they were preheated to 1600 K. Strict size ranges were used which included -30+35 mesh and -120+140 mesh. The properties of this coke are detailed in Chapter 5.

Two types of reactors were used. One had the same dimensions as Reactor II in Chapter 4. The only difference was that it employed an alumina crucible and omitted the mullite thermocouple protection tube. The other reactor was an expanded version of Reactor II. The dimensions of this reactor are given in Table 2. For clarity, the former reactor will be denoted the short reactor while the latter expanded version will be denoted the long reactor. As no thermocouple protection tube was used, the temperature was measured by dipping an inconel sheathed thermocouple in the bubbling salt bath before and after the reaction rate experiments.

For the chemical reactions carried out in this chapter, the input oxidant was 0.10 atm oxygen. The experimental system of Chapter 4 was used with the steam generator at room temperature. Consequently there was a small concentration (3.1%) of steam in the reactant gas. However, as the steam is much less reactive, its contribution to the reaction

Table 2. The dimensions of materials used in constructing the long reactor. All dimensions of the mullite materials are given in inches.

	ID	x	OD	x	LENGTH
REACTANT INJECTION TUBE	3/16"	x	1/2"	x	36"
PRODUCT EXIT TUBE	1/4"	x	3/8"	x	18"
CERAMIC MULLITE CRUCIBLE	2"	x	2 1/4"	x	18"
SOLID INJECTION TUBE	7/8"	x	1"	x	12"
REACTANT TUBE BUBBLE INJECTION POINT (ABOVE THE INSIDE BASE OF THE CERAMIC MULLITE CRUCIBLE)	7/8"				
REACTANT TUBE INCLINATION (FROM VERTICAL)	1.3°				
REACTOR FREE VOLUME	780		cm ³		

rate may be neglected as discussed in Chapter 5. The total pressure of the reactor was one atmosphere.

As we are considering the addition of large amounts of particles in this chapter, the reaction rate will diminish as the oxidant is consumed. This may be corrected to the rate at zero conversion by assuming a reaction order of unity as discussed in Chapter 3.

Salt chargings and ambient molten salt heights for the two reactors are given in Table 3. The molar ratio of sodium oxide to phosphorus pentoxide was selected to be 1.31 which is the same as that used in Chapter 4.

For these experiments, an extension of the analysis for bubbling molten salt reactors was required. In Chapter 4, only the flowrate was measured. Here we also will obtain the average bubble size as well as an estimate of the gas hold-up.

To measure the average bubble size, we first observe that when a bubble bursts on the surface of the molten bath, a pressure pulse is produced. This pressure pulse then propagates through the product tube. For the cold model described in Chapter 2, such pressure pulses could be detected by a piezoceramic crystal both on the input gas stream (measuring the pulse as the bubble was expelled from the submerged orifice) and on the exit gas stream. Due to the necessity of heating the input flow, the crystal could not

Table 3. Reaction parameters for the short and long reactors.

SHORT REACTOR:	SODIUM PHOSPHATE SALT	220 grams (Dry Basis)*
	SALT COMPOSITION	$\text{Na}_2\text{O}/\text{P}_2\text{O}_5 = 1.31$
LONG REACTOR:	SODIUM PHOSPHATE SALT	440 grams (Dry Basis)*
	SALT COMPOSITION	$\text{Na}_2\text{O}/\text{P}_2\text{O}_5 = 1.31$

THE AMBIENT SALT HEIGHT ABOVE THE INSIDE BASE OF THE MULLITE CRUCIBLE AND THE AMBIENT SALT HEIGHT ABOVE THE POINT OF BUBBLE INJECTION (THE CASE WITH NO GAS FLOW THROUGH THE REACTOR).

T (K)	SHORT REACTOR		LONG REACTOR	
	MOLTEN SALT HEIGHT ABOVE BASE (cm)	HEIGHT ABOVE BUBBLE INJECTION (cm)	MOLTEN SALT HEIGHT ABOVE BASE (cm)	HEIGHT ABOVE BUBBLE INJECTION (cm)
965	-	-	10.49	8.27
976	5.70	4.75	-	-
1000	5.72	4.77	-	-

*The salt weight is for the dehydrated salt.

be attached to the input gas stream. That is, heating crystals beyond their Curie temperatures (which are quite low for these crystals) will destroy their piezoelectric properties. Hence the crystal was attached to the product flow tube downstream from the reactor a sufficient distance to allow air cooling of the product gases. Figure 2 presents the schematic of the piezoceramic bubble detector. The crystal was 0.98 inches in diameter and 0.01 inches thick with attached silver electrodes. It was obtained from Gulton Industries. After attaching chromel leads, the crystal was suspended by the leads inside of a funnel as shown in Figure 2. This geometry was found to give an adequate response. The environment of the detector (ie, with the electrical load on the furnace) necessitated shielding the detector and its leads. This was accomplished with grounded aluminum foil.

Sample oscilloscope outputs are included in Figures 3 through 5. As is seen, the output is well above the noise level. Baseline fluctuation was observed due to the suspension of the crystal by the leads. Firm attachment, while eliminating baseline fluctuations, gave a diminished signal. As the rise time for bubble's pressure pulse is only about 20 milliseconds, it is apparent that very rapid bubbling rates may be detected.

The gas hold-up was measured by dipping a mullite tube into the melt. The height at a certain flowrate was then

Pressure Pulse (—) Traverses Outlet Tube and Impinges on Crystal

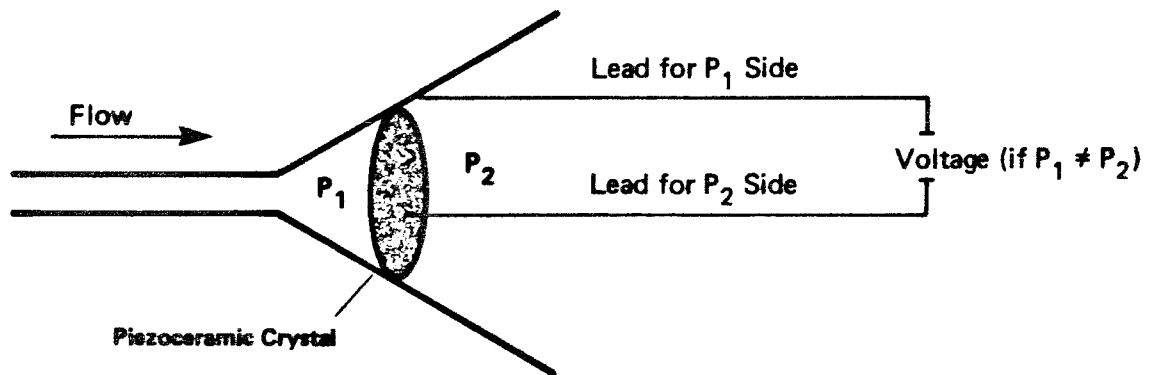
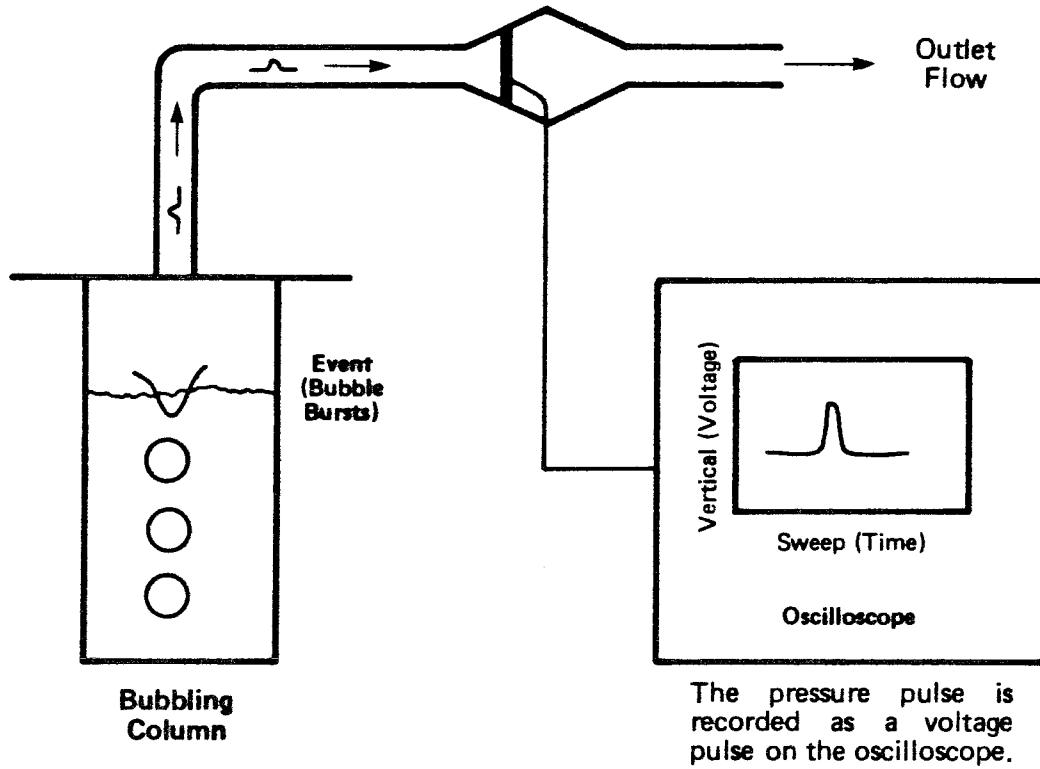
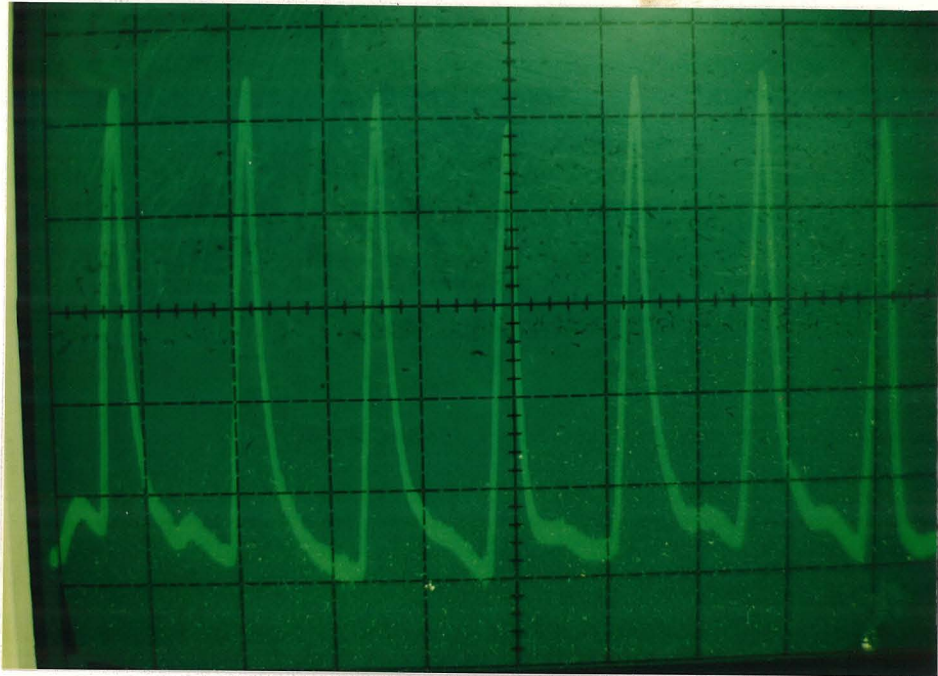
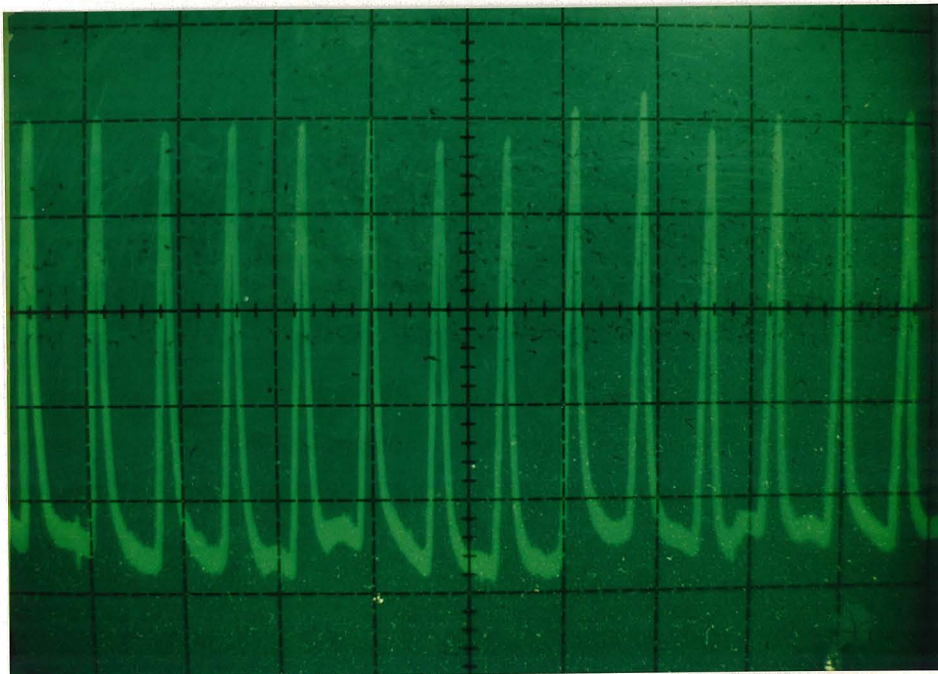


Figure 2. The Piezoceramic Bubble Detector

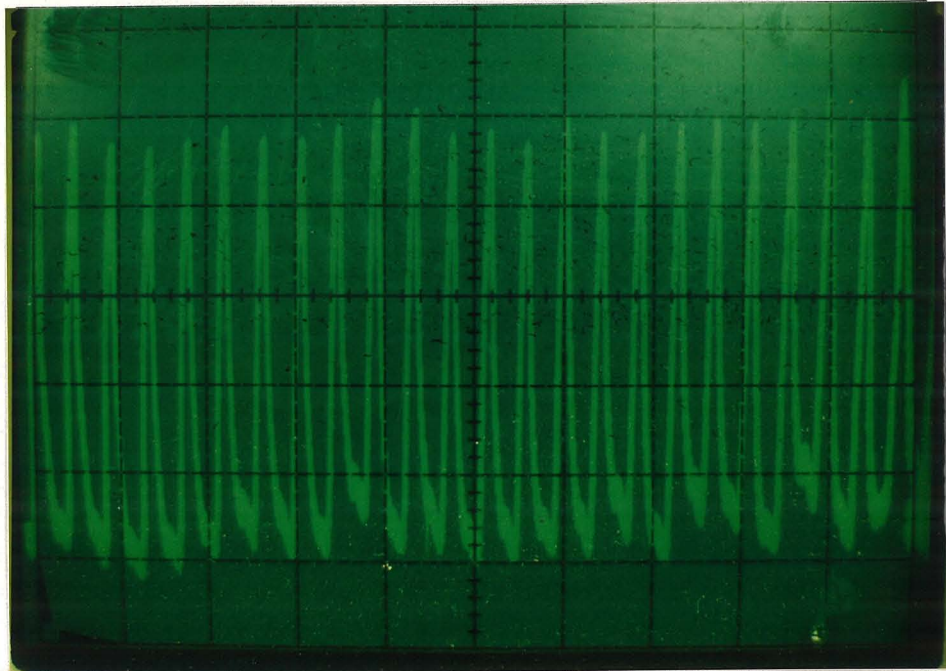


Superficial Velocity = 0.13 cm/s
Bubble Volume = 4.1 cm³

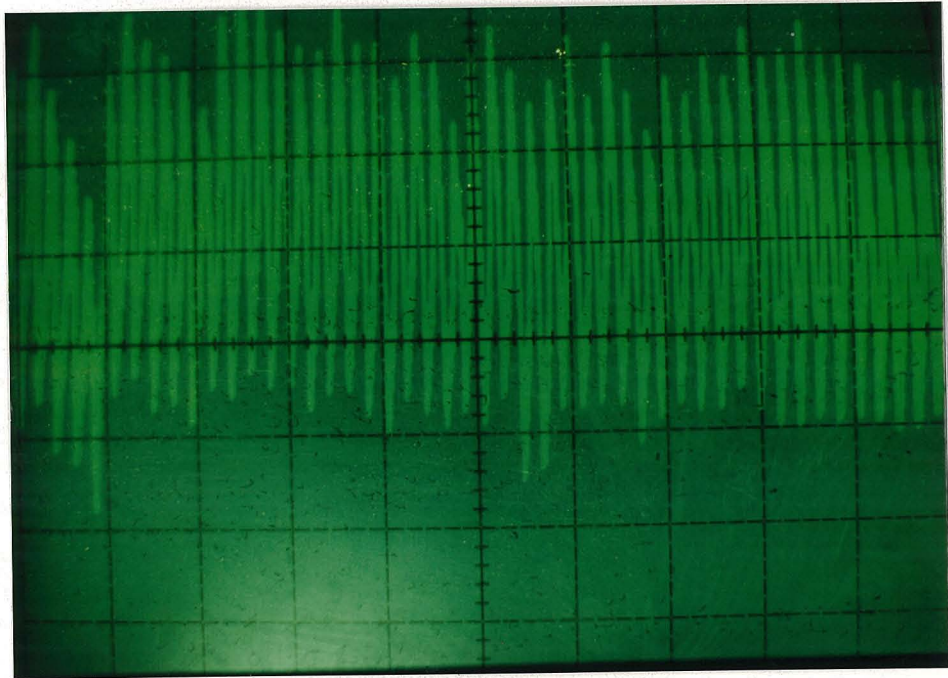


Superficial Velocity = 0.38 cm/s
Bubble Volume = 5.5 cm³

Figure 3. Bubble detection in the molten salt reactor at low flowrates at 976 K. The horizontal sweep is one second per division.



Superficial Velocity = 0.94 cm/s
Bubble Volume = 8.3 cm³



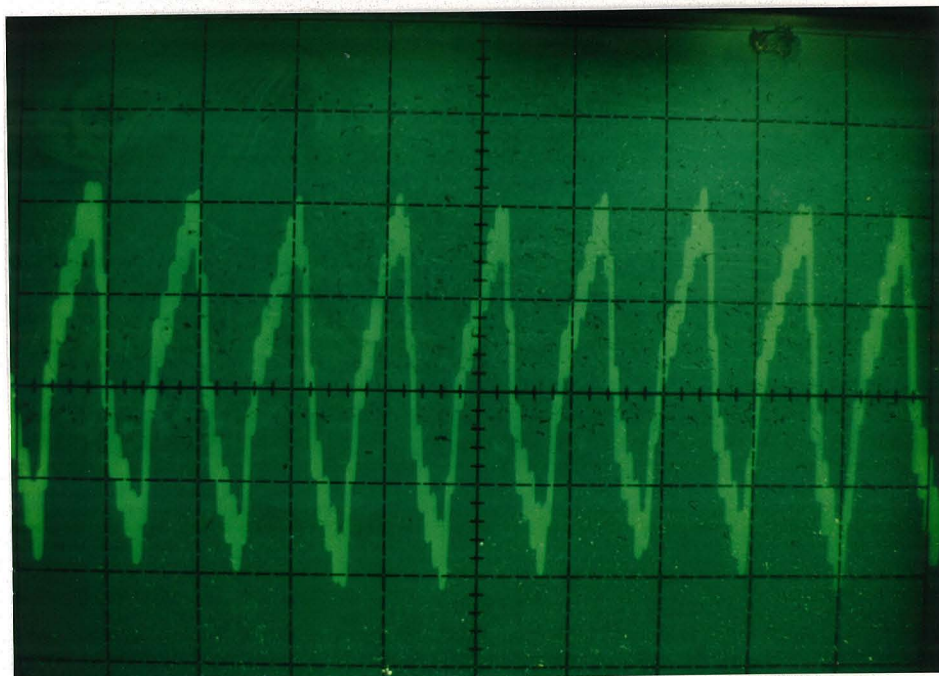
Superficial Velocity = 2.27 cm/s
Bubble Volume = 10.4 cm³

Figure 4. Bubble detection in the molten salt reactor at high flowrates at 976 K. The horizontal sweep is one second per division.



Superficial Velocity = 0.38 cm/s

Bubble Volume = 5.5 cm³



Superficial Velocity = 2.27 cm/s

Bubble Volume = 10.4 cm³

Figure 5. The difference in peak shapes for bubble detection in the molten salt reactor at low and high flowrates. The horizontal sweep is 0.2 seconds per division. The temperature is 976 K.

compared to the ambient height thus yielding the hold-up, ϵ . This method is admittedly very poor. The dipstick acts as an obstruction and modifies the gas hold-up by its presence in the flow. The molten salt was also found to be irregularly dispersed on the dipstick. Thus the gas hold-up measurements are only very qualitative.

6.3 Results and Discussion

Here we will deal in turn with three topics. First, fluid mechanics will be discussed by referring to the results from the bubble detection system. Second, we shall present the results of the reaction rate experiments for the short reactor. Finally, the results of the long reactor will be presented.

6.3.1 Fluid Mechanical Considerations

As is apparent by examining Figures 3 through 5, bubble frequencies were quite constant for a given flowrate. Bubble volumes are then obtained by dividing the flowrate by the frequency. The results of the change in bubble volume with flowrate are given in Figure 6 for 976 K in the short reactor. It is seen that the average bubble volume increases with increasing flowrate. It would also be seen that the bubble size appears to approach a maximum value at the higher flowrates.

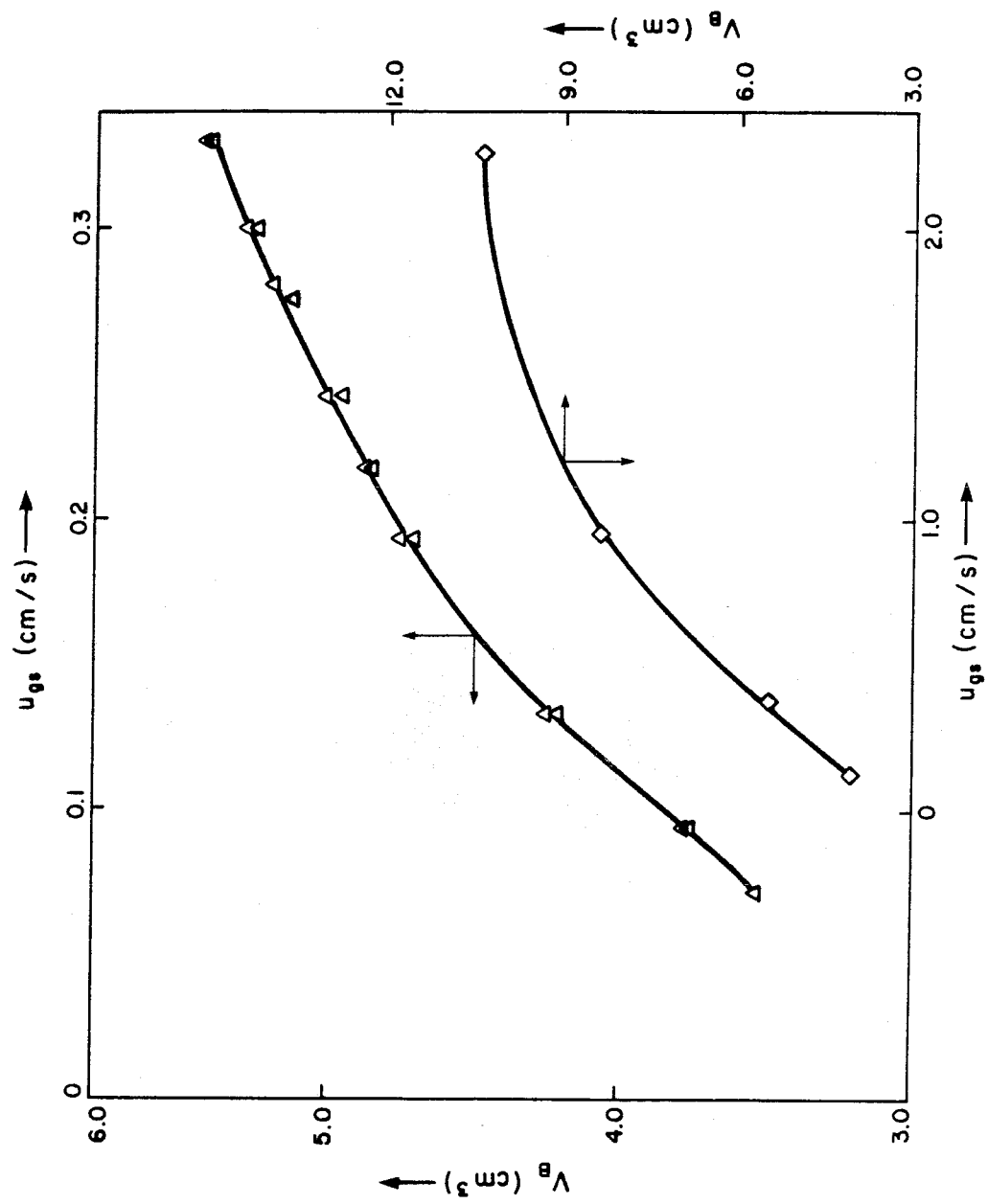


Figure 6. The change in average bubble volume with flowrate at 976 K in the short reactor.

The average bubble volume, $\langle V_B \rangle$, is also much larger than that observed in Chapter 2. And due to the invariant size observed, it is apparent that no break-up or coalescence phenomena can occur. If these mechanisms were operative, the bubble size distribution would be broader and measured bubble frequencies could not be so regular. That these large bubbles do not break-up is the result of four related properties of our system. First the bubbles do not have sufficient residence time in the reactor for break-up to ensue. Secondly, molten sodium phosphate has approximately three times the surface tension of the water which stabilizes the bubbles. The molten phosphate is also much more viscous than the water. This retards the growth of Taylor instabilities and coupled with the small residence time of the bubbles in the system, it will effectively prevent bubble break-up. Finally, the most striking difference is that the orifice in this case is inverted from that of Chapter 2 and correspondingly more difficult to analyze. Using equation 19 of Chapter 2, a larger bubble size would be expected due to the larger size of the molten salt orifice (.47 cm. ID as compared to 0.37 cm. ID in Chapter 2) and the increased surface tension of the molten salt.

The results of the measurement of average bubble volume and gas hold-up for all temperatures and flowrates used to measure the reaction rate of carbon particles are given in

Table 4. The deviations in bubble volumes were significantly different for the two reactors. The results are given in Table 5. Here the standard deviation corresponds to that estimated by averaging the results of five experiments for the short reactor. Each experiment corresponded to the average frequency of approximately 10-20 bubble pulses. For the long reactor, ten experiments were averaged. It is seen in Table 5 that the standard deviation in bubble size is substantially greater for the long reactor. This is a result of the increased salt height allowing more residence time for bubble break-up to ensue in the long reactor.

6.3.2 Reaction Rate Results for the Short Reactor

Figure 7 presents the result of increasing the particle load in the reactor. Here -120+140 mesh sponge coke II particles were reacted with oxygen. The reaction rate is seen to diminish. This cannot be explained by oxygen depletion. The maximum conversion of oxygen was 20% of the input. A reaction order of unity would then only multiply the maximum rate in Figure 7 by 1.1.

The indirect mechanism cannot account for this phenomenon. The results of Chapter 3 indicate the indirect reaction rate is several orders of magnitude below the gas-phase (exposed) rate. If we extrapolate the results of Chapter 5 to 1000 K, the reaction rate of -120+140 mesh particles in the gas phase

Reactor	T(K)	Flowrate Number Designation	Average Bubble Volume $\langle V_B \rangle$ (cm ³)	Reactor Superficial Gas Velocity u_{gs} (cm/s)	Gas Hold-up (ϵ)
Short	1000	1	3.34	0.433	0.186
Short	976	2	5.47	0.376	0.168
Short	976	3	8.32	0.944	0.218
Long	965	4	9.15	0.503	0.110
Long	965	5	10.7	1.17	0.192
Long	965	6	10.8	1.61	0.200

Table 4. The flowrate parameters for the experiments.

Table 5. The estimated standard deviation, S_D , in bubble volume for different flowrates and ambient salt heights.

Flowrate Designation Number	Ambient Salt Height Above Bubbler (cm)	$\langle V_B \rangle$ (cm ³)	u_{gs} (cm/s)	$S_D / \langle V_B \rangle$ (%)
1	4.77	3.34	0.433	0.4
2	4.75	5.47	0.376	0.3
3	4.75	8.32	0.944	0.3
4	8.27	9.15	0.503	5.9
5	8.27	10.7	1.17	6.7
6	8.27	10.8	1.61	6.5

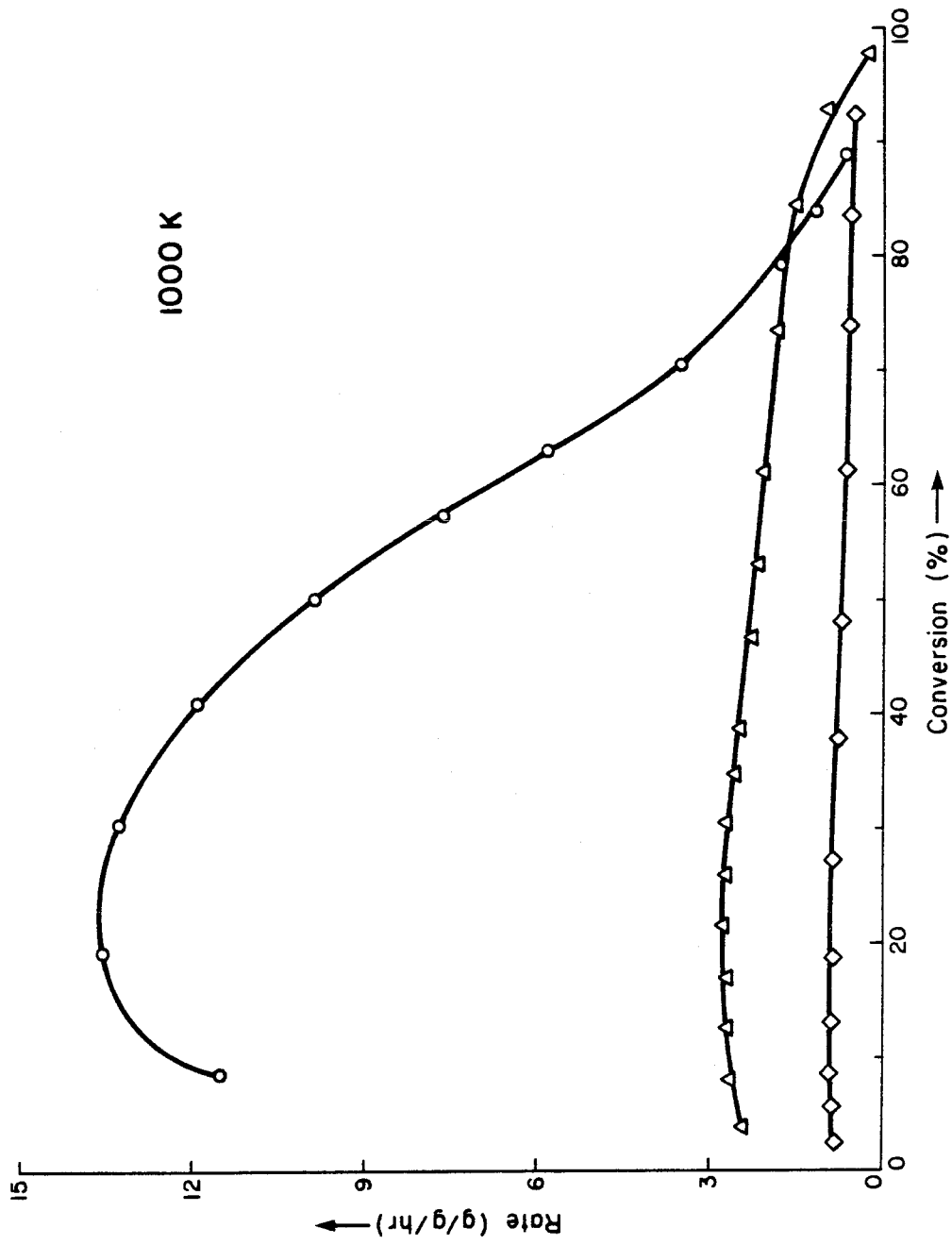


Figure 7. The particle loading effect at flowrate 1 in the short reactor. These results are for -120+140 mesh sponge coke II particles. The input oxidant is 0.10 atm. oxygen. O, 3.2 mg.; Δ, 24.3 mg.; ◇, 107 mg.

is about 9 g/g/hr. The reaction rate in a slurry is of the same order of magnitude as the gas phase results or higher. Hence the direct mechanism must be dominant. This is further discussed in Appendix I.

An added possibility is incomplete dispersion of the carbon particles. Cold flow experiments with water columns using 0.1 cm^3 bubbles indicated complete dispersion of -120+140 Eccospheres VT at similar bubble number densities. Bubble volumes and gas hold-ups were substantially larger for the molten salt experiments. The viscosity of molten phosphate is also substantially above that of water. Consequently there is more head for induced countercurrent flow and the particles have substantially smaller terminal velocities in the molten salt reactor.

The only possible explanation of this effect is the saturation of the bubbles by the particles. This apparently occurs at quite low particle number densities in the present case. To examine this hypothesis, the flowrate was varied. Figure 8 indicates the results at 976 K. As is seen, an increased flowrate substantially increases the rate of gasification. The larger bubbles and increased bubble density thus seem to counteract the saturation effect.

6.3.3 Reaction Rate Results for the Long Reactor

A similar type of behavior was observed for the long reactor for large chargings of -120+140 mesh coke particles

$P_{O_2} = 0.10 \text{ atm}$
 976 K

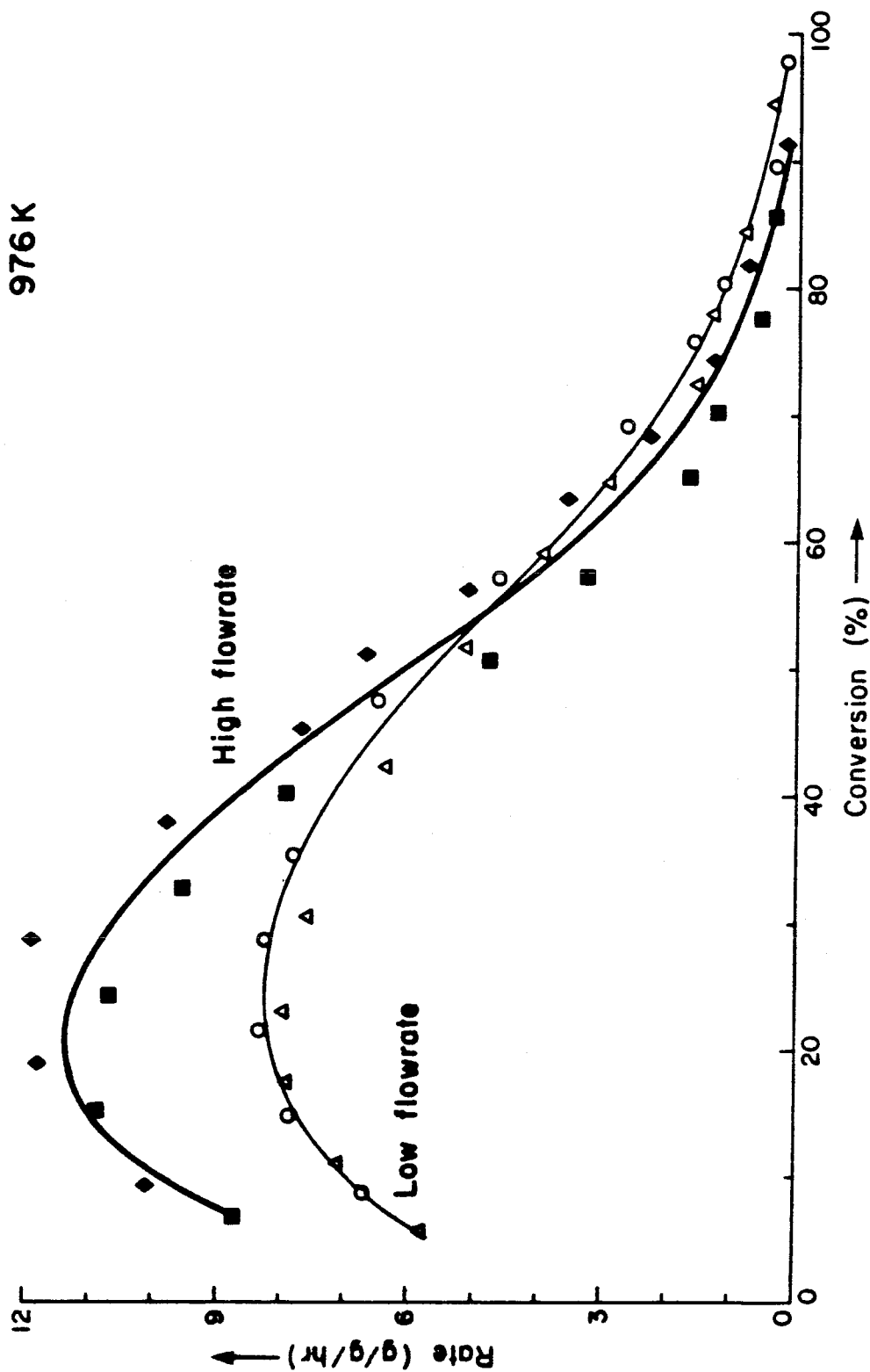


Figure 8. The flowrate effect in the short reactor. These results are for -120+140 mesh sponge coke II particles. The input oxidant is 0.10 atm. oxygen. O, Flowrate 2 and 4.7 mg.; Δ, Flowrate 2 and 6.3 mg.; ■, Flowrate 3 and 6.4 mg.; ◆, Flowrate 3 and 5.6 mg.

as is seen by referring to Figure 9. Figure 10 gives the results for -30+35 mesh coke particles. Both curves indicate similar behavior. Again conversion was less than 20% of the input oxygen and as such, depletion cannot account for the decreased rate. The specific reaction rate at 30% conversion is compared graphically with the weight fraction of carbon, ϕ_w , in Figure 11. Here the reaction rate has been extrapolated to that at zero oxygen conversion by assuming an oxygen order of unity. It is seen that both curves have the same general shape with the curve for the larger carbon particles located below that of the smaller particles.

Figure 12 presents the results of increasing the particle loading at flowrate 5. At this higher flowrate, in contrast to the previous results, the reaction rate increases with increasing particle loadings. The ultimate behavior at this flowrate is indicated in Figure 13 where at large particle loadings, a decline in the reaction rate with increasing particle loading is once again observed. While the maximum cannot be accounted for, these results ultimately conform to predictions outlined in Table 1. The results of these high flowrate experiments are compared in Figure 14. Here we have plotted the maximum rates and the rates at 50% conversion as a function of the weight fraction of carbon in the

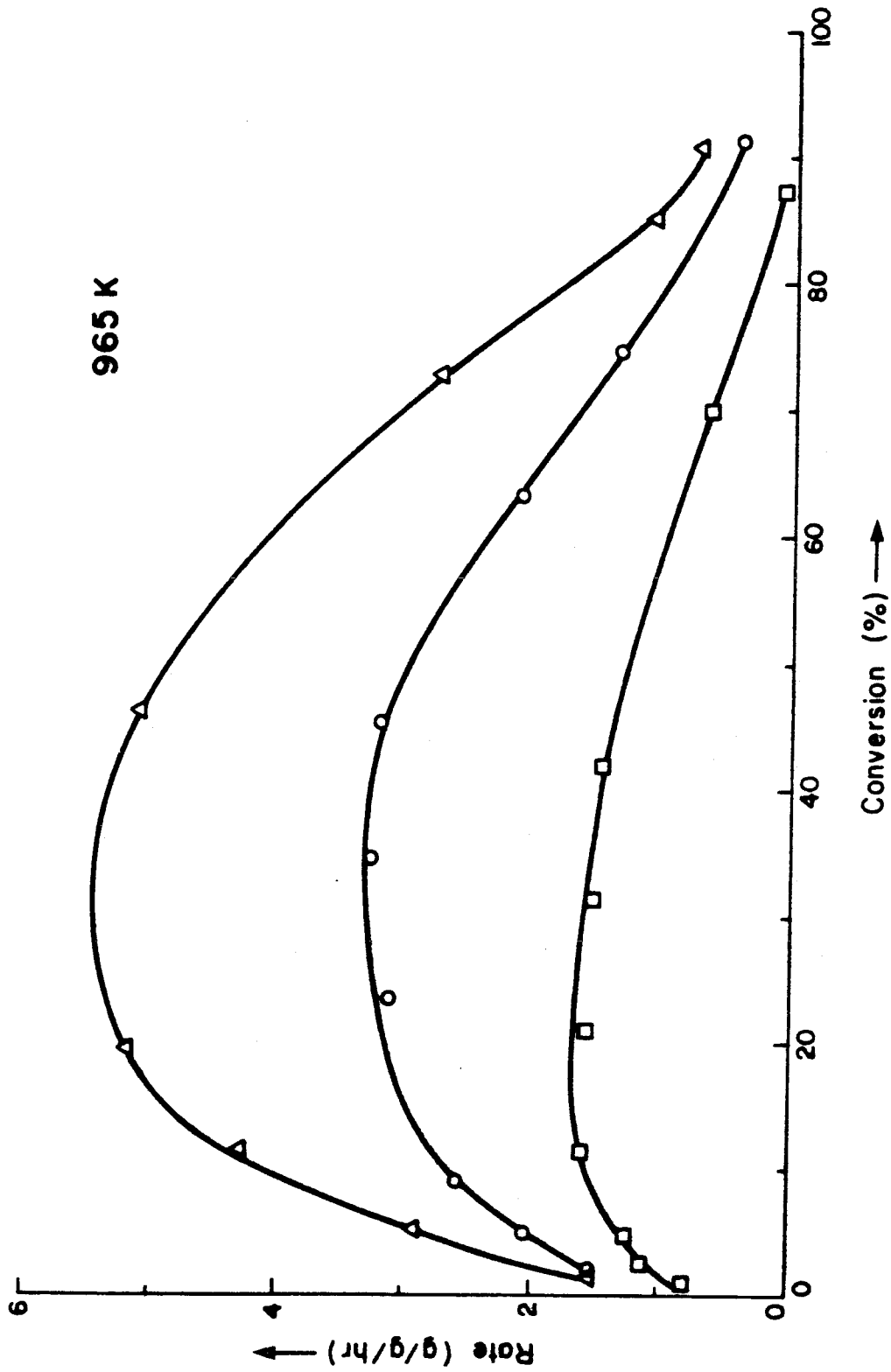


Figure 9. The effect of increasing the particle loading at Flowrate 4 in the long reactor. These results are for -120+140 mesh sponge coke II particles. The input oxidant is 0.10 atm. oxygen. Δ , 18.8 mg.; \circ , 30.0 mg.; \square , 60.8 mg.

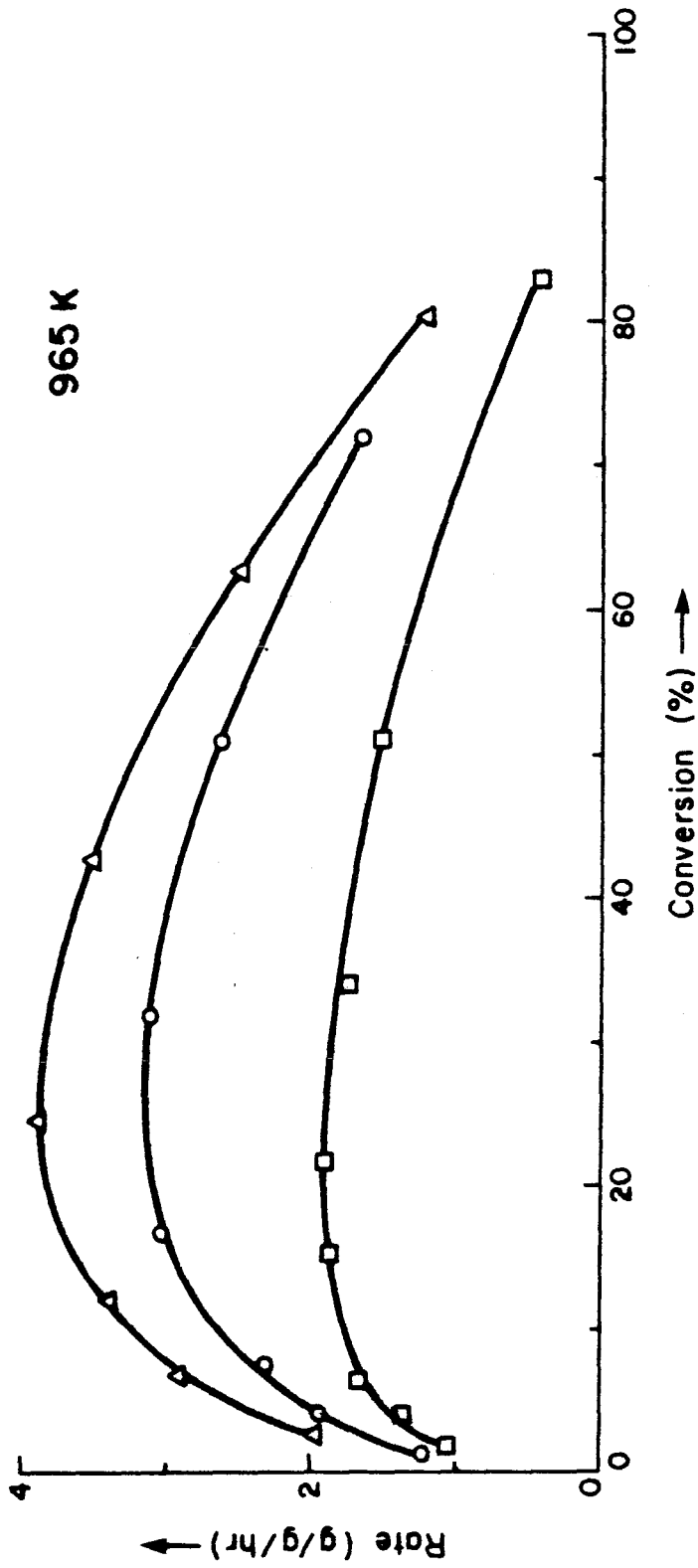


Figure 10. The effect of increasing the particle loading at flowrate 4 in the long reactor. These results are for -30+35 mesh sponge coke II particles. The input oxidant is 0.10 atm. oxygen.
 A, 23.6 mg.; O, 28.6 mg.; \diamond , 52.4 mg.

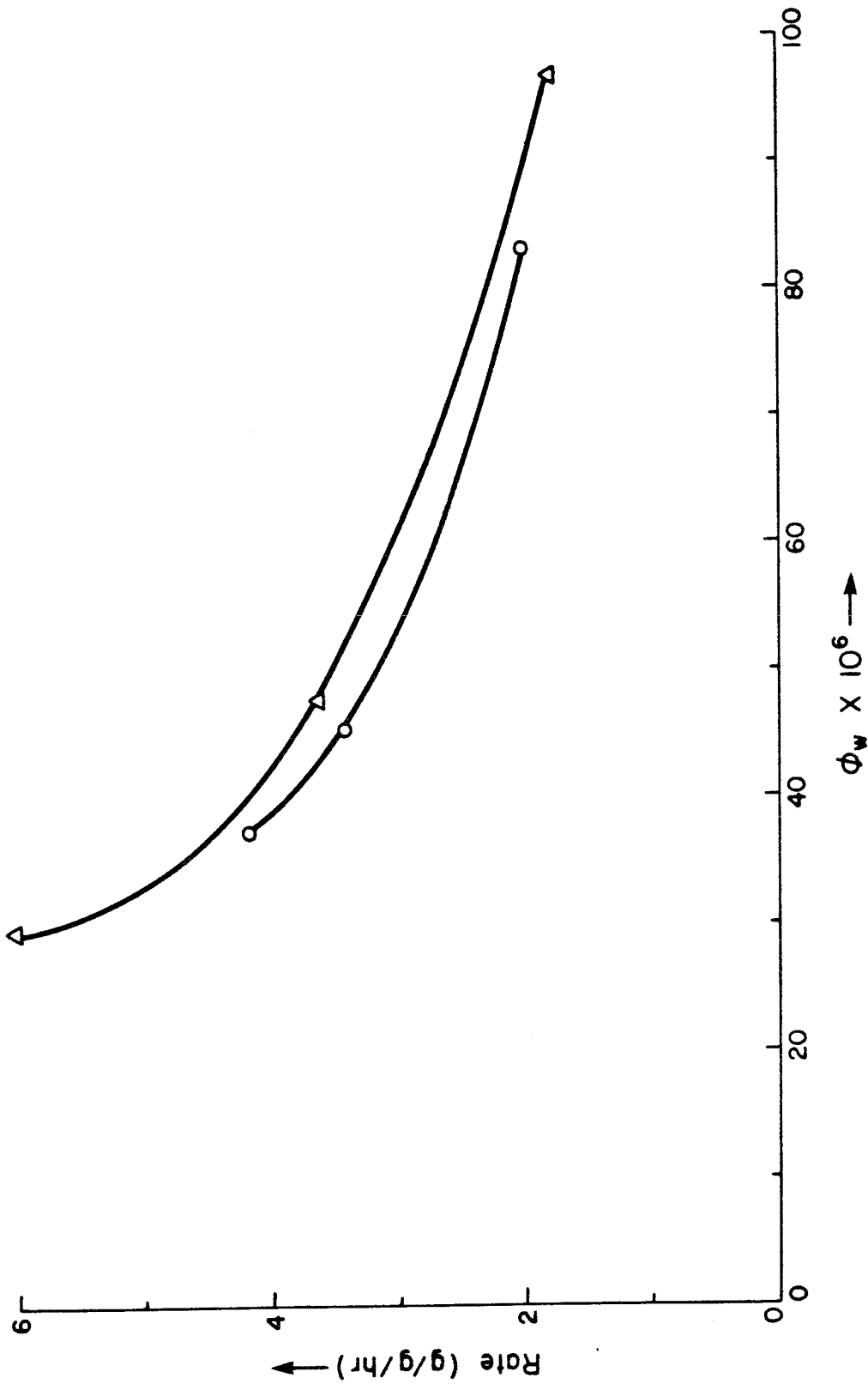


Figure 11. The change in the specific reaction rate with weight fraction of particles. These results are for flowrate 4 in the long reactor. The oxidant is 0.10 atm. oxygen. The specific rates are at 30% conversion. Δ , -120+140 mesh sponge coke II particles; O, -30+35 sponge coke II particles.

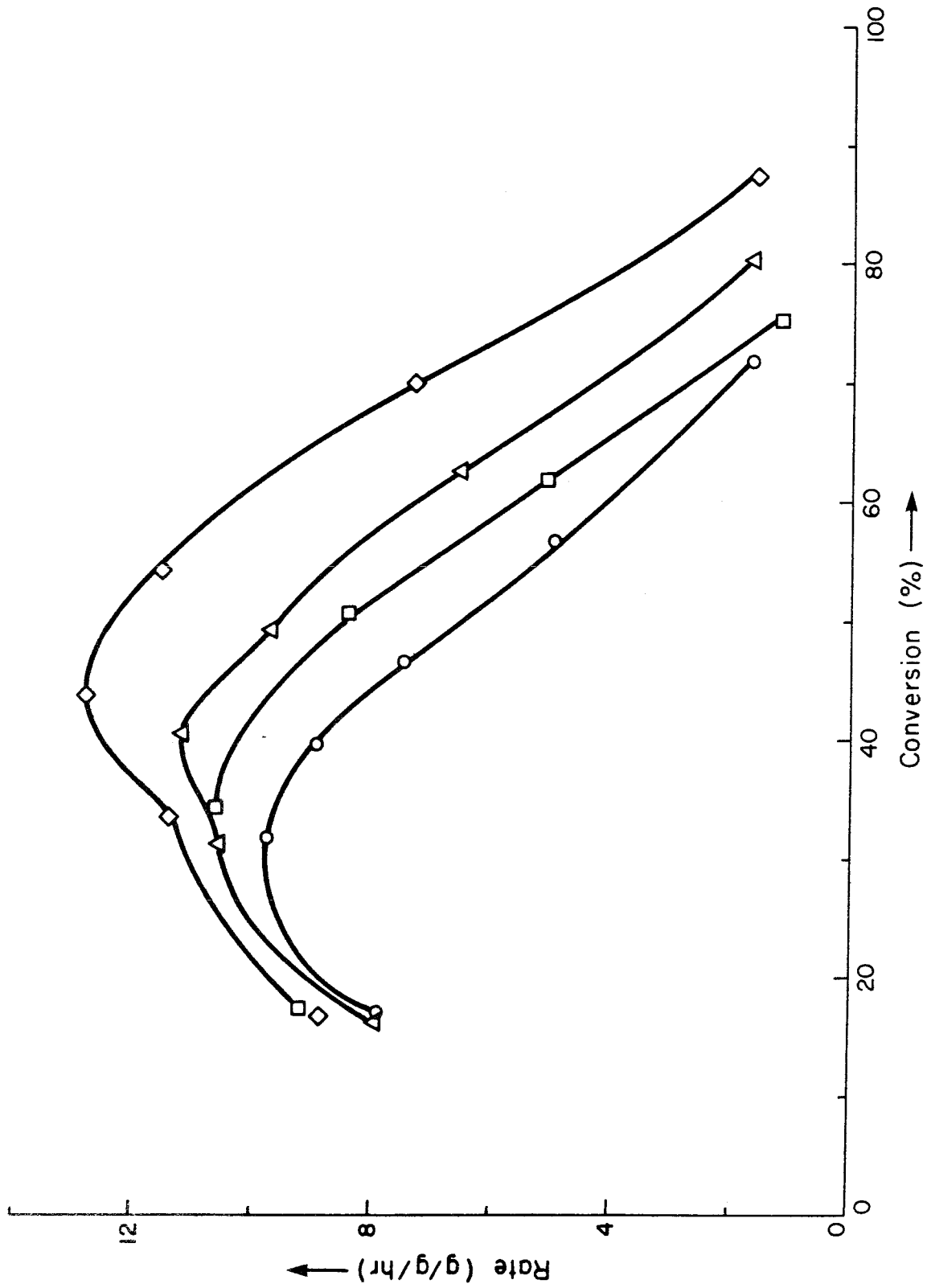


Figure 12. The effect of increasing the particle loading at flowrate 5 in the long reactor. These results are for -120+140 mesh sponge coke II particles. The input oxidant is 0.10 atm. oxygen. ○, 4.4 mg.; □, 8.6 mg.; ◇, 15.9 mg.; Δ, 16.6 mg.

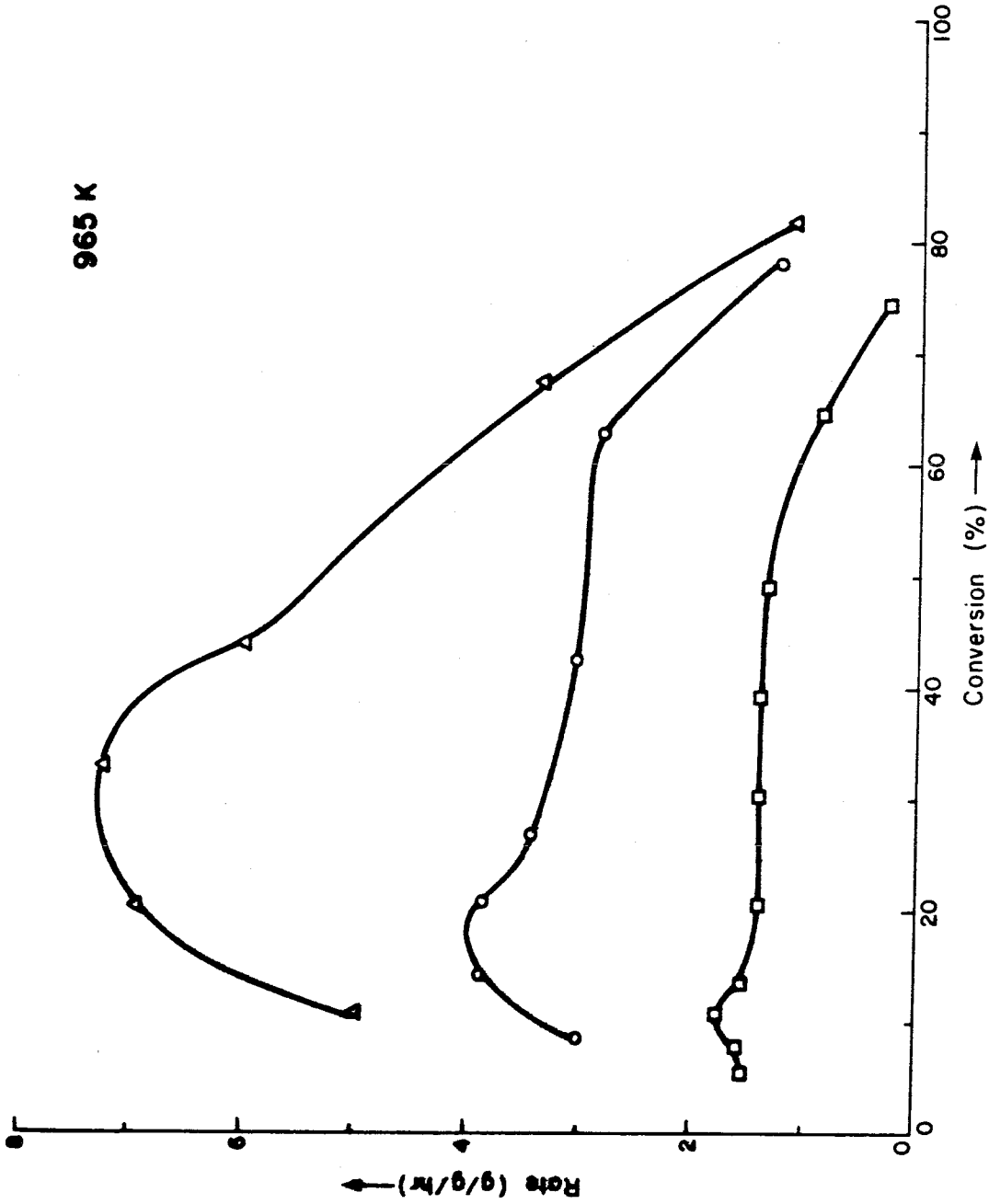


Figure 13. The effect of increasing the particle loading at flowrate 5 in the long reactor. These results are for -120+140 mesh sponge coke II particles. The input oxidant is 0.10 atm. oxygen. Δ , 45.7 mg.; O, 102 mg.; \square , 223 mg.

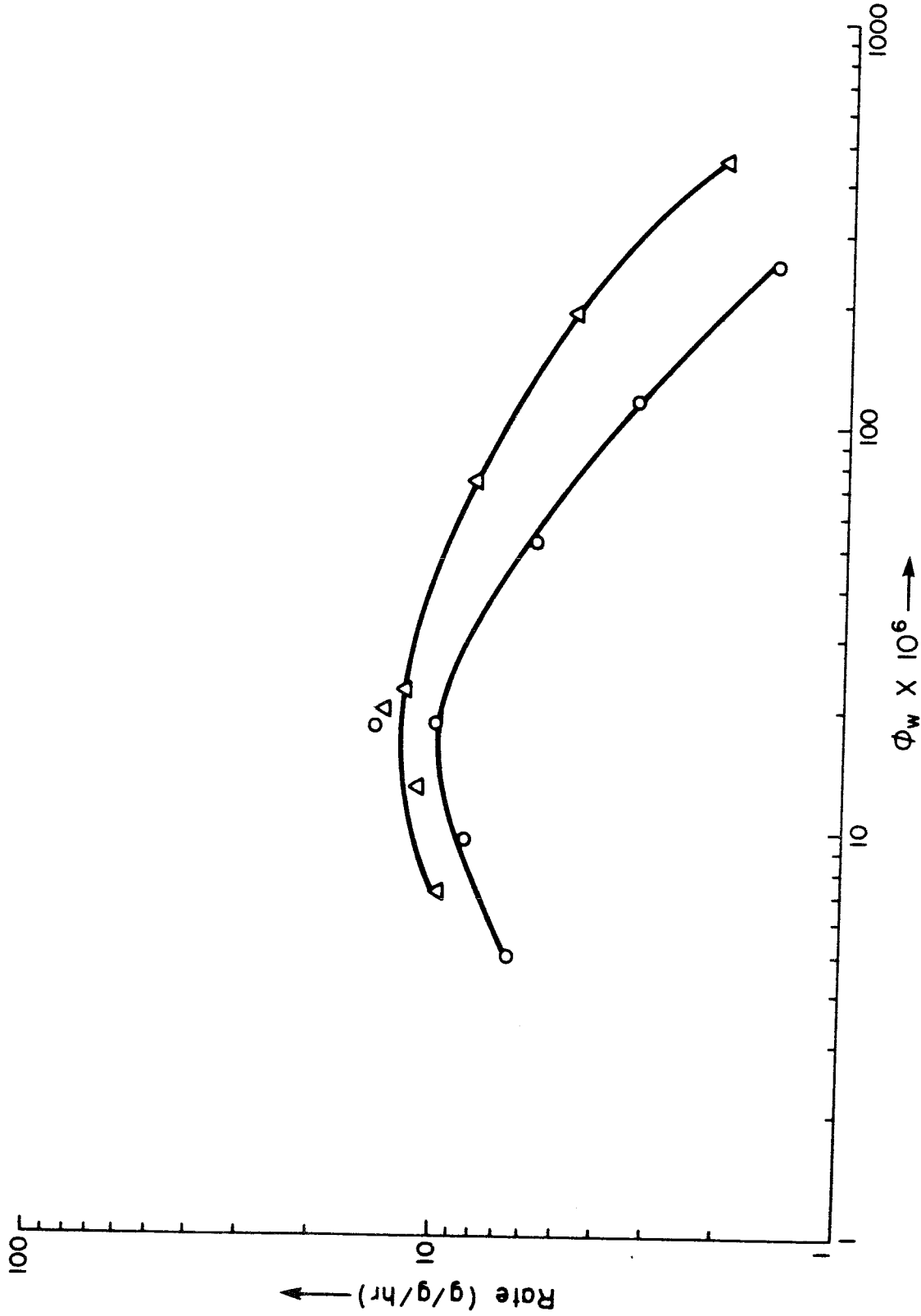


Figure 14. The change in the specific reaction rate with weight fraction of particles. These results are for flowrate 5 in the long reactor and for -120+140 mesh sponge coke II particles. The oxidant is 0.10 atm. oxygen. Δ , specific rate at maximum; O, specific rate at 50% conversion.

melt. Once again the rates were extrapolated to zero oxygen conversion.

A peculiar effect is observed at the higher flowrates. At the larger particle loadings in Figure 12, a peculiar maximum becomes apparent. This maximum is more pronounced in Figure 13 where for increased particle loadings, it propagates to the lower left of the diagram.

An interesting phenomenon detailed in Table 6 is that the absolute reaction rate apparently is quite constant for the -120+140 mesh particles at flowrate 4. For the -30+35 mesh particles, the absolute reaction rate is still constant but somewhat less than that of the smaller particles. This is consistent with a maximum number of particles being entrained on a given bubble. Using the maximum rate obtained in Chapter 5 for these particles exposed directly to gaseous oxygen at 964 K, we see that this corresponds to less than 10 mg. being entrained per bubble. This corresponds to the utilization of only a small part of the bubble for stable particle attachment.

Recalling again results of Chapter 5, the maximum rate of calcined sponge coke II particles exposed directly to 0.10 atm. oxygen at 964 K was 5.6 g/g/hr. For the smaller particle loadings at 965 K in the long reactor, the observed reaction rate was substantially above this value. Thus the salt has a catalytic activity which is apparently beyond that

Table 6. The maximum rates for the experiments of Figures 9 and 10. Flowrate 4 was employed. Here the rates have been corrected for finite oxygen consumption by assuming an order with respect to oxygen of unity.

Particle Size	Amount Added (mg)	Maximum Rate (g/hr)
-120+140 mesh	18.8	0.113
-120+140 mesh	30.0	0.110
-120+140 mesh	60.8	0.114
-30+35 mesh	23.6	0.100
-30+35 mesh	28.6	0.098
-30+35 mesh	52.4	0.111

presented in Chapter 4. This greater catalytic effect is the result of the substantially better carbon -- molten salt contacting in the slurry reactor. This was previously discussed in Chapter 4. Hence the salt apparently catalyzes the reaction rate, but this effect may be obscured by the fluid mechanics.

We end by presenting a result using flowrate 6. A phenomenon observed in these bubbling experiments was that fluctuations in the carbon oxide concentration were observed near the end of an experiment. These were monitored at a high flowrate to minimize mixing effects apparent in the system (see Appendix II). Such fluctuations are shown in Figure 15 where the carbon dioxide fraction in the offgas is plotted with time. As this flow system cannot respond quickly to extreme fluctuations due to capacitance, little significance can be attached to shape of the maxima. Fluctuations are however definite. This is most likely caused by unsteady bubble-particle contacting near the tail end of the carbon conversion. That is, carbon particles in the molten bath may not all convert at equivalent rates. In the beginning stages, the observed rate is averaged over a large number of particles and is steady. At the tail end, there are fewer particles and hence the fluctuations. Admittedly it is surprising that such phenomena may be observed in a system with such a large capacitance. Such

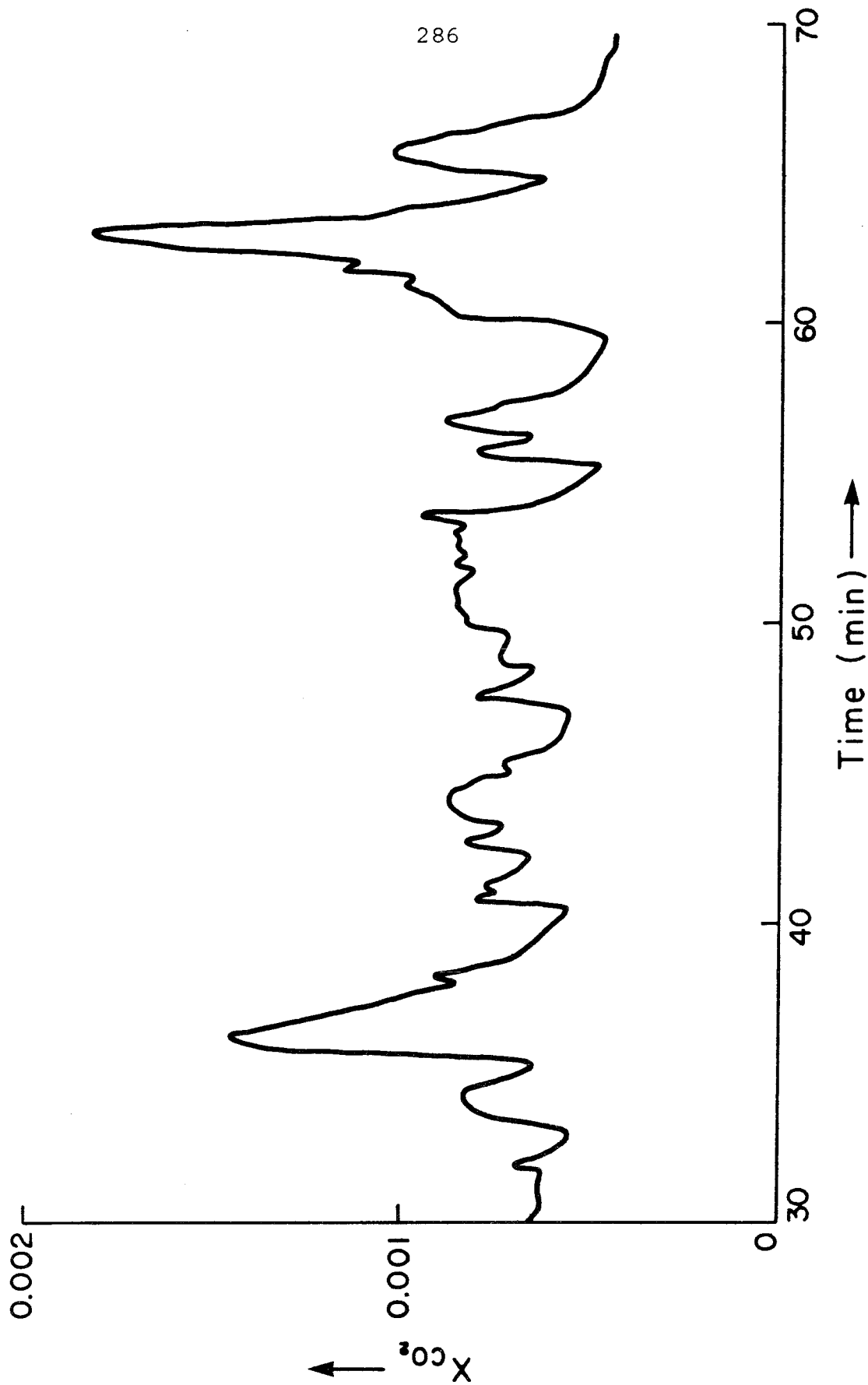


Figure 15. The fluctuations in the observed CO_2 concentration in the tail end of the conversion curve. These results are for flowrate 6 in the long reactor and for -120+140 mesh sponge coke II particles.

results were not observed in the gas phase experiments of Chapters 4 and 5 with large numbers of small particles. Hence these fluctuations serve as an added confirmation of the direct mechanism in molten sodium phosphate.

One final point is that the actual contacting of a particle with the bubble has been deduced and not observed. The particles due to their size and the viscosity of the molten salt have very small settling velocities ($N_{Re} \sim 10^{-4}$ for a 100 μ coke particle). This raises the question of whether the particle can push aside the liquid fast enough to actually pierce the interface. This question, although important, is beyond the scope of the present study.

6.4 Conclusions

1. The direct mechanism is dominant for the reaction of carbon particles in molten phosphate.
2. Saturation of the bubbles by the particles occurs at very low particle loadings. Such saturation leads to peculiar effects.

NOTATION

- A_{PI} = The single particle surface area on the gas-liquid interface (cm^2)
- C_G = The gaseous reactant concentration (moles/cm^3)
- f = $3\pi\eta r_B r_P$ (cm^2)
- h = The column height (cm)
- h_s = The column height required for the bubble to saturate with particles (cm)
- k' = $k_{RG} A_{PI} C_G$ (hr^{-1})
- k_{RG} = The reaction rate at the particle's surface in the gas phase (cm/hr)
- m = The number of moles per carbon particle (moles)
- N_P = The total number of particles
- N_{PI} = The number of particles on the gas-liquid interface
- N_s = The maximum number of particles that may be attached to a given bubble
- r_B = The bubble radius (cm)
- R_C = The rate of particle-bubble contact (hr^{-1})
- R_{dir} = The rate of the direct reaction (moles/hr)
- R_I = The specific reaction rate in a dilute slurry of particles where the bubble does not become saturated with particles (hr^{-1})
- R_{II} = The specific reaction rate in a slurry of particles where the bubble becomes saturated with particles partway up the column (hr^{-1})

- R_{III} = The specific reaction rate in a slurry of particles where the bubble becomes saturated with particles at the bottom of the column (hr^{-1})
- $R_{II,b}$ = The specific reaction rate in a slurry of particles from the bottom of the column to h_s (hr^{-1})
- r_p = The particle radius (cm)
- S_D = The estimated standard deviation in bubble volumes (cm^3)
- t = The time (hr)
- u_B = The bubble rise velocity (cm/hr)
- u_{gs} = The gas superficial velocity (cm/hr)
- V = The total reactor liquid volume (cm^3)
- $\langle V_B \rangle$ = The average bubble volume (cm^3)

Greek Letters

$$\alpha = (k_{RG} A_{PI} C_G N_S) / m \quad (\text{hr}^{-1})$$

$$\beta = (N_S V) / (6 \pi \eta r_B r_P h)$$

ϵ = The gas hold-up in the column

η = The correction factor for the amount of bubble-particle contact due to non-ideal effects

τ = The residence time of the bubble (hr)

CHAPTER 7

THE GASIFICATION OF CHAR IN
MOLTEN PHOSPHATE SLURRIES

7.1 Introduction

Here we shall not attempt to include all relevant literature on the gasification of char by steam. Parent coal rank has a definite effect on the reactivity of its char as demonstrated by Field (1). And while coal is highly impure and the carbon in the char reacts with an intrinsic catalytic effect, the addition of more impurities can increase the reactivity (2,3). Also extraction of impurities can decrease the reactivity (4).

A most important difference between this study and previous studies is that we shall not preheat the char above the reaction temperature. While this effectively removes the temperature-time effect on reactivity, an actual gasification system will not preheat char fed into it. Such pretreatment would adversely affect the reactivity. However, calcined char may be studied more carefully, and Linares-Solano et al (4), found the reactivity of a range of chars to be given by:

$$\frac{1}{n_0} \frac{dn}{dt} = k_w \quad (1)$$

Here k_w is a constant characteristic of the char, temperature, and steam concentration. n is the number of moles of carbon with n_0 being the initial number of moles.

The gasification of coal in molten salt, specifically in molten carbonate, has been studied by M. W. Kellogg (5) and is currently being studied by Atomics International (6).

7.2 Experimental

The carbon selected for study was a subbituminous char supplied by Occidental Research. Its properties are given in Table 1. Two distinct differences are observed as compared to the coke. The char has substantial ash content, and there is no particle size effect on the BET surface area. The average pore diameter is seen to be markedly below that of petroleum coke, and the char is substantially more porous.

The experimental system employed to measure the reactivity of the char was the same as that detailed for Chapter 4. Specifically Reactor I was used for the no salt experiments and Reactor II was used for the salt experiments.

7.3 Results and Discussion

Here first we will discuss the reactivity of the char without salt. The second section of this chapter will deal with the reactivity of the char in a bubbling molten salt slurry reactor.

7.3.1 The Reaction Rate of Char with No Salt

Size ranges from -60+80 mesh to -200+230 mesh were observed to have equivalent reactivities in steam. Arbitrarily, -120+140 mesh particles were selected for the reaction rate studies presented here. The reaction rate was observed to

Table 1a. The composition of the subbituminous char.

COMPOSITION	
<u>Component</u>	<u>Weight %</u>
Carbon	74.2
Hydrogen	2.1
Nitrogen	1.5
Sulfur	1.2
Oxygen (by diff)	2.3
Ash	18.7
Total	100.0 %
Volatile Matter	11.9 %

Table 1b. The nitrogen BET surface area and liquid nitrogen porosity of the subbituminous char.

Sample	Surface Area (m ² /g)	Porosity (10 ⁻³ cm ³ /g)	Average Pore Diameter (Å)
-60+80 Mesh	132 ± 4	-	-
-120+140 Mesh	135 ± 2	78.3 ± 1.1	23

decay exponentially with time. Hence our rate expression is:

$$\frac{dn}{dt} = -k_c n_0 \exp(-k_c t) \quad (2)$$

This is equivalent to the rate expression observed by Linares-Solano et al (4) if n_0 in equation 1 is replaced by n . Reproducibility was excellent as seen in Table 2 and Figure 1 for typical experiments. While obvious due to the form of equation 2, the reaction rate versus conversion curve is shown in Figure 2 to compare these results to the petroleum coke experiments. It is clearly seen that the char follows a different reaction rate curve.

An initial concern was the effect of mixing in the reaction system on the observed rate of reaction. This effect is discussed in Appendix II. It is found that the reaction rate is followed closely by the system after allowing a suitable induction period. The effect of laminar flow through connection tubes on the observed rates is discussed in Appendix III. This effect also may be neglected as it only produces a simple time delay.

The water order was measured at 1113 K and the results follow in Figure 3. It is found to be 0.44 ± 0.03 which is reasonable as an order between zero and unity is typically observed.

A peculiar effect is indicated in Figure 4. Here we present the Arrhenius plot for k_c . At low steam concentrations,

Table 2. Reaction Rate Data For Occidental Char at 1113 K and 26.3% H₂O.

Experiment 21	
Time (Minutes)	Rate (gmoles/hour)
1.50	.145
1.75	.133
2.00	.117
2.25	.103
2.50	.0937
2.75	.0809
3.00	.0701
3.25	.0648
3.50	.0584
3.75	.0541
4.00	.0487
4.75	.0450
4.50	.0420
4.75	.0395
5.00	.0353
$k_c = 24.4 \text{ hr}^{-1}$	
Correlation Coefficient = -0.995	

Experiment 22	
Time (Minutes)	Rate (gmoles/Hour)
1.00	.264
1.25	.243
1.50	.224
1.75	.205
2.00	.185
2.25	.165
2.50	.150
2.75	.130
3.00	.116
3.50	.0963
3.75	.0851
4.00	.0791
4.25	.0720
4.50	.0673
4.75	.0614
5.00	.0572
5.25	.0516
5.50	.0451
5.75	.0409
6.00	.0371
6.25	.0341
$k_c = 23.7 \text{ hr}^{-1}$	
Correlation Coefficient = -0.999	

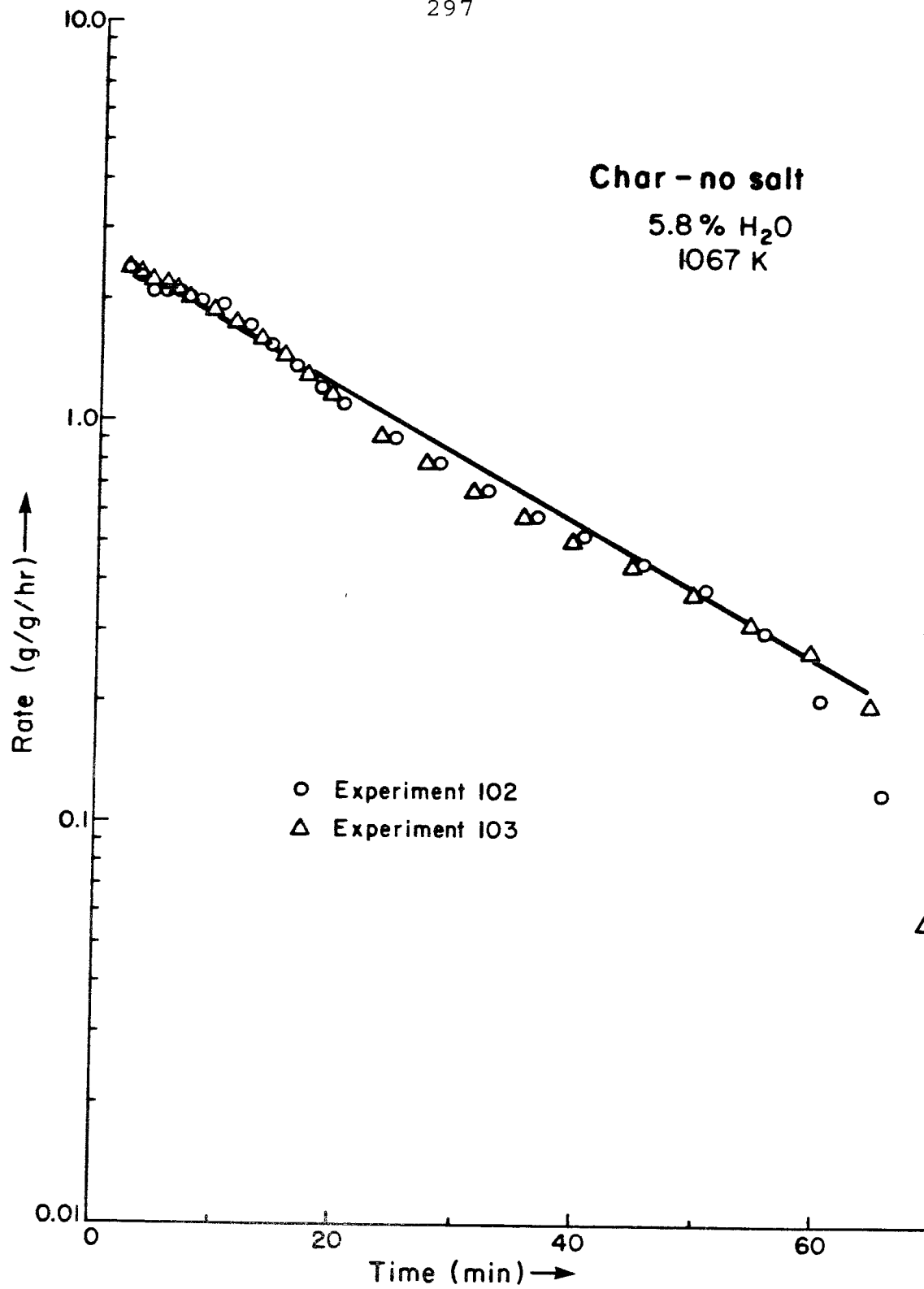


Figure 1. The change in the specific reaction rate with time.

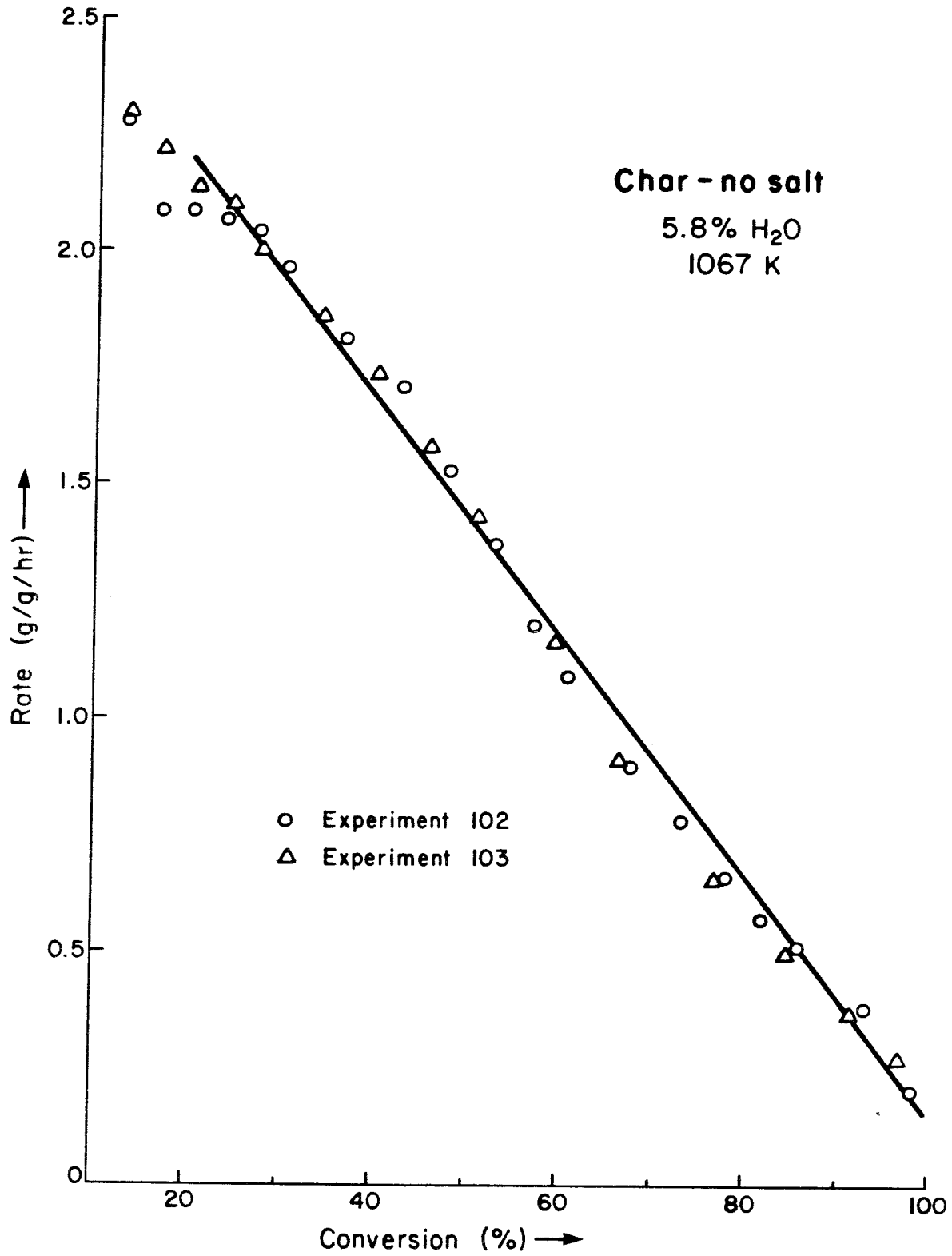


Figure 2. The reaction rate vs. conversion curve follows a straight line for the char particles.

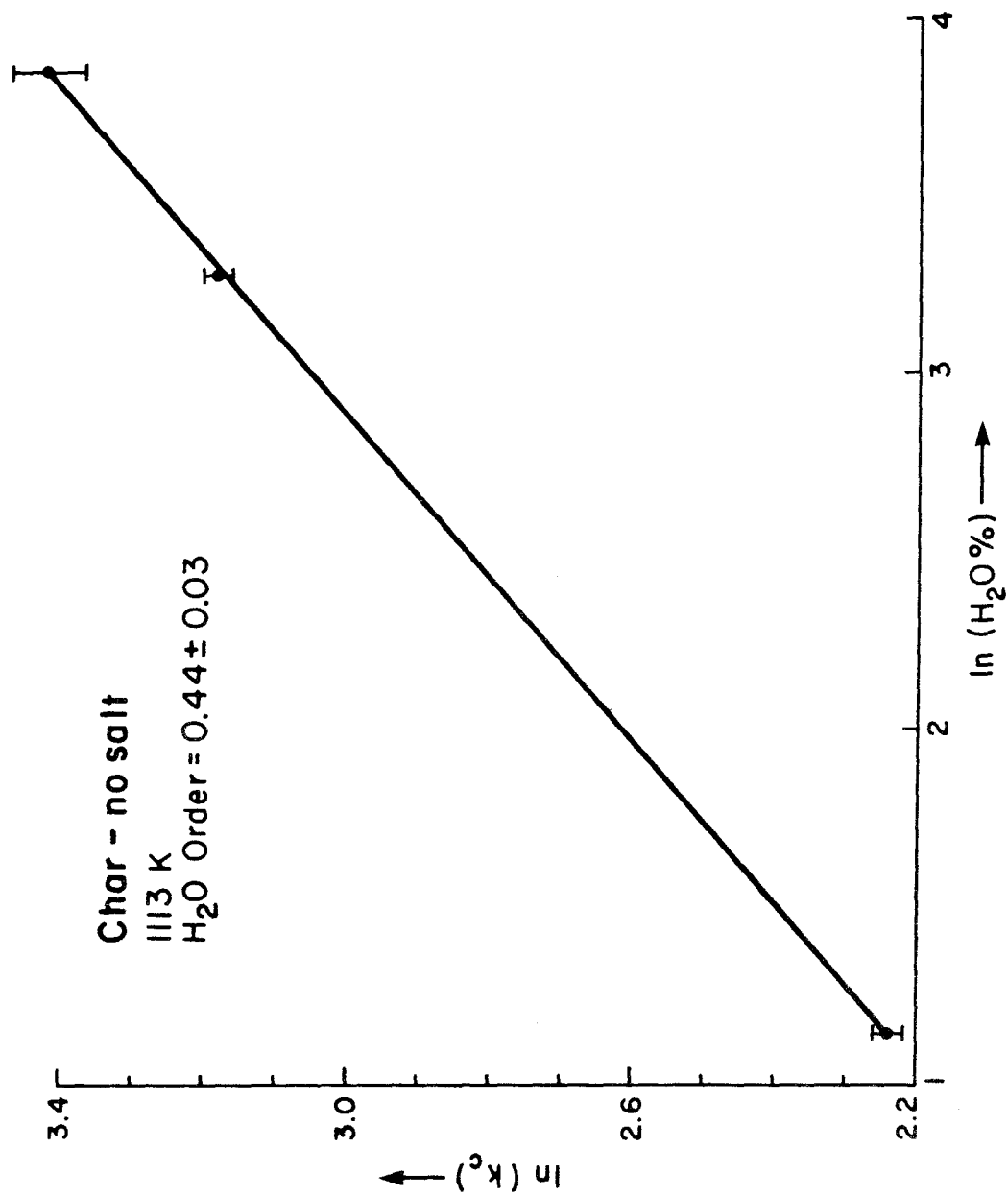


Figure 3. The change in k_c with water concentration.

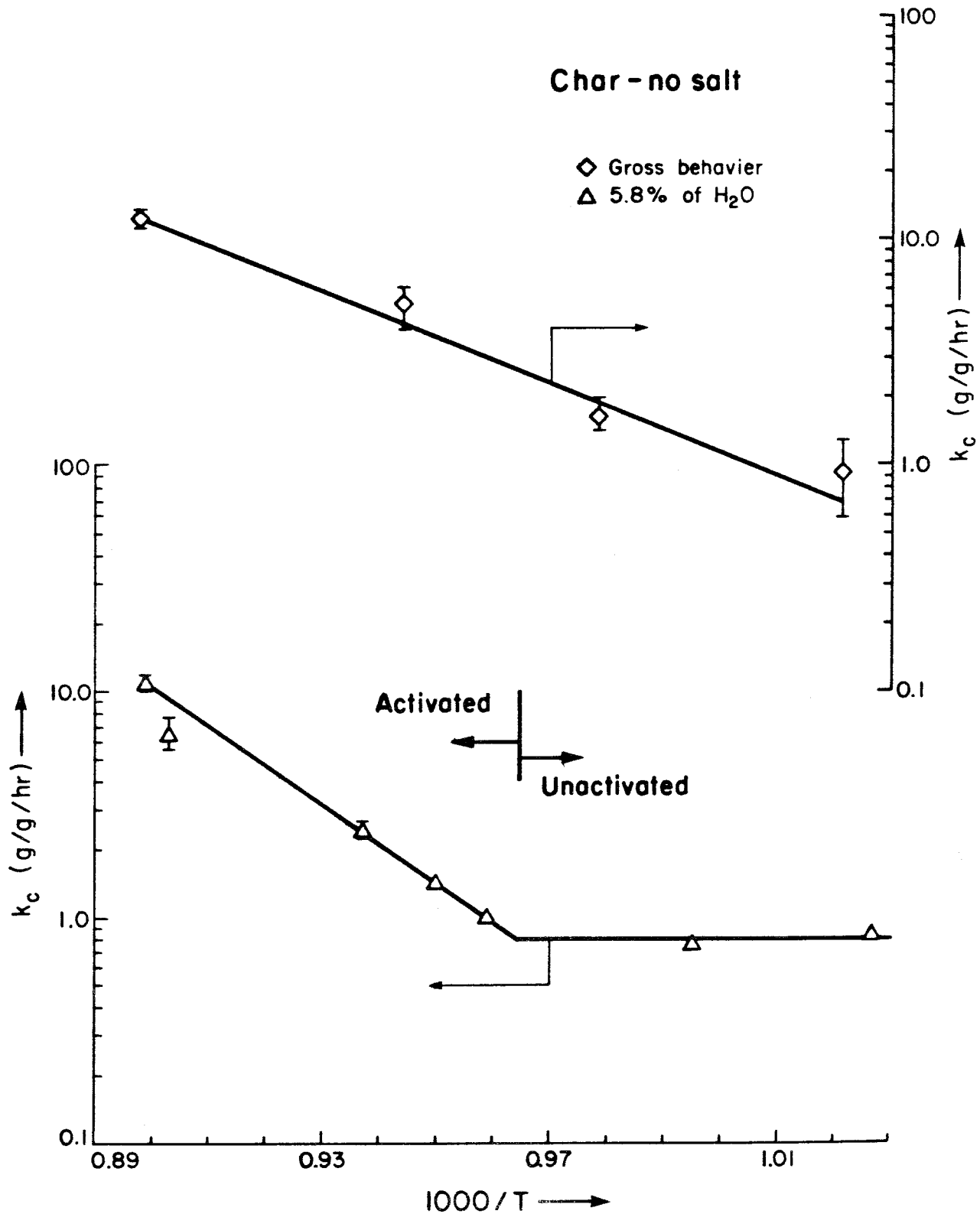


Figure 4. The Arrhenius plot for the change in k_c with temperature.

k_c has a constant value for the lower temperatures. k_c then becomes activated at approximately 1040 K. And for the higher temperatures, the activation energy is 80 Kcal/gmole which is quite close to the activation energy of the pure steam-carbon reaction. The gross behavior is also plotted which does not include the low water concentration results. This is seen to be a more conventional Arrhenius plot. It is these results which will be taken as the typical reactivity of our char. The gross reaction rate expression as obtained by a least squares fit is:

$$k_c = 1.45 \times 10^{10} \exp \frac{-43,500}{RT} X_{H_2O}^{0.44} \quad (3)$$

Here X_{H_2O} is the water fraction with R being the gas constant in cal/gmole K.

The explanation of the low steam concentration results above is that the char was not preheated to high temperatures. Thus as the char is gasified, fixed carbon is being converted chemically to other forms by thermal pyrolysis. Hence the competition between conversion to CO_x and thermal conversion of the chemical form of the carbon gives peculiar effects. Such effects are discussed in more detail in Chapter 5.

7.3.2 The Reaction Rate of Char in Molten Salt Slurries

Fluid mechanical variables were measured as discussed in Chapter 6. Table 3 presents the results for the flowrates and temperatures studied in this chapter.

T(K)	Ambient Salt Height Above the Bubble Injection Point (cm)	Average Bubble Volume $\langle V_B \rangle$ (cm ³)	Reactor Superficial Gas Velocity u_{gs} (cm/s)	Gas Hold-Up (ϵ)
1041	4.80	7.24	0.487	0.122
1124	4.86	6.87	0.527	0.187

Table 3. The flowrate parameters for the char experiments.

The reaction rate expression (equation 3) is compared to the specific rate observed in the slurry reactor for two temperatures in Figure 5. The rate is seen to be substantially below that of the exposed experiments. This may be contrasted to the results in the previous chapter where the decline in the slurry reactor reaction rate was not as great. One possible explanation is that the char particles can be expected to have a substantially smaller contact angle than petroleum coke with the molten salt. That is, the high ash content effectively attracts the molten salt and hence diminishes the contact angle. Another effect is that the char utilizes more interior pore area than the coke during the course of its conversion to CO_x . A largely nonporous particle's surface area is immediately exposed to the oxidant upon bursting through the bubble's interface. A porous particle experiences a time delay to establish steady state gas phase reaction characteristics as finite time must be allowed for transport of the oxidant into the particle's pore structure. This time delay will decrease the reaction rate of the porous particle beyond that of a nonporous particle when comparing the results of the direct reaction rate in a slurry to gas phase (exposed) results. The magnitude of this effect will depend on the average residence time of a particle on a given bubble as well as the collision frequency of the particle with bubbles.

The saturation effect detailed in Chapter 6 was also observed. For -120+140 mesh char particles, the results are

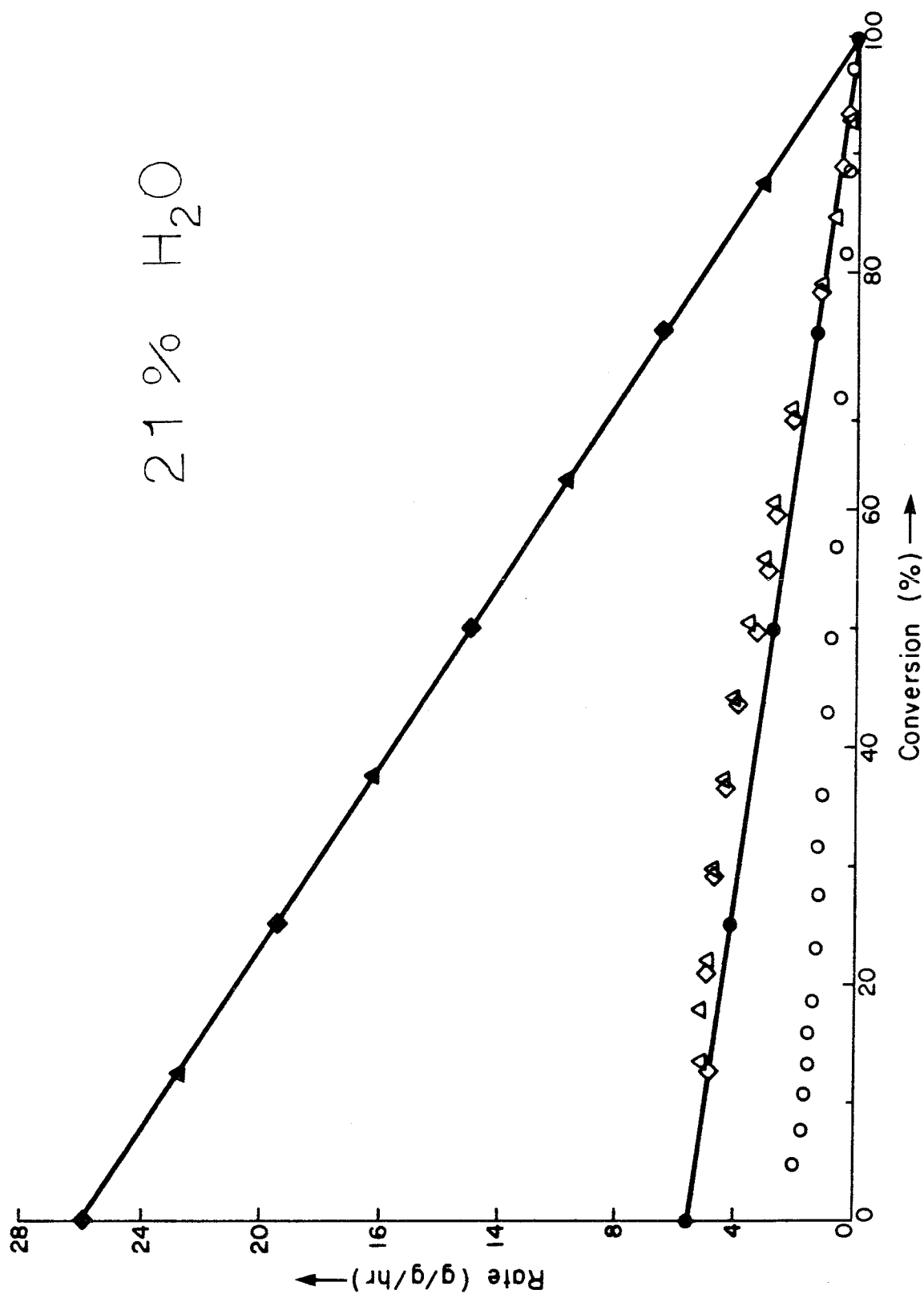


Figure 5. The comparison of gas phase results with the reaction rate of char in a molten phosphate slurry. The gas phase results are from equation 3. Gas phase results: ●, 1041 K; ▲, 1124 K. Molten phosphate slurry: ○, 1041 K and 3.6 mg.; ◇, 1124 K and 5.2 mg.

given in Figure 6. Here again conversion of the oxidant cannot account for this behavior. Total steam conversion was less than 10% in all cases. This coupled with the low reaction order with respect to steam would result in a reaction rate decline of less than 3% due to finite steam consumption. The reaction rate of -60+80 mesh char particles was also measured at 1124 K. No significant difference was observed in their reactivity as compared to the -120+140 mesh particles.

Hence char exhibits the same general features as the petroleum coke in molten salt slurries. Thus the decrease in reactivity in molten phosphate slurries is not attributable to the phosphate chemically inhibiting the rate. Inhibition is due to the complex fluid mechanics of the molten salt gasification process.

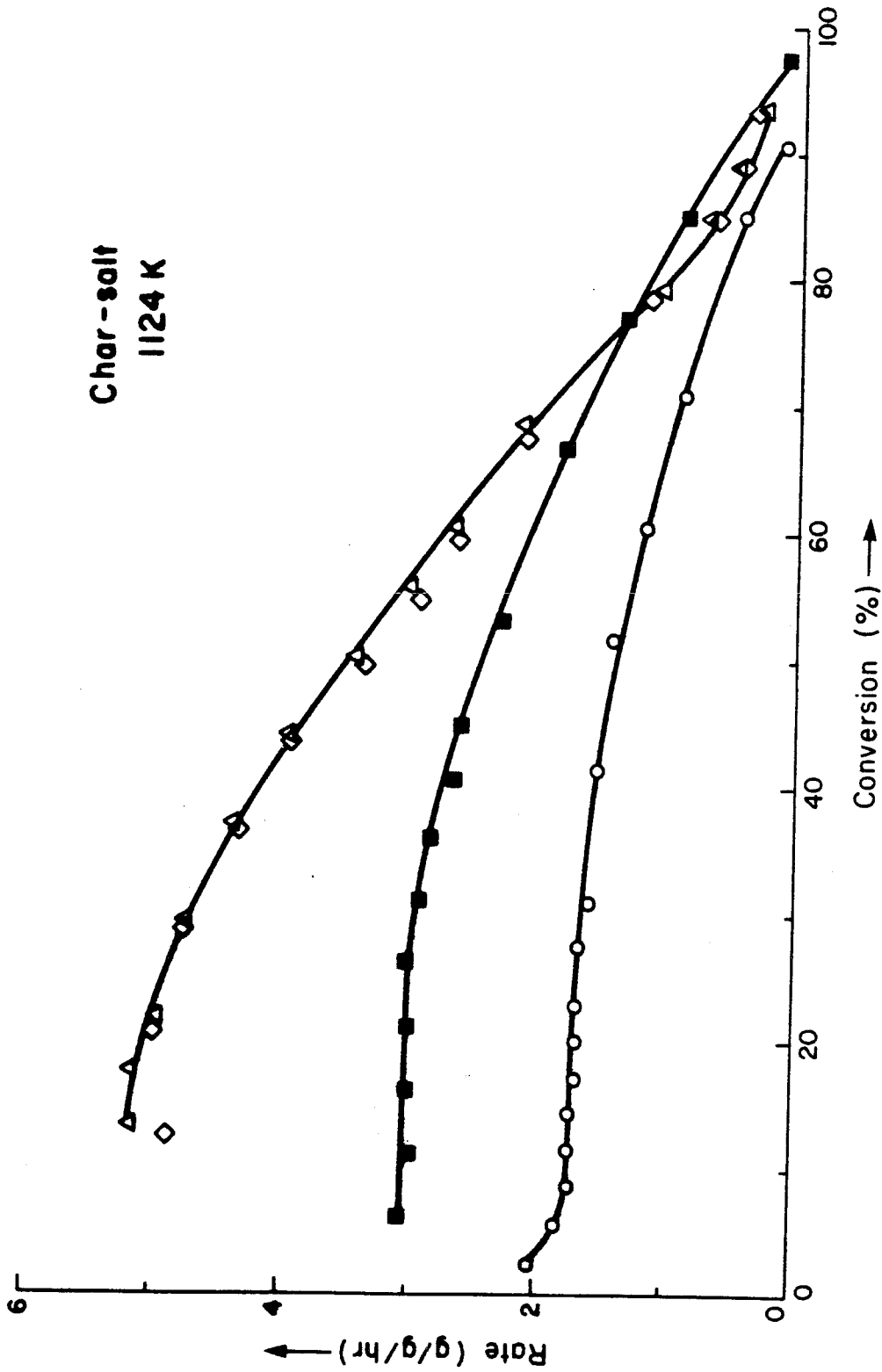


Figure 6. The effect of increasing the particle loading in the bubbling slurry reactor (reactor II). These results are for -120+140 mesh char particles. The input oxidant concentration is 21% H_2O .
 Δ and \diamond , 5.2 mg.; \blacksquare , 19.0 mg.; \circ , 50.4 mg.

REFERENCES

1. Field, M. A., *Combustion and Flame*, 14, 237 (1970)
2. Kayembe, N., and Pulsifier, A. H., *Fuel*, 55, 211 (1976)
3. Willson, W. G., Sealock, L. J., Jr., Hoodmaker, F. C., Hoffman, R. W., Stinson, D. L., and Cox, J. L., in Coal Gasification, p. 203, Division of Fuel Chemistry No. 131, American Chemical Society, Washington, D. C. (1974)
4. Linares-Solano, A., Mahajan, O. P., and Walker, P. L., Jr., *Fuel*, 58, 327 (1979)
5. Le Francois, P. A., Barclay, K. M., and Skaperdus, G. T., in Fuel Gasification, p. 64, Advances in Chemistry Series No. 69, American Chemical Society, Washington, D. C. (1967)
6. Trilling, C. A., Division of Fuel Chemistry, American Chemical Society, Preprints, Volume 22, No. 1, p. 185 (1977)

CHAPTER 8

THE GASIFICATION OF RESIDUAL OIL
IN MOLTEN PHOSPHATE SLURRIES

8.1 Introduction

Here we shall demonstrate residual oil steam reforming in molten sodium phosphate. The results presented in this chapter shall deal with two topics. First of all, we are interested in what hydrocarbons evolve during the experiment and their relative concentrations. Undoubtedly the bulk of the hydrocarbons are produced simply by thermal pyrolysis of the residual oil. Secondly we shall be concerned with the residual coke formed during the steam reforming experiment. We are principally concerned with its reactivity relative to the types of coke previously studied.

8.2 Experimental

Vacuum residual oil supplied by Texaco was used. The properties and composition of this oil are given in Table 1. It is seen to be a very viscous liquid with the approximate empirical formula $C H_{1.5}$. It has a relatively high sulfur content with very little ash. To effectively flow the residual oil in the experiments of this chapter, it was necessary to heat it to 400 K.

A different reaction vessel than those employed in Chapters 3 through 7 was needed to study steam reforming of residual oil in molten phosphates. The reaction vessel dimensions and the reaction parameters are given in Table 2. The reactor was sealed from the atmosphere in this case by

Table 1. Composition and properties of the Texaco vacuum residual oil.

COMPOSITION			
Major Components	Weight %	Trace Components	PPM
Carbon	85.2	Nickel	6.9
Hydrogen	10.5	Vanadium	11.1
Nitrogen	0.3	Iron	36.6
Sulfur	4.0	Chloride	71.
Ash	0.012		

VARIOUS PROPERTIES			
Gross Heating Value		10.1	kcal/g
Density at 301 K		0.999	g/cm ³
Viscosity	- 344 K	4000	cp
	372 K	360	cp
	400 K	90	cp

Table 2. Dimensions of the materials used to assemble the reactor and the reaction parameters.

DIMENSIONS IN INCHES	ID x OD x LENGTH
ALUMINA REACTANT INJECTION TUBE	3/8" x 1/2" x 18"
CERAMIC MULLITE CRUCIBLE	2" x 2 1/4" x 12"
REACTANT TUBE BUBBLE INJECTION POINT (ABOVE THE INSIDE BASE OF THE CERAMIC MULLITE CRUCIBLE)	5/8"

REACTION PARAMETERS

SODIUM PHOSPHATE SALT	400 grams (Dry Basis)*
SALT COMPOSITION	$\text{Na}_2\text{O}/\text{P}_2\text{O}_5 = 1.31$

THE AMBIENT SALT HEIGHT ABOVE THE INSIDE BASE OF THE MULLITE CRUCIBLE AND THE AMBIENT SALT HEIGHT ABOVE THE POINT OF BUBBLE INJECTION (THE CASE WITH NO GAS FLOW THROUGH THE REACTOR).

T (K)	MOLTEN SALT HEIGHT ABOVE BASE (cm)	HEIGHT ABOVE BUBBLE INJECTION (cm)
1100	9.83	8.25

* The salt weight is for the dehydrated salt.

a McDanel Universal Seal. This seal is accomplished by compressing a viton gasket between a stainless steel disk and the top of the ceramic tube. The seal is attached to the ceramic crucible via a hose clamp. As viton is used, this seal is only stable to 600 K, and the ceramic reactor must be subjected to an extreme temperature gradient. Hence caution was taken to prevent thermal shock failure.

The experimental system is shown in Figures 1 and 2.

Figure 1 is a detailed design of the reactor section. The residual oil was atomized by passing it through a Spraying System Company narrow angle atomizer. It was very difficult at the relatively low flowrates used in these experiments to attain a steady rate of residual oil feeding. Consequently the complex design of Figure 1 was needed. Thirty minutes prior to an experiment, valve I was opened allowing the heated residual oil to flow to the atomizer. During this time, a small flow was supplied through the system with valve III opened to bypass the atomizer. This small flow was necessary to prevent plugging of the reactant injection tube by the molten phosphate. Immediately prior to an experiment, valve I was closed. The flow was then increased to the reaction flowrate and the bypass valve (valve III) closed. Then a small bleed flow of nitrogen through needle valve I was supplied to push the residual oil through the atomizer. Calibration runs revealed that about 40 mg of residual oil were supplied in this manner.

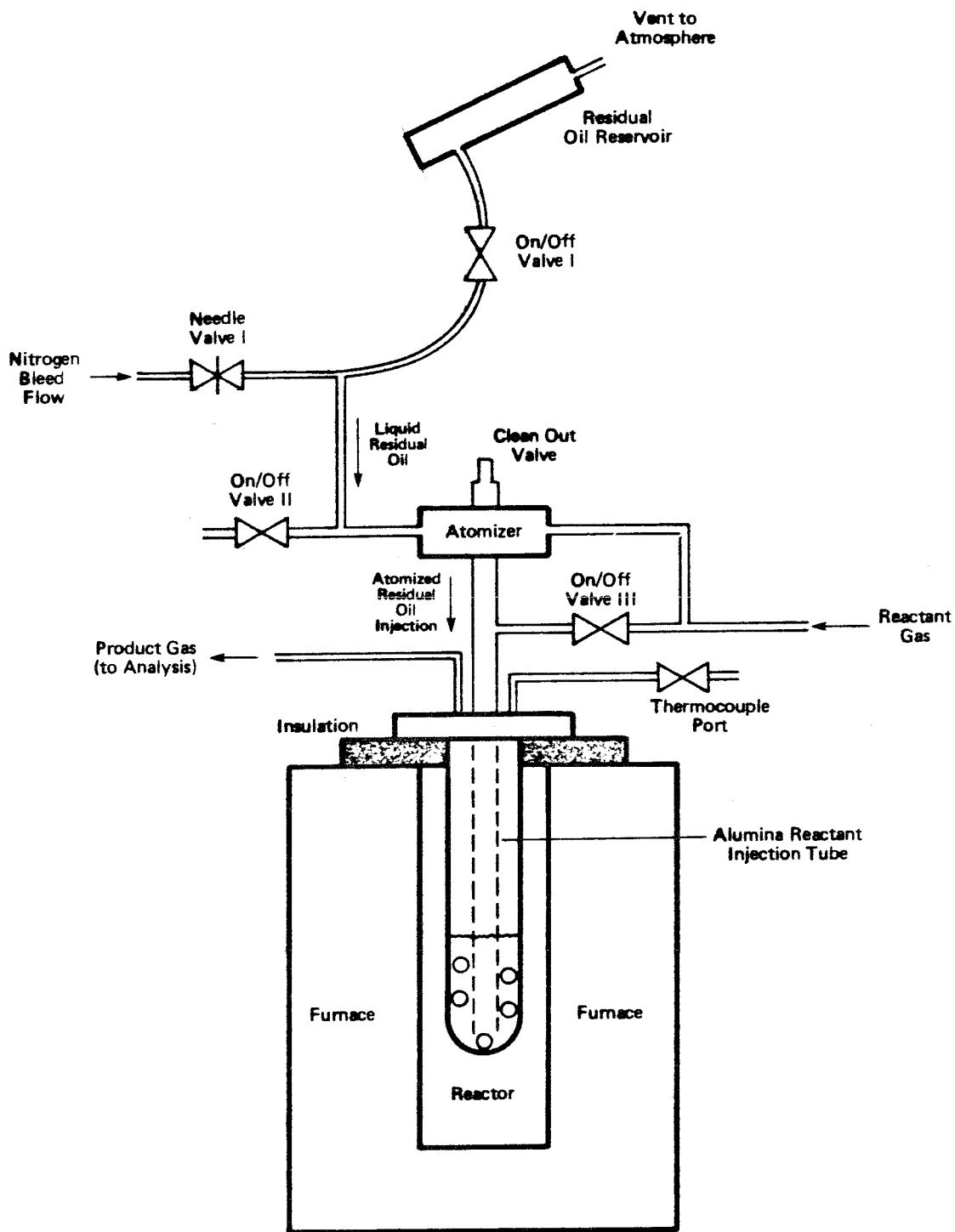


Figure 1. The reactor section of the experimental apparatus for the steam reforming of residual oil.

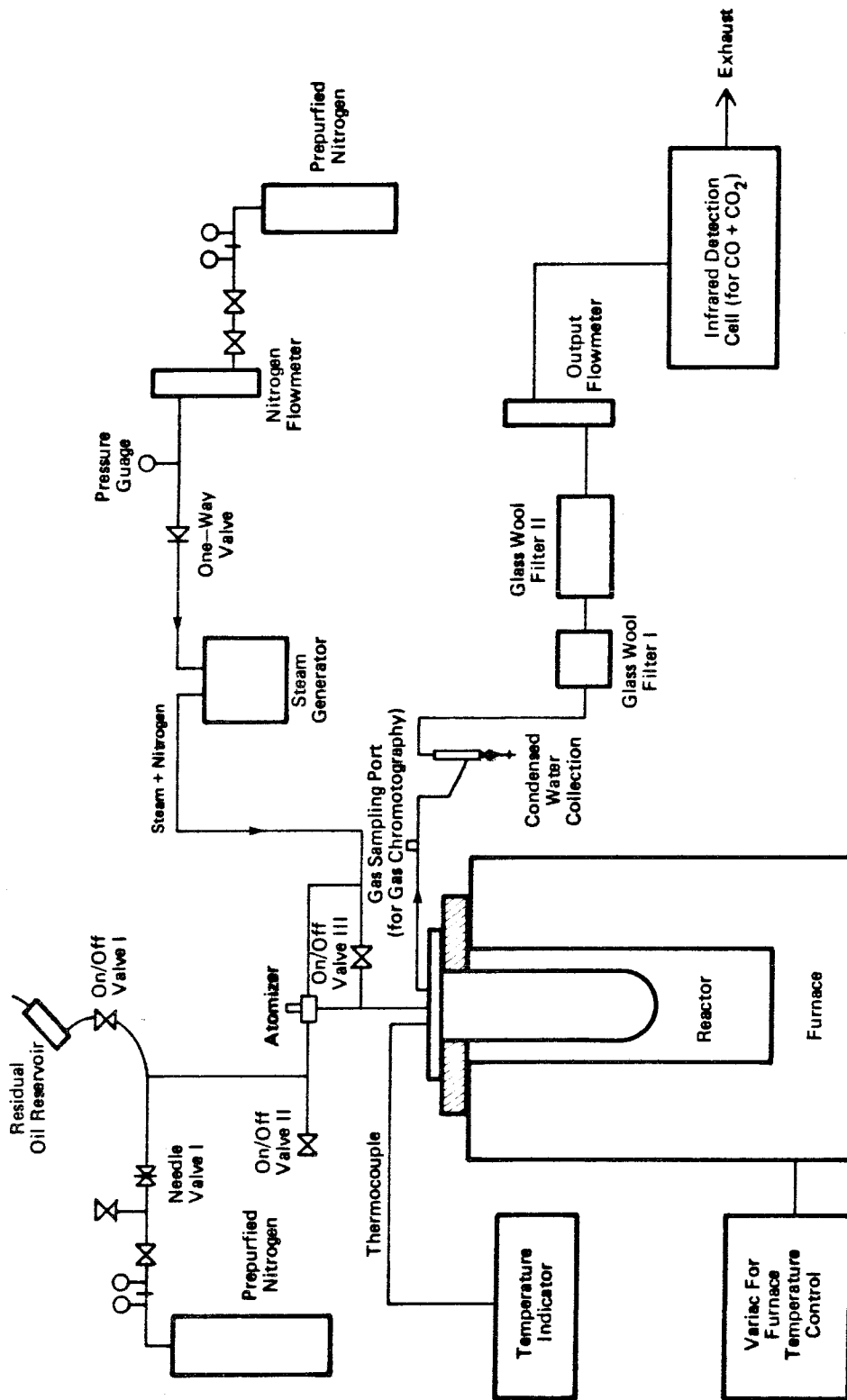


Figure 2. The experimental system for the steam reforming of residual oil.

For the first thirty minutes of an experiment, flowrate 1 in Table 3 was supplied. In this time all available residual oil (beyond valve I) was atomized. Then the bypass valve (valve III) was opened, and the flowrate was decreased to flowrate 2 in Table 3.

The higher flowrate did not allow complete conversion of the residual oil and a large amount evolved as gas or tar. It also undoubtedly caused some of the carbon formed in the bed to be entrained. The lower flowrate did not cause carbon entrainment. Hence it allowed the reaction rate of residual carbon in the molten salt bath to be measured.

Figure 2 details the total system. Prepurified nitrogen containing less than 50 ppm oxygen was passed through the constant temperature bath detailed in Chapter 4. The product gas had unreacted heavy oils as well as carbon particles. Consequently the gas was filtered by two series glass wool filters. After this filtering, the output flow was measured to insure no leakage, and the CO_x concentration was analyzed by infrared absorption.

A gas sampling port was used to obtain samples for gas chromatography. Two chromatographs were used. One had a thermal conductivity detector. Separation was effected by a 1/4" x 15' column packed with -60+80 mesh molecular sieve held at 100°C. The molecular sieve consisted of 33% 5A and 66% 13X. This chromatograph was used to detect the hydrogen

Flowrate Designation Number	Reactor Superficial Gas Velocity u_{gs} (cm/s)	Steam Concentration H_2O (%)	Gas Hold-up (ϵ)	Space Time (s)
1	7.27	10.	0.416	2.7
2	0.62	20.	-	32.

Table 3. The flowrates used in the residual oil steam reforming experiments.

concentration relative to methane. Unfortunately, the CO concentration was below the detection level of this chromatograph.

Methane and other hydrocarbons to C₈ were analyzed by a flame ionization detector. Absolute concentrations and relative concentrations were obtained by appropriate calibration. Here the column was packed with -45+60 mesh Poropak Q. A suitable separation was obtained using a 1/8" x 6' column and temperature programming. The column was held at 50°C for two minutes and then heated to 220°C at 8°C per minute. This attained an adequate separation for straight chain hydrocarbons to C₈, benzene, toluene, and xylene as well as methanol and ethanol. Olefinic hydrocarbons were separated from their aliphatic counterparts to C₄. And branched chains were separated from straight chains to C₆.

A final note is added on the hold-up value for the high flowrate indicated in Table 3. After cooling, system examination revealed the alumina reactant injection tube to be completely dissolved to a level corresponding to the hold-up value given. It was assumed that this corresponded to the higher flowrate. The reactor was found to be coated with salt to within five centimeters of the top. This would correspond to a gas hold-up of 0.608. It was assumed coating to this level was caused by splashing and frothing.

The system was heated to a higher temperature after experiments were performed at 1100 K. Here the product exit tube became plugged with entrained carbon, and thus while experiments were performed, no data were collected. This is when the reactant injection tube was most likely completely dissolved. Hence it is assumed that for the 1100 K experiments, the reactor was intact.

8.3 Results and Discussion

Significant amounts of unconverted tars were found on the glass wool filters. The toluene soluble fraction of these tars was analyzed by ^1H NMR spectroscopy. Here as in Chapter 5, extreme care was taken to remove residual toluene by drying the extract in a vacuum at 100°C for more than 72 hours. The spectra for the extract and the residual oil are shown in Figure 3. CDCl_3 was the solvent in both cases. The structure and hydrogen concentrations are given in Table 4. It is seen that the extract is highly aromatic and contains two aliphatic peaks which are existent in the residual oil. The similarity between the product extract and the sponge coke extract of Chapter 5 is apparent. And it is reasonable to presume that this extract is typical of the coke in the reactor. Hence sponge coke results should be quite applicable to the prediction of the reaction rate of carbonized residual oil in molten salts. The product extract here is

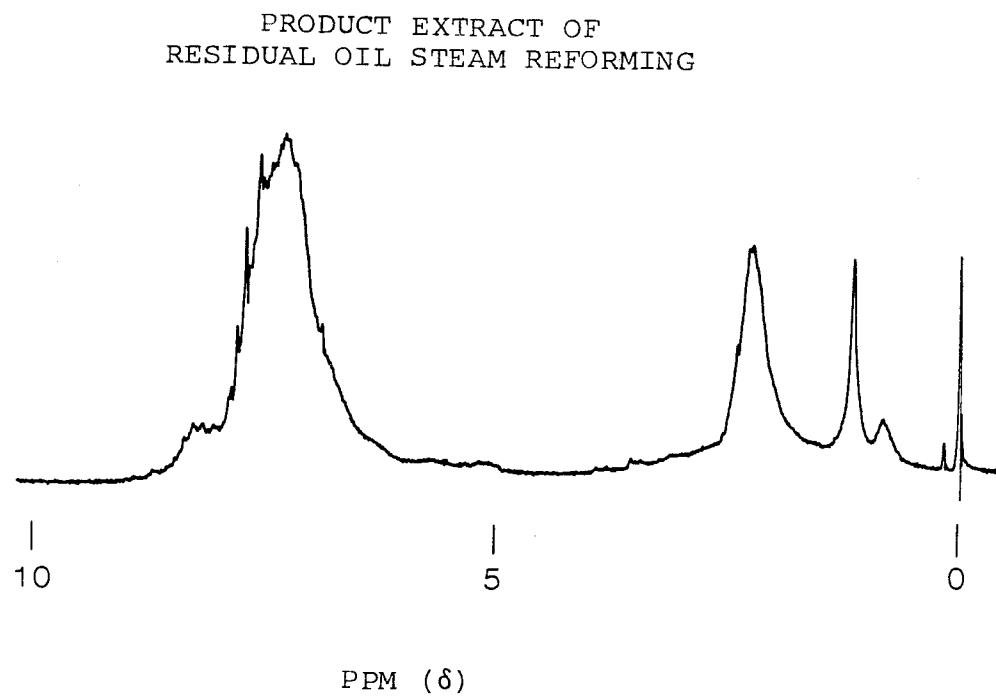
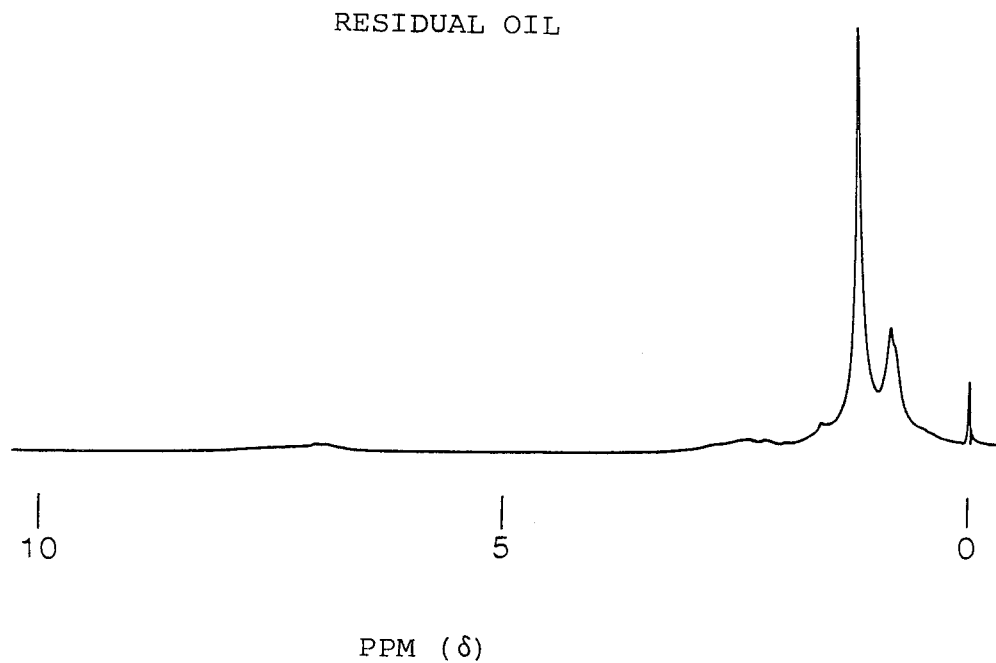


Figure 3. ^1H NMR Spectra of residual oil and the toluene extract of the collected product of residual oil steam reforming at 1100 K.

Range-PPM (from TMS)	Designation	RESIDUAL OIL			PRODUCT EXTRACT OF RESIDUAL OIL STEAM REFORMING		
		Percentage (of total H)	Position (PPM)	Structure Type	Percentage (of total H)	Position (PPM)	Structure Type
5.5-9.0	Aromatic & Phenolic	6.5			62	8.2 7.3	Shoulder Peak
4.7-5.5	Olefinic	0			2		
2.0-4.5	Alpha to Aromatic	10.3			21	2.3	Peak
0.5-2.0	Beta to Aromatic & Further	83.2	1.2 0.8	Peak Peak	15	1.2 0.8	Peak Peak

Table 4. The hydrogen concentrations in the various ranges of the NMR spectra.

more highly aromatic than that of the sponge coke due to the higher temperature treatment.

A sample gas chromatogram is given in Figure 4. Here a calibration sample is compared to a sample of the residual oil steam reforming product gas. Slight translations were caused by the necessity of switching the attenuation to indicate the smaller peaks in the product gas sample. However all retention times and peak areas were recorded by an on-line integrator.

Three experimental runs were performed at 1100 K. These all entailed thirty minutes of residual oil injection. The flowrate was then lowered and the reaction rate of the residual carbon in the bed was followed for a length of time, T. For the first experiment, T was 100 minutes. For the second experiment, T was 270 minutes. In the final experiment, a leak developed after the residual oil injection period. Consequently the reaction rate of the residual carbon could not be obtained for the final run.

One particular problem for these experiments was that the reaction rate did not decay to zero during the observation of the reaction rate of the residual carbon. This is a result of a significant amount of carbon in the colder parts of the reactor. Such carbon was deposited by condensation of unreacted hydrocarbons and carbon entrainment from the molten salt bath. This carbon was likely deposited during residual oil injection. Hence to observe the reaction rate of the

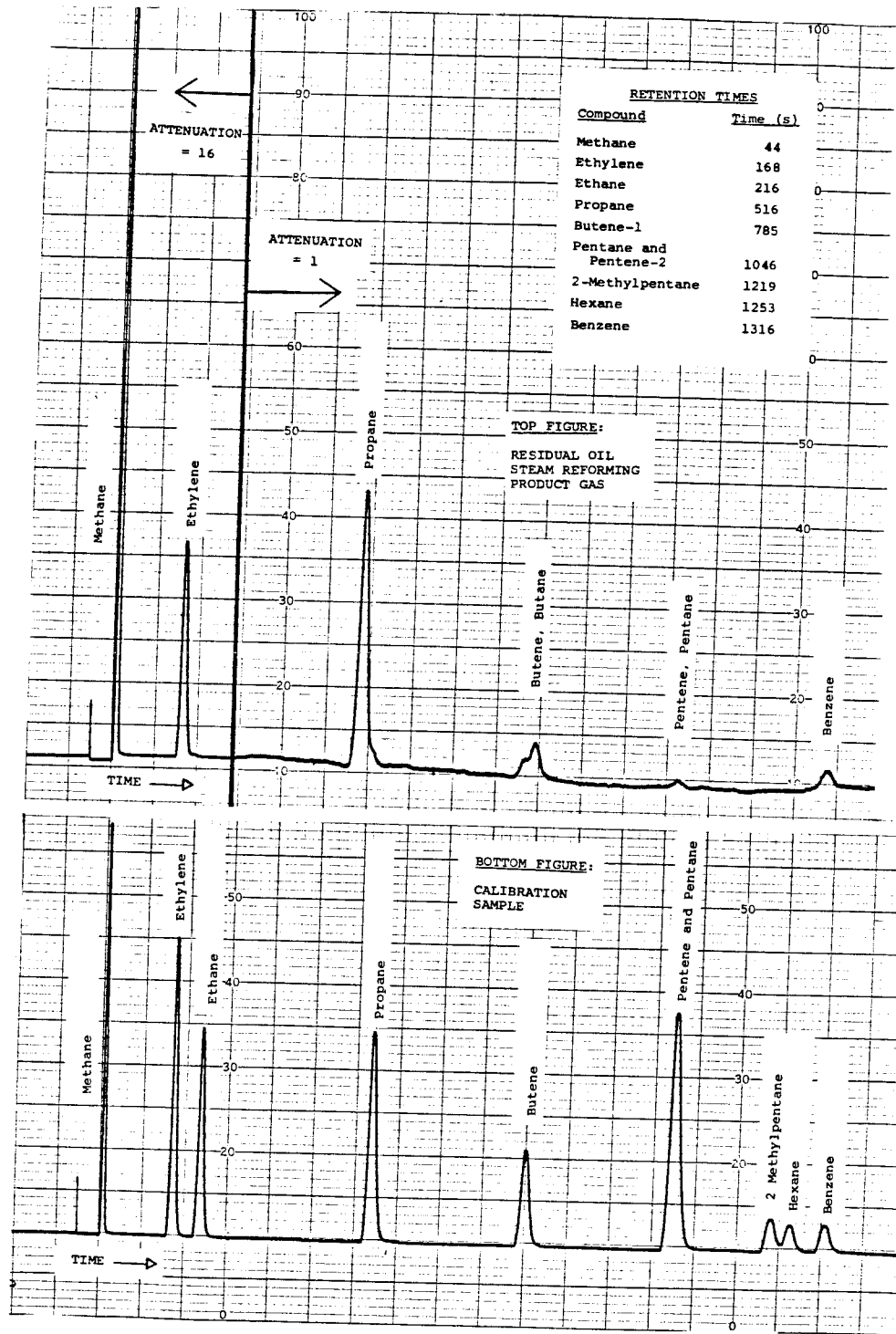


Figure 4. A sample gas chromatogram of the product gas of residual oil steam reforming at 1100 K as compared to a calibration sample.

residual carbon in the bed, one must observe the rate until a constant rate is attained. It is this background reaction rate which is attributable to the carbon in the colder sections of the reactor.

The results of the reaction rate of the residual carbon are presented in Table 5. Here the steam concentration was 20% with a negligible amount converted. The reaction rate given is the rate observed after residual oil injection. Here a suitable period had to be allowed for the system to stabilize to the lower flowrate. This took approximately eight to ten minutes. The reaction rate results are probably better for experiment 2 due to the longer observation time. Upon examination, the results indicate that experiment one had not decayed to a constant rate at $T = 100$ minutes. The two reaction rates obtained are also compared in Table 5 to the reaction rate of green sponge petroleum coke from Chapter 4. Both the salt (R_S) and no salt (R_{NS}) cases agree quite well with the data.

The results of two typical hydrocarbon analyses are presented in Table 6. It is seen that methane and ethylene comprise the bulk of the hydrocarbons evolved and have approximately the same concentrations. This composition may be compared to typical analyses of steam reforming and cracking product gases of other hydrocarbons in Appendix IV.

Table 5. The reaction rate of residual carbon in the molten salt bath compared to the reaction rate of green sponge petroleum coke from Chapter 4. The temperature is 1100 K, and the steam concentration is 20%.

Specific Rate (Experiment 1)	Specific Rate (Experiment 2)	R_{NS} (Chapter 4)	R_S (Chapter 4)
1.5 g/g/hr.	0.6 g/g/hr.	0.6 g/g/hr.	0.6 g/g/hr.

Table 6. Product gas distributions for residual oil steam reforming. The time indicated for the sample is from the beginning of the experiment.

Component	Experiment 2 (1.5 Minutes) (%)	Experiment 3 (2.5 Minutes) (%)
Methane	11	8.8
Ethylene	12	8.3
Ethane	0.58	0.36
Propane	2.3	0.95
Butene	*	0.03
Butane	*	0.08
Butene + Butane	0.32	(0.11)
Benzene	0.04	0.01
Hydrogen	*	3.4
Carbon Monoxide	0.16	0.15
Carbon Dioxide	0.015	0.014
H ₂ O	10.	10.
Nitrogen	Balance	Balance

* Unavailable

Figure 5 presents the change in product evolution with time for the beginning of the experiment (during residual oil injection). It is likely that the bulk of residual oil injection occurred during the initial stages of the experiment. Hence the hydrocarbons concentrations decline with time. Analysis of the gas after residual oil injection (ie, when flowrate 2 was used) revealed that small amounts of methane and ethylene were still being produced.

It is apparent that lighter hydrocarbons are substantially favored. And only straight chain hydrocarbons except for benzene were detectable. Also while hydrocarbon concentrations decline, the CO_x concentration remains relatively constant. This is a result of the carbon-steam reaction being slow and serving as the rate controlling step as discussed in Chapter 1.

8.4 Conclusions

1. The coke formed during residual oil steam reforming in molten phosphate closely resembles sponge coke. Both its reactivity to steam and hydrogen structure are quite similar to green sponge coke.

2. Hydrocarbons evolved during residual oil steam reforming include predominantly equal amounts of methane and ethylene. Trace amounts of benzene are also found in the offgas. Straight chain hydrocarbons are evolved with the amount decreasing as the chain length is increased.

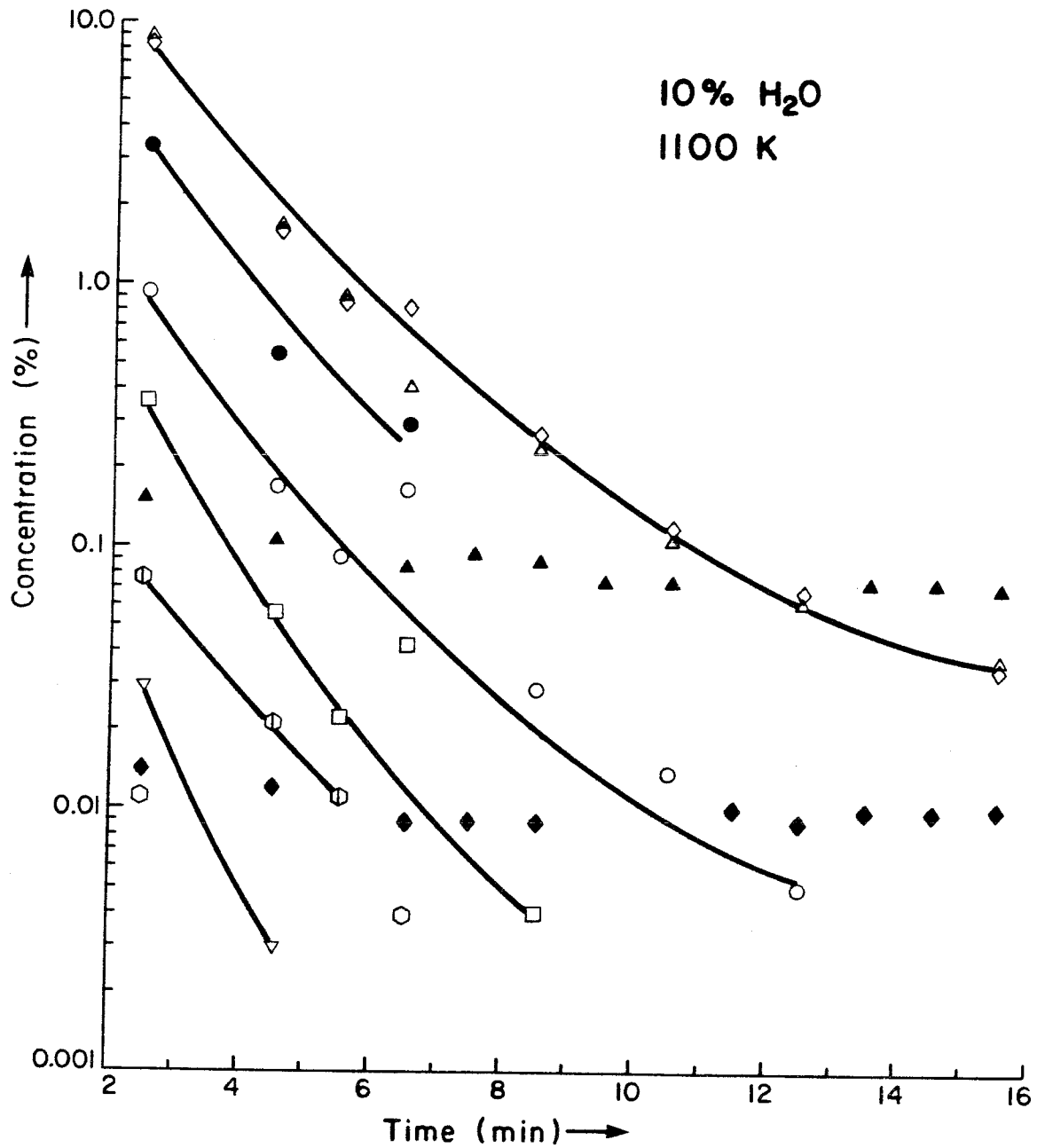


Figure 5. The evolution of hydrocarbon and carbon oxides with time for experiment 3. The time is from the beginning of residual oil injection. \blacktriangle , Methane; \blacklozenge , Ethylene; \square , Ethane; \circ , Propane; \blacktriangledown , Butene; \blacklozenge , Butane; \blacklozenge , Benzene; \bullet , Hydrogen; \blacktriangle , Carbon Monoxide; \blacklozenge , Carbon Dioxide.

CHAPTER 9

THE DESIGN OF CERAMIC REACTORS
FOR CONTAINING MOLTEN
SODIUM PHOSPHATE

9.1 Introduction

Here we shall discuss the design of our mullite reactors. Results shall be in the form of photographs which illustrate the discussion. First we shall begin by discussing the corrosive nature of molten salts and a possible method for containing the molten phosphate -- the use of inorganic coatings. Next we shall present the schematics and discussion of a large system which failed. We shall then discuss the relatively smaller systems which were used. Finally we shall discuss the modes of attack of the molten phosphate on fused ceramic materials.

9.2 Glazing

Fused inorganic materials are nonporous and as such resist corrosion well due to the limited area of contact with the molten salt. The problem with employing fused materials is that they are sensitive to thermal shock. On the other hand, porous solids such as castable refractories have high resistance to thermal shock failure. However the pores are penetrated by capillary action of the molten salt. This results in severe attack for the case of castolast G of Harbison-Walker Corporation. Here we shall use the term castable to refer to castolast G.

The most useful compromise is to apply a fused ceramic coating to the castable (1). This was performed in this laboratory. To retard corrosion a useful glaze must

have a glossy coating to minimize the total amount of surface area exposed to the molten salt. This requires a glaze with flint or silica. At first two industrial glazes were tried as obtained from Stewart's of California. HF-11 was a high silica glaze and was found to be totally absorbed by the pore structure of the castable. AM906 is a high potash feldspar glaze and is more viscous than HF-11. It was observed not to be completely absorbed into the pore structure of the castable. A suitable glaze (B-1) was also developed. The composition of this glaze is given in Table 1. These two glazes were then applied to cast crucibles by calcination to 2200°F for five hours.

The glazed crucibles were then tested for their resistance to corrosion. Corrosion testing consisted of contact with the molten phosphate in an inactive mode (no bubbling) for 12 hours and in an active mode (bubbling) for 2 hours at 1535°F. Corrosive attack was severe for Glaze AM906 and somewhat less severe for glaze B-1. Corrosion in these cases occurred where the glaze was thin. Pits were then etched out by the action of the molten phosphate. The results are shown in Figure 1. The bottom picture is a broken away section of the crucible glazed with AM906 to clearly show the pitting.

It was observed that baked magnesium zirconium flakes were not measurably dissolved by molten phosphate. Glaze B-2 was then developed. The composition and properties of

Table 1 . The compositions and properties of the glazes developed to resist corrosion by molten phosphate.

Component	Glaze B-1 Weight %	Glaze B-2 Weight %
Potash Feldspar	65.6	
Kingman Feldspar		58.3
Kaolin	15.2	
Mg/Zr Silicate		30.7
Flint	11.8	6.2
Whiting	7.4	4.8
Maturing Temperature	2200 ^o F	2300 ^o F
Softening Temperature	<2000 ^o F	>2000 ^o F



Figure 1 . Corrosion of glazes B-1 and AM906 upon exposure to molten sodium phosphate at 1540°F. Exposure consisted of 12 hours at ambient conditions plus 2 hours in the active, bubbling mode. The glazes were applied to Castolast G.

this glaze are given in Table 1. It was found to bond well with the castable. It may be seen as applied to the annular reactor in Figure 4.

A glazing procedure which is most suitable to resisting molten phosphate corrosion is to apply both an underglaze and overglaze. Here the application of the underglaze which is absorbed by the porous castable fills the pores somewhat. An overglaze is then applied which supplies the major resistance to corrosion. Should a crack develop in the overglaze, the underglaze will retard the corrosion.

9.3 The Large System

Some discussion is appropriate pertaining to a large system constructed in this laboratory for measuring the rate of gasification of petroleum coke and residual oil in sodium phosphate. Little data was generated with this system due to the corrosive nature of molten sodium phosphate.

9.3.1 The Annular Reactor

Originally an annular reactor was designed as detailed in Figure 2. Figure 3 shows the broken away base of the finished reactor. The reactor was constructed of alumina parts anchored and sealed in castable. After molding, the reactor was baked to remove molding wax in the various parts of the reactor and to mature the castable.

A weak feature of such reactors is their inside base where the inlet gas is supplied. Here the molten phosphate

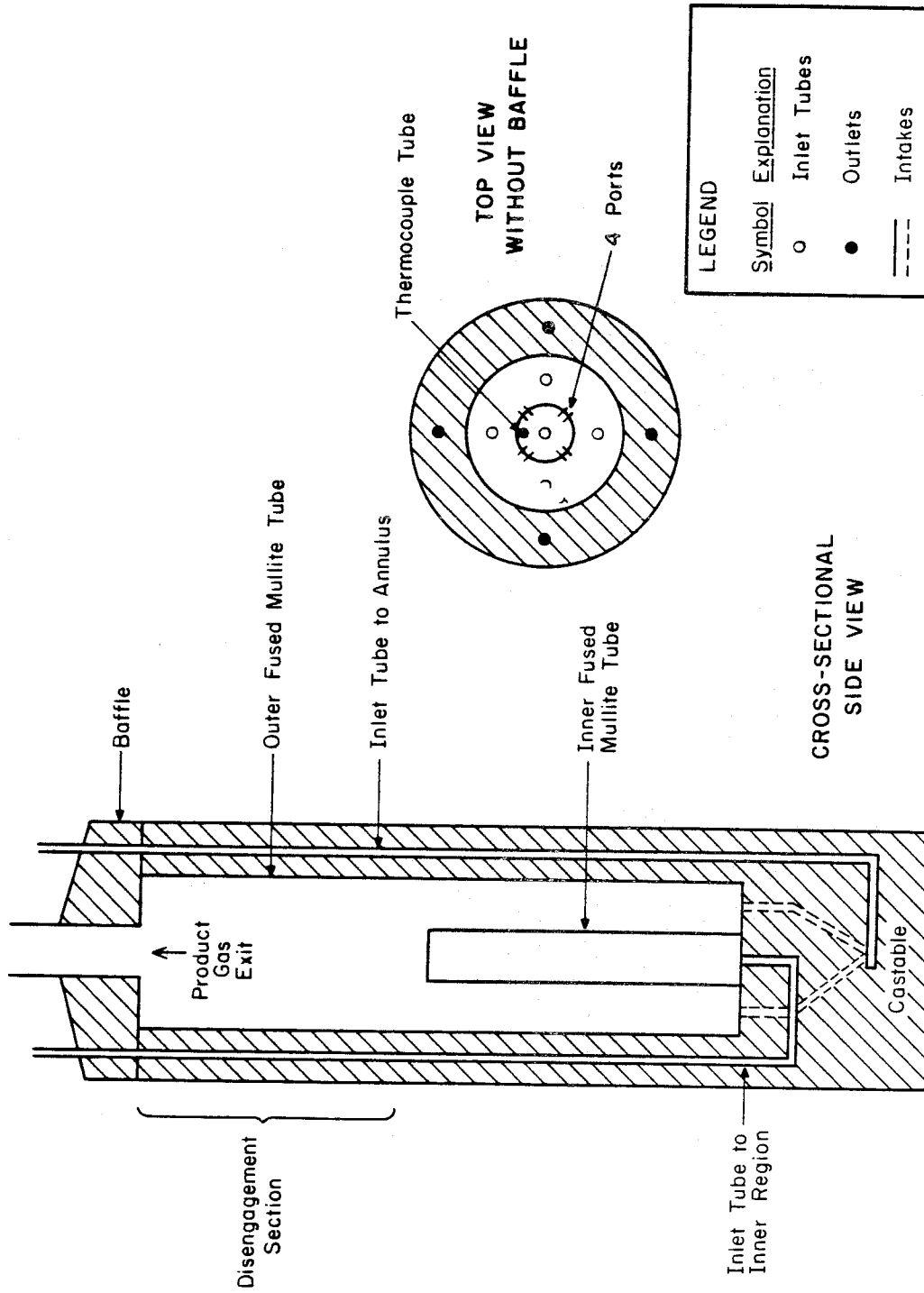
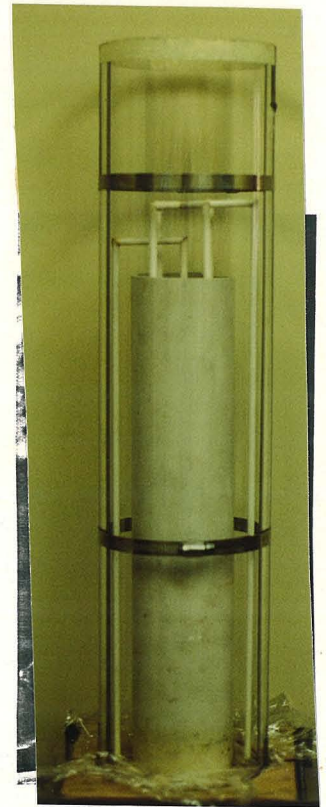


Figure 2. Schematic of the annular reactor.



TOP VIEW OF THE
CASTING SET-UP



THE OVERALL
CASTING SET-UP



THE BOTTOM SECTION OF THE CAST REACTOR

Figure 3. The casting set-up and a broken away section of the completed annular reactor. In the bottom picture, the inner core was not subjected to the stress caused by expansion of the outer fused mullite tube.

is directly exposed to the castable. In the first annular reactor constructed, the bottom was heavily coated with glaze B-1. The inlet tubes were sealed with this glaze, and sodium phosphate was added. The reactor was then heated to 1600^oF and thus exposed to molten phosphate for 24 hours in the inactive mode. Upon cooling, examination of the base of the reactor revealed no penetration of the salt into the castable refractory indicating the glaze had resisted the corrosion well.

For the second reactor, the double glazing procedure was used. A low viscosity underglaze (HF-11) which soaks into the pore structure of the castolast was applied, and the reactor was slowly baked to 1550 K. After cooling a high viscosity, silicate based overglaze (B-2) was applied, and the reactor was again baked to 1550 K. This did not seal the reactor to water and the overglaze was re-applied twice to the inside and outside. Leakage could not be stopped in the reactor, and on the final firing, the interior tube cracked.

This reactor although it failed did demonstrate some design criteria. Castable expands very little on heating and much less than the fused parts. This differential thermal expansion allows the fused parts to push out the castable on heating. Upon cooling, a void is created between the castable and the fused ceramic. This process also adversely

affects the strength of the castable. Indeed the annular reactor castable parts freely broke away until the base of the outer tube was reached as shown in Figure 3. Below this the castable firmly held. It was also found that centrally placed 1/4" OD fused alumina tubes cracked the castable if the overall castable width was less than 3/4".

Sealing with glazing material was impossible due to large voids in the castable. While fine pore structure may be filled by the underglaze, the large voids will provide liquid with a route to escape. Surprisingly, as pictures show in Figure 4, the glazing on the reactor bottom did not crack even though it was approximately 1/2" thick. Thus the method developed for glazing the reactors is sound. The weakness is that the gas was supplied by inlet tubes located at the bottom of the reactor. Salt intrusion into these inlets and hence into the castable proper cannot be effectively prevented from ultimately escaping from the ceramic vessel.

9.3.2 The Large Reactor System

After the failure of the annular reactor, a simpler reactor design was attempted. A schematic of this reactor is given in Figure 5. As is seen, it employed a mullite crucible for the reaction vessel. Reactant injection tubes as well as the thermocouple protection tubes were sealed in place by using the castable refractory. This was then housed

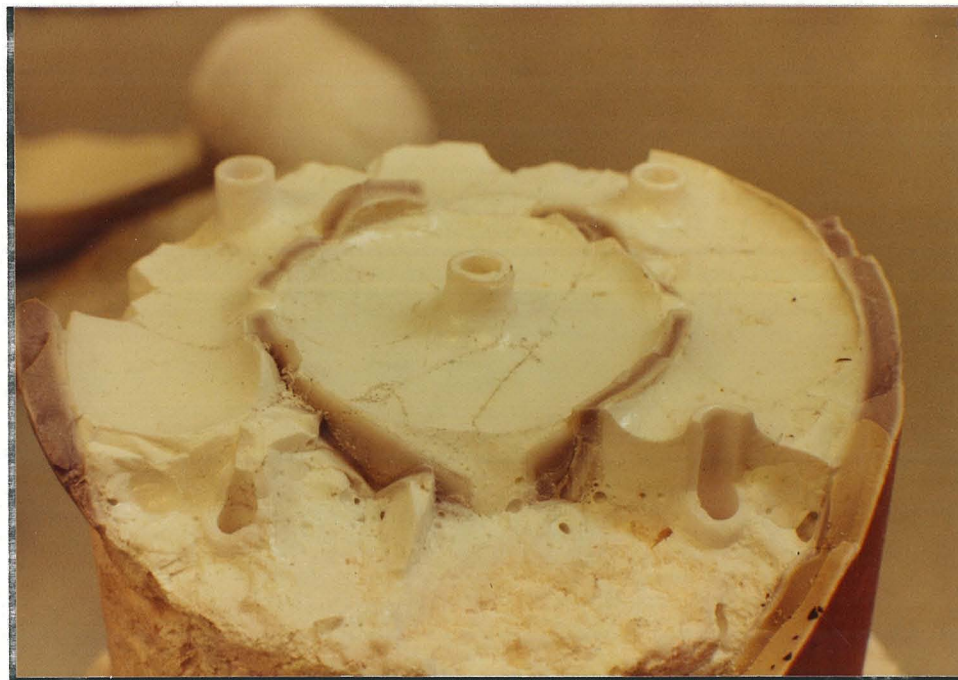


Figure 4. Bottom sections of the glazed annular reactor. HF-11 was applied as an underglaze. The overglaze, B-2, is seen.

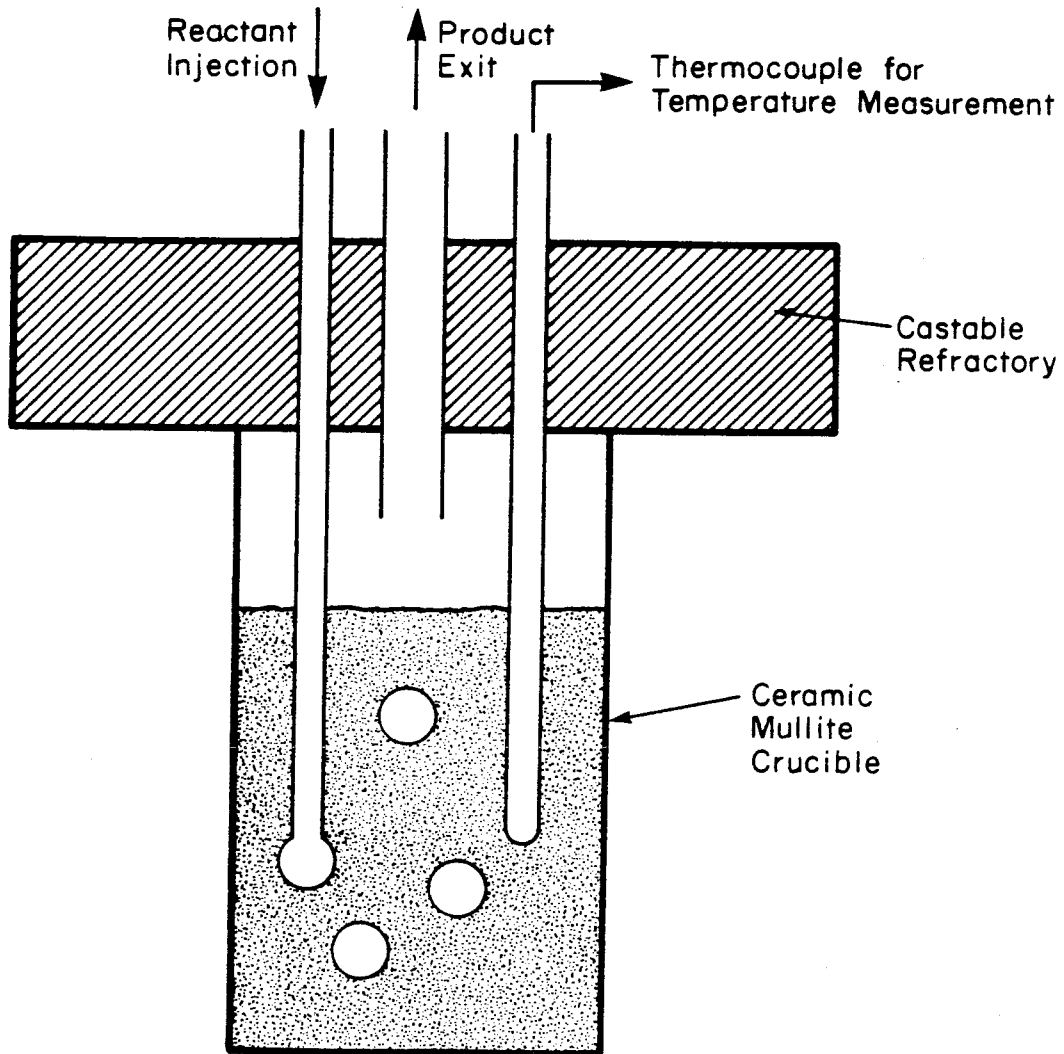


FIGURE 5. System I. Large Reactor for the Study of the Rate of Carbon Particle Gasification in a Slurry.

in an inconel reaction shell which sealed the reaction vessel from the atmosphere. The furnace section of the system is shown schematically in Figure 6. Two reactant inlet tubes were used and are designated as the inner tube and outer tube inlets. The nomenclature was carried over from the annular reactor previously discussed. A solids feeder was specially constructed to allow feeding of carbon particles. The screw conveyor dumped the carbon onto a vibrating plate which fed carbon into the system continuously.

It is also noted that a nitrogen sweep vessel was used to help insulate the parts of the reactor which needed to be disassembled after use from oxidation. The vessel was composed of a ceramic clay. This worked somewhat as after firing, it was possible to disassemble metal parts which had been heated to 1800°F.

The total system is shown in Figure 7a. Analysis consisted of TCD and FID gas chromatography for hydrocarbons and fixed gases. CO_x detection was accomplished by infrared absorption. For clarity numerous controllers are not shown. A large steam generation system was constructed. This is shown in Figure 7b. It was found that steam could be generated successfully and without oscillatory fluctuations by a suitably large pressure on the inlet water and preheating the water to its saturation temperature before entering the steam generation tubes. However due to the extensive maintenance required for the upkeep of the steam generator, later attempts to operate

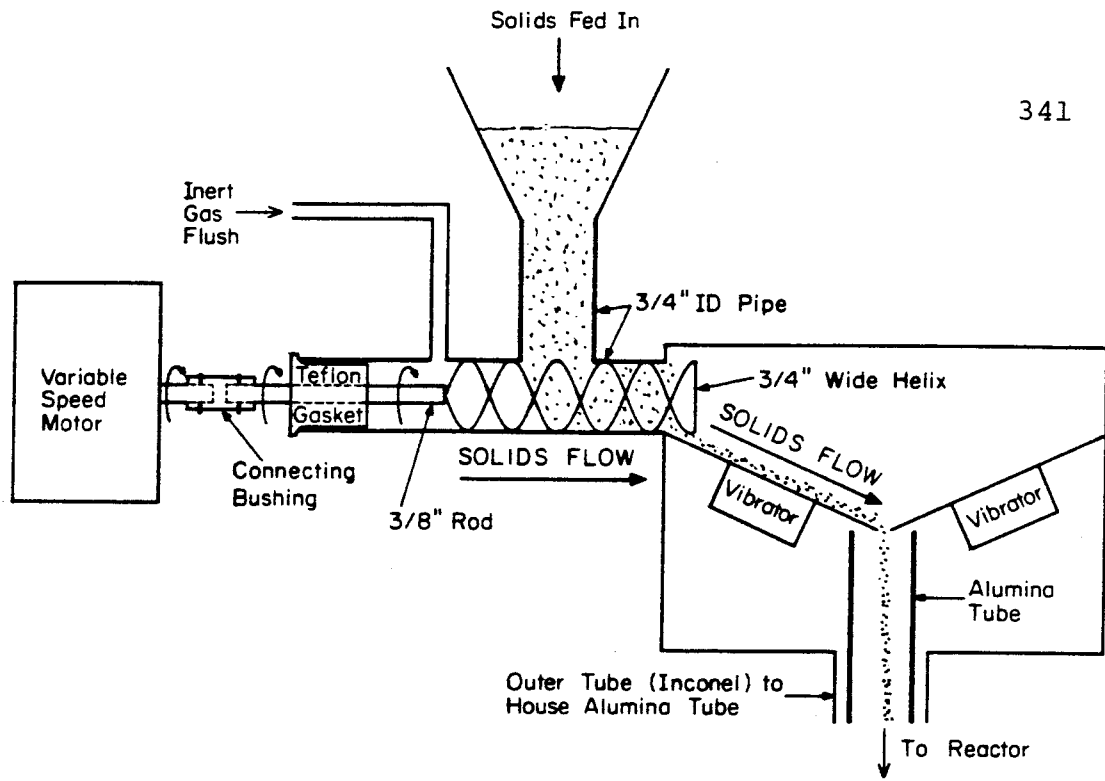
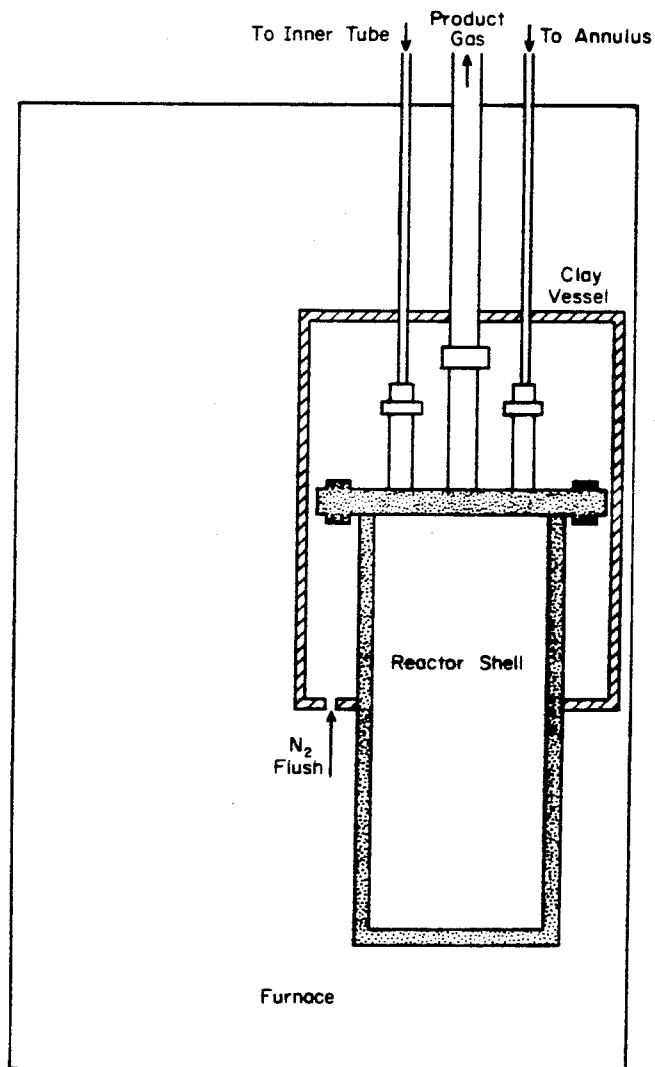


Figure 6. The Reactor Section of the Large System.



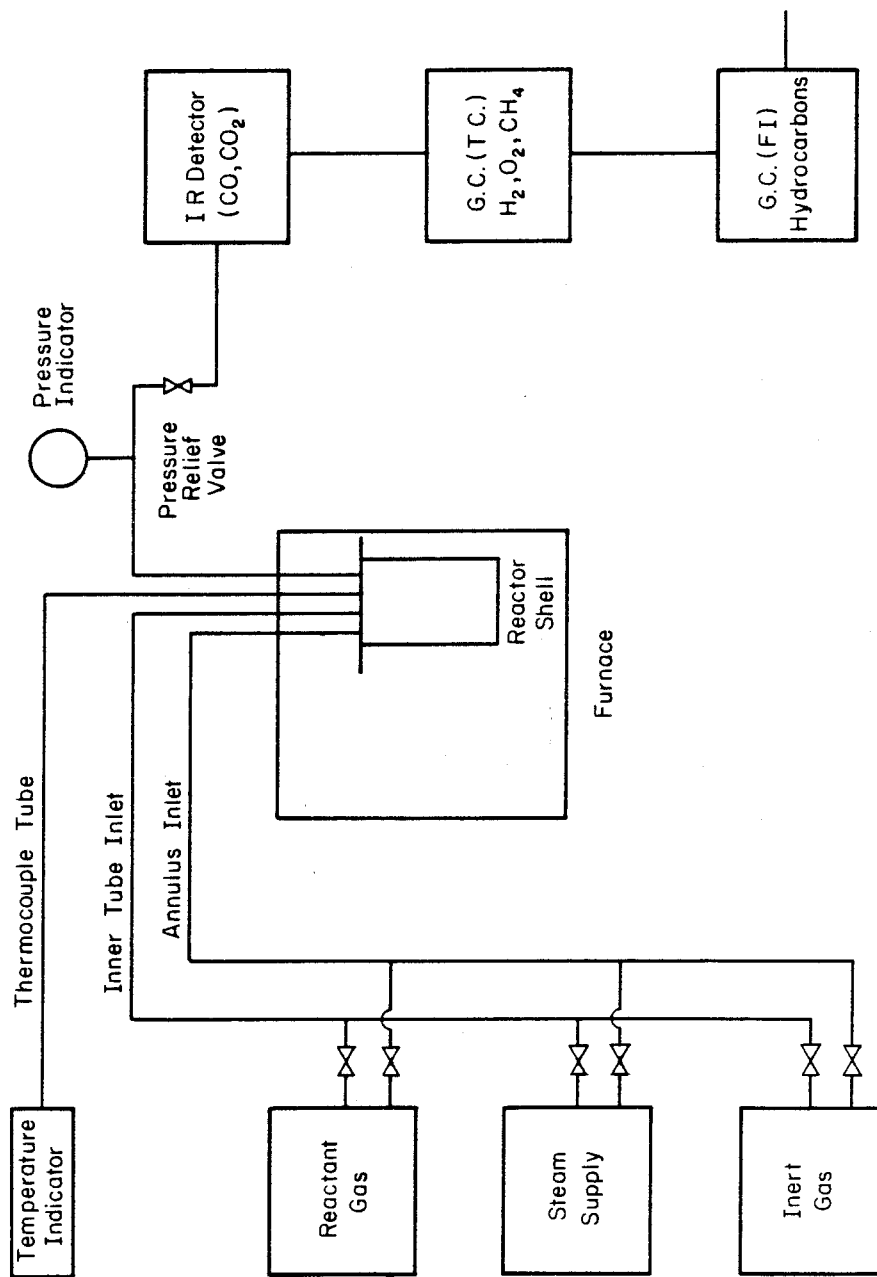


Figure 7a. The experimental set-up for the large system.

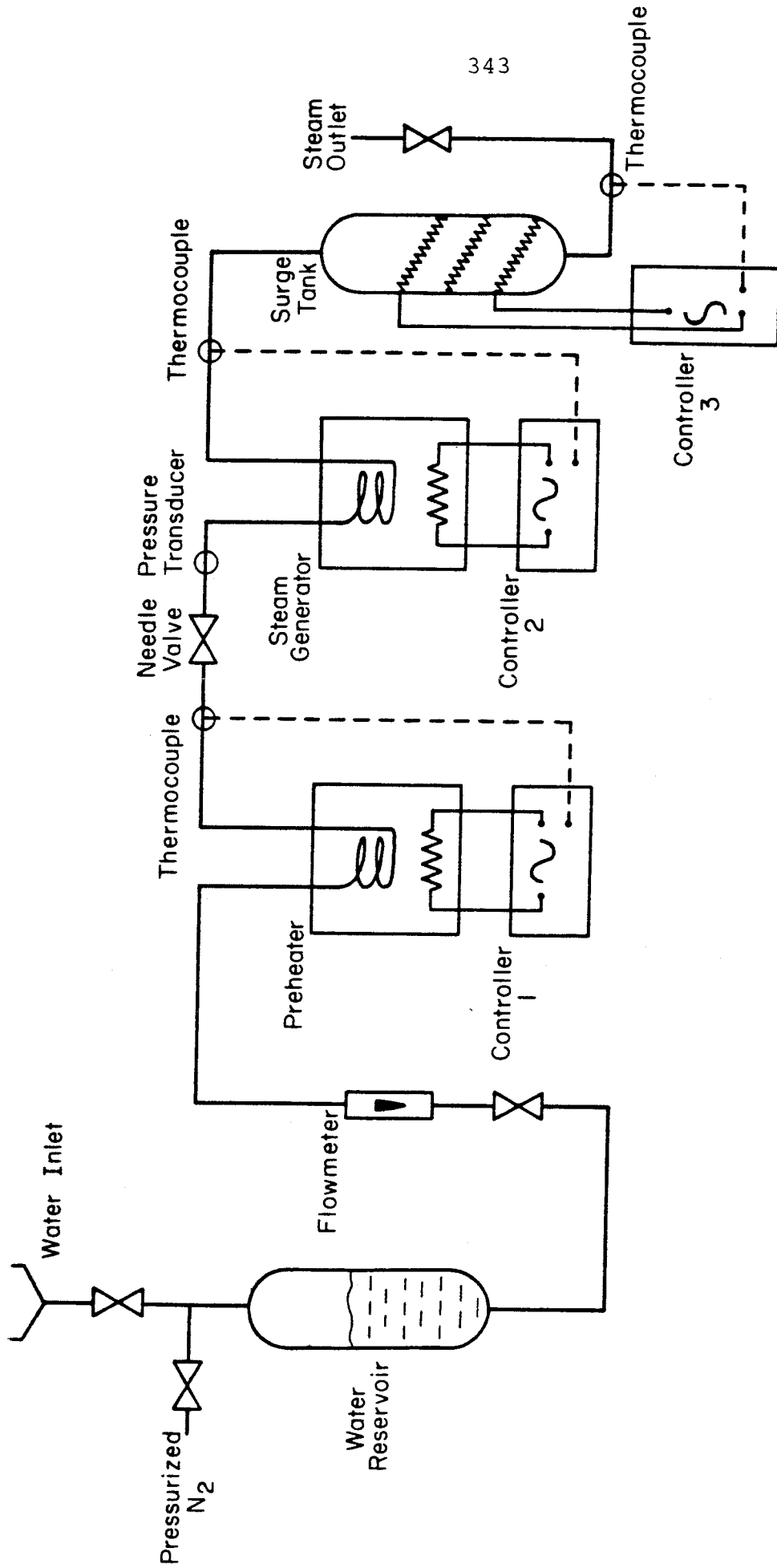
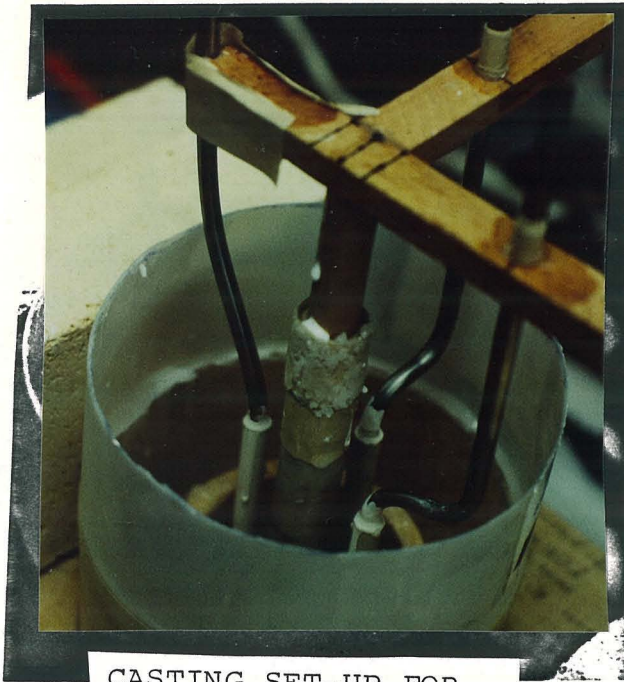


Figure 7b. The steam generator for the large system.

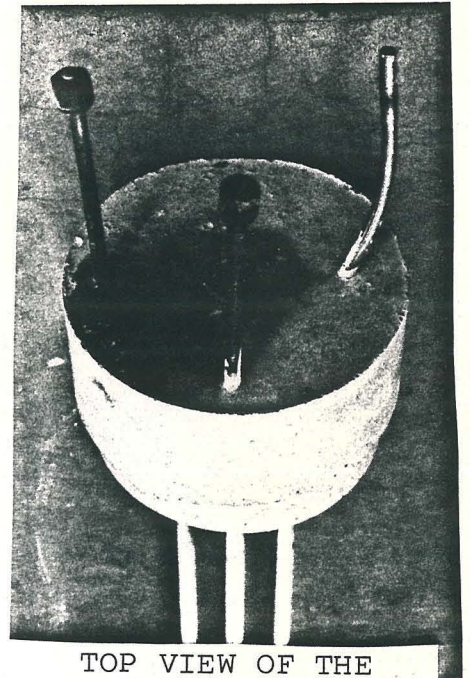
the large system relied on the relatively simpler steam generator discussed in Chapter 4. It was also quite obviously necessary to heat all input lines into the system to insure against steam condensation. To guard against shorts and heater failures, indicators and controllers were used with thermocouples attached to all critical points.

The casting sequence is indicated in Figure 8. Here we accomplished high temperature seals from inconel tubes to mullite tubes by the use of castable refractory. For the gas distributor the inconel tubes were machined and protruded inside the mullite tubes. They were glued in place. Such glueing is important as this not only sealed the casting configuration but upon heating to the reaction temperatures where the glue was destroyed, the spacing provided by the void created allowed for the differential thermal expansion of the mullite and inconel tube. The casting also sealed the reactant injection tubes and thermocouple tube into place.

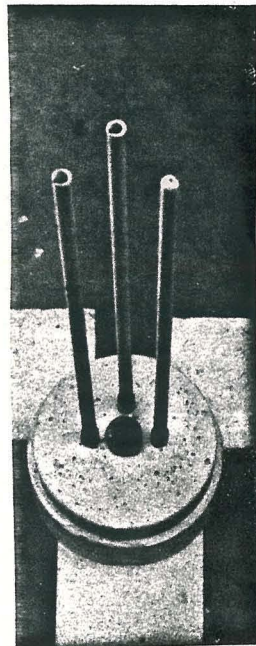
Figure 9 indicates the sealing method. Here the inconel tubes from the gas distributor protruded through the pipes in the bottom picture. These were then sealed with swagelok fittings to the inside tubes in the top picture. The ultimate seal from the atmosphere was then accomplished by rotating the large outer fitting into place. Thus we effectively have a double seal. The interior seal enables the reactant gas to be bubbled through the molten salt reactor. The outer seal



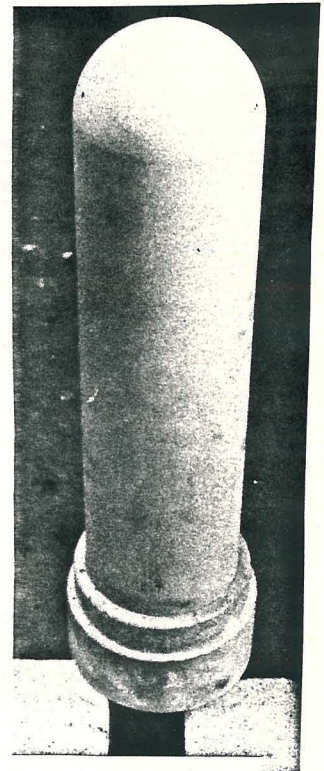
CASTING SET-UP FOR ACCOMPLISHING HIGH TEMPERATURE MULLITE TO METAL TUBE SEALS



TOP VIEW OF THE COMPLETED GAS DISTRIBUTOR



BOTTOM VIEW OF THE COMPLETED GAS DISTRIBUTOR



COMPLETED REACTOR

Figure 8. The component parts of the large molten salt reactor.

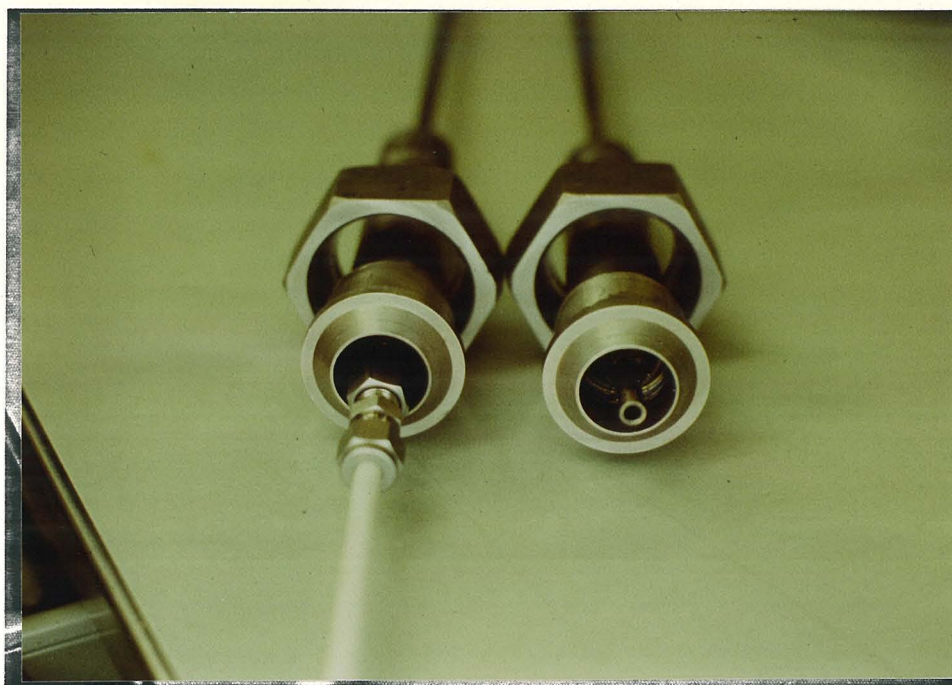
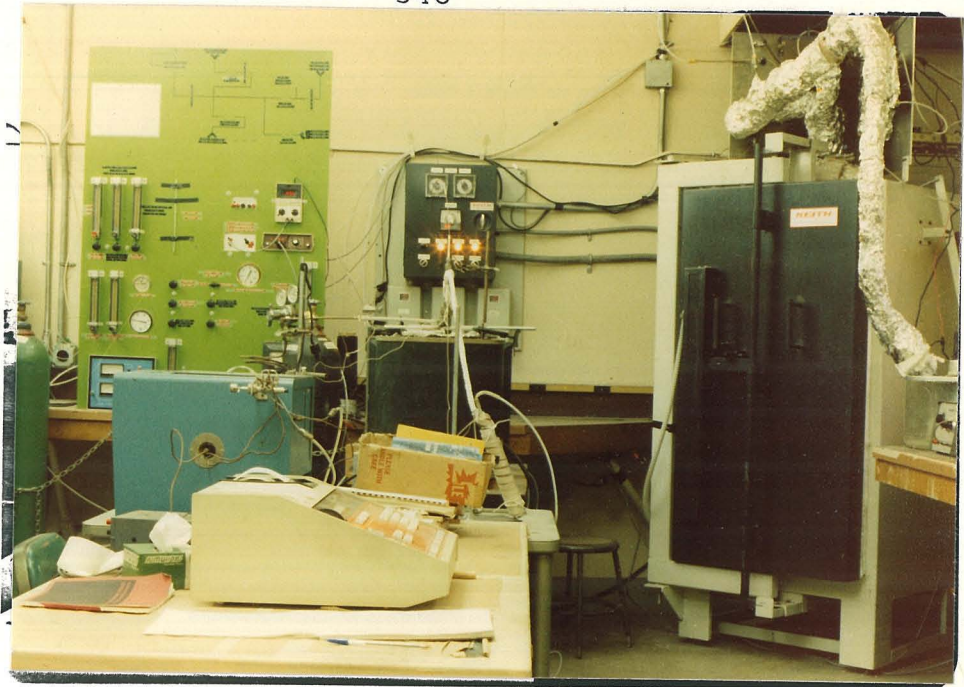


Figure 9. The metal tubes from the top of the gas distributor protruded through the fittings in the bottom picture. These were then attached with a swagelok fitting to the inner tubes in the top picture. The large outer fittings were then fastened sealing the reactor from the atmosphere.

allows the product gas to be collected and prevents oxygen encroachment from the atmosphere.

Figure 10 shows the system in place in the furnace without the nitrogen sweep vessel. Also the completely assembled system is shown in Figure 10. The top flange of the inconel shell was sealed by the use of ceramic paper. This type of sealing worked very well. Graphite based seals were completely oxidized even though oxygen access was impaired by the nature of the seal. That is, the oxygen had to penetrate a well machined flat metal flange to access the seal. An added note is appropriate on heating metals to very high temperatures and disassembling them. If the disassembling requires threads, it is best to have a very loose pitch. Fine pitches have a tendency to gaul. Gauling was severe for the fine pitched threads indicated in the bottom of Figure 9, and these could not always be disassembled. The flange bolts had a very broad pitch and were easily disassembled.

The overall system was found to be well sealed. And all parts of the reactor worked. The ultimate failure of this system was the relatively long time required for heat-up and stabilization. Before such stabilization could take place, the reactant injection ceramic tubes were dissolved by the salt. Thus, while the design features are sound, a more suitable material should be used for the parts of the reactor which directly contact the molten salt.



Overall Experimental System

Assembled Reaction
Vessel placed in
the Furnace

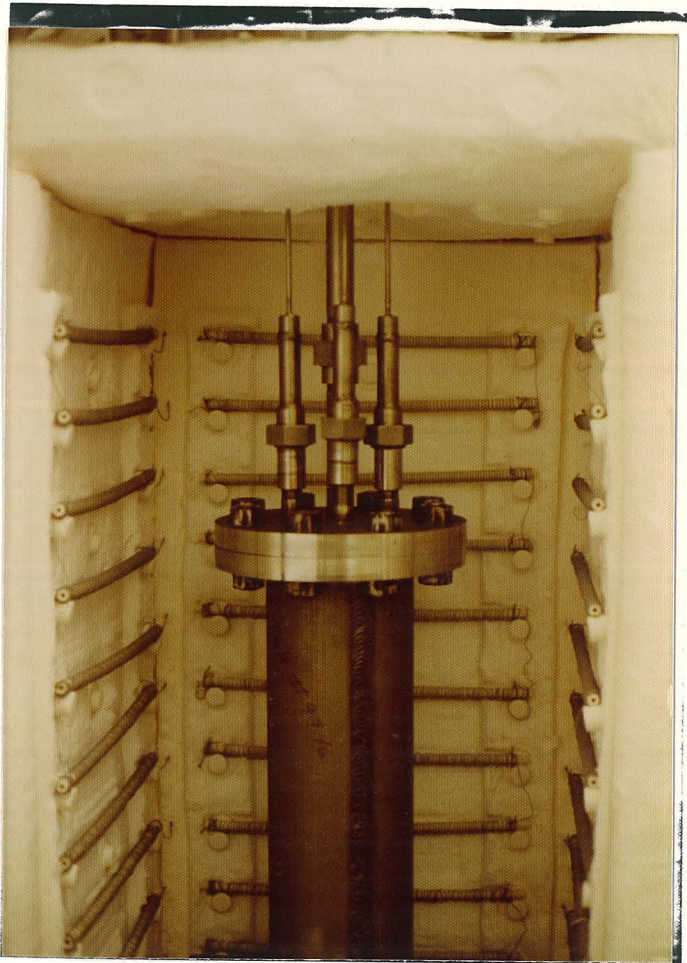


Figure 10. The assembled reactor and the overall experimental system.

Here we have detailed this failure for one purpose. This failure was time consuming and expensive. It is discussed here to hopefully prevent its recurrence. The advantages of an annular reactor were apparent in theory. It allows, as discussed in Chapter 3, both an oxidizing and reducing chamber. It is conceivable that such an annular system with appropriate plumbing could readily accomplish the objectives of Figure 2 in Chapter 1. Such a design for high temperature reactions in molten salts requires more extensive consideration of the extremely corrosive nature of molten salts.

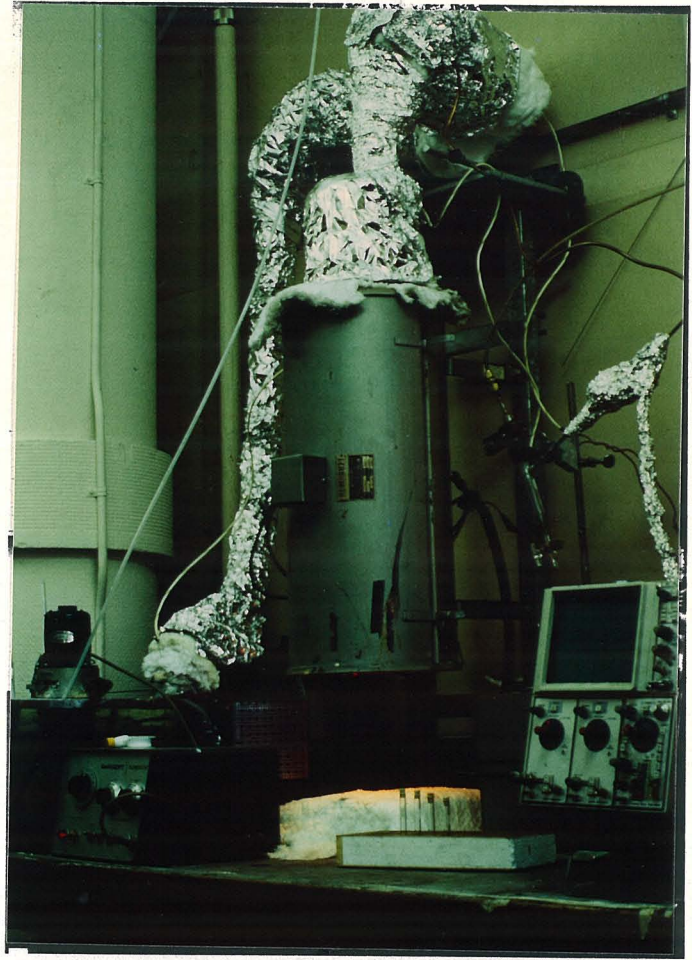
9.4 The Small Reactor System

After the failure of the large reactor, a relatively smaller system was designed. It worked very well in that it required relatively short heat-up times and allowed experiments to be performed before ultimate failure due to corrosion.

Figure 11 shows the experimental set for the small system. As shown in the bottom picture of Figure 11, the mullite tube reactor section was placed in a tubular furnace. The residual oil reactor is shown in Figure 12.

Figure 13 shows the component mullite parts of a small reactor and the assembled reactor. Here it is noted that these types of reactors were used to generate the results

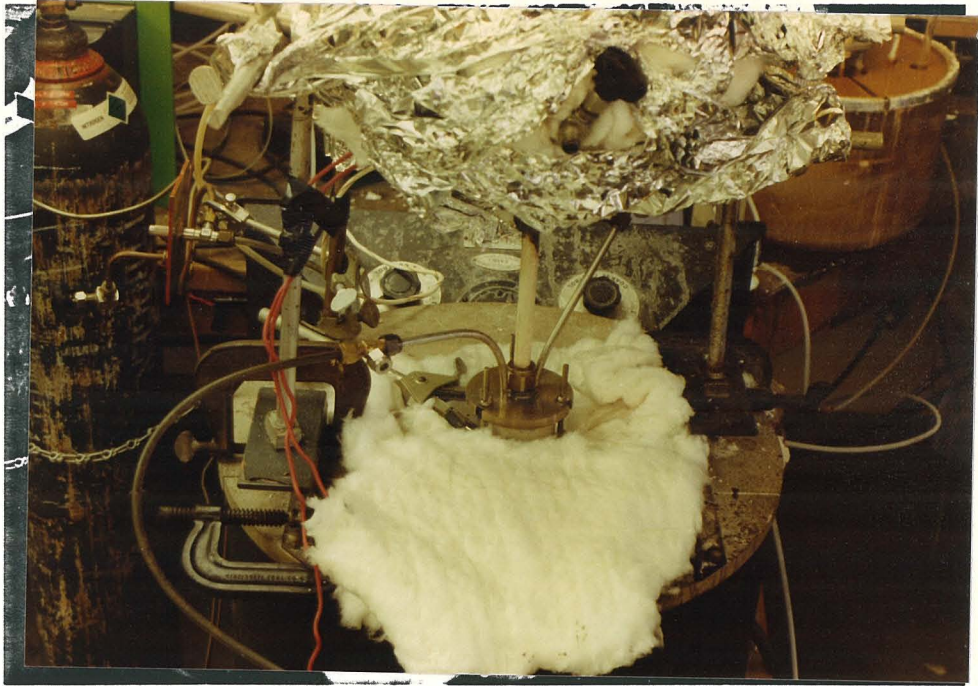
The Small System



Reactor
Placement
in the
Furnace



Figure 11. The experimental set-up for the small system which was used to generate the data presented in Chapters 4 through 7.



Close-up of the residual oil reactor as placed in the furnace

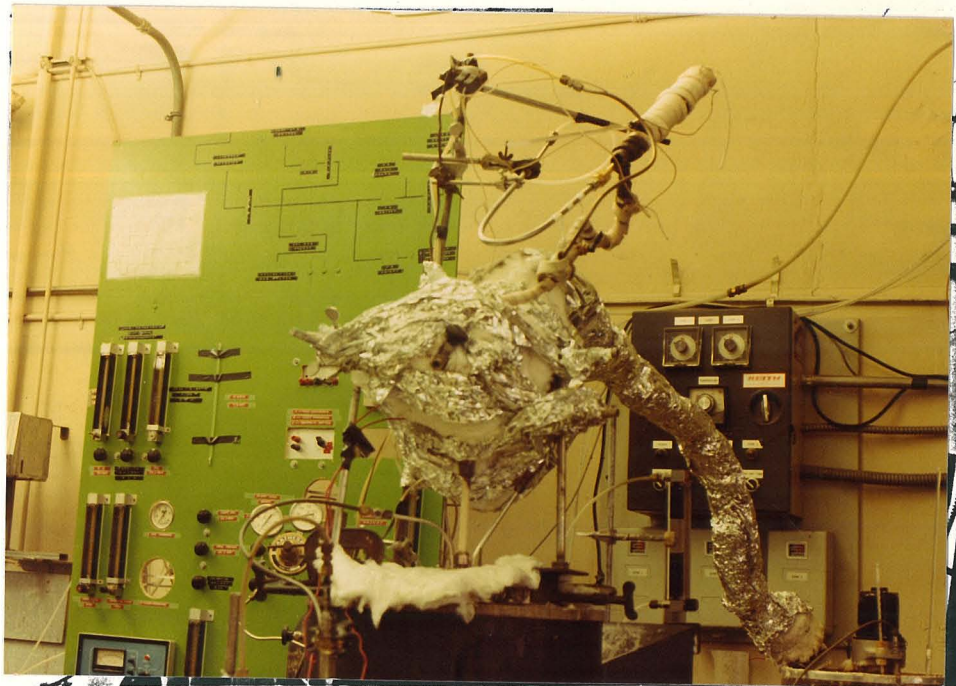


Figure 12. The residual oil reactor experimental set-up which was used to collect the data presented in Chapter 8.

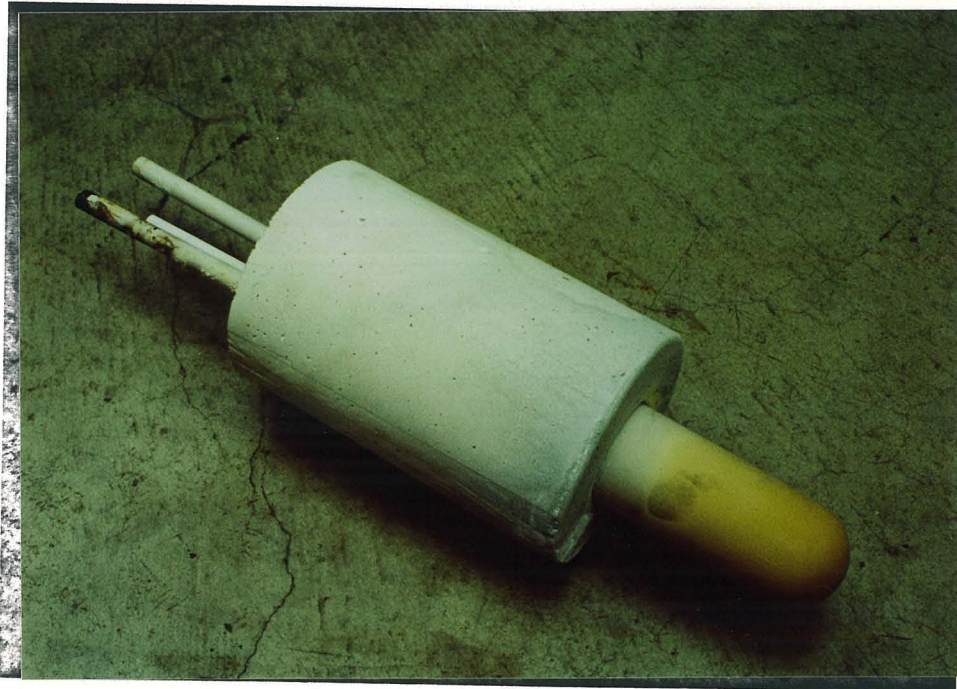
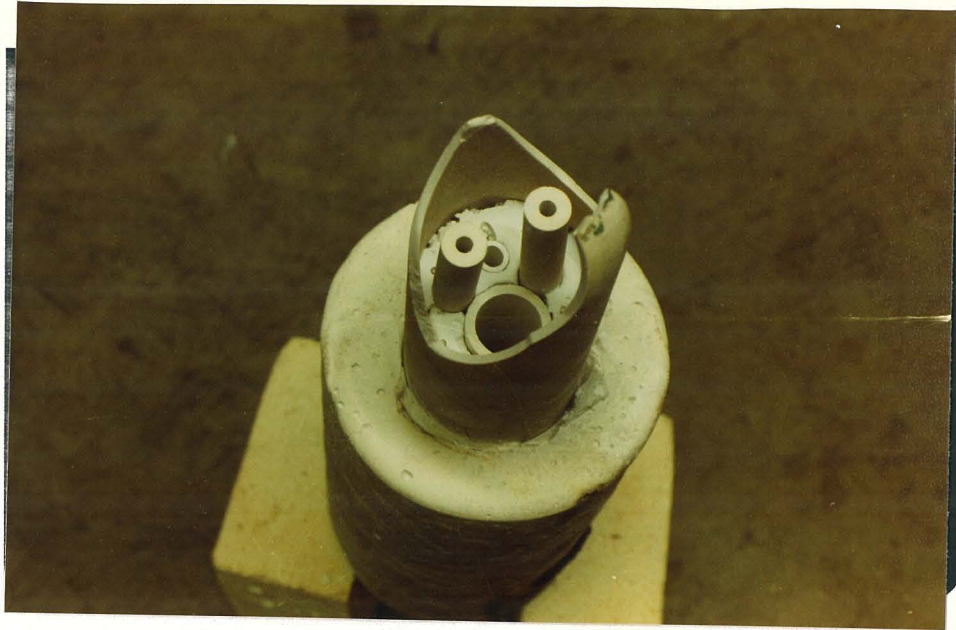


Figure 13. The component mullite parts and the completed small reactor. Shown is Reactor I.

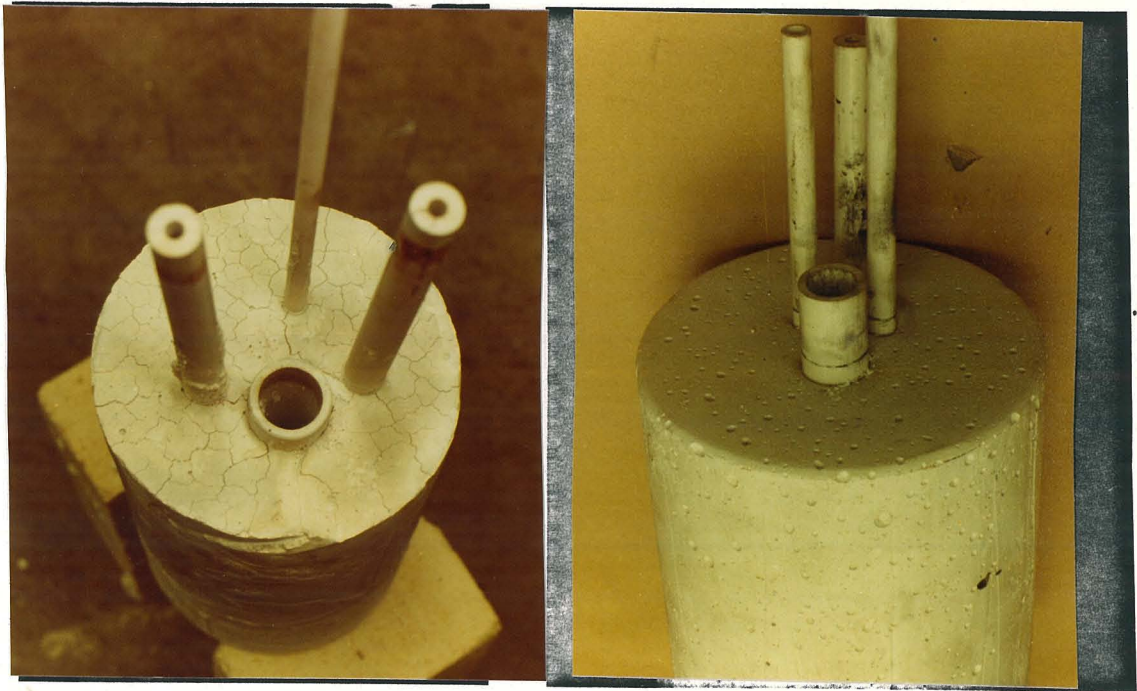
presented in Chapters 4 through 7. Figure 14 shows a broken away section of a small reactor and illustrates that very good seals are created by casting mullite parts into place.

The most important aspects of such reactors are nuances in their design. A castolast section eight inches long was found to work adequately. This essentially alleviates temperature gradients on the ceramic crucible by creating a shallow temperature gradient where the mullite crucible connects onto the castable. The extreme gradients produced by the residual oil reactor set-up generally crack the crucible. This is apparently alleviated by going to smaller diameter crucibles.

The mullite tube projected two inches into the castable seal. As stated before, the differential expansion of mullite vs. the castable presents problems. This is alleviated by pouring the castable thick (ie, with less water) in the top section (cold section) of the reactor. Near the bottom section (where the crucible is attached), the castable should contain more water. This makes the castable in the bottom section weaker and more porous, and the mullite as it expands easily crushes the castable. This then alleviates stresses on the crucible. Carried out to the extreme, no seal could be accomplished. Thus this feature requires compromise.



Broken away bottom section of Reactor I.



Castolast G provided seals for
the mullite tubes.

Figure 14. Castolast G provided an excellent method of sealing fused mullite parts into a reactor configuration.

9.5 Failure Modes of Fused Ceramic Reactors

Here we will discuss thermal shock failure initially. We will then discuss the corrosive attack on the mullite parts of the reactors.

9.5.1 Thermal Shock Failure

The most common failure was due to thermal shock. It should be noted that we are heating glass materials to high temperatures. Temperature gradients in the furnace caused such failures. Also the crucibles seemed to have slight flaws which caused some of the failures. Figure 15 gives some examples of thermal shock failure. This generally produced a long thin crack in the reactor. Then by capillary action, the molten salt was drawn out of the reactor rapidly.

This type of failure may be minimized by appropriate design, ie, the use of castable to alleviate temperature gradients. This also requires extensive inspection and replacement of furnace elements as inconsistencies in the heat supplied around the reaction vessel led to several failures.

9.5.2 Corrosion of the Ceramic Mullite Tubes

The corrosiveness of the salt was found to be much worse in the bubbling, active mode than under ambient (no gas flow) conditions for the lower temperatures (<1300K).



Figure 15 . Examples of thermal shock failure of fused mullite crucibles. Even though the cracks produced were fine and the molten salt was quite viscous, capillary forces drew the salt through such cracks in a relatively short time.

The peculiar "necking" of the tubes indicated in Figures 16 and 17 is due to the bubbling bath corroding the tube at the expanded height less so than where salt continuously contacted the tube. A close-up of this is shown in Figure 18.

At higher temperatures, the inside of the reactant injection tube was corroded as shown in Figure 19. Here severe inactive mode corrosion was at work and a bubbling mode was not necessary for substantial corrosion. Thus the corrosion of mullite by sodium phosphate is apparently an activated process.

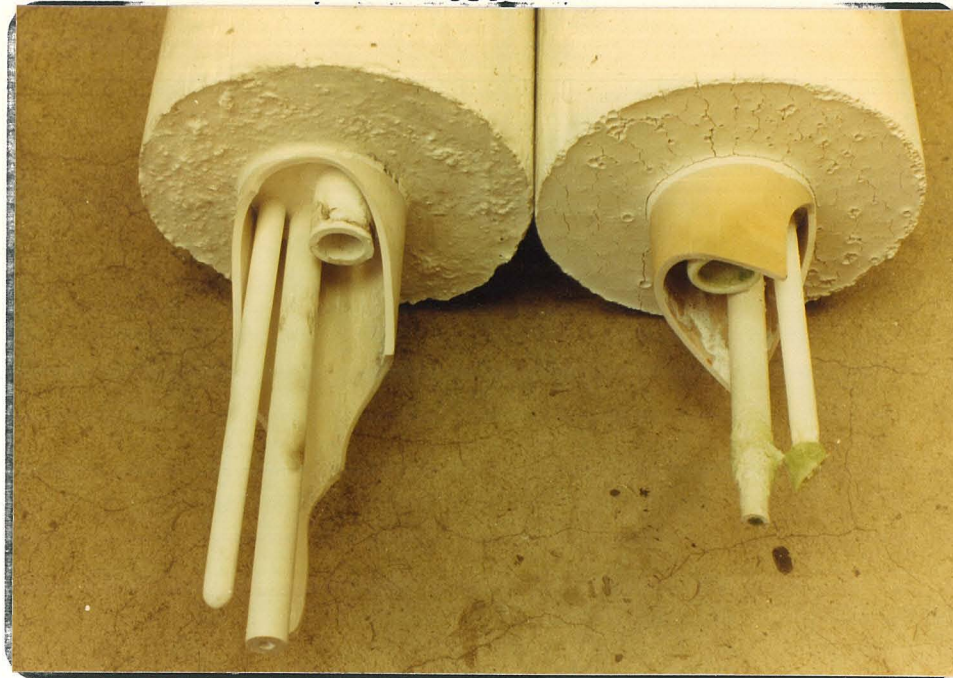
9.5.3 Corrosion of the Ceramic Crucibles

The typical failure mode of the crucibles is indicated by the bands shown in Figure 20. These were located near the ambient salt height. The ceramic crucibles became very thin at this point after substantial exposure to the molten salt. It was these bands which produced failure of the reactors when thermal shock failure did not occur. The reactant injection tubes did not fail as they had substantially thicker walls than the crucible.

High purity alumina was employed in some experiments. No difference in corrosion resistance was noted between mullite and alumina. Hence due to the mullite being less expensive, it was used for the bulk of the experiments.

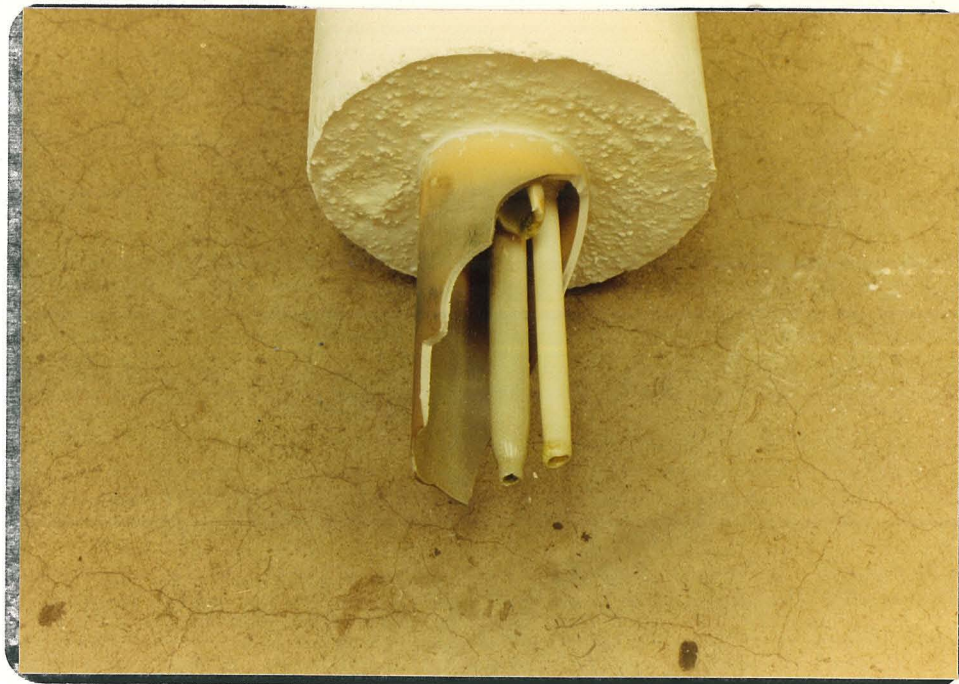


Figure 16. Examples of the corrosion of the mullite reactant injection tube in bubbling situations. The top and bottom right pictures include an uncorroded mullite tube for comparison. The reactant tube is apparently corroded to the level of the gas-liquid bed.



No Molten Salt Exposure

Molten Salt Exposure



Molten Salt Exposure

Figure 17. Examples of necking corrosion of the mullite reactant injection tubes. Exposure to the molten salt was approximately 100 hours with about 10 hours in the active, bubbling mode. The temperature was kept well below 1200 K.



Figure 18. Close-ups of the necking corrosion of the mullite reactant injection tubes. The tube to the right in both pictures is the thermocouple tube while that to the left is the reactant injection tube.

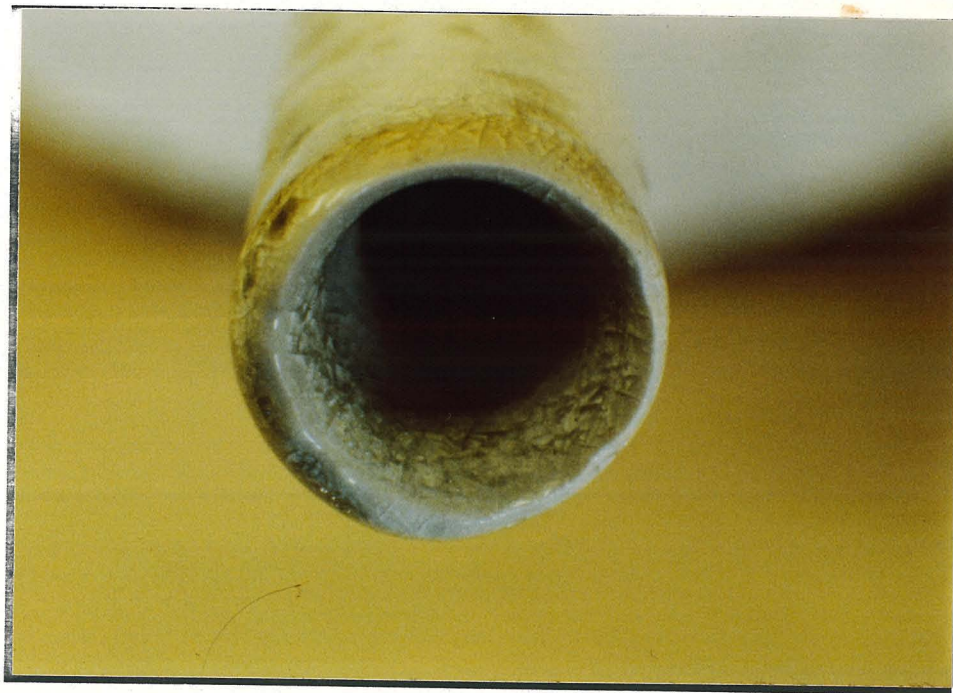
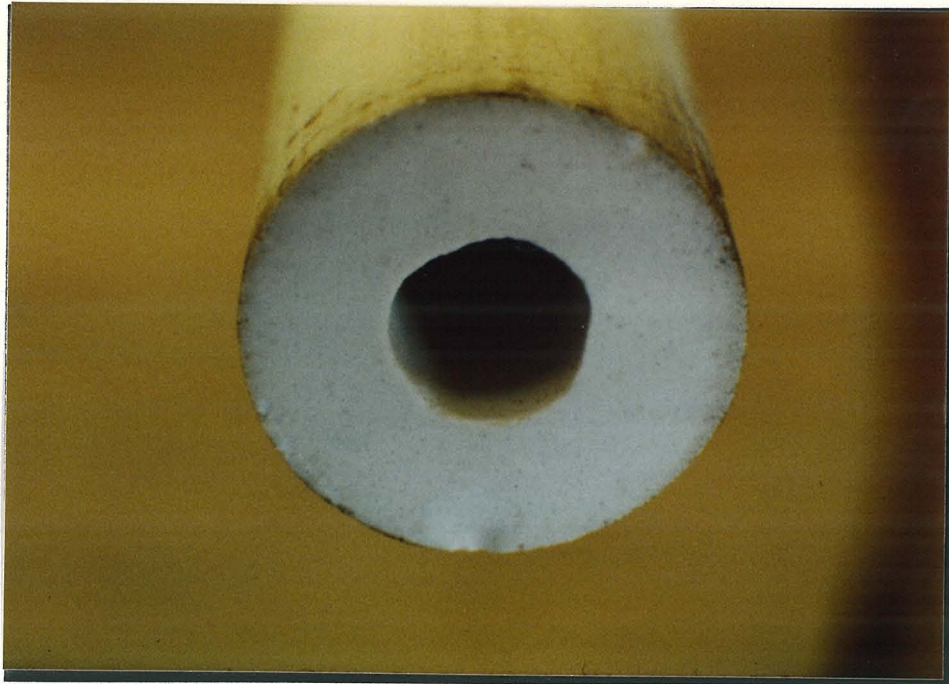


Figure 19. For high temperatures, the interior of the reactant injection tube is significantly corroded. The bottom picture is for approximately 24 hours of molten salt exposure at 1300 K. The tube was in an active bubbling mode for two hours. This may be compared to the top picture which is an unexposed tube at the same magnification.

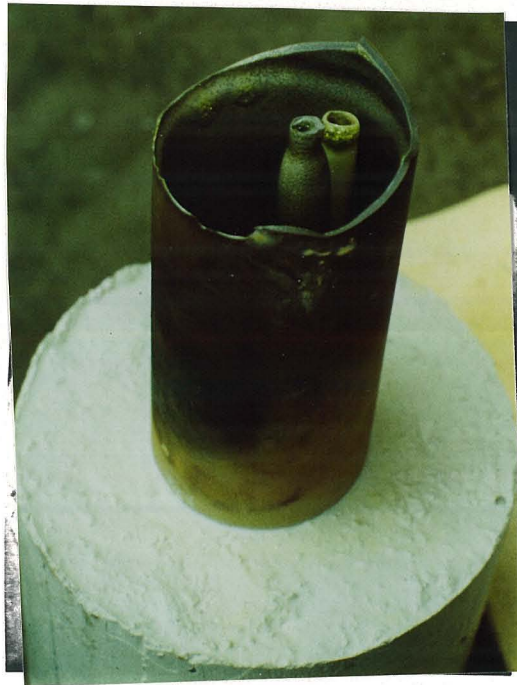
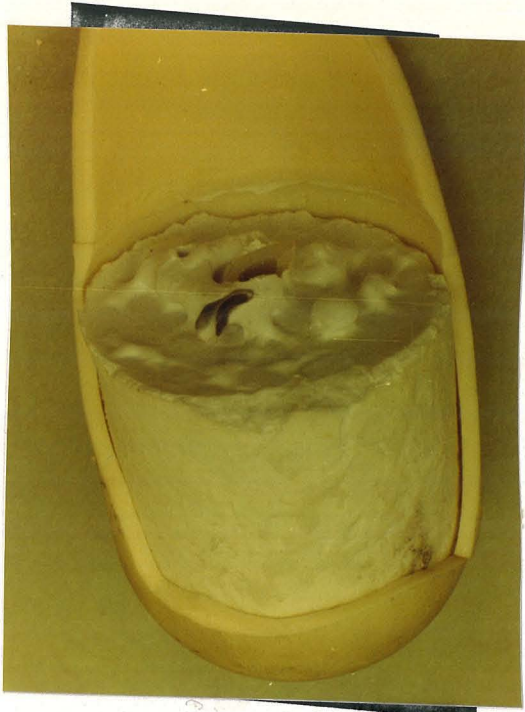


Figure 20. The bands seen in the crucibles in the above pictures are heavily corroded sections. Such corrosion produced a ring slightly above the ambient molten salt level.

9.6 Conclusions

Mullite is a poor method of containing molten sodium phosphate. However this should not discourage its use. The mullite is quite strong and may be sealed into any configuration using castable refractory. Such reactors seem to have promise but require application where the mullite is not so severely corroded.

The most promising method of containing molten salts outside of platinum or a cold wall reactor employing frozen phosphate is the use of inorganic coatings. Glaze composition should entail a large concentration of silicates which seemingly have low solubilities in molten phosphates. However extensive development and testing is need beyond that supplied here.

REFERENCES

1. Parmelee, C. W., Ceramic Glazes, Cahners Books, Boston Massachusetts (1973)

CHAPTER 10

CONCLUSIONS AND RECOMMENDATIONS

10.1 Introduction

This thesis has given an overview of the general features of the molten salt gasification process. Here we will begin by summarizing the conclusions of this study. Also due to the scope of this project, several problems could not be fully investigated. Thus the second section of this chapter will include recommendations for further research. We shall conclude this chapter with a critique of the molten salt gasification process.

10.2 General Conclusions

In Chapters 3 through 7, the gasification of carbon particles in bubbling molten phosphate slurries was shown to follow the direct reaction mechanism where particles come into direct contact with the gas in the bubble. This is enhanced by the covalent nature of the carbonaceous solid and the ionic nature of the molten salt creating a large contact angle. The other contributory factor is the low solubility of oxygen in the melt. This retards the rate of the indirect reaction mechanism.

Molten sodium phosphate does catalyze the carbon-steam and carbon-oxygen reaction. The magnitude of this effect is limited by the large molten salt-carbon contact angle. Contact with the catalytic media is confined to a small portion of the particle's external surface area.

One must realize the two effects described above before proceeding. The reaction rate of carbon particles in a molten salt slurry may be inhibited as compared to gas phase kinetics. This is not a chemical inhibition of the reaction rate by the molten phosphate. Indeed it catalyzes the gasification reaction. Inhibition is caused by the rate of carbon particle-bubble contacting being slow. Hence a transport effect may be confused with a chemical effect if appropriate precautions are not taken.

An important part of this study was examining the reaction rate of a carbon particles in a variety of reactor configurations. To properly assess a gasification process, the kinetics of the carbon reaction in the gas phase must be initially studied. This establishes a base case and enables one to assess what effect the gasification scheme actually has. The reactivity of one char tells one very little about how another char may react. This also holds true for petroleum coke. Hence one must establish the base case for the type of carbon that is being gasified by the process.

This project ended with an experimental study of the steam reforming of residual oil in molten sodium phosphate. The residual oil employed had a low concentration of aromatic hydrocarbons. And the carbonized residual oil in the molten phosphate was found to closely resemble sponge petroleum coke. Hence the performance of the molten salt gasification

process as applied to residual oil steam reforming can be assessed by the use of a delayed coke product. It is the gasification of this coke which will determine the ultimate throughput of residual oil as its reaction rate controls the overall gasification scheme.

10.3 Recommendations for Further Research

We have repeatedly dealt with the effect of particle wetting characteristics on the performance of bubble column slurry reactors. Several aspects of these types of columns were dealt with in Chapter 2. The analysis however was far from being complete.

At the outset, an interesting fluid mechanical question is raised by bubble slowdown in particle suspensions. The nature of slowdown of bubbles rising through a suspension of nonwetting particles must be due to the increased drag on a particle laden bubble. To further elucidate the nature of this requires more extensive experimentation and a theoretical analysis. As flotation is an extensively applied industrial process, such further analysis is easily economically justified.

An intriguing aspect is the effect of particle wetting properties on bubble coalescence. It is generally undesirable to have bubbles coalesce in slurry reactors as one wants to maximize the amount of interfacial area and hence decrease

(not increase) average bubble size. That is, if one supplies the energy required to create a large amount of interfacial area, one does not want this energy dissipated by bubble coalescence. It thus seems justifiable to investigate bubble coalescence as a function of particle wetting properties. The effect of additives such as surfactants should also be studied. Such additives may be found to adsorb onto the particle and demote its coalescing character. And rather than measure the bubble coalescence rate indirectly by observing the change in total void fraction, a more appropriate experiment would be to measure bubble coalescence rates directly with the use of high speed photography. By injecting two or several bubbles at a time into a given column, a direct measurement of the rate of coalescence may be obtained.

The location of particles entrained on a bubble is also of interest. It is presumed intuitively that these should be swept hydrodynamically to the rear of the bubble. The question of how long on average they reside there is of substantial importance to the direct mechanism.

Finally the rate of direct contact of the particle with the bubble must be further studied. Of central importance is how long it takes for the particle to penetrate the gas-liquid interface. Here the direct mechanism was deduced and not directly observed. This

yielded a consistent picture. To reinforce this hypothesis, an estimate of how long it takes the particle to force liquid out of its path on its way to the gas in the bubble must be made. While briefly discussed in Chapter 2, this question is clearly deserving of further research.

10.4 Critique of the Molten Salt Gasification Process

Gasification in molten salts will not proceed until the corrosion problem is solved. This problem was briefly discussed in Chapter 9. The use of inorganic coatings (glazes) on porous supports seems to be a reasonable method of containment. This does require overfiring of the system to cure the glaze. It is strongly recommended that any further engineering studies of molten salts include an initial and thorough investigation of the corrosion problem.

The reaction rate of petroleum coke and char in molten phosphate may be inhibited as compared to the gas phase reaction rates by the fluid mechanics of the system. For higher bubble densities and more dilute particle loadings, the reaction rate in a slurry will be slightly above that in the gas phase due to the catalytic effect of the salt. Such a slight increase in the rate clearly does not justify the system economically. This is particularly true if one realizes the development work needed to solve the corrosion problem.

For a dispersion medium as well as a good heat transfer agent, molten salts are attractive. One not so obvious characteristic is their use with agglomerating particles. In Chapter 4, the addition of large amounts of agglomerating green sponge coke particles had an adverse effect on the reaction rate. Hence while it is acknowledged that a molten liquid medium can handle agglomerating carbons, the performance will decline due to the agglomeration. In large systems, such agglomeration may be retarded by the method of particle introduction. Hydrodynamic forces may also assist in breaking up agglomerated carbon particles. This hydrodynamic assistance depends on the binding force of agglomeration and on the particle size. That is, below a certain particle size, the particle will simply follow the liquid streamlines and shearing effects will be minimal.

I will conclude here with three salient points if further research is conducted on the gasification of carbonaceous materials in molten phosphates:

1. Corrosion containment is currently impossible unless a cold-walled reactor is employed. The use of hot-walled reactors will lead to dissolution of the reactor material. Care should be taken as these impurities could adversely affect the results.

2. Pumping when needed in such a system may be supplied by gas lift. Such pumping can provide steady liquid flows throughout an enclosed system.

3. One must examine the system's fluid mechanics carefully. The process may exhibit an overall inhibitory effect or an overall catalytic effect as compared to gas phase (no salt) results. Inhibition if observed will be caused by transport limitations and not by chemical inhibition of the gasification reaction by the molten phosphate.

APPENDICES

Appendix I. Bubble Rise Velocities in Molten Sodium Phosphate

The data for hold-up and superficial gas velocity were used to obtain the bubble rise velocity from (See Chapter 2):

$$\epsilon = \frac{u_{gs}}{u_B} \quad (\text{I-1})$$

Data from Chapter 6 and 7 were used as experiments entailed measuring hold-up, superficial velocity, and average bubble volume. The velocities obtained are indicated with their average bubble volumes in Table I-1. A least squares fit of the log of the rise velocity verses the log of bubble volume yielded:

$$u_B = 0.52 \langle V_B \rangle \quad (\text{I-2})$$

It is seen that bubble rise velocities are very slow due principally to the viscosity of the fluid and wall effects. Using maximum hold-up values, there can be at most five bubbles at a given time in our columns. The rate of mass transfer may then be calculated using values developed for the diffusion coefficient and gas solubility from Chapter 3 in correlations recommended by Perry and Chilton (1). Here we incorporate the results of Table I-1 in predicting the bubble Reynold's number. By assuming zero concentration in the bulk liquid, the maximum overall rate of mass transfer is about 10^{-4} to 10^{-5} moles/hr. This rate of mass transfer

Table I-1. The change in bubble rise velocity with bubble volume.

u_B (cm/s)	$\langle V_B \rangle$ (cm ³)
2.2	5.5
2.3	3.3
2.8	6.9
4.0	7.2
4.3	8.3
4.6	9.2
6.1	10.7
8.1	10.8

corresponds to no more than one milligram per hour of carbon reacting. Hence we must conclude that the indirect reaction rate mechanism cannot account for the slurry reactor rates observed in Chapters 6 and 7. It is acknowledged that mass transfer correlations have not been tested for high temperatures or for ionic melts. They are also not universally applicable for low temperature liquids. However the overall rate of oxidant transfer to the carbon in the melt proper would be further retarded by the resistances near and at the particle's surface discussed in Chapter 3.

These results are acknowledged to be very qualitative as mass transfer correlations for bubble columns are generally too specific to be applied universally (2). The low mass transfer rate presented here is due to the small driving force caused by the very low solubility of oxygen in molten sodium phosphate.

APPENDIX I - REFERENCES

1. Chemical Engineers' Handbook, Fifth Edition, (R. H. Perry and C. H. Chilton, eds.), McGraw-Hill, New York (1973)
2. Charpentier, J. C., Advances in Chemical Engineering, 11, 1 (1981)

Appendix II. The Effect of Mixing on the Observed Reaction Rate.

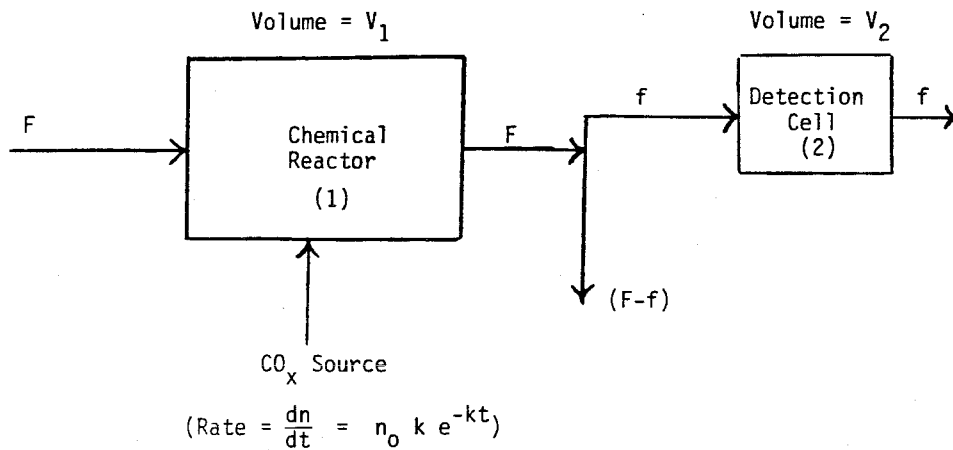
Mixing effects in the reactor and the infrared detection cell were of concern as experiments entailed following a dynamic (not static or steady state) reacting species. The basic concern here is the obscuring of the basic reaction rate as measured by the average concentration change in the detection cell with time.

The system was modelled as shown in Figure II-1. Here a flow F enters a well mixed reactor of volume, V_1 , where a source of CO_x exists. Upon exiting the reactor, a portion of the flow, $F-f$, is lost as the gas cools and the water vapor condenses leaving a flow, f , to enter the detection cell of volume, V_2 , which is also assumed well mixed. The resulting concentration in the infrared detection cell is given by:

$$C_2(t) = \frac{F k n_0}{V_1 V_2} \left\{ \frac{e^{-kt}}{\left(k - \frac{1}{\tau_1}\right) \left(k - \frac{1}{\tau_2}\right)} + \frac{e^{-t/\tau_1}}{\left(\frac{1}{\tau_1} - k\right) \left(\frac{1}{\tau_1} - \frac{1}{\tau_2}\right)} + \frac{e^{-t/\tau_2}}{\left(\frac{1}{\tau_2} - k\right) \left(\frac{1}{\tau_2} - \frac{1}{\tau_1}\right)} \right\}$$

The rate measured by such an experimental set up is simply $fC_2(t)$. Using typical values of τ_1 and τ_2 ; the rate constant, k , was found to measured accurately (from the slope of $\ln(fC_2(t))$ vs. time) after allowing for an induction period.

Figure II-1. The system model. Here we are simulating the gasification of char in a well mixed reactor.



Governing Differential Equations:

1. $\frac{dc_1}{dt} + c_1/\tau_1 = \frac{k n_0 e^{-kt}}{V_1}$
2. $\frac{dc_2}{dt} + c_2/\tau_2 = \frac{F c_1}{V_2}$
3. Boundary Conditions $C_1(0) = C_2(0) = 0$.

where: F = flowrate into Reactor (1) (cm^3/min)

f = Flowrate into Detector (2) (cm^3/min)

c_1 = CO_x Concentration in Reactor (1) (gmol/cm^3)

c_2 = CO_x Concentration for Reactor (2) (gmol/cm^3)

$\tau_1 = V_1/F$

$\tau_2 = V_2/f$

n = Moles of Carbon at Time t

n_0 = Initial Moles of Carbon at Time 0

k = Reaction Rate (min.^{-1})

This requires:

$$\frac{1}{k} > \tau_2 > \tau_1$$

Thus at a given flowrate, this indicates that k has a maximum measurable value. This maximum value was safely avoided in all experiments.

Appendix III. The Mixing Effects Caused by Laminar Flow

A possible effect in addition to that discussed in Appendix II is laminar flow in the connecting tubes from the reactor to the detection cell obscuring the measured reaction rate expression. Figure III-1 presents a schematic of the problem along with the governing partial differential equation and relevant boundary conditions.

First it is apparent that the flux across a tube cross-

$$\int u \frac{\partial c}{\partial z} dA \gg \int D \frac{\partial^2 c}{\partial z^2} dA \quad (\text{III-1})$$

section is principally governed by convection for fast enough flows (equation III-1). After eliminating axial diffusion and using the dimensionless variables:

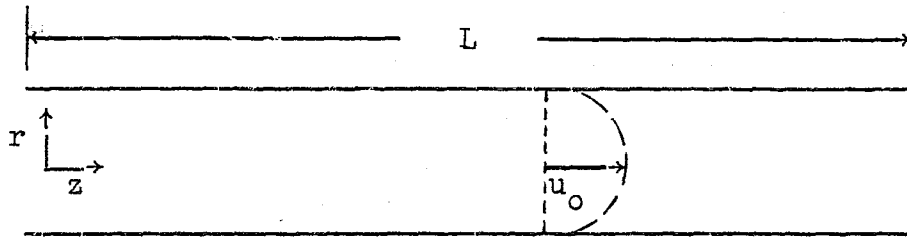
$$\xi = z/L ; \quad \eta = r/a ; \quad \psi = c/c_o ; \quad \tau = \frac{tu_o}{2L} \quad (\text{III-2})$$

we have:

$$\frac{\partial \psi}{\partial \tau} + (1-\eta^2) \frac{\partial \psi}{\partial \xi} = \frac{2DL}{u_o a^2} \left\{ \frac{1}{\eta} \frac{\partial}{\partial \eta} \left(\eta \frac{\partial \psi}{\partial \eta} \right) \right\} \quad (\text{III-4})$$

If it is further assumed that radial variations in concentration dissipate quickly as compared to appreciable effects becoming noticeable due to convection, this problem may be solved using the method of Taylor(1). The solution follows:

Figure III-1. The Problem Schematic and the Governing Equation.



$$D \left(\frac{\partial^2 c}{\partial r^2} + \frac{1}{r} \frac{\partial c}{\partial r} + \frac{\partial^2 c}{\partial z^2} \right) = \frac{\partial c}{\partial t} + u_0 \left(1 - \frac{r^2}{a^2} \right) \frac{\partial c}{\partial z}$$

Boundary Conditions:

$$z = 0 \quad c = c_0 e^{-kt}$$

$$z = L \quad \frac{\partial c}{\partial z} = 0$$

$$t = 0 \quad c = 0$$

$$z > 0 \quad c = 0$$

Where:

- D = The Diffusion Coefficient
- c = The Concentration
- u_0 = The Maximum Velocity in the Laminar Velocity Profile
- a = The Tube Radius
- z = The Axial Position
- L = The Total Length of the Tube
- t = The Time

$$\psi = e^{-\kappa\tau} e^{\eta\delta} \left\{ \frac{\sinh(\beta\gamma)}{\sinh(\beta\delta)} + \frac{\beta \cosh(\beta\gamma)}{\beta \cosh(\beta\delta)} \right\}$$

$$- e^{(2\eta-\tau)\delta/2} \sum_{n=1}^{\infty} \left[\frac{e^{-(\lambda_n^2\tau\delta/2)}}{\kappa - (1+\lambda_n^2)\delta/2} \left\{ \frac{\lambda_n \sin(\lambda_n\gamma) + \lambda_n^2 \cos(\lambda_n\gamma)}{(1+1/\delta)\cos(\lambda_n\delta) - \sin(\lambda_n\delta)} \right\} \right]$$

where: $\delta = \frac{48 DL}{a^2 u_0}$

$$\beta = \sqrt{1 - \frac{2\kappa}{\delta}}$$

(III-4)

$$\lambda_n = -\tan(\lambda_n\delta)$$

$$\kappa = \frac{2Lk}{u_0}$$

$$\gamma = \delta(1-\eta)$$

As applied to experiments presented in this thesis, δ is of the order of 10^4 . Consequently the solution is stiff as $e^{\eta\delta}$ is very large for η greater than zero. But for τ greater

than three which corresponds to less than two minutes for our experiment, the second term is negligible for all η . Thus we have at $\eta = 1$:

$$\psi = \frac{\beta e^{\delta} e^{-\kappa\tau}}{\sinh(\beta\delta) + \beta \cosh(\beta\delta)} = K e^{-\kappa\tau} \quad (\text{III-5})$$

As $\beta\delta \gg 1$:

$$K \approx \frac{2\beta}{1 + \beta} e^{(1-\beta)\delta} \quad (\text{III-6})$$

β is very close to unity if κ is not too large (as is the present case). Hence if we expand β in a Taylor series, we have:

$$\psi \approx e^{-\kappa(\tau-1)} = e^{-k(t - \frac{2L}{u_0})} \quad (\text{III-7})$$

Thus after allowing a short induction period, the input is followed with only a simple time delay. This delay corresponds to the average residence time of the species in the tube.

APPENDIX III - REFERENCE

1. Taylor, G., Proc. Royal Society (London), A219,
186 (1953)

Appendix IV. Thermal Pyrolysis and Steam Reforming Experiments

Here we shall deal in turn with three topics. First typical product distributions for thermal cracking and steam reforming of light hydrocarbon gases will be given. Secondly we shall present the products of green sponge petroleum coke pyrolysis. We will conclude with some carbon entrainment experiments.

IV.1 Thermal Cracking and Steam Reforming

The reactor employed for these studies was tubular. Its characteristics are given in Table IV-1. The reactions were carried out on the surface of molten sodium phosphate as well as on the surface of fused mullite. The composition of the molten salt was $\text{Na}_2\text{O}/\text{P}_2\text{O}_5 = 1.31$ molar.

Typical product distributions are given in Tables IV-2 and IV-3 for the cracking of methane on the surface of fused mullite and molten salt respectively. The feed contained a small amount of ethane. Acetylene and ethylene are produced from the feed methane and ethane directly. The amounts of acetylene and ethylene increase with temperature.

Typical product distributions for the cracking of ethylene are presented in Table IV-4. The rates of cracking are substantially higher than those for methane cracking, and the products contained C_4 and higher hydrocarbons in addition to H_2 , C_1 , C_2 , and C_3 hydrocarbons.

Table IV-1. The Volume and Surface Area of Reactor III.

<u>Reactor III</u>	<u>Volume, cm³</u>	<u>Surface Area, cm²</u>	<u>Surface to Volume, cm⁻¹</u>
Without Salt	63	110	1.7
With Salt	45	81	1.8

Table IV-2. Typical Product Distribution in the Cracking
of Methane on Mullite, Reactor III.

T, °K	1127	1178
Feed		
CH ₄ %	99.63	99.63
C ₂ H ₆	0.37	0.37
Flow Rate, gmols/hr	0.29	0.29
Product		
H ₂ %	3.94	21.02
CH ₄	95.56	78.09
C ₂ H ₂	0.00	0.00
C ₂ H ₄	0.37	0.76
C ₂ H ₆	0.09	0.08
C ₃ H _x	0.05	0.06
Flow Rate, gmols/hr	0.30	0.33

Table IV-3. Typical Product Distribution in the Cracking of Methane on Molten Sodium Phosphate, Reactor III.

T, K	1127	1178
Feed		
CH ₄ %	99.63	99.63
C ₂ H ₆	0.37	0.37
Flow Rate gmols/hr	0.29	0.29
Product		
H ₂ %	1.83	11.23
CH ₄	97.62	87.16
C ₂ H ₂	0.00	0.32
C ₂ H ₄	0.37	1.15
C ₂ H ₆	0.11	0.14
C ₃ H _x	0.07	0.01
Flow Rate gmols/hr	0.30	0.31

Table IV-4. Typical Product Distribution in the Cracking of Ethylene, Reactor III.

	Mullite	Molten Sodium Phosphate
Temperature, K	1115	1115
Feed		
Flow Rate, gmols/hr	0.22	0.22
Product		
H ₂	37.2	27.6
CH ₄	32.2	32.6
C ₂ H ₂	0.1	0.9
C ₂ H ₄	25.2	32.6
C ₂ H ₆	4.4	4.3
C ₃ H _x	0.4	1.0
C ₄ H _x	0.5	1.0
C ₅ ⁺ *	Trace	Trace
Flow Rate, gmols/hr	0.26	0.25

*Trace amounts of these species were observed, but GC sensitivity was not high enough to record the amount.

Table IV-5 indicates typical product distributions for methane steam reforming on molten sodium phosphate. Steam here was supplied in substantial amounts employing the steam generator outlined in Chapter 10 (Figure 7b of Chapter 10).

IV.2 Pyrolysis Products of Green Sponge Coke

Unclassified green sponge coke I particles (see Chapter 4) were pyrolyzed and gasified by adding them to the large reactor of Chapter 10. This reactor had a very large free volume, and hence these results are only qualitative. The results represent an integrated product distribution over time and are given in Table IV-6. Methane is the predominant product, and a large amount of benzene also evolves.

IV.3 Carbon Retention and Entrainment

For these experiments, the reactor shown in Figure IV-1 was employed. This consisted of a mullite tube completely surrounded by a castable container. During operation, the two phase fluid expands to occupy the mullite tube below the castable. A baffle plate (not shown) prevents the entrainment of the melt into the exit tube.

In the steam reforming experiments it was observed that a significant amount of the formed coke was entrained with the product stream. This amount can be determined at steady

Table IV-5. Typical Product Distribution in the Steam Reforming of Methane on Molten Sodium Phosphate, Reactor III.

T, K	1170	1220
Feed	-	
H ₂ O%	79.9	79.9
CH ₄	20.0	20.0
C ₂ H ₆	0.07	0.07
Flow Rate, gmols/hr	1.46	1.46
Product		
H ₂ O%	79.7	79.5
CO	0.02	0.03
CO ₂	0.03	0.05
H ₂	0.21	0.71
CH ₄	19.9	19.6
C ₂ H ₂	0.00	0.02
C ₂ H ₄	0.04	0.08
C ₂ H ₆	0.04	0.03
Flow Rate, gmols/hr	1.46	1.46

Table IV-6. Pyrolysis Products of Unclassified Green Sponge Coke I at 1120 K. Distributions Given Relative to Methane.

Hydrocarbon	20% H ₂ O/80% N ₂	Air
Methane	1.0	1.0
Ethane	0.010	0.003
Ethylene	0.054	0.087
C ₃	0.003	Trace
C ₅	0.052	0.008
Benzene	0.020	0.10

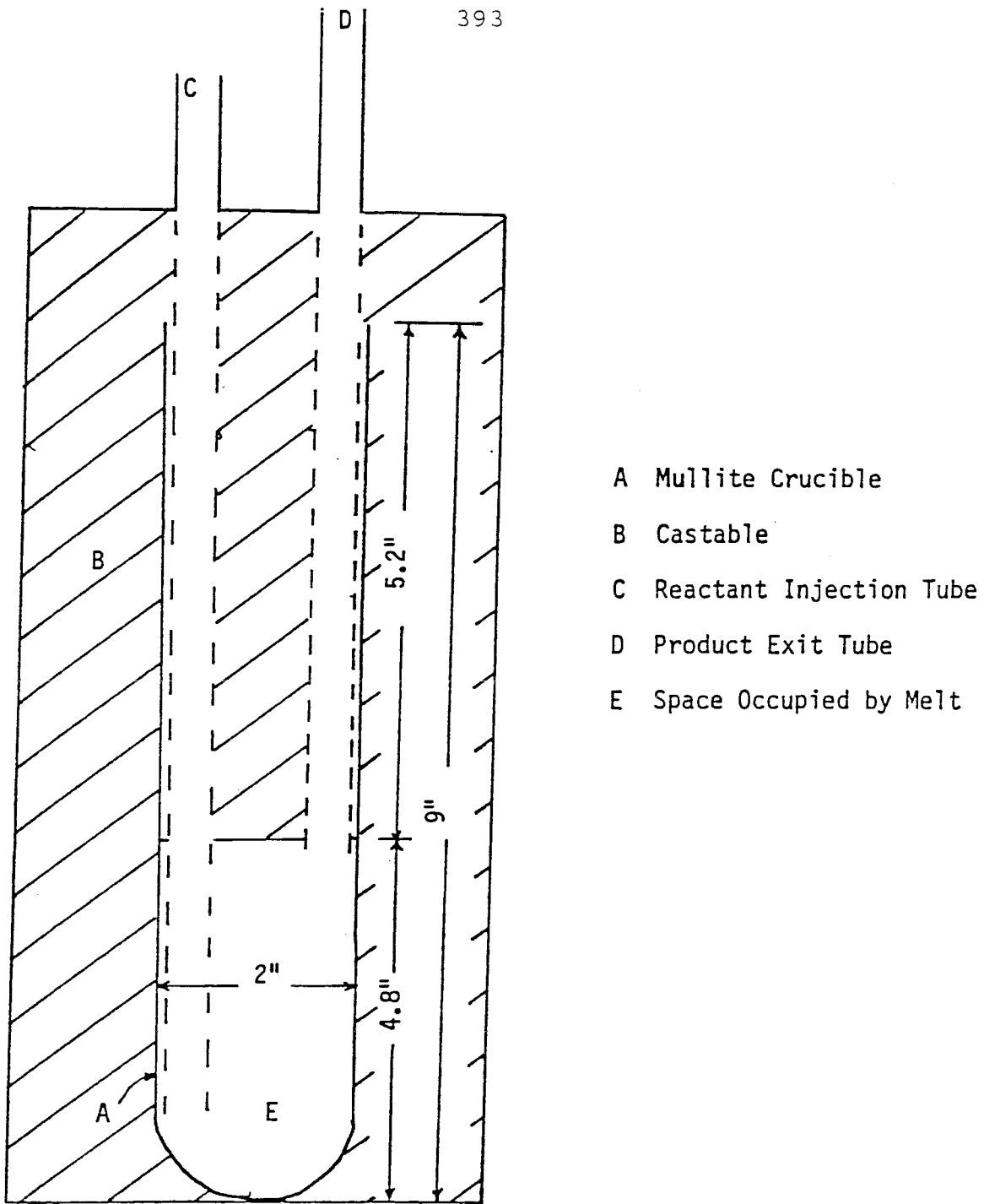


Figure IV-1. The Reactor Used to Study Carbon Retention and Entrainment.

state by the following carbon balance:

$$XN_{in}(\text{CH}_4) = N_{out}(\text{CO}) + N_{out}(\text{CO}_2) + N_{out}(\text{C})$$

Where X is the methane conversion, N indicates molar flow rate and in, out indicate input (feed) and output (product) streams. The fraction of methane converted to entrained carbon is:

$$\xi = \frac{N_{out}(\text{C})}{XN_{in}(\text{CH}_4)}$$

The results of these calculations are given Table IV-7. About 60% of the methane converted is in the form of entrained coke. In the experiments reported in Table IV-7 the reactant was bubbled through a pool of melt about 3 cm. deep.

Experiments were also performed to determine the amount of coke retained at steady state in the steam reforming of methane in molten phosphate. The determination was made by measuring the total amount of carbon oxides evolved after the flow of methane was shut off. Two cases were studied. In one the gases were bubbled through the melt employing the reactor of Figure IV-1. In the other the gases passed over a stationary surface of molten salt in a simple tubular reactor. The data are presented in Table IV-8 and show that the amount of coke retained in both bubbling and non-bubbling flows is very small.

Table IV-7. Steady State Carbon Entrainment

T (K)	Entrained Carbon % of Carbon Produced
1109	55
1116	43
1149	84
1152	75
1156	86
1159	65
1159	66
1160	63
1161	73
1200	60
1289	51
1293	41

T (K)	Superficial Velocity (cm/s)	Weight Fraction of Carbon in Melt	Weight of Carbon Per Unit Interfacial Area (g/cm ²)
1059 (B)	2.4	2.8×10^{-5}	5.0×10^{-6}
1059 (B)	2.5	2.1	6.9
1162 (B)	1.0	2.9	9.0
1170 (NB)	7.7	5.3	20.7
1220 (NB)	8.0	9.5	37.4

(B): bubbling flow

(NB): flow past a fixed surface

Table IV-8. Steady State Retention of Carbon

A few visual observations were made on the nature of the carbon retained in the reactor:

a. In the cracking experiments on fused mullite, a shiny carbon layer was found coating the walls of the reactor.

b. In cracking experiments in molten salt with the methane bubbling through the salt, carbon was found evenly dispersed throughout the salt.

c. In the steam reforming of methane, all carbon was found in the space above the salt. The salt was clear and appeared devoid of carbon.

d. A fine graphite powder was mixed with the molten salt using a stream of nitrogen and the system was cooled. No penetration of graphite into the bulk of the salt was observed.

Appendix V. The Materials used for Reactor Construction

Here we shall list the composition of the materials used. These are product specifications and are typical analyses. This is to list possible impurities in the molten phosphates due to the dissolution of the reactor.

Three materials were employed. Castolast G from Harbison-Walker Corporation was the castable used to seal the fused mullite and alumina parts into a reactor configuration. While this material was not used to directly contain the molten salt, it did have some contact with the expanded salt baths. The materials which were used to contain the salt were fused mullite (McDanel MV-30) and fused alumina (McDanel 998). These were supplied by McDanel Refractory Company. The compositions are listed in Table V-1.

Molten sodium phosphates were made by fusing mixtures of $(\text{NaPO}_3)_6$ (sodium metaphosphate) and $\text{Na}_4\text{P}_2\text{O}_7 \cdot 10 \text{H}_2\text{O}$ (hydrated sodium pyrophosphate). Both phosphates were 'Baker Analyzed' reagents and yielded basic solutions in water. Equal weights of the metaphosphate and pyrophosphate gave a sodium oxide to phosphorus pentoxide molar ratio of 1.31.

Rapidly cooling the phosphate melts produced a translucent glass. Slower cooling allowed significant crystallization, and the product was a glass interspersed with crystallites.

Table V-1. The Compositions of the Materials Used to Construct the Reactors.

Compound	Castolast G (Weight %)	Fused Mullite (Weight %)	Fused Alumina (Weight %)
Al_2O_3	93.7	60.0	99.8
SiO_2	0.1	38.0	0.070
Fe_2O_3	0.3	0.5	0.025
CaO	5.6	0.1	0.030
Na_2O		0.2	0.005
K_2O		0.7	-
MgO		0.2	0.050
MnO		-	0.001
Ga_2O_3		-	0.009
TiO_2		0.5	0.004

In some cases, an amorphous powder could be created by extremely slow cooling. Glasses produced by fusion in mullite crucibles (MV-30) were found to contain significant amounts of Al^{+3} and silica thus confirming the dissolution of the reactor material.